NASA

National Aeronautics and
Space Administration

NASA CR-135197
MCR77-131

FINAL REPORT

CHARACTERIZATION OF CRACK GROWTH

UNDER COMBINED LOADING

By

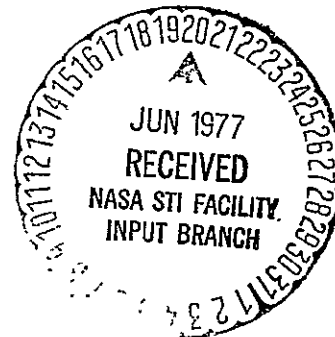A. Feldman, F. W. Smith and A. Holston, Jr.

MARTIN MARIETTA CORPORATION
Denver Division

Prepared for:

National Aeronautics and Space Administration

NASA Lewis Research Center
Contract NAS3-17810

Gordon T. Smith, Program Manager

1. Report No. NASA CR-	2. Government Accession No.	3. Recipient's Catalog No.	
4. Title and Subtitle Characterization of Crack Growth Under Combined Loading		5. Report Date June 1977	
		6. Performing Organization Code	
7. Author(s) A. Feldman, F. W. Smith, A. Holston, Jr.		8. Performing Organization Report No. MCR-77-131	
9. Performing Organization Name and Address Martin Marietta Corporation P. O. Box 179 Denver, Colorado 80201		10. Work Unit No.	
		11. Contract or Grant No. NAS3-17810	
12. Sponsoring Agency Name and Address National Aeronautics and Space Aministration Lewis Research Center Cleveland, Ohio 44135		13. Type of Report and Period Covered Final Report 6 June 1974 – 15 March 1977	
		14. Sponsoring Agency Code	

15. Supplementary Notes

16. Abstract

Room-temperature static and cyclic tests were made on 21 aluminum plates in the shape of a 91.4x91.4-cm (36x36-in.) Maltese cross with 45° flaws to develop crack growth and fracture toughness data under mixed-mode conditions. Alloy thickness combinations were 2219-T87 1.55- and 0.64-cm (0.61- and 0.25-in.) thick and 7075-T7351 1.27-cm (0.50-in.) thick. During cyclic testing, it was impossible to maintain a high proportion of shear-mode deformation on the crack tips. Cracks either branched or turned. Under static loading, cracks remained straight if shear stress intensity exceeded normal stress intensity. Mixed-mode crack-growth rate data compared reasonably well with published single-mode data, and measured crack displacements agreed with the straight and branched crack analyses. Values of critical strain energy release rate at fracture for pure shear were approximately 50% higher than for pure normal opening, and there was a large reduction in normal stress intensity at fracture in the presence of high shear stress intensity. Net section stresses were well into the inelastic range when fracture occurred under high shear on the cracks.

17. Key Words (Selected by Author(s)) Fracture Mechanics Through Cracks Flaw Growth Fracture Toughness Combined Modes I and II	18. Distribution Statement Distribution of this document is unlimited.		
19. Security Classif. (of this report) Unclassified	20. Security Classif. (of this page) Unclassified	21. No. of Pages 240	22. Price

FOREWORD

This report is submitted by Martin Marietta Aerospace, Denver Division, in fulfillment of Contract NAS3-17810, Characterization of Crack Growth under Combined Loading, and covers the entire effort performed under that contract. This effort was accomplished between 6 June 1974 and 15 March 1977.

TABLE OF CONTENTS

LIST OF FIGURES

LIST OF TABLES

SUMMARY

An experimental program to develop grack growth and fracture toughness data under mixed mode conditions was undertaken. In a unique mixed-mode machine, room-temperature tests were made of 21 flawed aluminum plates in the shape of a 91x91-cm (36x36-in.) modified Maltese cross. Six were 2219-T87 1.55-cm (0.61-in.) thick; four were 2219-T87 0.64-cm (0.35-in.) thick; and eleven were 7075-T7351 1.27-cm (0.50-in.) thick. Ten specimens were tested statically to fracture, five were tested cyclically then statically, and six were only tested cyclically, under loads ranging from pure tension on the flaw tip to pure shear. All flaws were oriented 45° to the loading directions. Analysis of test results was directed to computing critical strain energy release rates, G_{cr}, and strain energy release rate, ΔG, versus crack growth rate, $\Delta a/\Delta N$. Stress intensities were computed from coefficients derived from finite-element analyses of straight, Z-shaped, and branched cracks. The Maltese cross shape permitted any combination of K_I and K_{II} with a 45° flaw orientation. Stress intensity coefficients were nearly constant for a range of crack lengths. The area of strain uniformity under biaxial load in the center of an unflawed specimen extended for a diameter of about 25.4 cm (10 in.).

During cyclic testing, it was impossible to maintain a high proportion of shear-mode deformation on the crack tips. The cracks either branched or turned, resulting in crack fronts with little shear. Under static loading to fracture, straight 45° cracks remained straight only when shear stress intensity exceeded normal stress intensity, otherwise they turned.

Mixed-mode crack-growth rate data, analyzed in terms of G, compared reasonably well with published single-mode data. There was little difference in the effectiveness of analyses used to analyze crack growth data. Straight and branched cracks were analyzed using Holston factors, and Z-shaped cracks using Iida factors, yet there was not an abrupt change in computed quantities when cracks changed configuration. Measured crack displacement during cyclic tests agreed well with straight and branched crack analyses over the range of applicability.

In fracture tests, values of G_{cr} for pure shear were approximately 50% higher than G_{cr} for pure normal opening, and there was a large reduction in K_I resulting from application of K_{II}. However, net section stresses were well into the inelastic range when fracture occurred with high shear. Values of G_{cr} were affected by the relation between flaw growth direction and rolling direction for the 7075-T7351 alloy but apparently not for 2219-T87.

INTRODUCTION

Technical Background

The development of linear elastic fracture mechanics has provided concepts and data to designers that may be used to formulate criteria for the structural design of elements and the selection of materials. These criteria are based on characterization of flaw growth in the element by parameters that describe the stress field near the ends of the flaw. The specification of this stress field for an arbitrary loading condition requires determination of the three stress intensity parameters K_I, K_{II} and K_{III}. These parameters provide a convenient means of relating the stress field conditions to the crack loading conditions. Loading conditions such that displacements are normal to the crack plane (opening mode) are represented by the parameter K_I. Loading conditions producing shear displacements parallel to the crack plane and in the plane of the specimen are represented by K_{II}, and loading conditions producing shear parallel to the crack plane and perpendicular to the specimen are presented by K_{III}.

Most fracture mechanics work, both analytical and experimental, has focused on the opening $\left(K_I\right)$ mode of deformation. Tensile specimens were loaded normal to the flaw; analyses were developed for different configurations with loadings that produced only the opening mode. However most structures experience at least biaxial loading. For example a spherical tank has equal biaxial stresses and a cylindrical pressure vessel has a 2 to 1 stress state. Furthermore the flaw may be oriented at any angle relative to the principal stresses since the flaws are uncontrollable. Thus the opening mode is a special case, with the combined or mixed mode being the general case.

In the past the mixed-mode problem has been ignored in most designs. The flaw has been assumed to be oriented perpendicular to the largest principal stress. Then allowable flaw sizes have been established based on the critical value of K_I and flaw growth has been calculated considering only K_I. This approach has been unavoidable due to the lack of understanding of the mixed-mode problem and the corresponding absence of appropriate data. However, there is no reason to believe that it is necessarily conservative.

Only limited data are available for definition of the effects produced by the introduction of shear loading that is concurrent with the opening mode load. Information developed during a recent NASA program, NAS3-14346 (ref. 1), has revealed that a significant reduction in the tensile load-carrying ability of a cracked 4340 steel member may accompany the application of mode II loading conditions. Limited data on some 5000- and 7000-series aluminum alloys obtained from the literature show much less degradation than was found for the 4340 steel alloy. The degradation effect of combined modes I and II mixed-mode loading appears to be material-dependent for static fracture conditions and virtually undefined for cyclic conditions. Crack-growth data--both static and cyclic--for materials of structural interest in aerospace hardware are needed to evaluate the consequences of high shear loading conditions. The continued lack of data concerning the mixed-mode fracture behavior will continue to block use of fracture control measures in the design of aerospace hardware and may lead to serious structural deficiencies.

Objective

The objective of this program was to develop crack growth and fracture toughness data under combined loading "mixed-mode" conditions. To accomplish this objective aluminum plates with through flaws have been cyclically and statically tested under biaxial loading and the resulting data analyzed. The purpose of this work was also to establish the applicability of various theories of flaw growth and fracture to mixed-mode conditions. To this end the test results have been compared with predictions gained from the methods of analyses.

Scope

The objectives were pursued through a program of room temperature testing in a unique machine of 21 flawed aluminum plates in the shape of a 91.4x91.4-cm (36x36-in.) modified Maltese cross. All flaws were through the thickness, 5- to 10-cm (2- to 4-in.) long and oriented 45 deg to the directions of load application. Three combinations of alloy and thickness were employed--six specimens were 2219-T87 1.55-cm (0.61-in.) thick, four specimens were 2219-T87 0.64-cm (0.25-in.) thick, and 11 specimens were 7075-T7351 1.27-cm (0.50-in.) thick.

4

Ten specimens were tested statically to failure, requiring one to three minutes to fracture. The mixed-mode combination of loads ranged from pure tension on the flaw tip $\left(K_I\right)$ to pure shear $\left(K_{II}\right)$. Five specimens were tested cyclically until substantial crack growth was realized and then tested statically to fracture. The six remaining specimens were tested only cyclically. Although the cyclic tests were also intended to span the full range from pure K_I to pure K_{II}, curved crack trajectories and branching phenomena resulted in essentially removing shear from the crack tips.

The analysis of the test results consisted of (1) computing critical stress intensities, K_{Ic} and K_{IIc}, and critical strain energy release rates, G_{cr}, for the static tests based on plots of the crack growth resistance, R, and (2) plotting strain energy release rate, G, versus crack growth rate, and compliance versus crack length for all the cyclic tests. The test results are compared with predictions derived from the theories of Griffith as modified by Irwin (extended), Erdogan and Sih (maximum stress), and Sih (strain energy density). Variables taken into account in the analyses and comparisons were alloy, thickness, final rolling direction, and the effect of the ratio of K_I/K_{II}. Test results are also compared with data from other investigations.

Combined-Mode Fracture Data

The study was limited to determining the effects on static fracture and fatigue of combined modes I and II loading conditions. For static fracture conditions, the effects of combined modes I and II loading are commonly described in terms of an interaction diagram such as the one shown in figure 1. Figure 1 plots data from tests by a number of investigators using several materials in attempts to define modes I and II interaction effects. The data range from indicating little or no interaction effect for static fracture to indicating a very significant interaction effect. Additional data of a similar nature for 7075-T6 and 7075-T651 indicate almost no interaction effect in one case (ref. 2) and a fairly significant amount in another (ref. 3), although not as strong as the linear interaction seen by Shah (ref. 1) and Liu (ref. 4).

Ranganath and Goolsby (ref. 3) reported a significant effect on interaction of the material thickness. This implies that plasticity effects could play an important role in the interaction process. In fact, plastic zone sizes are quite different in modes I and II. The associated energies to produce fracture could then be quite different and the interaction diagram might depend on the way in which the modes I and II plasticity fields interact for structural metals.

It appears that the K_I and K_{II} calculations at fracture in most if not all of the referenced data assumed that the crack did not undergo out-of-plane growth before reaching instability and the K_I, K_{II} values plotted did not account for the out-of-plane crack growth that normally occurs in mixed modes I and II fracture situations. In this study, subcritical growth was experienced and attempts are made to present interaction data in which the effects of subcritical growth and growth direction were taken into account.

Theories of Fracture

Table I summarizes the various theories of fracture, some of which are intended to predict fracture under conditions of mixed-mode loading. Included in the table is information on the physical basis for the theory, the predicted ratio between mode I and mode II critical stress intensities, the predicted crack propagation direction, and the predicted interaction diagram.

Symbol	Source	Material
○	Shah (ref. 1)	4340 Steel
◊	Liu (ref. 4)	7075-T651 A
◇	Liu (ref. 4)	2024-T3 A
△	Wilson (ref. 18)	7178-T651 A
□	Pook (ref. 19)	DTD 5050 A
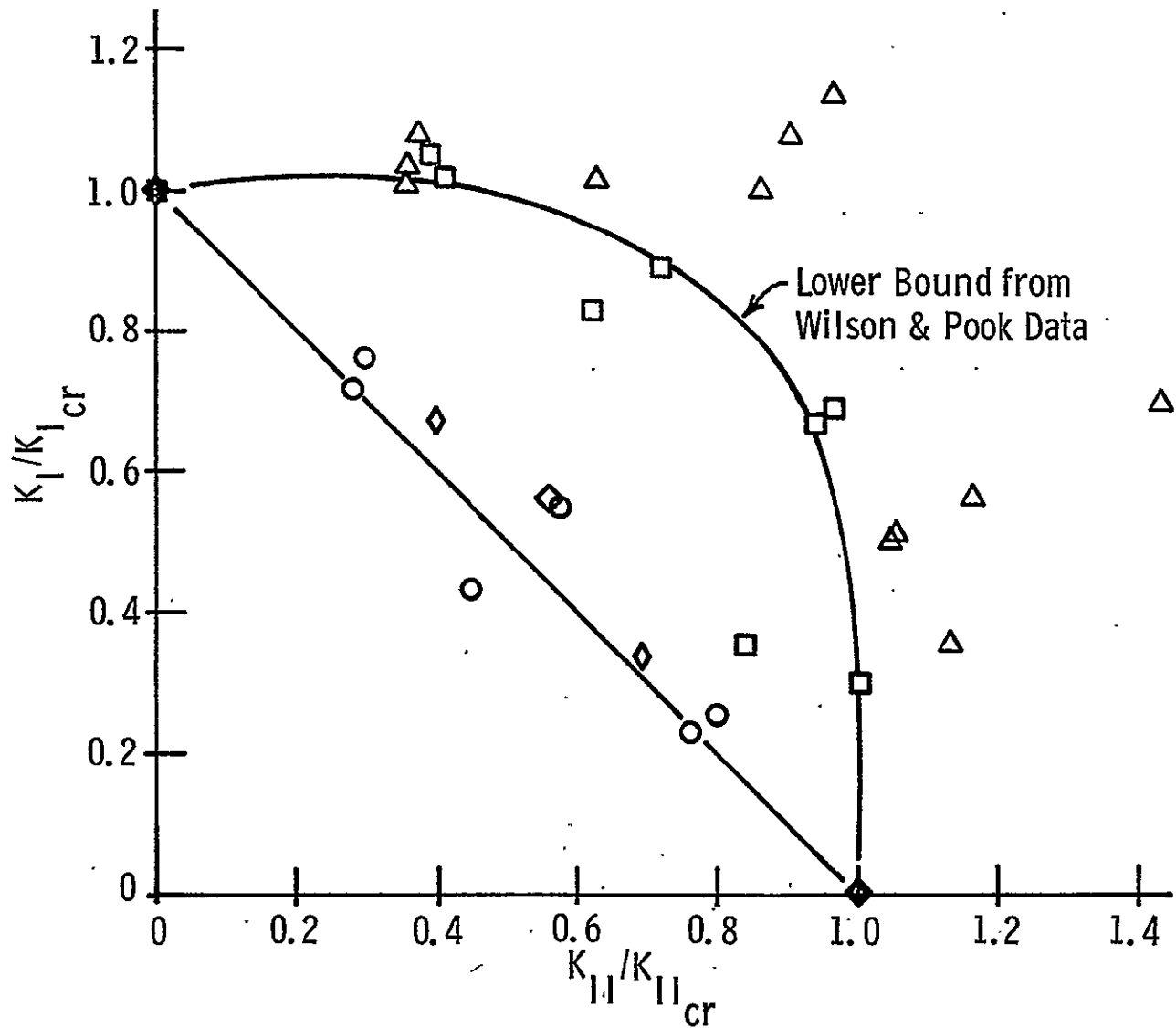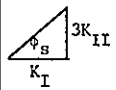
Figure 1. – Interaction of mixed-mode loading on plates.

TABLE I. – SUMMARY OF FRACTURE THEORIES

Identification	Basis	K_{IIc}/K_{Ic}	Fracture direction	Mode I and Mode II Interaction
Griffith	Strain energy release rate $$G = G_{cr}$$	Not applicable	Assumed colinear growth	Not applicable $G = G_{cr}$ $\dfrac{G}{G_{cr}} = 1$
Irwin/Griffith	Related K_I to G $$G = \frac{1-\nu^2}{E} K_I^2 = G_{cr} \text{ (plane strain)}$$	Not applicable	Assumed colinear growth	Not applicable $K_I = K_{Ic}$ $\dfrac{K_I}{K_{Ic}} = 1$
Extended Irwin/Griffith	Added shearing mode energies $$G = \frac{1-\nu^2}{E}\left[K_I^2 + K_{II}^2\right] = G_{cr} \text{ (plane strain)}$$	1.0	Valid only for colinear growth	$K_I^2 + K_{II}^2 = K_{Ic}^2$, $\dfrac{K_I^2}{K_{Ic}^2} + \dfrac{K_{II}^2}{K_{Ic}^2} = 1$
Maximum stress theory Erdogan, Sih (ref. 7)	Maximum tangential stress intensity $$\sigma_{\theta\theta}\sqrt{2\pi r} = \cos\frac{\theta}{2}\left(K_I \cos^2\frac{\theta}{2} - \frac{3}{2} K_{II} \sin\theta\right) = K_{Ic}$$ reduces to Irwin/Griffith for $K_{II} = 0$	0.866	Normal to maximum $\sigma_{\theta\theta}$ $$\theta_c = \sin^{-1}\left(\frac{1}{3}\sin\phi_s\right) - \phi_s$$ [triangle: ϕ_s, $3K_{II}$, K_I]	$\cos\dfrac{\theta}{2}\left(\dfrac{K_I}{K_{Ic}}\cos^2\dfrac{\theta_c}{2} - \dfrac{3}{2}\dfrac{K_{II}}{K_{Ic}}\sin\theta_c\right) = 1$
Strain energy density Sih (ref. 8)	Minimum strain energy density $$U = \frac{S}{r} \quad k_i = K_i/\sqrt{\pi}$$ $$S = S_{cr} = a_{11} k_1^2 + 2a_{12} k_1 k_2 + a_{22} k_2^2$$ Reduces to Irwin/Griffith for $K_{II} = 0$	$\left[\dfrac{3(1-2\nu)}{2-2\nu-\nu^2}\right]^{1/2}$	Direction of minimum S $$2(1-\nu)\sin(\theta_c - \phi_E) - 2\sin[2(\theta_c - \phi_E)] - \sin 2\theta_c = 0$$ [triangle: K_I, II]	$\left(\dfrac{K_I^2}{K_{Ic}^2} + \dfrac{K_{II}^2}{K_{Ic}^2}\right)\Big(a_{11}\sin^2\phi_E + 2 a_{12}\sin\phi_E\cos\phi_E + a_{22}\cos^2\phi_E\Big) = 1$ $a_{11} = \dfrac{(3-4\nu - \cos\theta_c)(1 + \cos\theta_c)}{4(1-2\nu)}$ $a_{12} = \dfrac{2\sin\theta\,[\cos\theta_c-(1-2\nu)]}{4(1-2\nu)}$ $a_{22} = \dfrac{4(1-\nu)(1-\cos\theta_c)}{4(1-2\nu)} + \dfrac{(1+\cos\theta_c)(3\cos\theta_c - 1)}{4(1-2\nu)}$

The first theory identified is the Griffith theory of fracture. This fracture theory is based on the concept that unstable crack propagation will occur when the strain energy released during an increment of crack growth is bigger than the energy necessary to drive the crack through the material. In this theory the energy required to drive the crack was considered to be surface energy associated with the new crack surface. Cracks are assumed to grow in the original plane of the crack, which is oriented normal to the applied tensile stress. In its originally stated form, this theory does not apply to situations involving mixed-mode fracture.

The second theory is identified as the Irwin/Griffith theory. The physical basis for this theory is the same as the physical basis for the Griffith theory, i.e., the strain energy release rate is considered to be the driving energy source for the fracture process. However, in this theory the energy required to drive the crack through the material is considered to be dominated by the energy of plasticity required to form a small plastic zone at the crack tip as the crack propagates through the material. This energy is thought to be very much larger than the surface energy of the Griffith theory. For conditions of highly constrained plasticity, a material property G_{cr} is considered to characterize the fracture process. This theory also introduces the notion of stress intensity factor and develops a relationship between the stress intensity factor and the strain energy release rate G by considering the amount of energy released as a crack in an elastic field grows by an incremental amount in the original plane of the crack. The fracture criterion is then recast by considering a critical value of stress intensity at failure known as fracture toughness. This theory also does not directly relate to conditions of mixed-mode fracture.

The third theory referred to is the extended Irwin/Griffith theory. This theory attempts to deal with problems of mixed-mode fracture on the same physical basis as used in the first two theories. In this case, however, the total strain energy release rate for a mixed-mode situation is computed by adding the strain energy release rates associated with the modes of fracture to be considered. It is important to note that adding the strain energy release rates due to the separate modes in this way is valid only as long as the crack is assumed to undergo incremental growth in the original plane of the crack. Fracture is still considered to occur when the strain energy release rate reaches a critical value. Under this assumption, the ratio of mode II fracture toughness to mode I fracture toughness is found to be unity. The predicted interaction is given by the equation shown for that case in table I, which is the equation of a circle in the first quadrant of a K_I, K_{II} space.

The extended Irwin/Griffith theory can be made applicable to situations of mode I, mode II loading where crack growth occurs in a plane other than the original plane of the crack. To do this it is necessary to know in advance, or be able to predict by an appropriate hypothesis, the angle at which crack growth will occur. The stress intensity factors appropriate for the new crack growth direction must then be calculated. In this manner the calculation of G through adding the strain energy release rates due to the active modes is compatible with the assumptions of the theory. This approach has been discussed by Cotterell (ref. 5), Hussain, et al. (ref. 6), and others.

The fourth theory to appear in table I is identified as the maximum stress theory discussed by Erdogan and Sih (ref. 7). The physical basis for this theory is the hypothesis that fracture occurs along a radial line emanating from the crack tip on which the tangential stress component is a maximum. It is further hypothesized that fracture occurs when the stress intensity factor for tangential stress along that line reaches a critical value, which is taken to be the fracture toughness of the material normally associated with a pure mode I test. This theory reduces to the Irwin/Griffith theory for a pure mode I situation. A ratio of mode II to mode I fracture toughness of 0.866 is predicted by this theory, and this value does not depend on the mechanical properties of the material. The predicted fracture direction is given by the equation shown in table I and depends on the ratio of applied mode II stress intensity to mode I stress intensity. The equation for the predicted interaction is also given in table I and, when plotted in a K_I, K_{II} space, has a shape similar to a parabola in the first quadrant.

The fifth theory shown is identified as the strain energy density theory due to Sih (ref. 8). The theoretical basis of this theory relates to calculation of the density of strain energy in the region near the tip of a crack loaded in mixed mode. The strain energy density is found to increase in a singular fashion as the crack tip is approached along a radial line. The intensity of this singularity is identified as S and is assumed to take on a critical value at fracture. Further, the direction of crack propagation is hypothesized to be predicted by the direction in which S takes on a minimum value. As the other theories described, this theory reduces to the Irwin/Griffith predictions for a pure mode I loading situation. The ratio of mode II fracture toughness to mode I fracture toughness predicted by this theory is shown in table I and is seen to depend on the elastic properties of the material. The equation that predicts the direction of crack growth is also given in the table and depends on the ratio of K_I to K_{II}. The equation for mode I, mode II interaction given in the table is found to again appear much like a parabola when plotted in the first quadrant of K_I, K_{II} space.

Figure 2 presents a plot of the angles of crack propagation predicted by the various theories and shows that, in the range of interest, there is little difference between the predictions of crack angle. Figure 3 is a plot of the interaction diagrams that are predicted by the various theories. Again, it is clear that there is very little difference between the theories in predicting mode I, mode II interaction.

Mixed-Mode Fatigue

Very little information is available concerning fatigue crack propagation under mixed-mode loading conditions. This is because cracks, when subjected to mixed-mode conditions, have been found to rotate their direction of propagation immediately on cyclic load application in such a way that they propagate in primarily a mode I condition. Iida and Kobayashi (ref. 9) considered mixed-mode crack propagation in 7075-T6 aluminum. The mixed-mode condition was obtained by placing a straight crack in a tension-loaded strip at an angle to the loading direction. Various degrees of mixed-mode loading were obtained by placing the crack in the plate at varying angles. It was found that immediately on onset of cyclic loading the crack began to turn in a way that would tend to make the crack plane perpendicular to the loading direction. This produced a crack configuration similar to that shown in Figure 4 taken from reference 9.

To properly analyze the test results, Iida and Kobayashi performed a finite element stress analysis of cracks with geometries similar to those shown in figure 4. Figure 5 shows the results of that analysis. The analysis clearly shows that as the crack grows along its path, out of the plane of the original crack, the stress intensity situation remains mixed mode for only a short interval after which the loading condition is primarily mode I. In connection with mixed-mode crack growth rates, Iida and Kobayashi concluded that the presence of mode II accelerates crack growth rate by 10 to 20% over that expected by a mode I fatigue test.

Roberts and Kibler (ref. 10) have also studied problems of mode II fatigue crack propagation. In their experiments, cracks were loaded in combined mode I and mode II where the mode II component of the load was cycled but the mode I component of the load was held steady. Under these circumstances it was possible to produce crack growth in the original plane of the crack. However, in some cases branching of the crack was observed. It was generally found that an increase in the steady, mode I load for a given cyclic amplitude of mode II variation increased the crack growth rate.
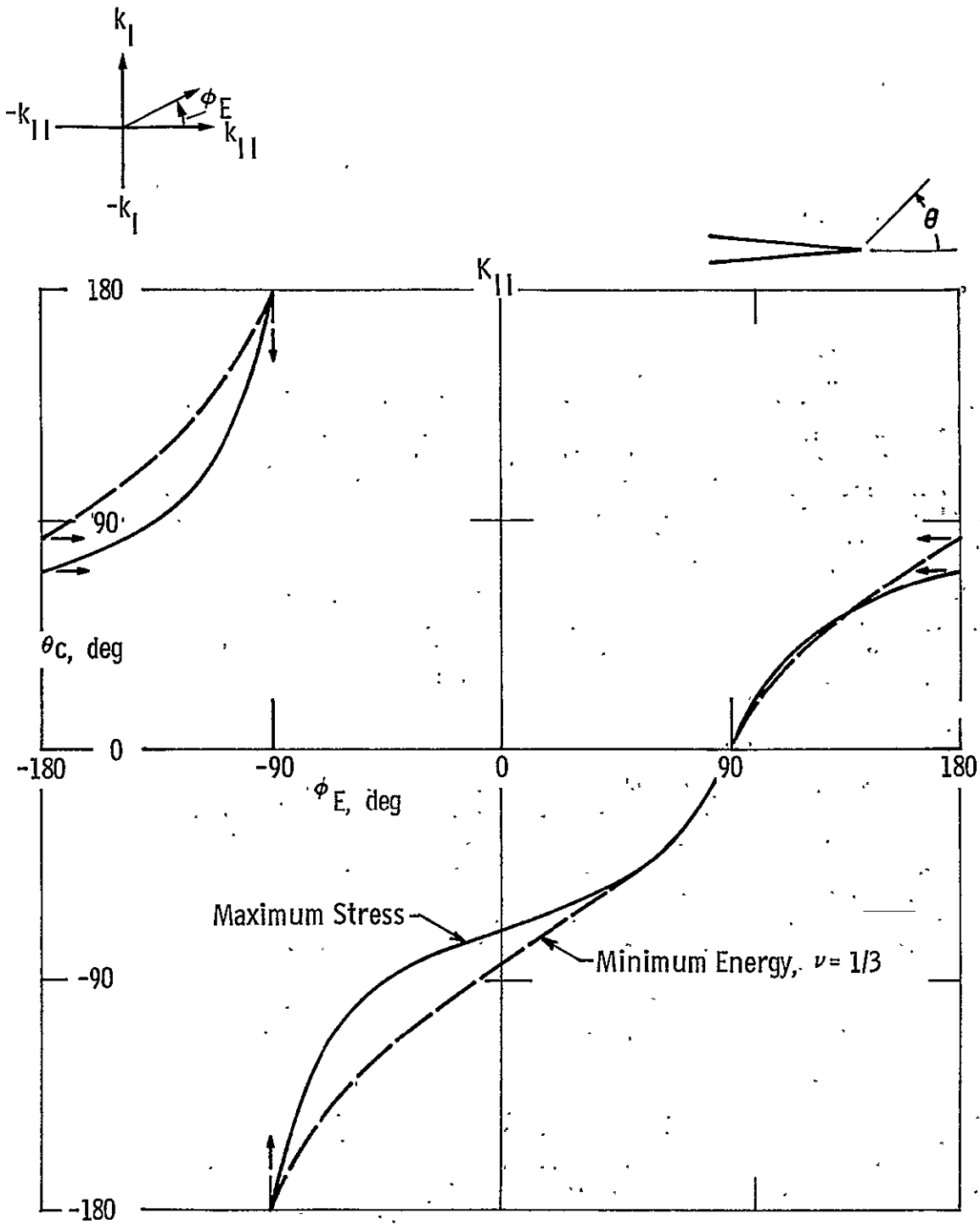
Figure 2. — Predicted fracture direction.
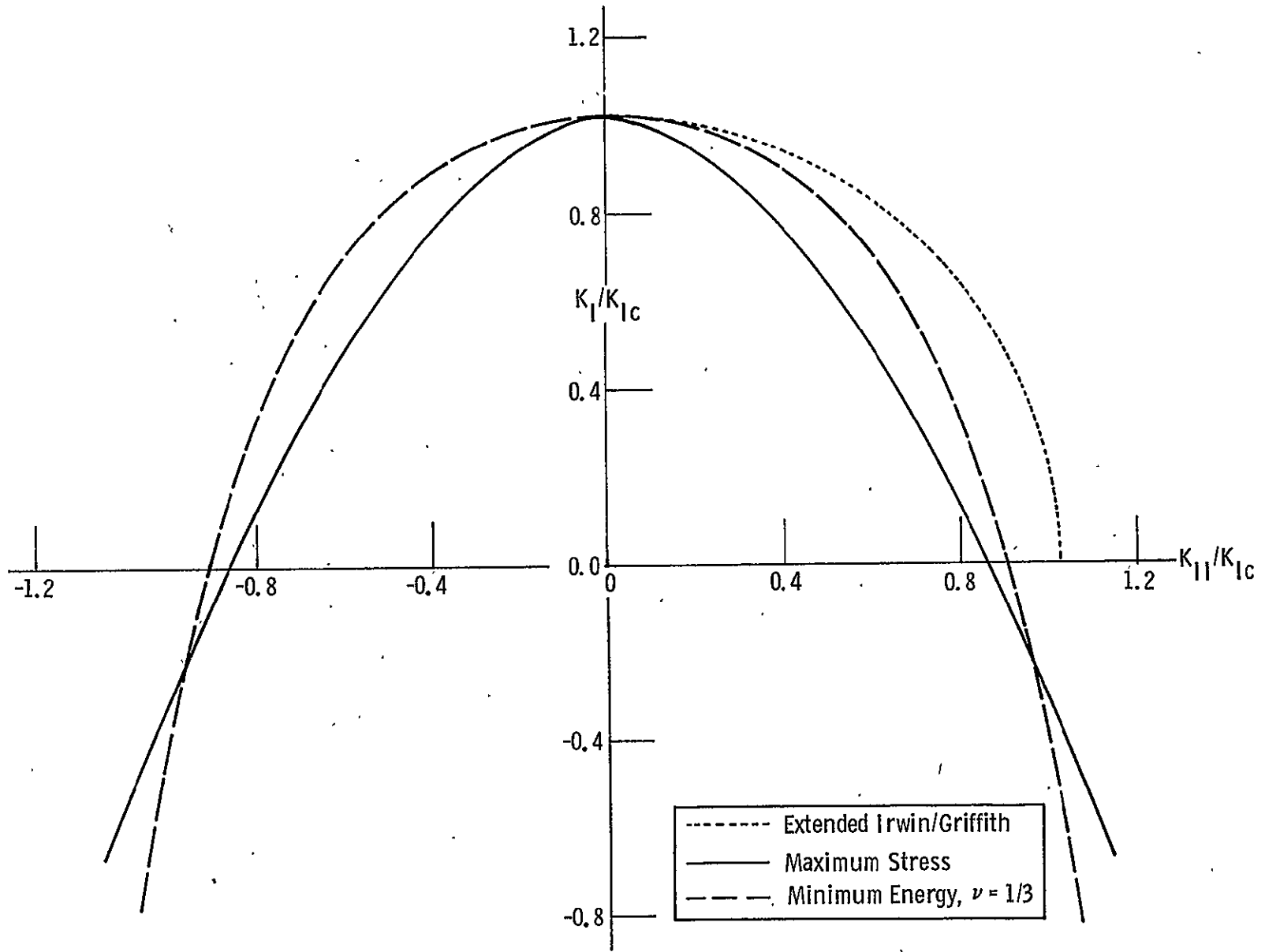
Figure 3. - Predicted interaction diagrams.
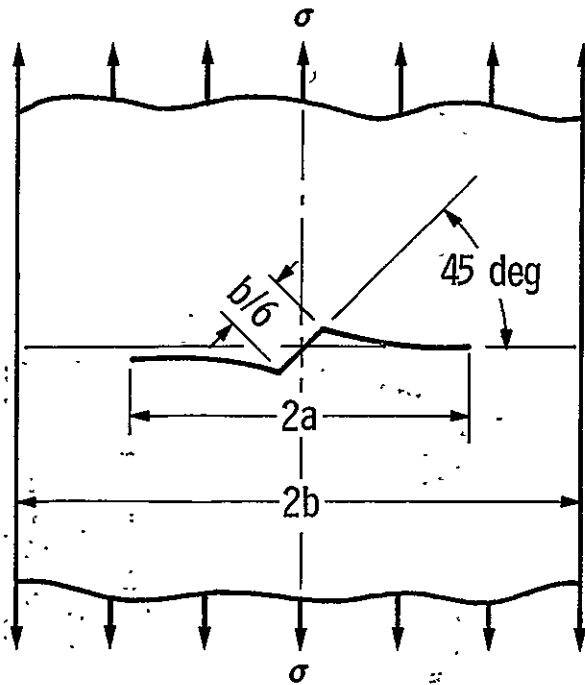
Initial Crack Orientation

Figure 4. - Crack extension pattern of an initially slanted crack.

Recently, Yokobori, *et al.*, (ref. 11) have conducted a series of torsional fatigue experiments on cracks in thin-walled hollow cylinders. The material used for these studies was 5083P-0 aluminum alloy. The experiments were conducted in a way that subjected the crack to alternating pure shear stress with no normal stress present. Under these loading conditions, the crack was found to branch at each of the crack tips as diagrammed in figure 6. This configuration implies that the branches of the growing cracks are subjected primarily to the mode I stress intensity factor during the growth portions of loading for each of the branches.

From the scant amount of information available on mixed-mode fatigue crack propagation, it is evident that little is understood about this phenomenon. Because the mode of crack growth in most of the experiments conducted to date has been primarily mode I, it has been possible to interpret available data in terms of the traditional mode I fatigue laws. There has also been sufficient evidence that the effect of cyclic mode II in the presence of mode I loading is to accelerate the crack growth rate, possibly by significant amounts. This effect makes further study of this type of phenomenon important.

14
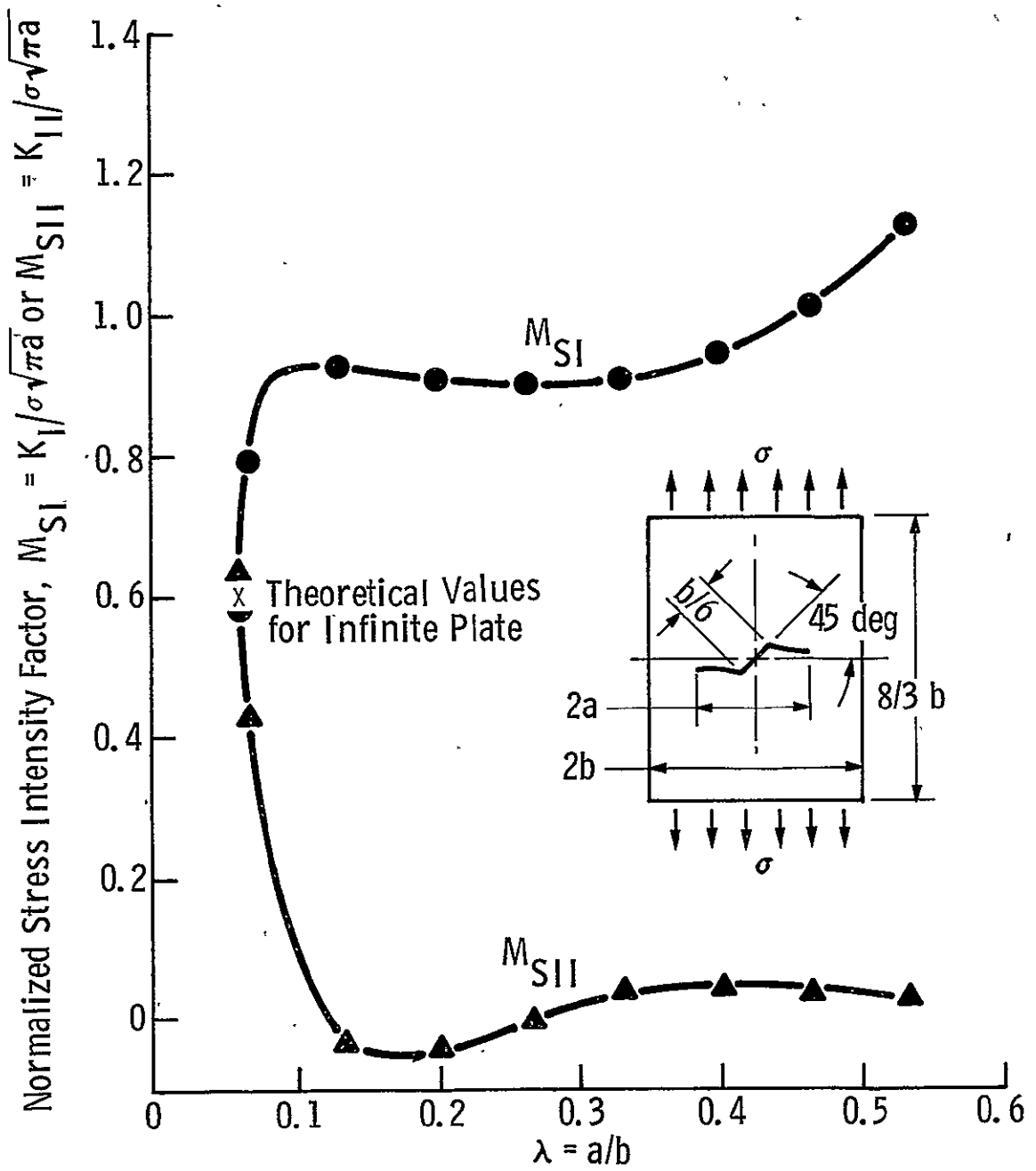
Figure 5. – Normalized stress intensity factors for a tension plate with initially slanted crack.
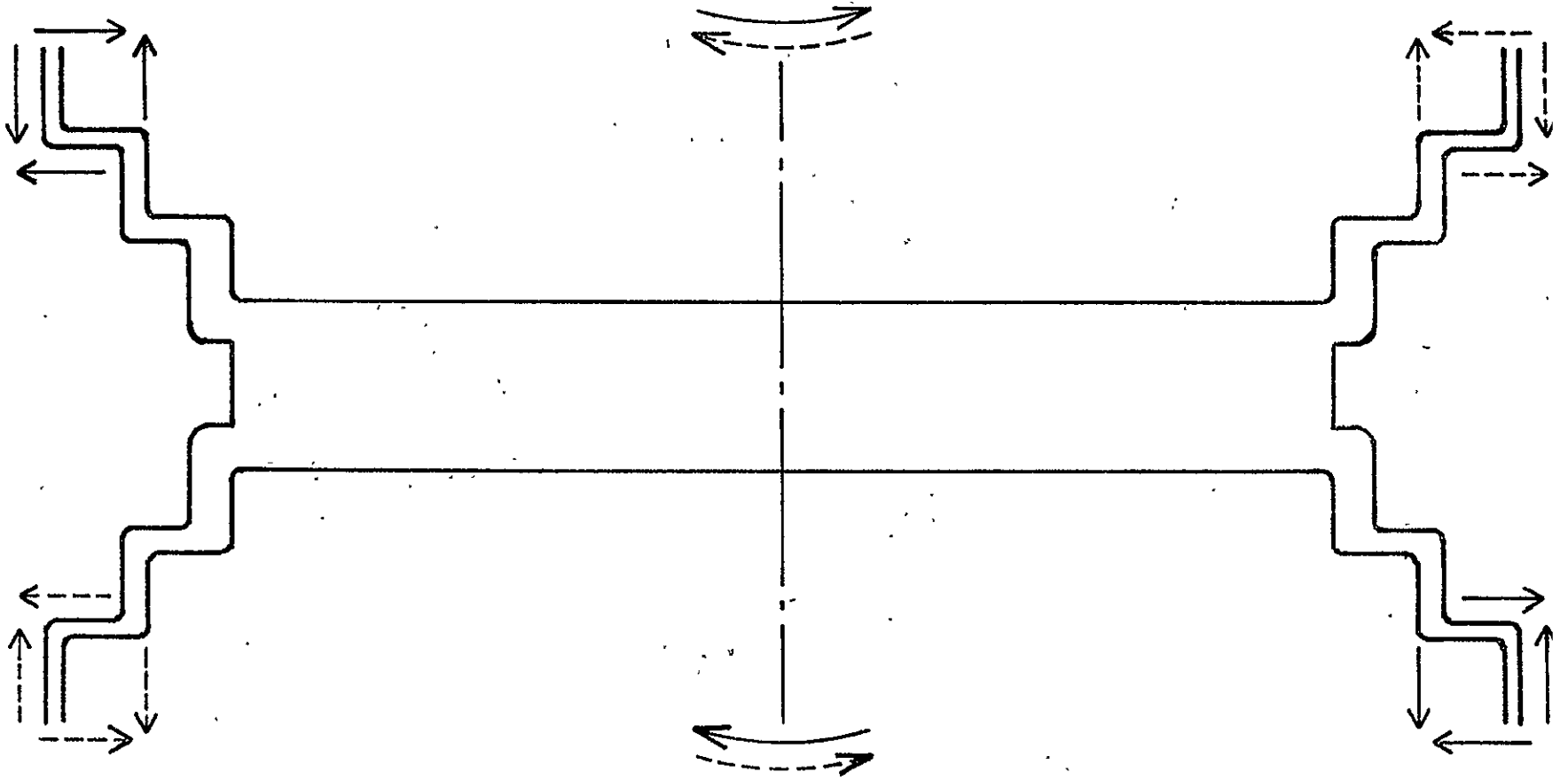
Figure 6. - Crack growth under mode II loading (ref. 11).

Biaxial Specimen Stress Analysis

The specimen used in this program was analyzed by Holston (ref. 12) using finite elements with mixed-mode crack tip singularity elements. The specimen geometry, including the crack, is shown in figure 7 and the normalized mode I and mode II stress intensity factors are given in figure 8. The flaw half-length scale used in figure 8 is shown in proportion to the specimen size in figure 7. In this program the tab width was 50.8 cm (20 in.).
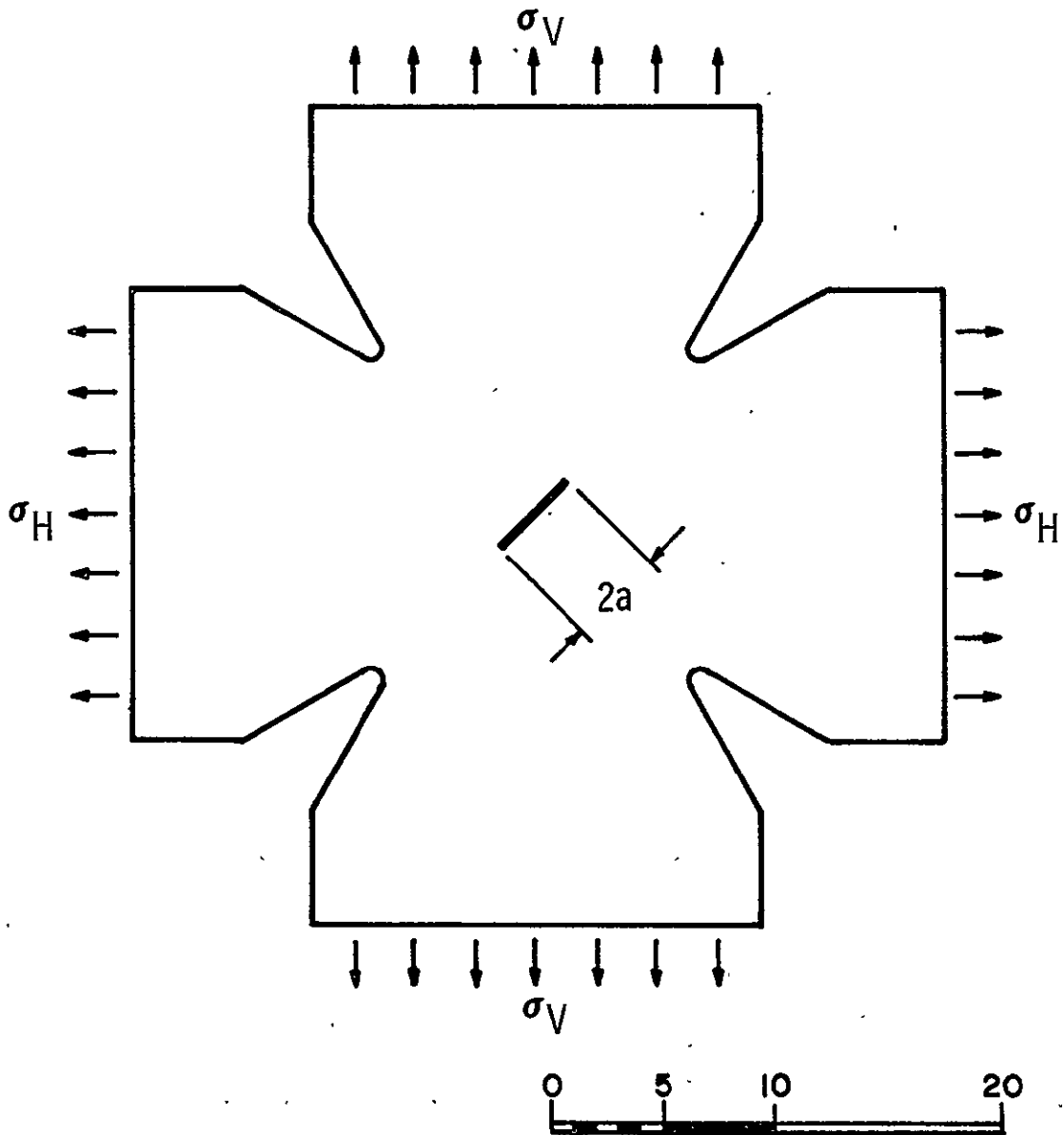
Figure 7. - Specimen geometry analyzed by Holston.
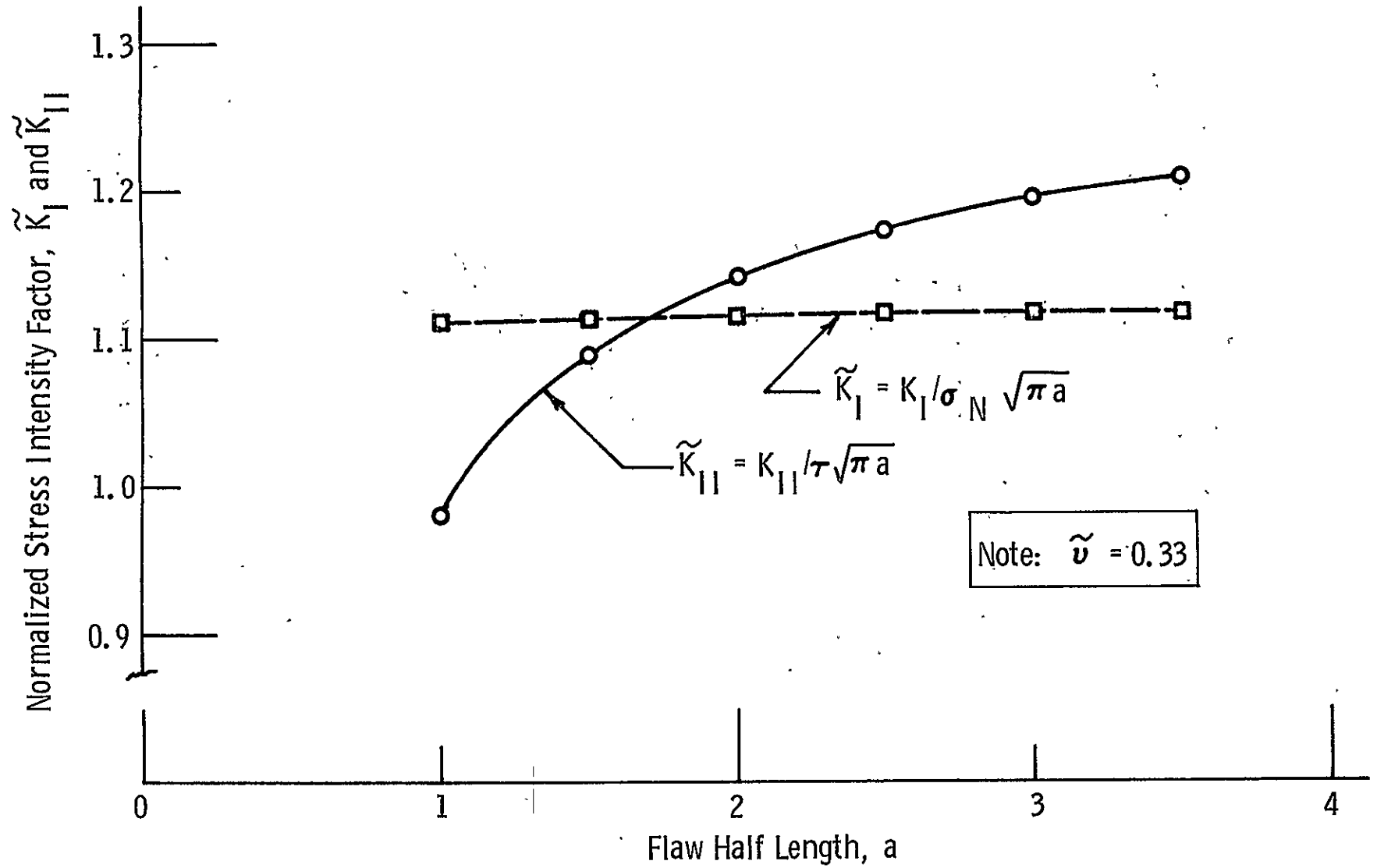
Figure 8. — Normalized stress intensity factors for Maltese cross specimen.

EXPERIMENTAL PROGRAM

Specimens

Materials. - Two aluminum alloys were investigated in this program—2219 in thicknesses of 1.55 and 0.64 cm (0.61 and 0.25 in.) and 7075 in a thickness of 1.27 cm (0.5 in.). The material was received in the form of plates 1.219 m (4 ft) by 3.658 m (12 ft). Each plate was cut into four specimen blanks 0.925 m (3 ft) square and four coupon blanks 0.3084 m (1 ft) by 0.925 m (3 ft). The thinner 2219 material was received in the T-87 condition. The thicker 2219 material was received in the T-37 condition, was cut, then aged at 177°C (350°F) for 18 hours to T-87. The 7075 was received as T-651, was cut, then aged at 163°C (325°F) for 28 hours to T-7351. Room temperature tension tests were made on 30.5-cm (12-in.) long full-thickness flat dogbone coupons, with a gage section 5-cm (2-in.) long by 1.27-cm (½-in.) wide, cut from the coupon blanks, two coupons for each direction from each alloy/thickness combination. There was one longitudinal strain gage on each coupon. The coupon test results are given in table II.

Preparation. - Fifteen 2.54-cm (1-in.) diameter holes were drilled along each edge of the specimen blank for attaching grip plates, and four 2.54-cm (1-in.) diameter holes were drilled to serve as the roots of notches later put in with a band saw. The plan form of the specimens is shown in figure 9.* They were full plate thickness. A 0.635-cm (¼-in.) diameter hole was drilled through the center of the plate to permit the insertion of a saber saw blade. A through flaw 5 to 10-cm (2 to 4-in.) long was then cut with a saber saw 45 deg to the loading axes of the specimen. The flaw width was 1.2 mm (3/64 in.). For the last 1¼ mm (0.05 in.) at each end of the saw cut, a special blade was used, made from two pieces of band saw blade welded together and then ground to a V. A steel razor blade was pulled through the flaw at each end to establish a sharp notch for starting a crack on the first two specimens. This practice was later abandoned because it did not improve the precracking behavior. After flaw cutting, both surfaces of the specimen were polished in the area around the flaw using an orbital sander with 200 grit, then 600 grit, emery cloth followed by buffing with a cloth wheel and jewelers' rouge. The specimen was then ready for flaw sharpening by precracking.

---

*Strain distributions for this shape are described in Appendix C.

TABLE II. – PROPERTIES OF PROGRAM PLATE MATERIAL

Alloy	Nominal thickness		Direction[a]	Yield strength, 0.2% Offset		Young's modulus		Ultimate strength		Elongation at failure, %
	cm	in.		$N/cm^2 \times 10^3$	$psi \times 10^3$	$N/cm^2 \times 10^6$	$psi \times 10^6$	$N/cm^2 \times 10^3$	$psi \times 10^3$	
2219-T87	1.55	0.61	L	39.2	56.8	7.4	10.8	48.2	69.9	12.0
			L	39.2	56.8	7.4	10.7	48.3	70.1	10.0
			Avg	39.2	56.8	7.4	10.8	48.3	70.0	11.0
			T	38.8	56.3	7.6	11.0	48.1	69.7	9.0
			T	38.3	55.5	7.4	10.8	47.8	69.4	9.0
			Avg	38.5	55.9	7.5	10.9	48.0	69.6	9.0
•7075-T7351	1.27	0.50	L	44.9	65.1	7.2	10.4	51.4	74.5	12.2
			L	45.0	65.2	7.2	10.4	51.4	74.6	12.2
			Avg	45.0	65.2	7.2	10.4	51.4	74.6	12.2
			T	45.0	65.2	7.3	10.6	51.7	75.0	11.2
			T	44.7	64.9	7.2	10.5	51.6	74.8	11.0
			Avg	44.8	65.0	7.3	10.6	51.6	74.9	11.1
2219-T87	0.64	0.25	L	37.6	54.5	7.2	10.5	46.9	68.0	10.0
			L	37.9	54.9	7.3	10.6	47.1	68.3	10.0
			Avg	37.7	54.7	7.2	10.5	47.0	68.2	10.0
			T	37.3	54.1	7.2	10.5	47.1	68.3	11.0
			T	37.4	54.3	7.2	10.4	47.2	68.5	11.0
			Avg	37.4	54.2	7.2	10.4	47.2	68.4	11.0

[a]L = Load applied in final rolling direction.

T = Load applied transverse to final rolling direction.
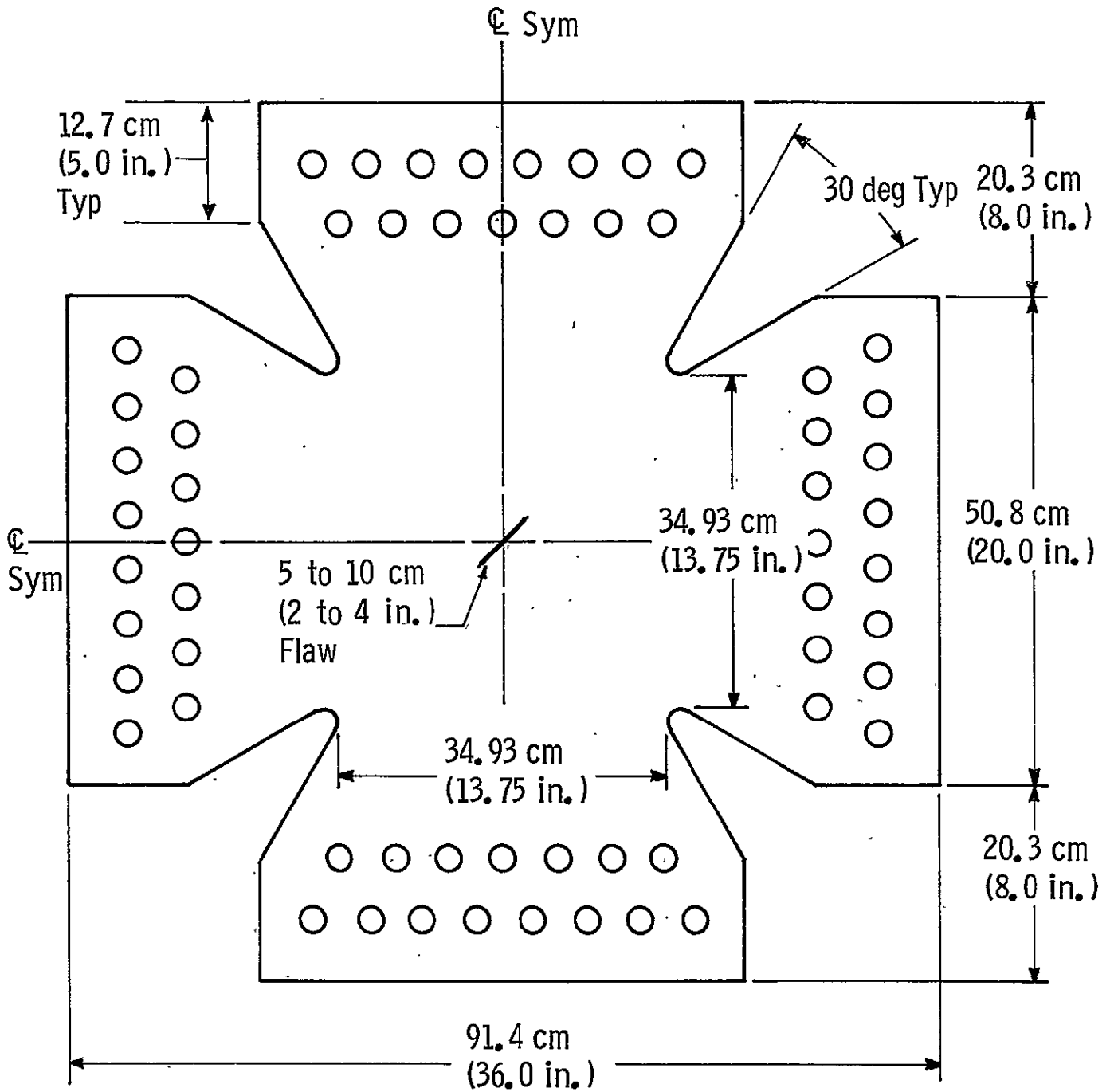
Figure 9. – Biaxial test specimen.

21

Precracking. - Precracking to sharpen the flaws was performed by loading the flaws hydraulically. A fixture was designed and built to accomplish this in a manner similar to that reported by Abbatiello and Derby (ref. 13). The precracker consisted of two 25x15-cm (10x6-in.) 4130 steel plates 5-cm (2-in.) thick as backup plates for two 2.4-mm (0.093-in.) thick O-ring retainer plates. The backup plates were held in place by 61-cm (2-ft) long clamping beams, one on either side of the test specimen (fig. 10 and 11). Hydraulic pressure was applied in one of two manners. Originally the hydraulic power supply of a 5-kip MTS testing machine was used at 7 cycles/second with the actuator bypassed. This limited the pressure to 2400 N/cm^2 (3500 psi). Later, hydraulic pressure was supplied by a hydraulic ram that was placed in the testing space in the testing machine and attached to the loading plates. In this way the ram became a pressure intensifier and pressures up to the design limit of the ram and hoses could be obtained (6900 N/cm^2 or 10 000 psi) although these levels were never needed. Development trials to determine pressure levels and number of cycles to obtain 1¼ to 2½ mm (50 to 100 mils) of crack growth were run to act as a guide for precracking the test specimens. These trials and the precracking parameters for the specimens, including the final flaw lengths, are presented in Appendix B.

Test Equipment

The equipment especially fabricated or gathered into systems for this program included the specimen grips, the testing machine, a COD gage holder for biaxial measurements, a compression fixture, and recording and data analyzing systems.

Grips. - Flat plate grips were used to transfer the load from the testing machine clevises to the specimens. Each set of grips consisted of eight plates, one for each side of each loading tab, with holes at one end to match the loading holes in the specimens and a large hole at the other end to accommodate the loading pin. Two sets of grips were used. A steel set was fabricated first to permit transferring the full capability of the testing machine into the specimens. When it was determined that the required load values were much less, an aluminum set was made to reduce weight and increase the efficiency of specimen installation and removal. The aluminum grip plates are shown attached to a specimen in figure 12.
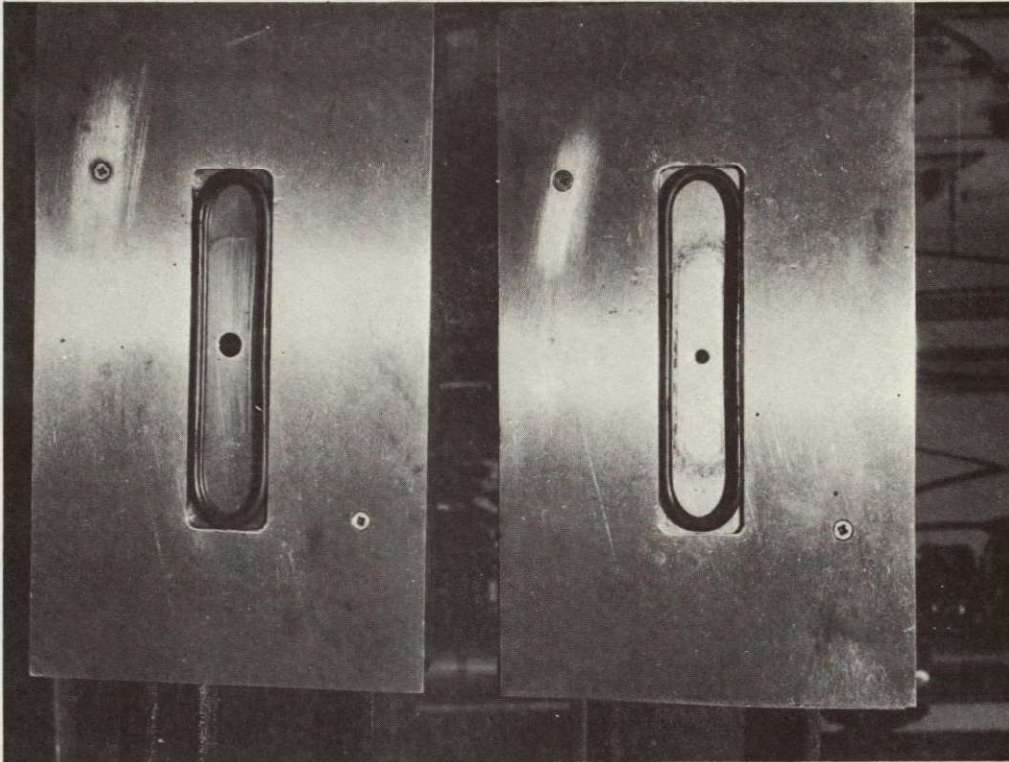
Figure 10. - Precracker O-ring retainer plates.
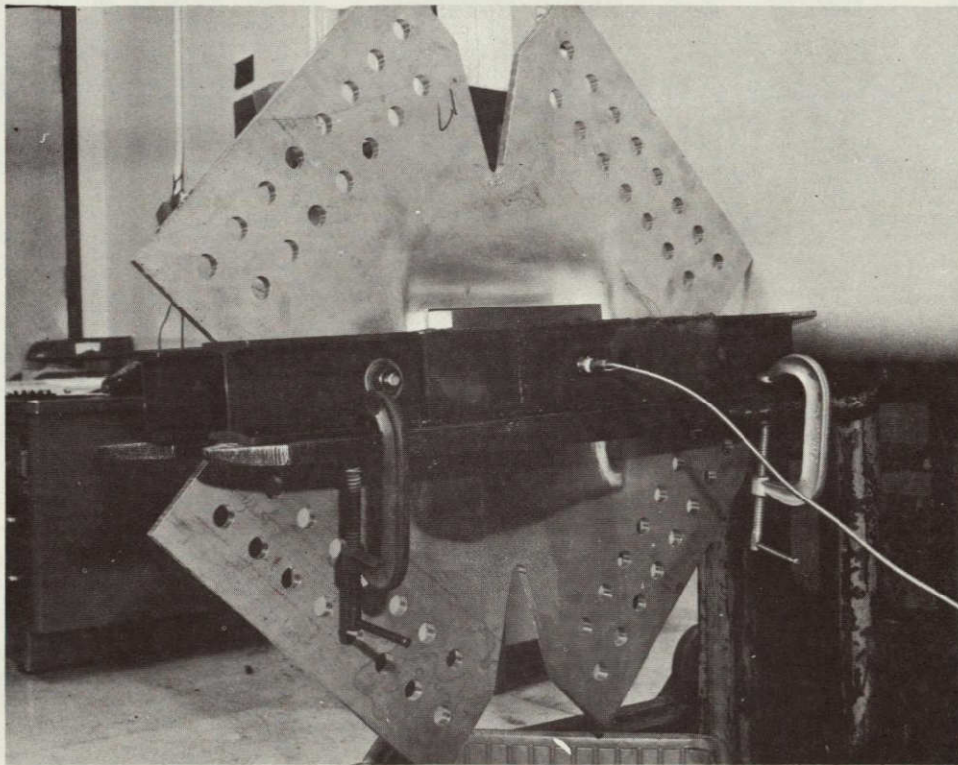
Figure 11. - Precracker in place on specimen.
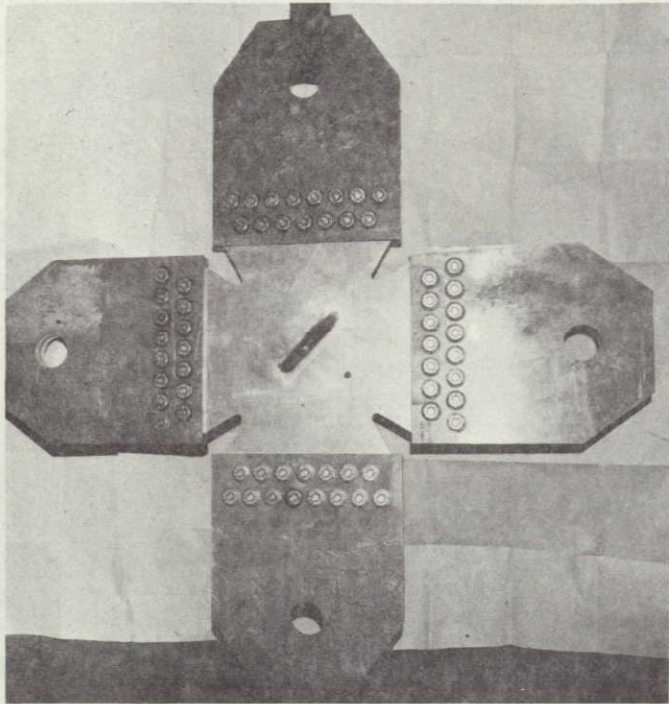
Figure 12. – Aluminum grip plates attached to specimen.

Testing machine. – A special biaxial testing machine, the mixed-mode testing machine (MMTM), was built for this program. It comprises a 1 million pound MTS universal testing machine, the vertical axis, to which has been added a specially supported horizontal axis, both under computer control. Both axes are operated off the same $0.53\text{-m}^3/\text{min}$ (140-gal/min) hydraulic power supply. Figure 13 is a view of the MMTM. Figure 14 is a schematic diagram of the horizontal axis. It fits between the four columns of the MTS machine and is located so the test specimen can be mounted between the two axes. The weight of the horizontal axis is reacted by a support system designed to minimize the "crosstalk" between axes. Functionally the horizontal axis is identical to the vertical axis. The frame reacts the load between the hydraulic actuators and the passive end whiffletree. A schematic diagram of the horizontal axis support system is shown in figure 15. By ultimately resting on compressed gas, the horizontal axis can move up and down with the horizontal centerline of the specimen without loading the specimen with its dead weight. The rams behave essentially as very soft springs. They are pinned at top and bottom to eliminate any longitudinal restraint of axial deformation of the horizontal axis frame. There is some loading of the specimen during cyclic operation of the vertical axis due to the inertia of the horizontal axis. This is a small amount and is discussed in Appendix C, Mixed-Mode System Checkout Summary Report, where the entire checkout procedure results are given because proper functioning of this system was so vital to the validity of the program test results.

24
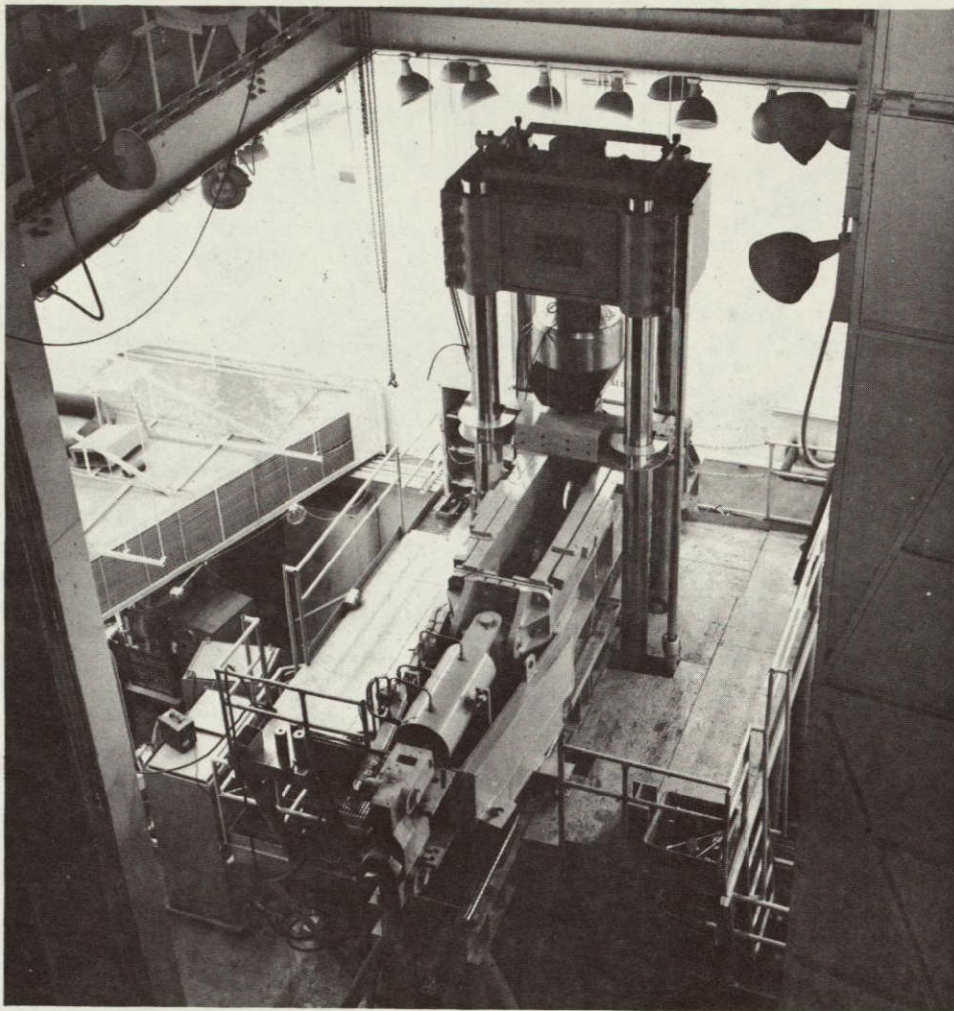
Figure 13. – Mixed–mode testing machine.
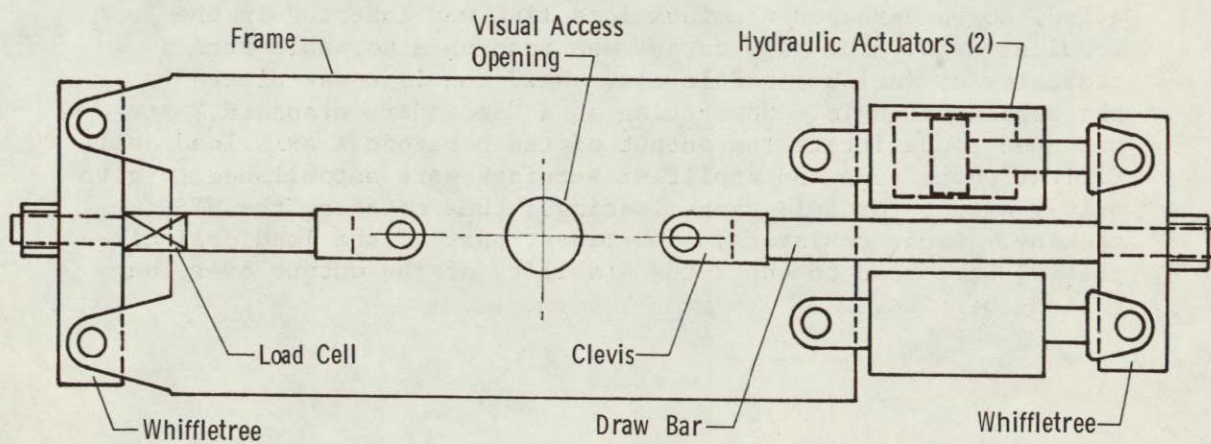
Figure 14. – Schematic diagram of horizontal axis.
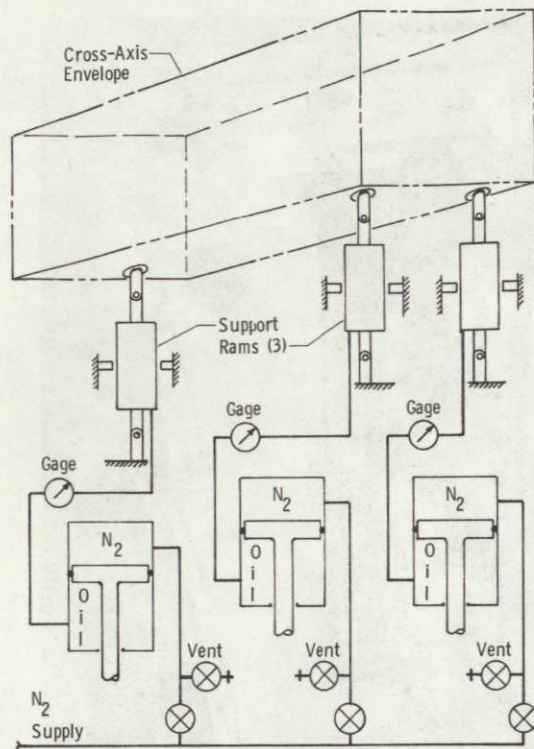
Figure 15. – Schematic diagram of horizontal axis support system.

The horizontal axis has its own load cell circuitry and power supply, balancing circuit, output amplifier, fail-safe circuits, and independent control of the servo valves. Thus it can be operated independently of the vertical axis, either manually or under computer control, or locked in with the vertical axis under computer control. The horizontal axis load cell and its circuitry was calibrated by comparing its output with that of the vertical axis, using a calibrated "load link" as an intermediary. First the MTS machine was calibrated in the standard fashion by the Denver Division Metrology Laboratory. Then an extensively strain-gaged, dogbone-shaped aluminum load link was inserted in the vertical axis. The gage output was read on a portable strain indicator at various load levels. Next the link was placed in the horizontal axis. Now acting as a "secondary standard," it was used to calibrate the output of the horizontal axis load cell. Excitation voltage and amplifier settings were established to give a 10-V output for full-range loadings, thus matching the MTS machine. Shunt resistors, a permanent part of the load cell circuitry, were used to check the stability of the output over long periods of time.

A PDP 11/05 Digital Equipment Corporation computer with 8k memory was used to control the mixed-mode machine for all testing, both cyclic and static. A two-channel arbitrary program exercised real-time control throughout a test run, making the computer a sophisticated function generator. Forty values of load versus time can be put on each axis before the program repeats, with the signal between values being either a ramp or a haversine. On this project the ramp function was always used and no more than 10 values were ever needed to define the cyclic load shape. Frequency of loading was not limited in the computer but rather by the flow rates of the hydraulic fluid, mass of the servo valves, elasticity of the structural components of the machine, etc, and depended on the load levels and faithfulness of response desired. The cyclic rate was kept below 30 cycles/minute because of the soft response of the horizontal axis, generally testing at a rate of 15 to 20 cycles/minute.

Biaxial displacement gage holder. - The analysis in Appendix A predicted both opening and shear deformations of the flaws in the specimens. A special device was designed and built to measure these deformations independently at the center of the flaw. It was a split cylinder that fits inside a ½-in. diameter hole at the flaw center. The cylinder halves incorporated knife edges and bearing wheels and were slotted to permit opening displacement and completely reversed transverse displacement without interference. Motion was detected by two double cantilever strain-gaged displacement measuring devices. One acted against a knife edge and bearing wheel located at the middepth of the specimen. It held the split cylinder in place while the adhesive dried and recorded the normal crack opening displacement (COD). The other acted against a knife edge and a wheel that protruded from the specimen and recorded crack shear displacement (CSD). Figure 16 presents a view of the disassembled cylinder and the two measuring devices. Figure 17 shows an in-plane view of the holder and gages mounted on a specimen. The normal mode opening measurement side is shown in figure 18 and the shear mode side in figure 19.

A new double cantilever gage was built for this program to match the performance of the Martin Marietta-built device shown in figure 19, except that the cantilever leaves were narrower than those shown in the figure to facilitate insertion into the middepth of the split cylinder. The biaxial gage assembly was operationally verified by mounting it into a plate cut in two to permit free motion of the parts in a testing machine or on the table of a traveling microscope. Motion was imposed in one principal direction while readings were taken in the other to determine whether there was "crosstalk." Motion of 0.76 mm (0.030 in.) in the "normal opening" direction resulted in motion in the "shear" direction of about 0.0025 mm (0.0001 in.) or 1 part in 300.
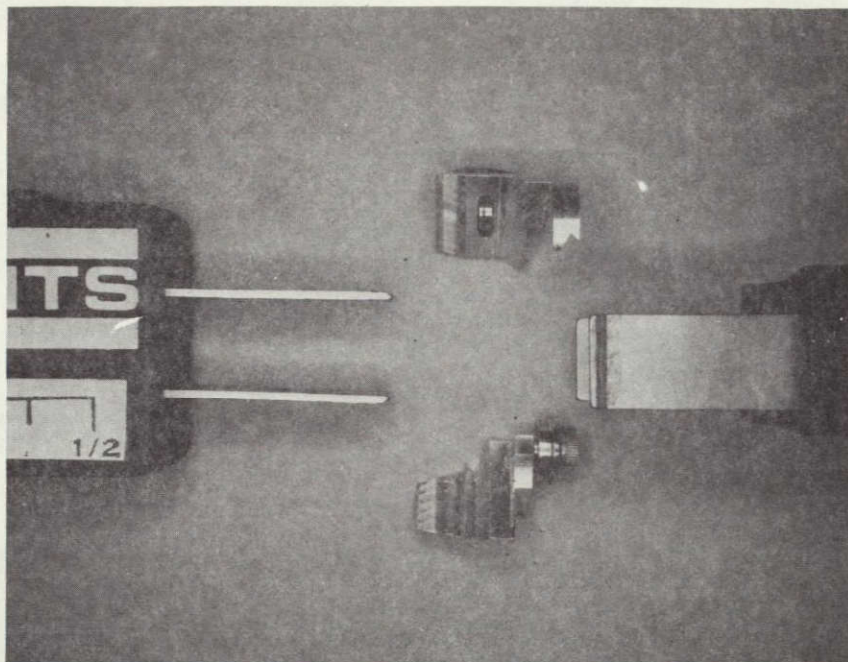
Figure 16. - Biaxial displacement gage holder disassembled.
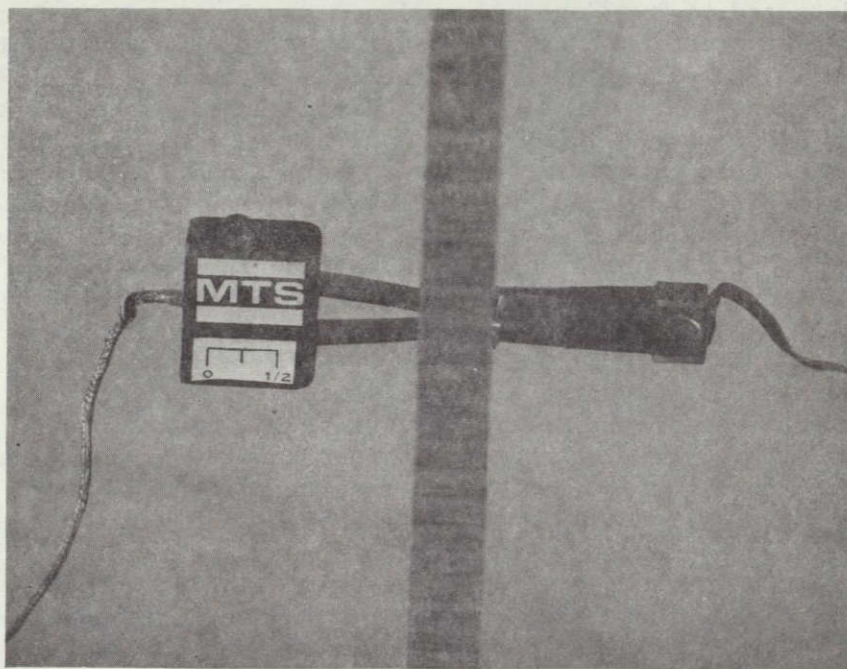
Figure 17. - Biaxial displacement gage assembly in place, in-plane view.
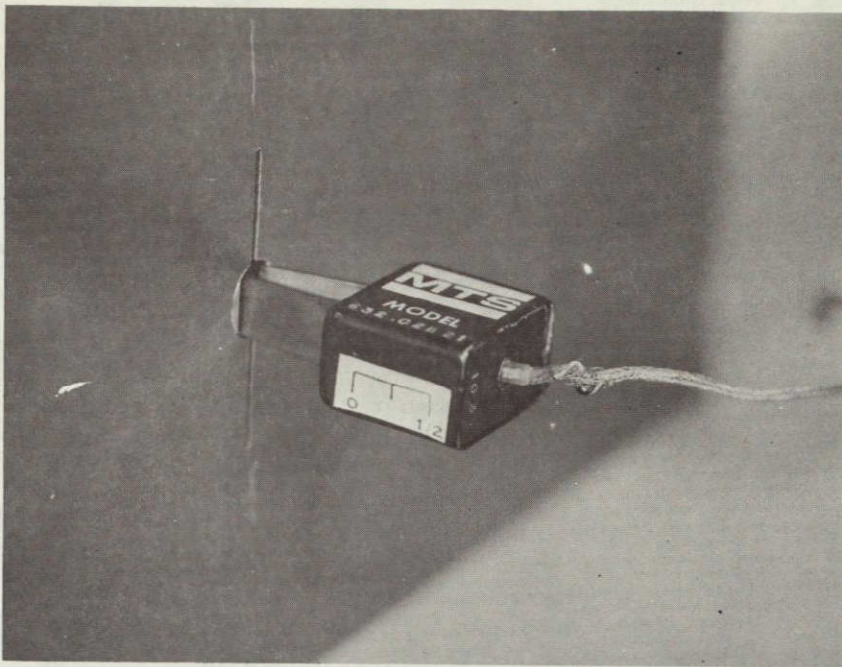
Figure 18. – Biaxial displacement gage assembly, normal opening side.
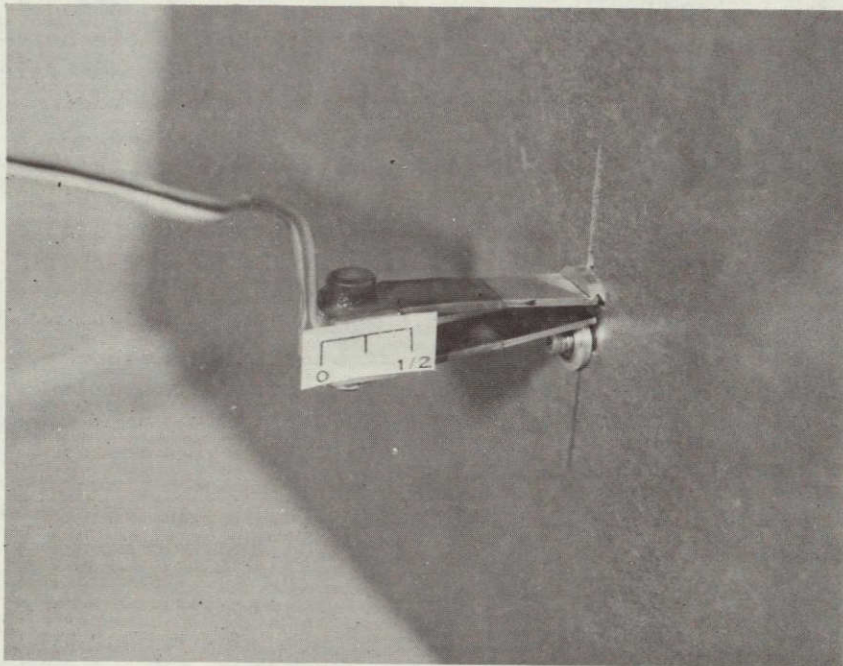
Figure 19. – Biaxial displacement gage assembly, shear mode side.

Compression fixture. - Some of the tests required compression
to be applied on one axis of loading. A fixture was designed and
built to permit the application of compressive loading on the
vertical axis while supporting the specimen and the grip plates
against lateral buckling. Figures 20 and 21 are two views of a
specimen ready for testing with the compression plates in place.
Figure 22 is a schematic of the system. The system consisted of
two compression plates, one on either side of the specimen, clamped
to the grip plates at one end and free to slide in a slot at the
other. The compression plate on one side was clamped at the op-
posite end from the compression plate on the other side. Each com-
pression plate had two 10-cm (4-in.) wide 2.5-cm (1-in.) thick bars
welded to it in the vicinity of the notch roots of the specimen.
These bars rested against the specimen and provided lateral sup-
port while permitting in-plane deformation of the specimen. Thus
all axial load introduced into the grip plates by the testing
machine was transmitted to the specimen except for the slight load
carried by friction in the slots or between the specimen and the
lateral support bars. These surfaces were lubricated before each
test. The compression plate had a hole in the center to permit
movies to be taken of crack growth and to provide access for the
crack displacement measuring gages. Buckling occurred in only
one test (SN-12) out of the eight in which the plates were used.

Monitoring and recording equipment. - Data were monitored and
recorded by several redundant sets of equipment. Three Dana model
5600 digital voltmeters were used to continuously monitor the hori-
zontal axis load cell and two load cells in the vertical load train,
the MTS load cell, and the strain gages on the bottom pull rod.
Instrumenting the bottom pull rod permitted it to be used as
another load cell to provide a check on the performance of the
horizontal axis support rams in keeping the horizontal axis weight
off the test specimen. These digital voltmeters were also used to
monitor the specimen installation and removal procedure and the
setting of preloads when required. A 25x43-cm (10x17-in.) X-Y
plotter was used as a diagnostic tool during the cyclic tests and
to record loads during the static tests. It was generally used
for recording the vertical axis load versus the horizontal axis
load. During the cyclic tests, it was thus possible to tell if
the loads bore the proper time phase relation to each other and
whether any adjustments had to be made in peak values by fine-
tuning span settings on the control consoles. During the static
tests, the plotter provided a permanent record of the fracture
loads. A teletype keyboard was used for inputting the two-channel
arbitrary programs into the computer and for periodically record-
ing the load cell feedback signals. It also made a permanent
typewritten record of the number of cycles of loading and the
elapsed time for each block of cycles. A cycle counter on the
machine control console provided a running total of cycles of
loading.
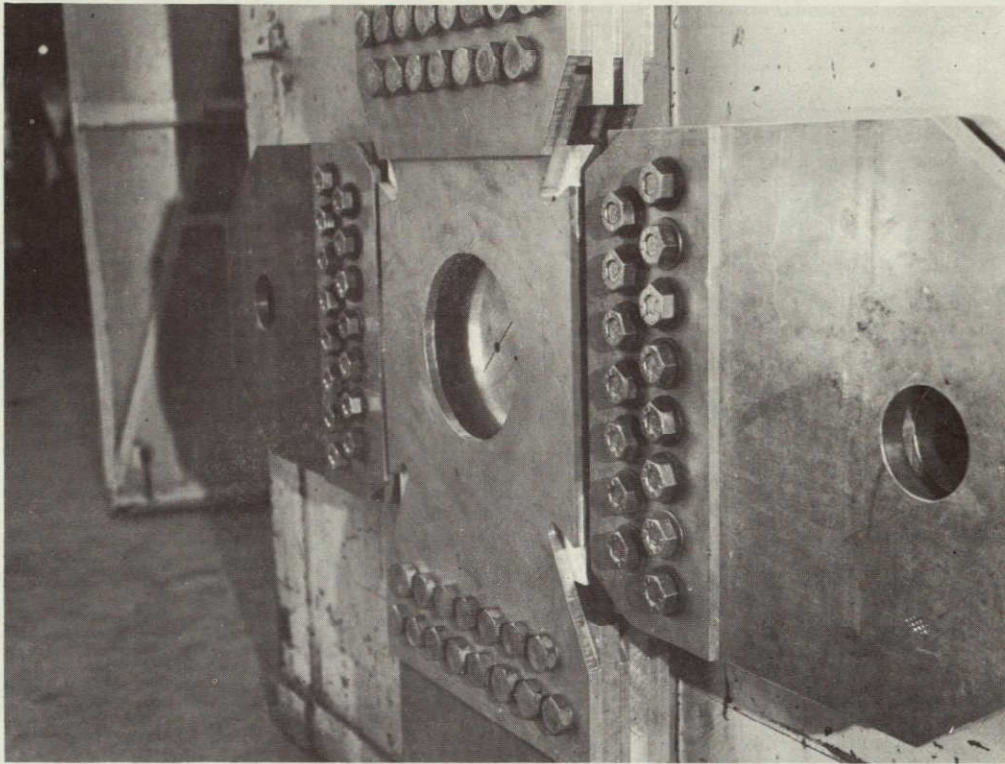
Figure 20. – Compression fixture installed on specimen, console side.
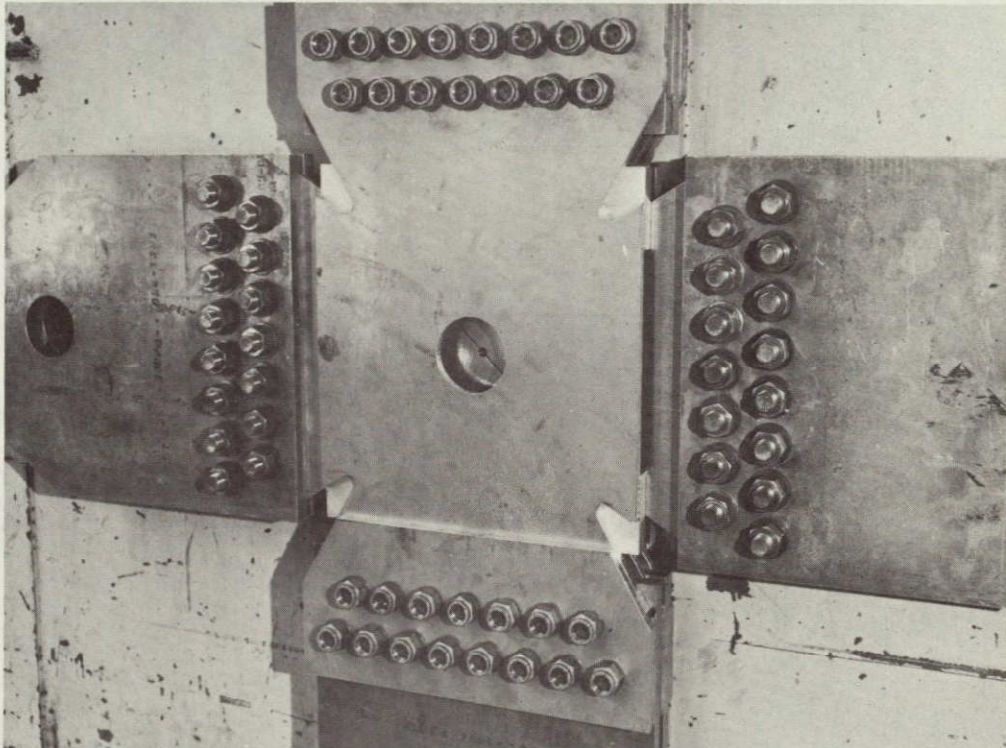
Figure 21. – Compression fixture installed on specimen, opposite side.

31
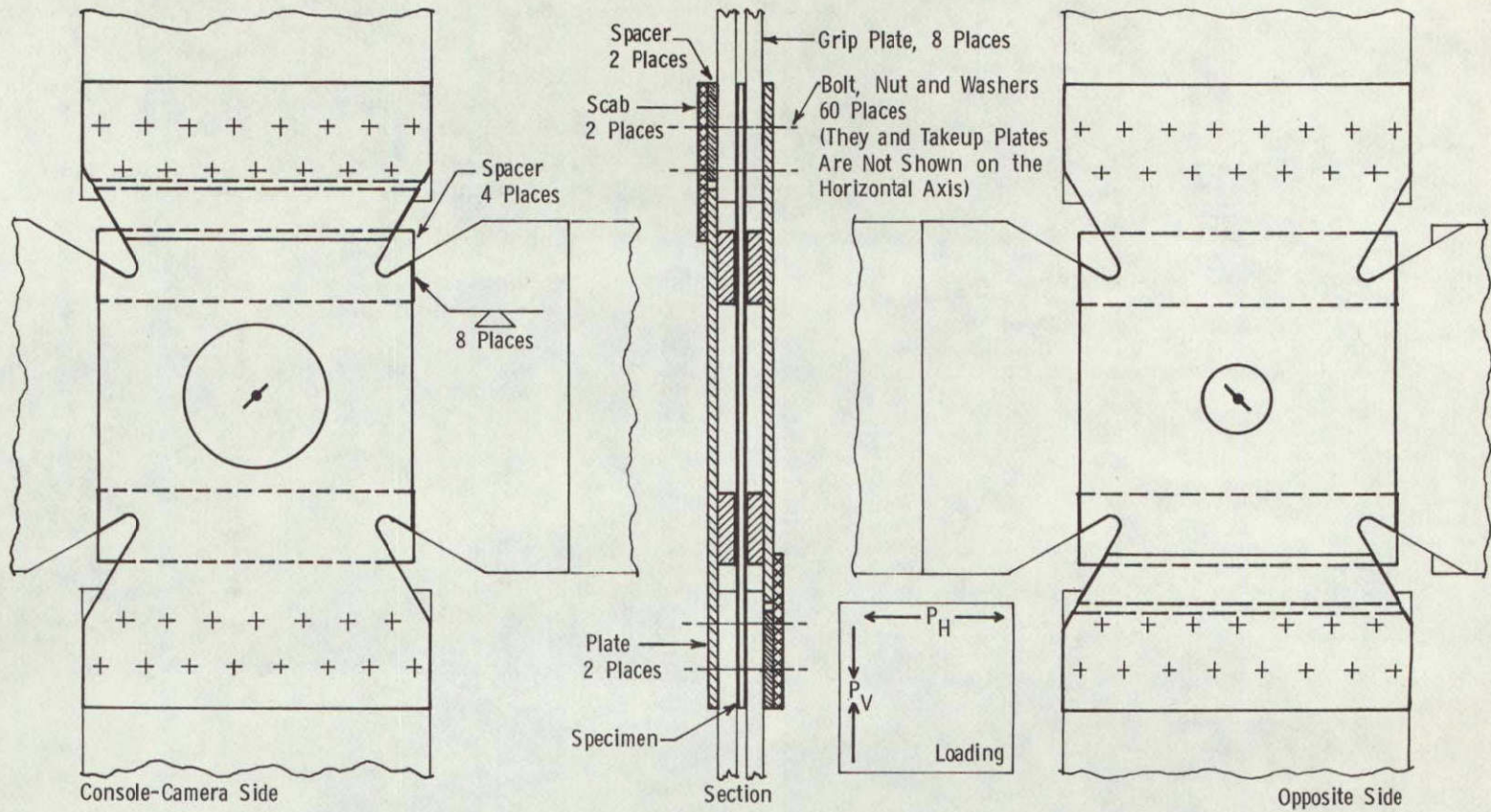
Figure 22. – Schematic diagram of compression fixture attached to specimen.

Both crack displacement gages, both load cell outputs, both loading piston displacements, and time of day were intermittently recorded on a Honeywell model 1612 visicorder during the cyclic tests and continuously during a static test. The displacement gages were excited by an independent power supply. All seven signals were amplified and conditioned in a Martin Marietta-built cart prior to being fed to the visicorder. The cart also contained calibration switches for all the channels. Two oscilloscopes were used to monitor whatever signals happened to be of interest at any time.

Subcritical crack growth and fracture were recorded with a D. B. Milliken model 5-2 camera. This camera has a variable framing speed of 1 to 500 frames/second with an accuracy of ±1%. It accommodates a 122-m (400-ft) roll of 16mm film. Film speed can be changed while the camera is running and two channels of time data (specific event blips and/or clocks) can be put on the film edges. It was run at 100 frames/second. Figure 23 is an enlargement of a frame from the motion pictures taken at 100 frames/second during the static test of specimen SN-18. The numbers are from light-emitting diodes attached to Fluke model 8000A digital voltmeters driven by the output of the load cells on each axis. The circles are scribed on the specimen at 0.254-cm (0.1-in.) intervals to aid in crack tip location. Crack growth versus load was established by projecting the film with an L and W photo-optical data analyzer, model 224-A, and measuring the projected crack length, suitably scaled, at each increment of load displayed on the digital voltmeter readouts in the picture.

A running historical log kept of each test recorded date, time of day, notes on any anomalies, nominal peak load values and cycle rates, number of cycles of loading for each load block and cumulative number of cycles, scribe mark number (see following section), and the symbol used to tie together the teletype record, visicorder record, and X-Y plot at any given time (usually an alphabetical letter). In addition, film speeds, static loading rates, observations on specimen behavior, and changes in record scale factors were recorded.

Test Procedures and Parameters

Specimen installation. - The first step in preparing a precracked specimen for test was to mount the grip plates. A 2.4x 2.4-m (8x8-ft) plywood assembly table with appropriately spaced standoffs was built to align the specimen and grip plates during assembly. Grip plate bolts were tightened with an impact wrench to a 135 to 200 N-m (100 to 150 ft-lb) torque. If the compression fixture was required, it was installed along with the grip plates. Next the 0.64-cm (¼-in.) center hole, used as a starter for flaw cutting, was enlarged to 1.28 cm (½ in.) by drilling and reaming and the crack displacement gage holder was bonded in place.
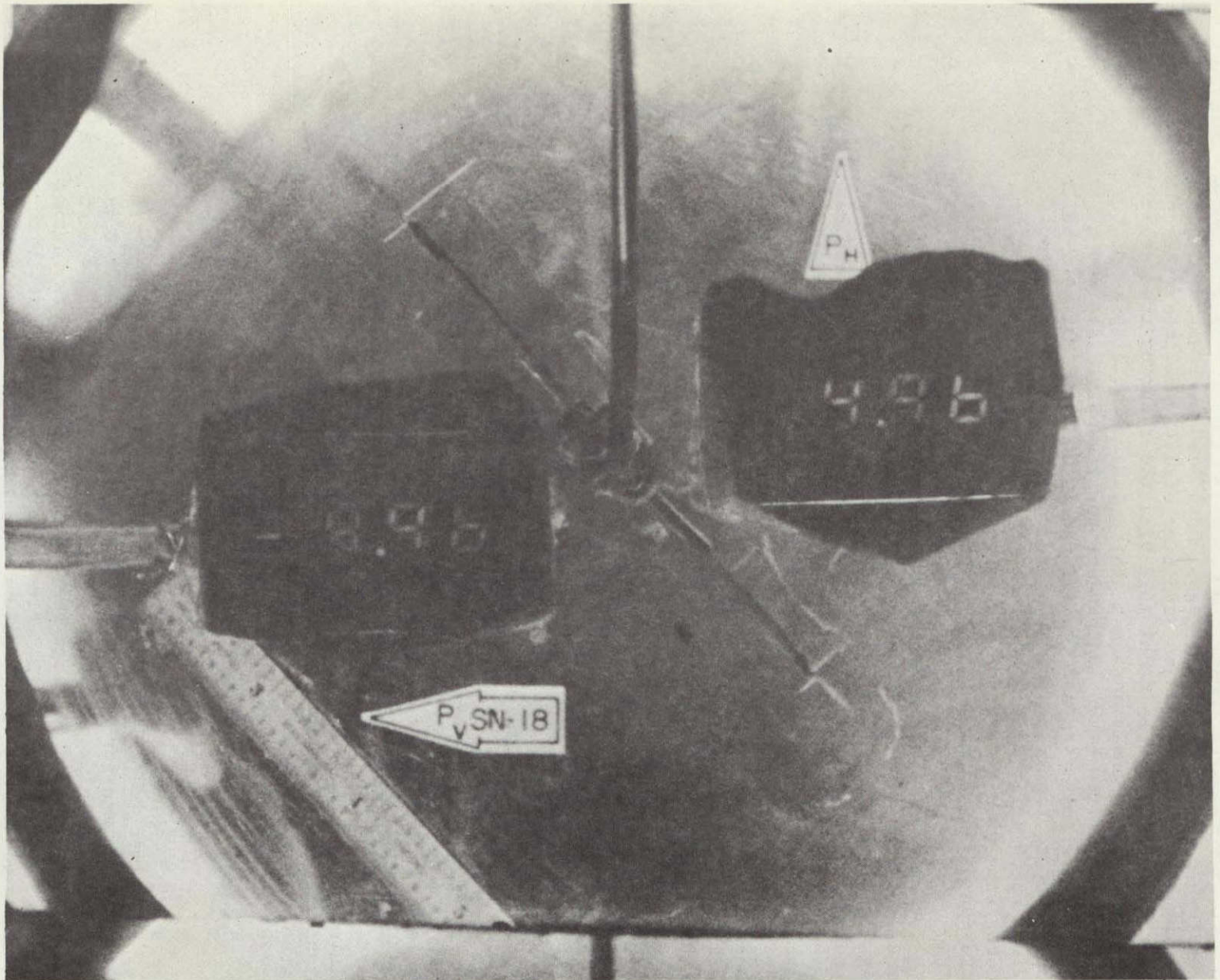
Figure 23. — Frame from high-speed motion picture of specimen SN-18
during static testing.

A scribe mark was made across the ends of the sharpened flaw and labeled 0. The horizontal axis was rolled out from between the vertical axis columns and the specimen with grip plates attached was lowered by crane between the horizontal axis side frames, proper note being taken of the final rolling direction and flaw direction. Shear pins were slipped through the grip loading holes and clevises on the horizontal axis load rods with appropriate shim plates to keep the specimen midplane on the load train center-line. The horizontal axis with specimen in place was then rolled back between the vertical axis columns. The support rams were attached and the horizontal axis was lifted about 3.8 cm (1½ in.) off its rails. Then the vertical axis shear pins were slipped into place, care being taken not to load the specimen by adjusting the support rams while monitoring both the upper and lower vertical axis load cells.

Amplifier gains on the crack displacement channels were adjusted before each test. Before they were inserted into the biaxial gage holder, the gages were exercised in a supermicrometer and the gains set to provide a convenient excursion of the traces on the visicorder. Calibrations on all the channels were checked with built-in shunt resistors. The computer was programmed according to a prepared test plan and the resulting computer output signals were verified on the X-Y plotter. Range settins, load limits, error limits, plotter and visicorder zero settings, etc were all reviewed. These settings were reviewed again and adjusted as needed after the hydraulic power supply was switched to the test pressure level and the loading pistons were adjusted to the zero load position. -

Load types and directions. - The objective of pursuing a test program that covered the range from pure K_I to pure K_{II} conditions on the flaw required several different loading schemes. It is theoretically possible to obtain the full range of K_I / K_{II} from zero to infinity on a 45-deg flaw by using the cyclic loading schemes shown in figure 24 provided the flaw remains at 45 deg to the loading axis while it grows. All the schemes shown (except E) were designed to reverse the direction of shear, or K_{II}, on each cycle. It was believed that reversing the shear on each cycle would cause the flaws to grow in a stair-step fashion on the microscopic scale, and that they would therefore appear straight on a gross scale. For the static tests, the scheme designation applies only to the first ramp of the load. No cyclic tests were made using scheme D (see Table III for the load type applied to each specimen). Because the crack branched or turned, the intended K_{II} / K_I ratios were often not obtained.
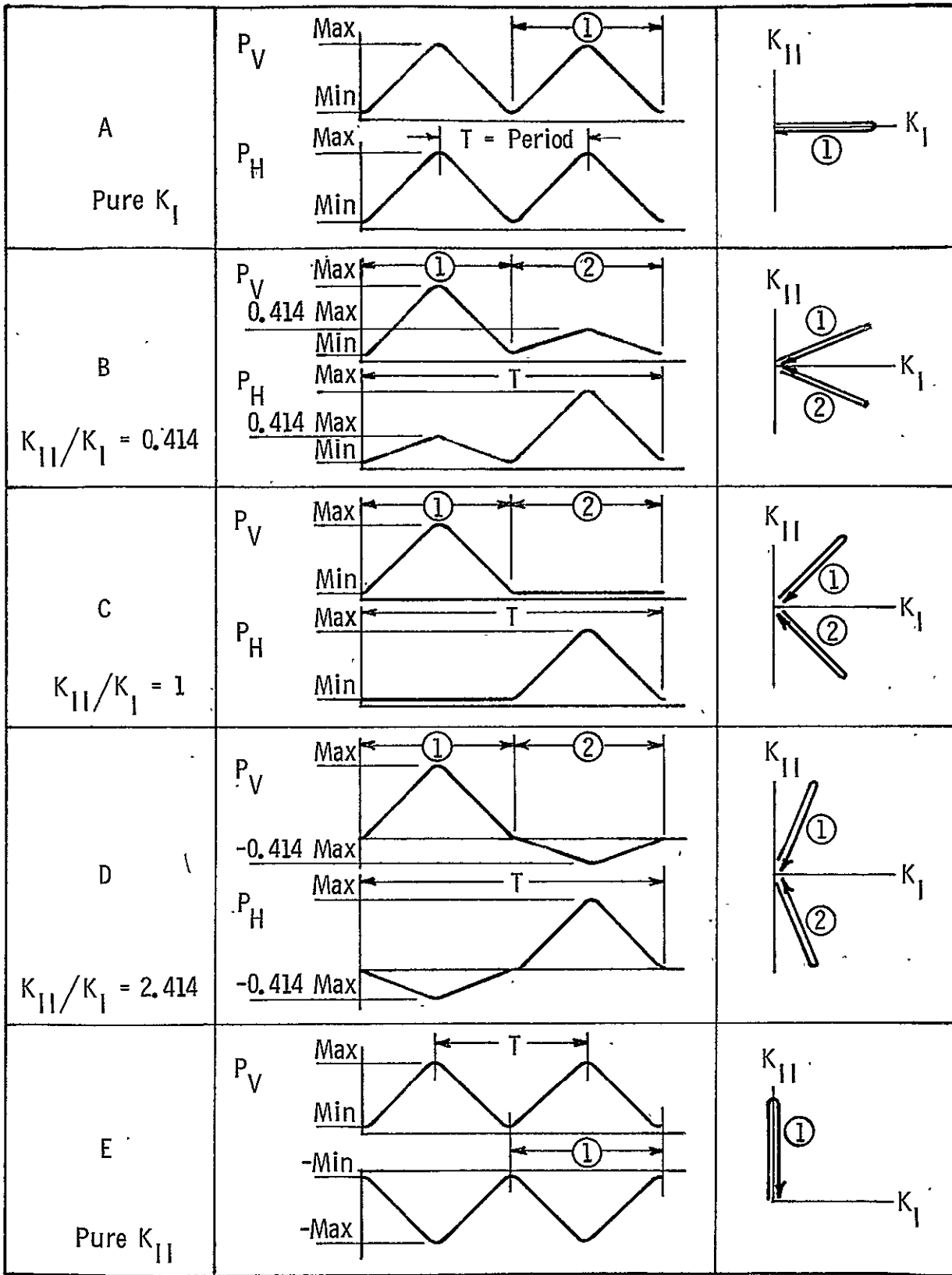
Figure 24. – Load schemes for various ratios of K_{II}/K_I.

TABLE III. – TEST PARAMETERS

Spec-imen	Alloy[a]	Thick-ness, cm (in.)	Final rolling direction in test machine[b]	Grip mate-rial[c]	Intended nominal K_I/K_{II}	Test Type		Load scheme	Initial Flaw Lengths			
						Cyclic	Static		$2a_i$, cm (in.)	$2a_i^H$, cm (in.)	$2a_i^I$, cm (in.)	$b\lambda/6$, cm (in.)
SN-1	2219	1.55 (0.61)	H	S	Pure K_I	Yes	No	A	6.541 (2.575)			8.64 (3.40)
SN-2	2219	1.55 (0.61)	V	S	Pure K_I	Yes	Yes	A	5.385 (2.120)	12.55 (4.94)	10.29 (4.05)	8.15 (3.21)
SN-3	2219	1.55 (0.61)	V	A	2.4	Yes	No	B	5.469 (2.153)			
SN-4	2219	1.55 (0.61)	H	S	1.0	Yes	Yes	C	5.423 (2.135)		9.09 (3.58)	5.423 (2.135)
SN-5	2219	0.64 (0.25)	H	A	2.4	Yes	Yes	B	5.283 (2.080)		7.82 (3.08)	5.283 (2.080)
SN-6	2219	0.64 (0.25)	H	S	Pure K_I	Yes	Yes	A	4.928 (1.940)	12.27 (4.83)		
SN-7	7075	1.27 (0.50)	V	S	Pure K_I	Yes	No[d]	A	5.166 (2.034)			9.09 (3.58)
SN-8	7075	1.27 (0.50)	H	A	2.4	Yes	No	B	6.375 (2.510)			
SN-9	7075	1.27 (0.50)	V	A	2.4	Yes	No[d]	B	5.474 (2.155)			5.474 (2.155)
SN-14	7075	1.27 (0.50)	V	A	2.4	Yes	Yes	B	5.029 (1.980)		7.52 (2.96)	5.84 (2.30)
SN-27	7075	1.27 (0.50)	H	A	Pure K_{II}	Yes	No	E	7.701 (3.032)		5.44 (2.14)	7.701 (3.032)
SN-11	2219	0.64 (0.25)	H	A	0.4	No	Yes	D	10.60 (4.175)	10.62 (4.18)		
SN-12	2219	0.64 (0.25)	H	A	Pure K_{II}	No	Yes	E	10.73 (4.225)	10.73 (4.23)	7.59 (2.99)	10.732 (4.225)
SN-15	7075	1.27 (0.50)	H	A	Pure K_I	No	Yes	A	10.26 (4.040)	10.26 (4.04)		
SN-16	7075	1.27 (0.50)	H	A	1.0	No	Yes	C	10.92 (4.300)		7.72 (3.04)	10.922 (4.300)
SN-17	2219	1.55 (0.61)	H	A	0.4	No	Yes	D	10.49 (4.130)	10.49 (4.13)		
SN-18	2219	1.55 (0.61)	H	A	Pure K_{II}	No	Yes	E	10.34 (4.070)	10.34 (4.07)		
SN-23	7075	1.27 (0.50)	H	A	1.0	No	Yes	C	10.57 (4.160)		7.47 (2.94)	10.566 (4.160)
SN-24	7075	1.27 (0.50)	H	A	Pure K_{II}	No	Yes	E	10.52 (4.140)	10.52 (4.14)		
SN-25	7075	1.27 (0.50)	V	A	Pure K_{II}	No	Yes	E	10.17 (4.005)	10.17 (4.01)		
SN-26	7075	1.27 (0.50)	H	A	0.4	No	Yes	D	10.72 (4.22)	10.72 (4.22)		

[a] 2219, temper T-87; 7075, temper T-7351.

[b] H – horizontal; V – vertical.

[c] S – steel; A – aluminum.

[d] Last cyclic load taken as a "static" test.

Direction of final rolling. – Care was taken to note the relation between the final rolling direction and the orientation of the specimen in the testing machine.` This relation was deliberately and frequently changed in the early stages of the program to eliminate any bias that might be due to always putting the rolling direction in the same axis. Later in the program it was changed to study the effect of rolling direction on the path of crack growth, fracture direction, and fracture loads. Final rolling directions are listed in table III.

Flaw size. – There are several values of "initial" flaw size associated with each specimen. The first is the length of the flaw after precracking, designated $2a_i$. The next is the arc length of curved flaws after cyclic testing but before static testing for specimens subjected to both types of tests and used for Holston's analysis $\left(\text{designated } 2a_i^H\right)$. There is also the projection of this length in the direction perpendicular to the final fracture direction used for Iida's analysis and designated $2a_i^I$. The designation $2a_i^I$ is also used for the projected length of branched cracks analyzed by the Iida method for fracture toughness. Finally, there is the equivalent linearized slant length for the Iida analysis used to establish the relation between the crack length and the plate width, designated $b_\lambda/6$. Figure 25 contains diagrams illustrating these various concepts of flaw length, as well as an illustration of the length designations used in the crack growth analyses. The values are given in Table III along with the other test parameters.

Cyclic test procedure. – The first step in performing the cyclic tests was to program the computer. It was assumed that both loading axes would behave as though infinitely stiff and follow the computer output exactly. A few cycles of load, usually less than 10, would then be applied and the loads recorded on the visicorder at a high rate of paper speed (10 cm/s). The difference in the time each axis reached its peak load could then be read easily to 0.01 seconds. Changes were made in the computer program for the vertical axis to delay it so the two axes would reach the peak loads simultaneously. This delay ranged from 0.03 to 0.07 second depending on the magnitude and rate of loading. The X-Y plotter was used to record vertical versus horizontal load before and after the program change. Figure 26 is an example of the plots obtained in this manner for SN-1 at the 565-kN (127-kip) load level.

After Precracking — For Curved Cracks — For Branched Cracks
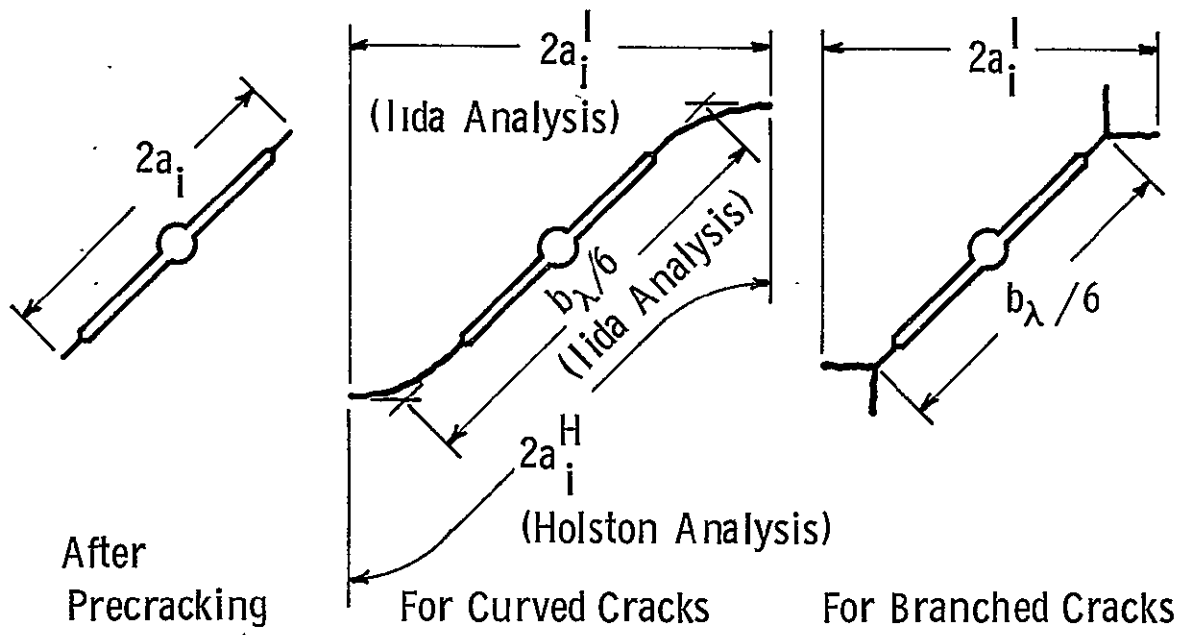
Starting Flaw Lengths for Static Tests
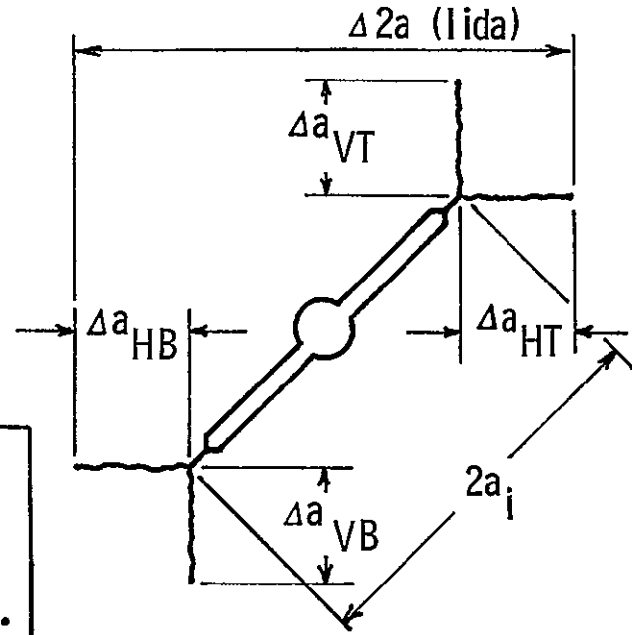
Note: T = top,
B = bottom,
V = vertical,
H = horizontal.

Holston analysis = Vertical crack $2a = 2a_i + \Delta a_{VT} + \Delta a_{VB}$,

horizontal crack $2a = 2a_i + \Delta a_{HT} + \Delta a_{HB}$.

Iida analysis = Vertical crack $2a = 1.414a_i + \Delta a_{VT} + \Delta a_{VB}$,

horizontal crack $2a = 1.414a_i + \Delta a_{HT} + \Delta a_{HB}$.

Figure 25. – Definition of crack lengths.
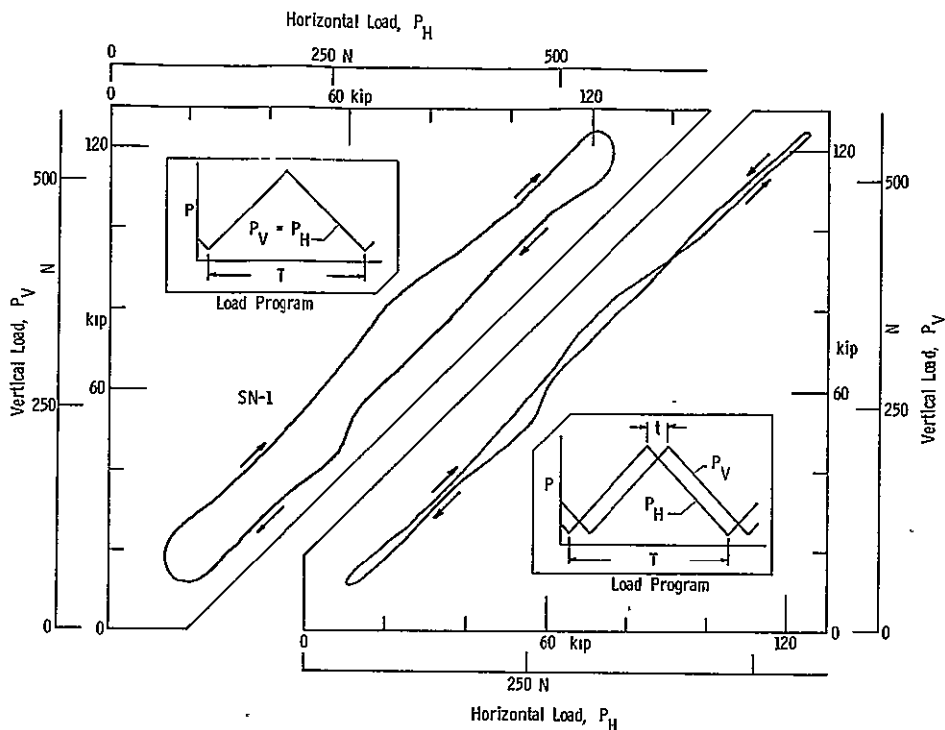
Figure 26. - Example of computer program change to overcome horizontal axis lag.

Cyclic load was applied in accordance with two different schedules. In some tests it was applied in 7 to 10 groups of three load blocks each. Each load block consisted of a number of cycles necessary to produce about 0.13 cm (0.050 in.) of flaw growth. Each of the three blocks in a group was run at approximately the same maximum load level although the stress intensity increased as the flaw length increased. Each group of three blocks was run at increasingly higher load levels, the first group at a stress intensity of about 25% of critical, with the maximum load being increased by 10 to 20% for each subsequent group. In other tests the load level was increased 5 to 10% after each load block. The ratio of minimum to maximum loads (R value) were always kept below 0.1 and generally below 0.05. Cyclic loading was generally continued until the crack growth rate reached 0.127 to 0.38 mm/cycle (5000 to 15000 micro-in./ cycle). In some cases it was continued to fracture. The cycle rate was generally 15 to 20 cycles per minute. In plates of finite extent, K_I and K_{II} are different functions of crack length even though the crack stays straight (see Appendix A, fig. A-11). Therefore to maintain a constant ratio of K_{II}/K_I as the crack grew it was necessary to slightly adjust the ratio of the load on one axis to the load on the other. Figure 27 contains curves of the ratios of loads as a function of half crack length for a

45-deg crack required to keep the K_{II}/K_I ratio constant. This chart was used as a guide even though the cracks often turned or branched, making the analysis not entirely valid. At the end of each load block, the locations of the tips of the crack were scribed on the specimen and noted in a data book. A section of oscillograph record was also taken to permit determination of the slope of a crack opening versus load plot, which is a measure of the compliance. Load from the vertical axis versus load from the horizontal axis was recorded on an X-Y recorder at the beginning of each load block to check the load ratios. The computer print-out and a cycle counter on the vertical axis console kept track of the number of cycles of loading at each load level. If the specimen was to be tested statically it was left in the machine. Otherwise it was removed and those that were still in one piece were either pulled apart or cut with a saw to expose the crack surface and to facilitate measurement of the distance between scribe marks.
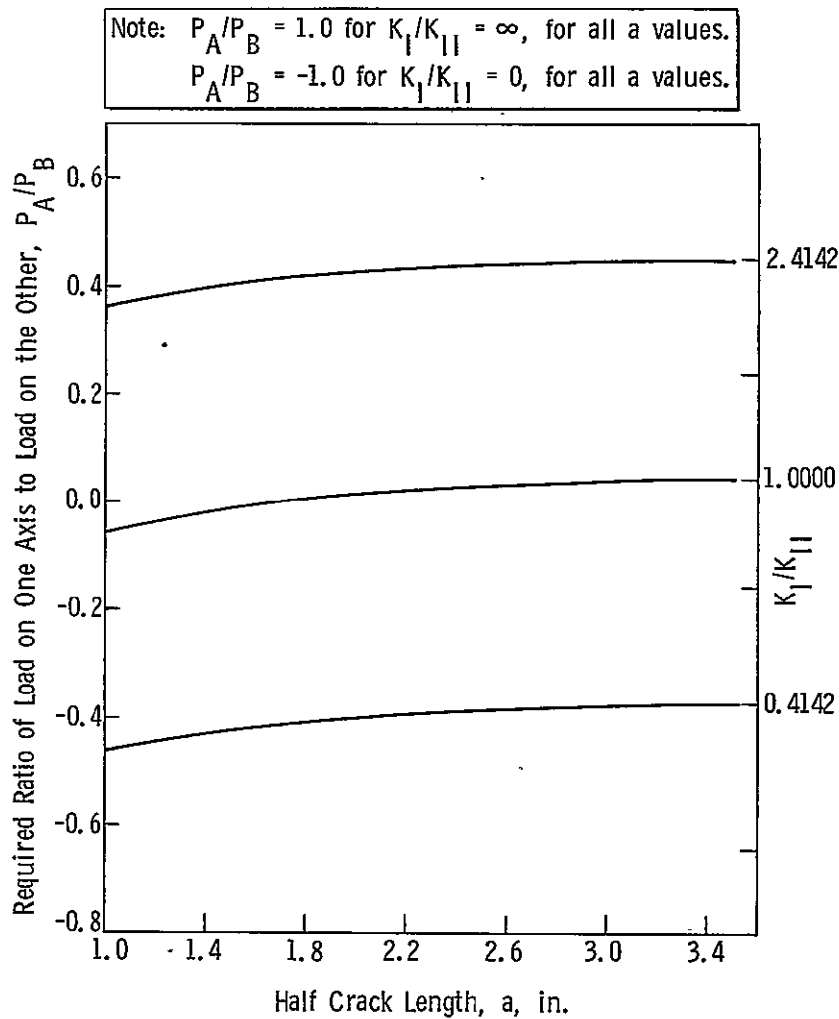
Figure 27. — Test load ratio chart.

Static test procedure. - The first step in performing the static tests again was to program the computer. There was no problem of horizontal axis lag because of the slow rate of loading. The rate used was 448 to 667 kN (100 to 150 kips) per minute for the axis with the higher load. The ratio of loads depended . on the desired K_I/K_{II} ratio. The program was carried well above the expected maximum load. The high-speed movie camera was mounted and focused and was turned on after some loading had taken place but before subcritical crack growth started. It was run at 100 frames/second to the end of the test. Oscillograph records were taken continuously throughout the test as was a record of loads on the X-Y plotter. When fracture occurred the error signals were generally great enough to shut off the machine, although in some instances failure was not violent and the machine was stopped manually. In some instances the crack displacement gages were removed before fracture to prevent damage to them. After the· test was over, the specimen was removed by reversing the procedure for specimen installation, except care had to be taken in unpinning the broken specimens as they were now generally in two distinct parts.

Experimental Observations and Primary Data

Because the type of analysis applied to the response of each specimen depended on that response, it is necessary to describe how the cracks grew and under what conditions. Therefore, a short description of the behavior of each specimen under test is given in Appendix D, which also contains tables of cyclic loading schedules and resultant crack lengths for all cyclic tests, and tables of loads and crack lengths taken from the high-speed movies for the static tests. Load and cycle data are very briefly summarized in table IV. Appendix E contains photographs of all specimens after testing. Characteristics of crack appearance and other pertinent notes about the specimens are summarized in table V.

Several general observations should be made. Great care was taken to align the loading axes of the testing machine and to locate the midplane of the specimens on the plane defined by these axes through the use of shims and spacers. Nevertheless there was evidence of specimen bending in almost all the tests. Sometimes the specimens appeared to move out of plane at the center as much as 0.6 cm ($\frac{1}{4}$ in.), while at other times no such movement was discernible although there was other evidence of bending. In the tests of specimens under pure K_I conditions there should

have been no response from the displacement gage measuring shear deformations (CSD). Yet in these tests (SN-1, 2, 6 and 7) the CSD did have some output from the very beginning of the tests.

TABLE IV. – SUMMARY OF LOAD AND CYCLE DATA

Specimen	Maximum cyclic load, kN (kip)	Total cycles	Load at start of subcritical crack growth, kN (kip)		Load at static fracture, kN (kip)	
			P_V	P_H	P_V	P_H
SN-1	575.6 (129.4)	52 263	----- -----	----- -----	----- -----	----- -----
SN-2	591.6 (133.0)	59 689	594.3 (133.6)	604.1 (135.8)	770.0 (173.1)	779.3 (175.2)
SN-3	489.3 (110.0)	22 654	----- -----	----- -----	----- -----	----- -----
SN-4	569.4 (128.0)	31 970	745.5 (167.6)	0 (0)	849.6 (191.0)	44.5 (10.0)
SN-5	264.7 (59.5)	43 105	323.4 (72.7)	137.9 (31.0)	545.4 (122.6)	230.4 (51.8)
SN-6	243.8 (54.8)	55 005	297.1 (66.8)	306.5 (68.9)	508.0 (114.2)	518.7 (116.6)
SN-7	511.5 (115.0)	40 455	----- -----	----- -----	----- -----	----- -----
SN-8	513.8 (115.5)	23 673	----- -----	----- -----	----- -----	----- -----
SN-9	502.6 (113.0)	39 306	----- -----	----- -----	----- -----	----- -----
SN-14	313.6 (70.5)	124 310	1023.0 (230.0)	0 (0)	1468.0 (330.0)	0 (0)
SN-27	435.9 (98.0)	26 326	----- -----	----- -----	----- -----	----- -----
SN-11	----- -----	----- -----	-153.0 (-34.4)	371.0 (83.4)	-256.2 (-57.6)	614.7 (138.2)
SN-12	----- -----	----- -----	-315.8 (-71.0)	314.0 (70.6)	-411.0[b] (-92.4)[b]	404.8[b] (91.0)[b]
SN-15	----- -----	----- -----	667.2 (150.0)	667.2 (150.0)	965.3 (217.0)	967.5 (217.5)
SN-16	----- -----	----- -----	0 (0)	794.0 (178.5)	0 (0)	1108.0 (249.0)
SN-17	----- -----	----- -----	a (a)	a (a)	-613.9 (-138.0)	1486.0 (334.0)
SN-18	----- -----	----- -----	-676.1 (-152.0)	680.6 (153.0)	-1103.0 (-248.0)	1130.0 (254.0)
SN-23	----- -----	----- -----	689.5 (155.0)	0 (0)	751.7 (169.0)	0 (0)
SN-24	----- -----	----- -----	-547.1 (-123.0)	547.1 (123.0)	-1034.0 (-232.5)	1025.0 (230.5)
SN-25	----- -----	----- -----	-578.3 (-130.0)	578.3 (130.0)	-1008.0 (-226.5)	1001.0 (225.0)
SN-26	----- -----	----- -----	a (a)	a (a)	-498.2 (-112.0)	1281.0[c] (288.0)[c]

[a]Undetermined.　[b]Buckled.　[c]Loading tab failure.

43

.TABLE V. - SUMMARY OF CRACK CHARACTERISTICS

Specimen	High-speed movies	Crack growth characteristics	Remarks
SN-1	No	Curved to horizontal.	No records of fracture.
SN-2	Yes	Curved to vertical.	--
SN-3	No	Branched, horizontal predominant.	Cyclic test stopped.
SN-4	Yes	Branched, horizontal predominant at fracture.	Tension normal to rolling direction in static test.
SN-5	Yes	Branched, horizontal predominant at fracture.	High tension normal to rolling direction in static test.
SN-6	Yes	Straight, then curved as shear lip formed.	--
SN-7	No	Curved to vertical.	Cycled to fracture.
SN-8	No	Branched, horizontal predominant.	Loading tab fracture during cycling.
SN-9	No	Branched, vertical predominant.	Cycled to fracture.
SN-14	Yes	Branched, horizontal predominant at fracture.	Shear not reversed on each cycle.
SN-27	No	Directly vertical with no curvature	Cycled to fracture. Shear not reversed.
SN-11	Yes	Straight into corners, no shear lip.	Tension parallel to rolling direction.
SN-12	Yes	Sharply curved to vertical.	Buckled under vertical compression.
SN-15	Yes	Gradual curve to horizontal.	--
SN-16	Yes	Vertical, then horizontal into corners.	Tension parallel to rolling direction.
SN-17	Yes	Straight into corners, no shear lip.	--
SN-18	Yes	Straight into corners, no shear lip.	--
SN-23	Yes	Horizontal. Compare with SN-16.	Tension normal to rolling direction.
SN-24	Yes	Straight into corners, no shear lip.	Tension parallel to rolling direction.
SN-25	Yes	Straight into corners, no shear lip.	Tension normal to rolling direction.
SN-26	Yes	Straight for short distance.	Loading tab fracture. No load readout in movies.

The fixture for holding the CSD had knife edges outside the plane of the specimen and bending produced some twisting of the gage that translated into an output. Once the crack turned so it was no longer at 45 deg to the loading axis, a response from the CSD was to be expected.

Similar behavior was exhibited by SN-27, which was to be a pure K_{II} cyclic test. There should have been no response from the crack opening displacement (COD) gage. The COD gage was mounted against knife edges at the midplane of the specimen. Ideally even if there were bending, there should have been no response. But the gage holder was adhesively bonded through the entire thickness of the specimen. Defects in this bond, torsion, or bending in the specimen would translate into COD gage response. There was such response.

If such imperfections in the testing operation were present as described for the five specimens discussed, it is only reasonable to assume that they existed in the other tests as well where both COD and CSD responses were expected. Some doubt exists therefore as to the validity of the COD and CSD measurements for anything except as a tool for monitoring the progress of the tests and qualitatively checking the response of the specimens.

As explained in the following descriptions of test procedures, scribe marks were used to establish the crack growth at the end of each block of cyclic loads. These scribe marks were placed where a crack penetrated the surface. Generally it was suspected that the crack was longer beneath the surface because there was a "dimple" on the surface. When the specimens were fractured this suspicion was confirmed. The crack fronts were not straight through the specimen from surface to surface, but rather exhibited tunneling. Tunneling was greatest when shear lips were most evident and was least when there were no shear lips.

ANALYSIS AND DATA INTERPRETATION

Data Reduction Techniques

Calculation of useful quantities such as stress intensity or crack growth rate requires considerable manipulation of primary data. Also, various analyses for stress intensity and related parameters use differing definitions for crack length, stress, etc. To permit verification of the interpretations that have been made and establish the consistency of the analyses, the manner in which the data was handled is reviewed below.

The key to calculation of R curves and strain energy release rates is calculation of the stress intensity, K. In general,

$$K = C\sigma\sqrt{\pi a} \qquad [1]$$

where C is a coefficient defining specimen and/or crack shape, and σ is some measure of stress in the flaw area (how this is computed will also influence C), and a is a measure of crack length.

Stress intensity at fracture, straight cracks – When the flaw.was not branched or curved and stayed straight during sub-critical crack growth under static testing, K values were computed using Holston's analysis (ref. 12). This approach was applied to SN-11, 15, 17, 18, 24, 25, and 26. It was also applied to SN-2 and 6 to see if it gave different results from other approaches described later. For Holston's analysis,

$$K_I = \tilde{K}_I \frac{P_V + P_H}{2A}\sqrt{\pi a} \qquad [2]$$

and

$$K_{II} = \tilde{K}_{II} \frac{P_V - P_H}{2A}\sqrt{\pi a} \qquad [3]$$

where $\tilde{K}_I$ and $\tilde{K}_{II}$ are shown in figure 8, A is the gross area of the loading tab (equal to 20t for customary units or 50.8t in SI units), and a is one-half the total crack length. Using a thus is the same as averaging the growth at each end of the crack.

Stress intensity at fracture, branched or curved cracks – When the flaw was branched or curved due to previous cyclic testing, or grew parallel to one of the loading axes during static test, K values were computed using Iida's analysis (ref. 9). This approach was applied to SN-2, 4, 5, 7, 9, 12, 14, 16, and 23. For Iida's analysis,

$$K_I = M_{SI} \frac{P_a}{A}\sqrt{\pi a} \qquad [4]$$

46

$$K_{II} = M_{SII} \frac{P_a}{A} \sqrt{\pi a} \qquad [5]$$

where M_{SI} and M_{SII} are shown in figure 5, P_a is the load perpendicular to the predominant crack direction or branch of interest, A is 40.23t in SI units or 15.84t in customary units, and a is one-half the projected crack length perpendicular to the load direction. The numbers 40.23 and 15.84 arise in the following manner. The Iida analysis for a 45° slant flaw assumes the original flaw length is one-half the plate width. It also assumes one principal stress is parallel to the plate length while the others are zero. To adapt the analysis to the Maltese Cross specimen and crack configurations, an equivalent plate width $\left(2b_\lambda\right)$ equal to 12 times the slant flaw length was used to compute Iida's λ, the ratio of projected crack length to plate width. For slant flaws that were nominally 5-cm (2-in.) long, the equivalent plate width was nominally 60 cm (24 in.). For branched cracks, each branch was handled individually and only the load perpendicular to the branch of interest was considered. To obtain the stress required in Iida's computation of stress intensity (which for Iida is simply P/2bt), Holston's finite-element analysis was used for the specimen configuration in the un-flawed state. The analysis yielded the following relation for stress at the center of the plate under uniaxial load:

$$\text{Stress parallel to load direction} = \sigma_a = \frac{P_a}{15.84t} \quad \text{(customary units)} \quad [6]$$

$$\text{or} \quad \frac{P_a}{40.23t} \quad \text{(SI units)}$$

$$\text{Stress perpendicular to load direction} = \sigma_b = - \frac{P_a}{151.8t} \quad \text{(customary units)} \quad [7]$$

$$\text{or} \quad - \frac{P_a}{385.6t} \quad \text{(SI units)}$$

where t is plate thickness. The accuracy of these relations was established with data obtained during checkout of the mixed-mode testing fixture. The strain measured at that time at the center of a 2.578-cm (1.015-in.) thick 2024 aluminum biaxial specimen under a uniaxial load of 444.8 kN (100 kips) was 610 μin./in. in the direction of the load. Computed strain using plane stress equations, a modulus of the aluminum of 7.17×10^6 N/cm^2 (10.4×10^6 psi), and the above relations between load and stress, is 619×10^{-6}. Agreement is within 1.5 %. It is interesting that the configuration of the specimen resulted in a small compressive stress transverse to the load direction under uniaxial load. For specimens SN-2 and 7, where cracks were curved, it was necessary to approximate the curved shape with straight lines as shown in figure 25 to get an equivalent plate width for computing λ.

The 45° portions of the flaws for these two specimens, when so approximated, were 8.15 cm (3.21 in.) for SN-2 and 9.09 cm (3.58 in.) for SN-7.

Stress intensity at fracture, arc crack - The crack shape in SN-6 was an arc. To compute the stress intensities at fracture and for drawing the R curve, the analysis in reference 14 page 21.1 was used. Figure 28 is taken from that page. The value of stress for use in the equations for K_I and K_{II} was computed from $\left(P_V + P_H\right)\big/ 2A$ where A equaled 44.91t in SI units or 17.68t in customary units. The numbers 44.91 and 17.68 come from Holston's finite-element analysis for the specimen configuration in the unflawed state under equal biaxial loads. The analysis yielded the following relation for stress at the center of the plate:

$$\text{Hydrostatic stress} = \sigma_c = \frac{P}{17.68t} \quad \text{(customary units)} \qquad [8]$$

$$\text{or} \quad \frac{P}{44.91t} \quad \text{(SI units)}$$

where P is applied in two perpendicular directions. As above, this relation for stress was verified during machine checkout. Strain measured at that time on the 2.578-cm (1.015-in.) thick checkout specimen under 444.8 kN (100 kips) biaxial load was 330 to 340 x 10^{-6}. Using plane stress equations, a modulus of 7.17 x 10^6 kN (10.4 x 10^6 psi), and the above relations between load and stress, the computed strain was 359 x 10^{-6}. Agreement is within 8%. In the arc crack analysis, R is the radius of the arc. For SN-6, the arc that seemed to best approximate crack shape had an R = 18.61 cm (7.327 in.).

K_{II}/K_I for calculating G - Note that in figures 5, 8, and 28 the variation with a of values of the coefficient of $\sigma\sqrt{\pi a}$ are different for K_I and K_{II}. Thus, the ratio of K_I to K_{II} changes with a, even if the loads remain constant and the shape of the crack does not change. When R curves were drawn, as explained in the following section, according to

$$R = \frac{1 - \upsilon^2}{E}\left(K_I{}^2 + K_{II}{}^2\right) \qquad [9]$$

for any set of corresponding loads and crack lengths, the ratio of experimental K_I to K_{II} was noted. When the G curve was drawn (again, see the following section), this changing ratio was taken into account in the following manner. For Holston's analysis,

$$G = \frac{1 - \upsilon^2}{E}\left(K_I{}^2 + K_{II}{}^2\right) \qquad [10]$$

$$= \frac{1 - \upsilon^2}{E}\left(K_I{}^2 + n^2 K_I{}^2\right) \qquad [11]$$

48
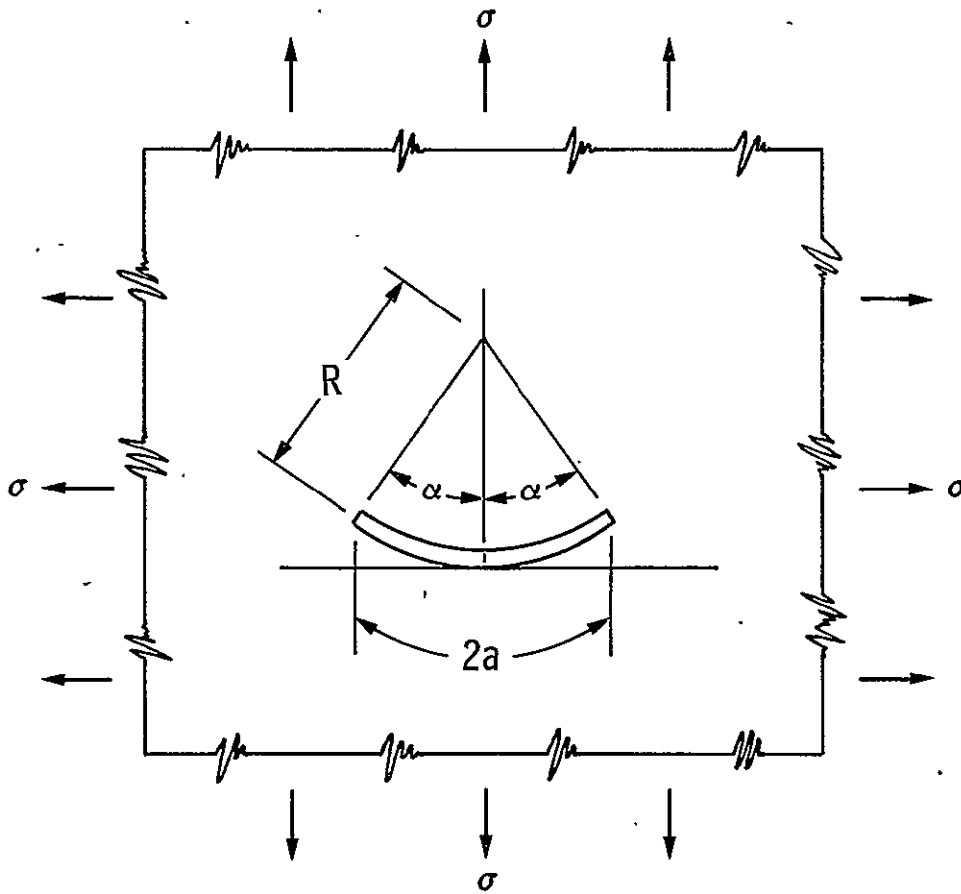
$$K_I = \sigma \sqrt{\pi R \sin\alpha} \quad \cdot \quad \frac{\cos \frac{\alpha}{2}}{1 + \sin^2 \frac{\alpha}{2}}$$

$$K_{II} = \sigma \sqrt{\pi R \sin\alpha} \quad \cdot \quad \frac{\sin \frac{\alpha}{2}}{1 + \sin^2 \frac{\alpha}{2}}$$

Figure 28. - Stress intensities for arc-shaped crack.

$$= \frac{1 - \upsilon^2}{E} K_I^2 \left(1 + n^2\right) = \frac{1 - \upsilon^2}{E} \tilde{K}_I^2 \ \sigma_N^2 \ \pi a \left(1 + n^2\right) \quad [12]$$

where n was the experimental value of K_{II}/K_I for each value of a. For Iida's analysis,

$$G = \frac{1 - \upsilon^2}{E} K_I^2 \left(1 + n^2\right) = \frac{1 - \upsilon^2}{E} M_{SI}^2 \ \sigma^2 \ \pi a \left(1 + n^2\right) \quad [13]$$

where again n was the experimental value of K_{II}/K_I. Because of the Iida formulation, n also equaled M_{SII}/M_{SI}. For the arc crack analysis,

$$G = \frac{1 - \upsilon^2}{E} K_I^2 \left(1 + n^2\right) = \frac{1 - \upsilon^2}{E} \ \sigma^2 \ \pi R \ \sin \alpha \left(\frac{\cos \frac{\alpha}{2}}{1 + \sin^2\frac{\alpha}{2}}\right)^2 \left(1 + n^2\right) \ [14]$$

where, as before, n was the experimental value of K_{II}/K_I. For this formulation, n also equaled $\tan (\alpha/2)$.

$\underline{\Delta G \text{ for crack growth rate curves}}$ – The formulation used for ΔG for crack growth rate curves was

$$\Delta G = G_{max} - G_{min} \quad [15]$$

where G_{max} was the value of G at the peak load, and G_{min} was the value at minimum load.

Now

$$G_{max} = \frac{1 - \upsilon^2}{E} \left(K_{Imax}^2 + K_{IImax}^2\right) \quad [16]$$

and

$$G_{min} = \frac{1 - \upsilon^2}{E} \left(K_{Imin}^2 + K_{IImin}^2\right) \quad [17]$$

so that

$$\Delta G = \frac{1 - \upsilon^2}{E} \left(K_{Imax}^2 + K_{IImax}^2 - K_{Imin}^2 - K_{IImin}^2\right) \quad [18]$$

Note that this is not the same as

$$\Delta G = \frac{1 - \upsilon^2}{E} \left[\left(\Delta K_I\right)^2 + \left(\Delta K_{II}\right)^2\right] \quad [19]$$

The value used to compute K values in equation 18 was the average value between the beginning of a block of cycles and the end. Whether the actual or projected length was used depended on whether the Holston or Iida analysis was used, which in turn depended on the shape of the crack as it grew. For SN-3, 4, and 6, only the Holston analysis was used. For SN-5 and 8, only the Iida analysis was used. For SN-1, 2, 7, and 9, both were used because the crack changed character as it grew. Similarly, the value of stress used in the computation of K_i depended on whether crack growth was being analyzed by the Holston or Iida approach. As before, for the static tests, for Holston,

$$\sigma_N = \frac{P_V + P'_H}{2A} \tag{20}$$

and
$$\tau = \frac{P_V - P_H}{2A} \tag{21}$$

where
$$A = 20t \text{ (customary units)} \tag{22}$$
$$\text{or } A = 50.8t \text{ (SI units)}$$

and, for Iida, equation 6 was used. The calculation of $\Delta a / \Delta N$ was always the average growth of the two ends of the flaw and both faces of the specimen.

Compliance - The general definition of compliance is deformation per unit load. Compliance was computed as follows for crack opening displacement (COD):

$$\frac{\Delta(COD)}{\left(\Delta P_V + \Delta P_H\right)/2} \tag{23}$$

and for crack shear displacement (CSD):

$$\frac{\Delta(CSD)}{\left(\Delta P_V - \Delta P_H\right)/2} \tag{24}$$

where ΔP was the difference between the maximum and minimum loads and $\Delta(CSD)$ or $\Delta(COD)$ the difference between the maximum and minimum gage response for the cycle for which compliance was being computed.

Static Fracture Experiments

A number of static fracture experiments were conducted in this program. In some cases, the experiment was conducted after mixed-mode cyclic loading with reversed shear. In others, the experiments were conducted immediately after the original fatigue sharpening of the crack. As described earlier, an attempt was made in all experiments to record crack length and load on both axes as functions of time throughout the final phase of the experiment. Because the thickness of materials tested was such that plane strain conditions for fracture were not maintained, significant subcritical crack growth was evident before final failure occurred. This implies the presence of a significant amount of plastic deformation in the fracture process, so it was decided to analyze the failure of these specimens in terms of the R-curve concept.

Figure 29 is a plot of G, strain energy release rate, versus a, crack length. The line labeled R Curve represents the amount of energy per unit crack area required to drive the crack through the material. This curve conceptually includes the energy necessary to form the large plastic zone associated with fracture in the specimens tested in this program. When high-speed motion-picture data
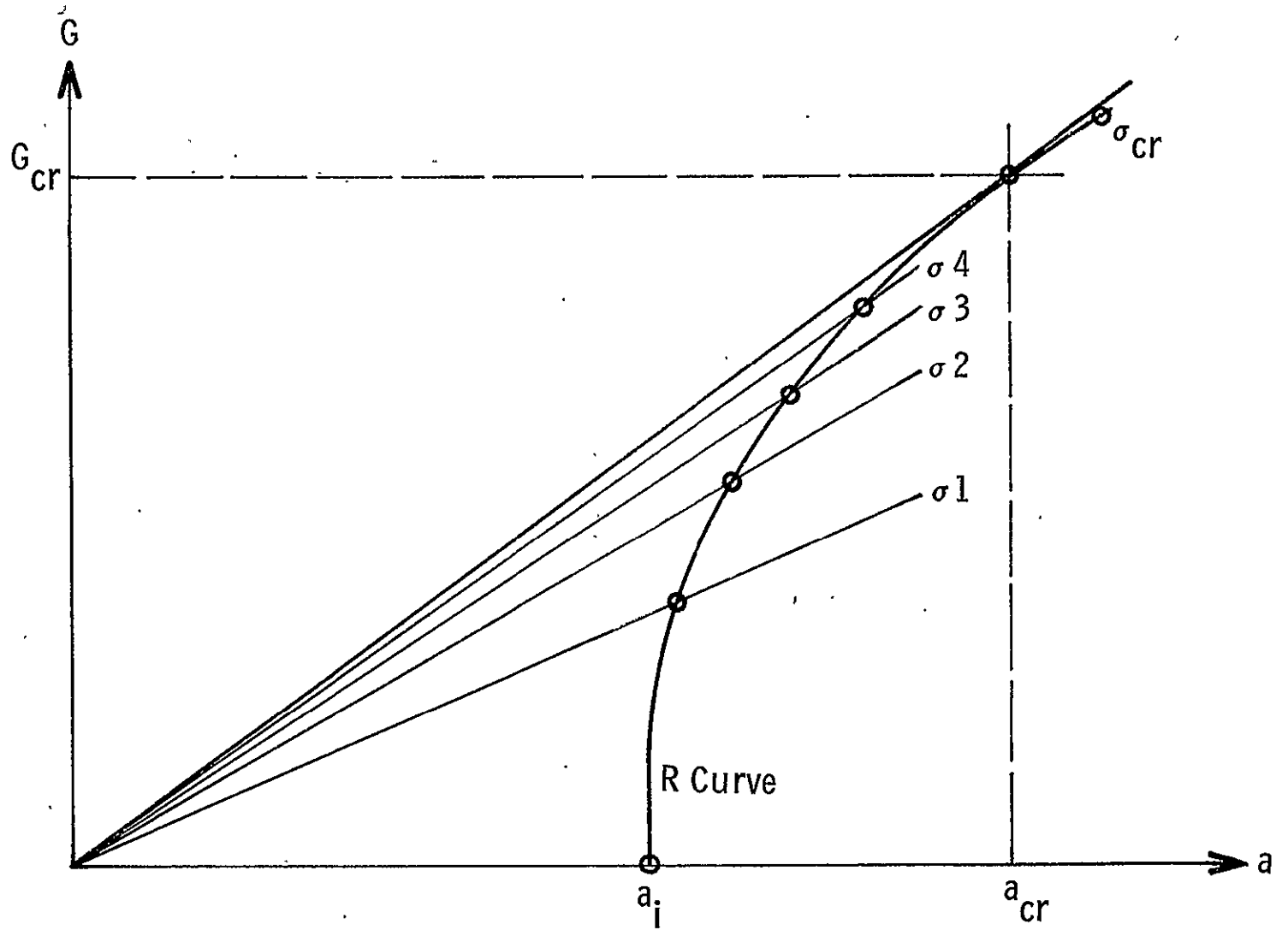
Figure 29. – R curve construction.

are available on crack length and load as the crack grows toward failure, it is possible to construct the R curve for each experiment as follows:

1) The point labeled a_i is initial crack length;

2) The line labeled σ_1 represents a theoretical calculation of G as a function of crack length for stress level σ_1. The stress level σ_1 and corresponding crack length are known from high-speed motion-picture data, so it is possible to compute a value for G that locates the data point on the R curve;

3) This process is repeated for stress levels σ_2, σ_3, etc, until a point of tangency is found between the R curve and the equation for G as a function of a;

4) The tangency point is taken to be the critical point at which rapid crack propogation occurs. This point identifies the critical stress, σ_{cr}, and critical crack length, a_{cr};

5) These quantities are used to compute G_{cr}, the critical strain energy release rate.

To construct the R curve from experimental data as described above, a method to calculate G is necessary. In the previous section, methods for calculating stress intensity factors K_I and K_{II} and the strain energy release rate were described. To repeat, in constructing the R curves for each static fracture experiment, the following equation was used:

$$G = \frac{1 - \upsilon^2}{E} \left(K_I{}^2 + \overline{K_{II}{}^2} \right) \qquad [10]$$

This expression correctly represents G as long as K_I and K_{II} values are computed for crack growth in the direction in which the crack actually is growing. As described in the previous section, every attempt was made to do this.

Figures 30 through 45 present R curve constructions for specimens on which there were enough data. Figures 30 and 31 present R curves for sample SN-2 calculated by two different analysis procedures. Figure 30 used the curves of Iida, and figure 31 used the calculations of Holston for the same specimen. Little difference is noted between the two R curves produced. Also, the critical value of G and critical crack length predicted by the two analysis procedures are very nearly equal. This lends credence to the use of Iida's analysis, which is valid only for uniaxial loading in a situation in which loading is actually biaxial. The results in figure 36 were computed using K_I and K_{II} expressions for a two-
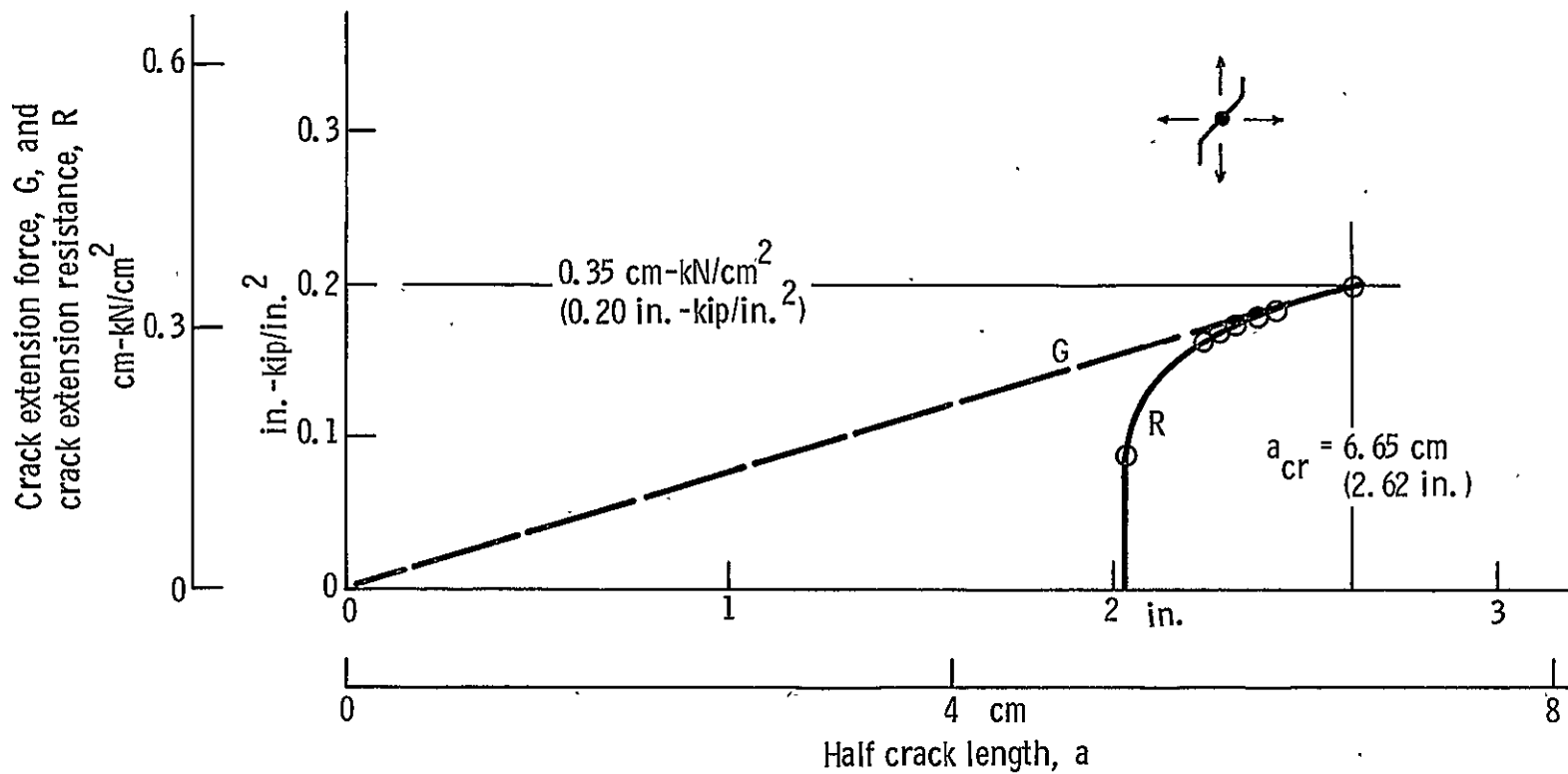
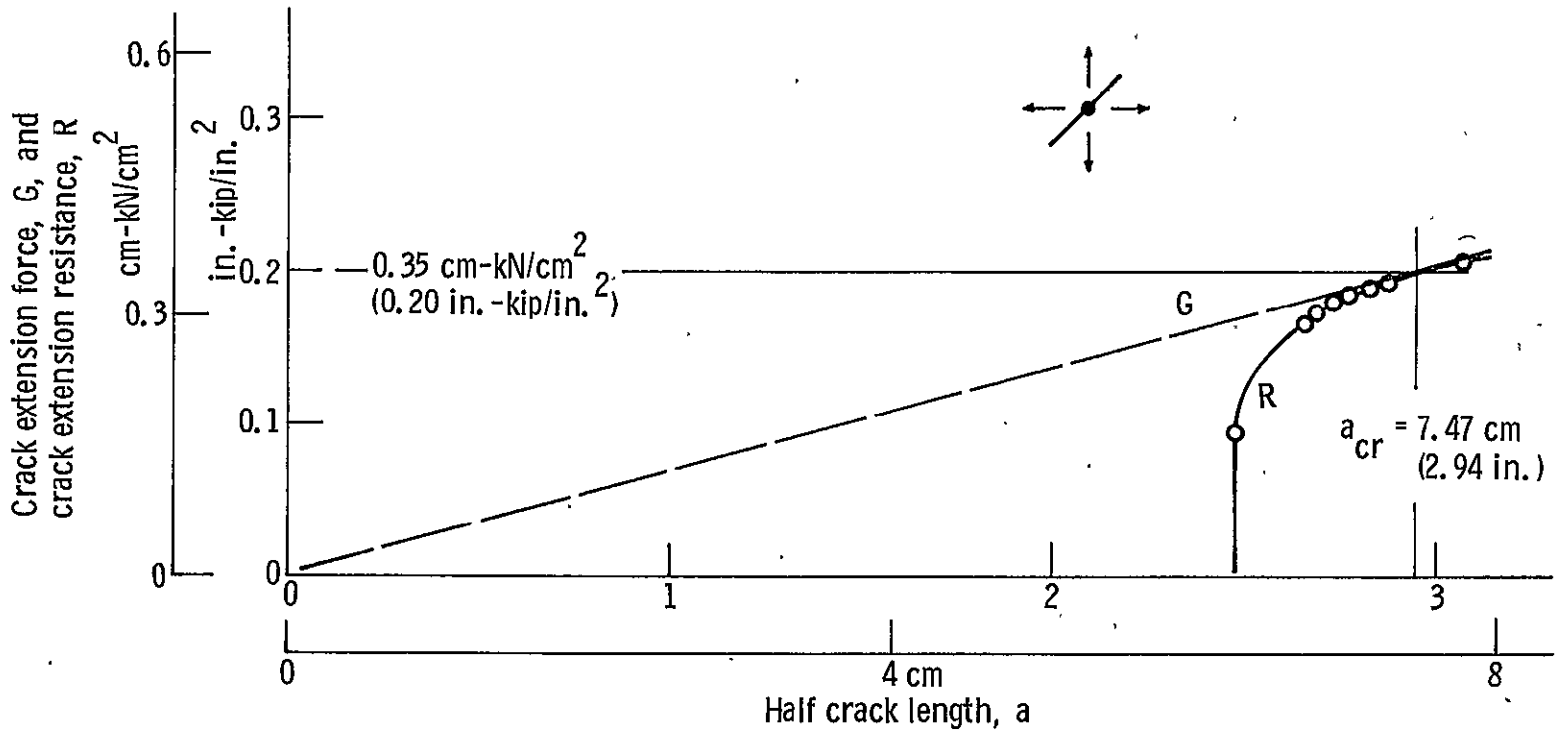Figure 30. – R curve for SN-2, Iida analysis.

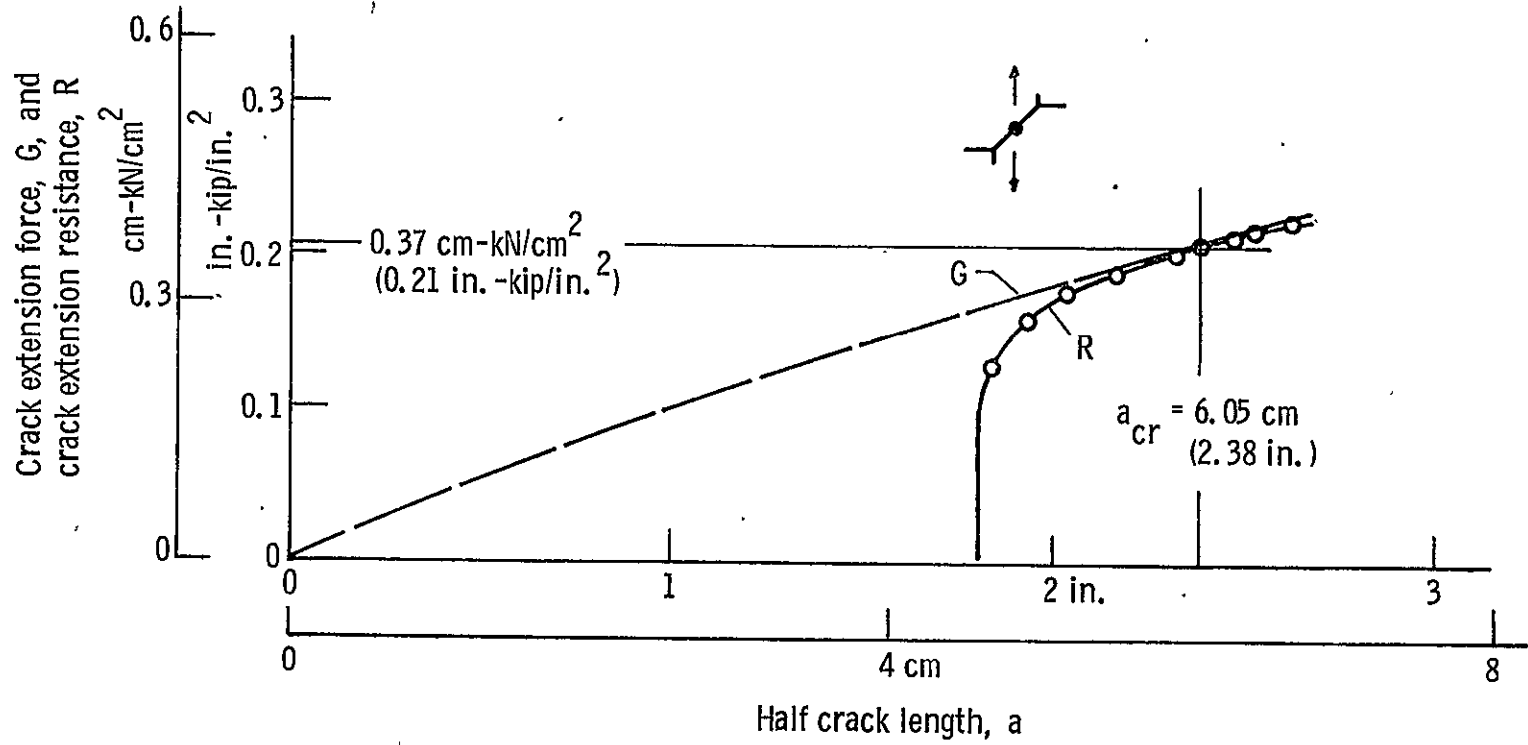Figure 31. – R curve for SN-2, Holston analysis.
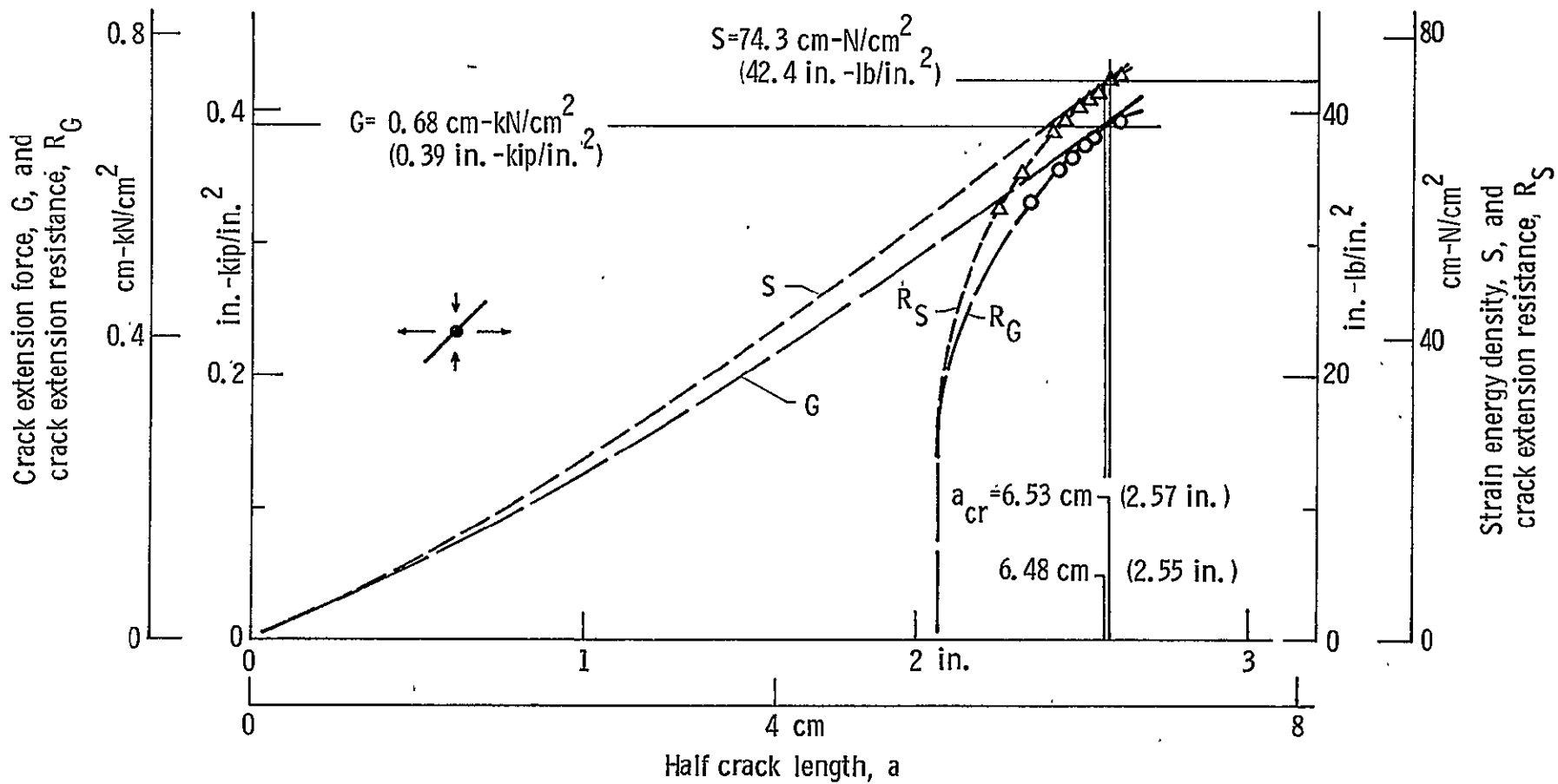
Figure 32. - R curve for SN-4.
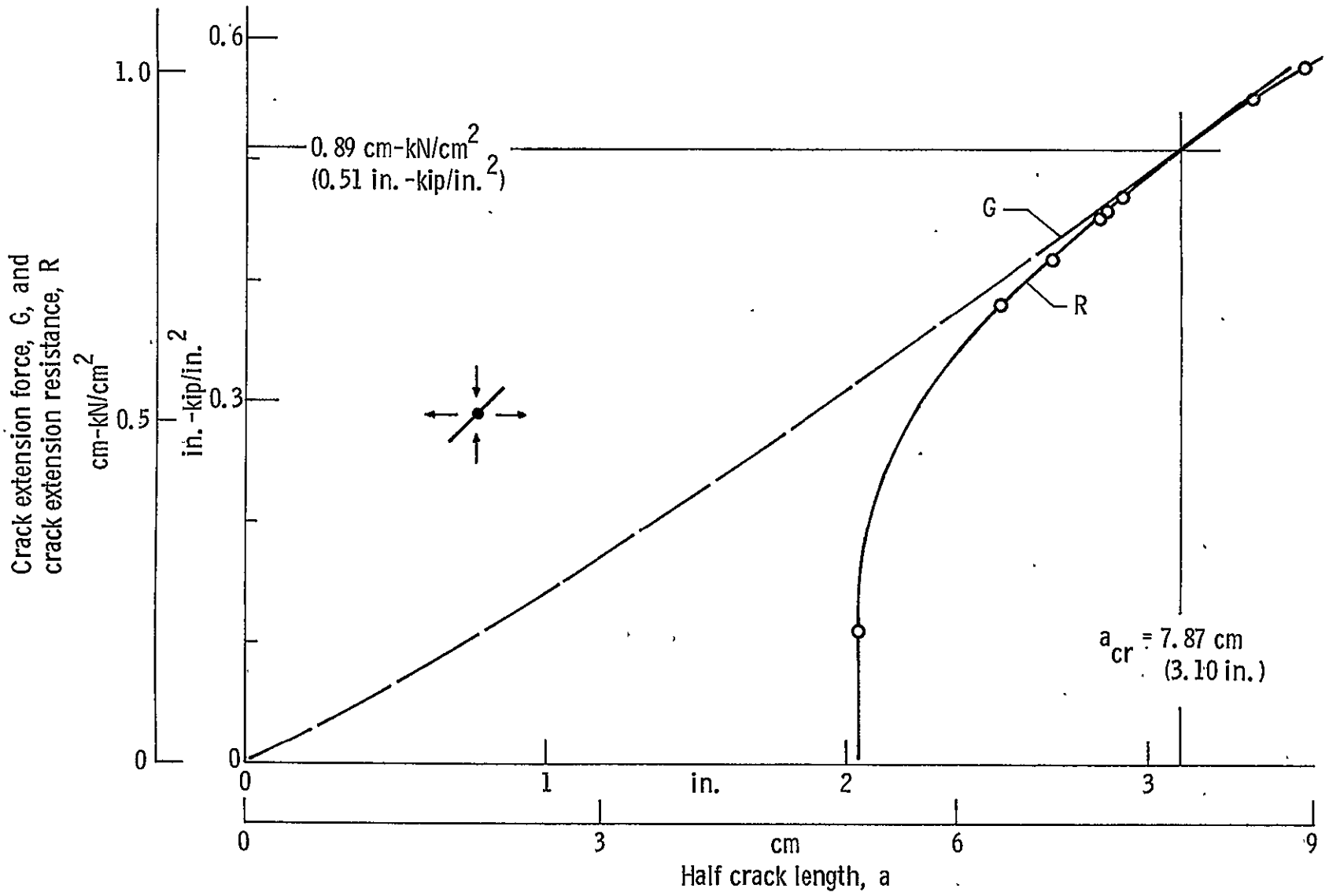
Figure 33. – R curve for SN-17.
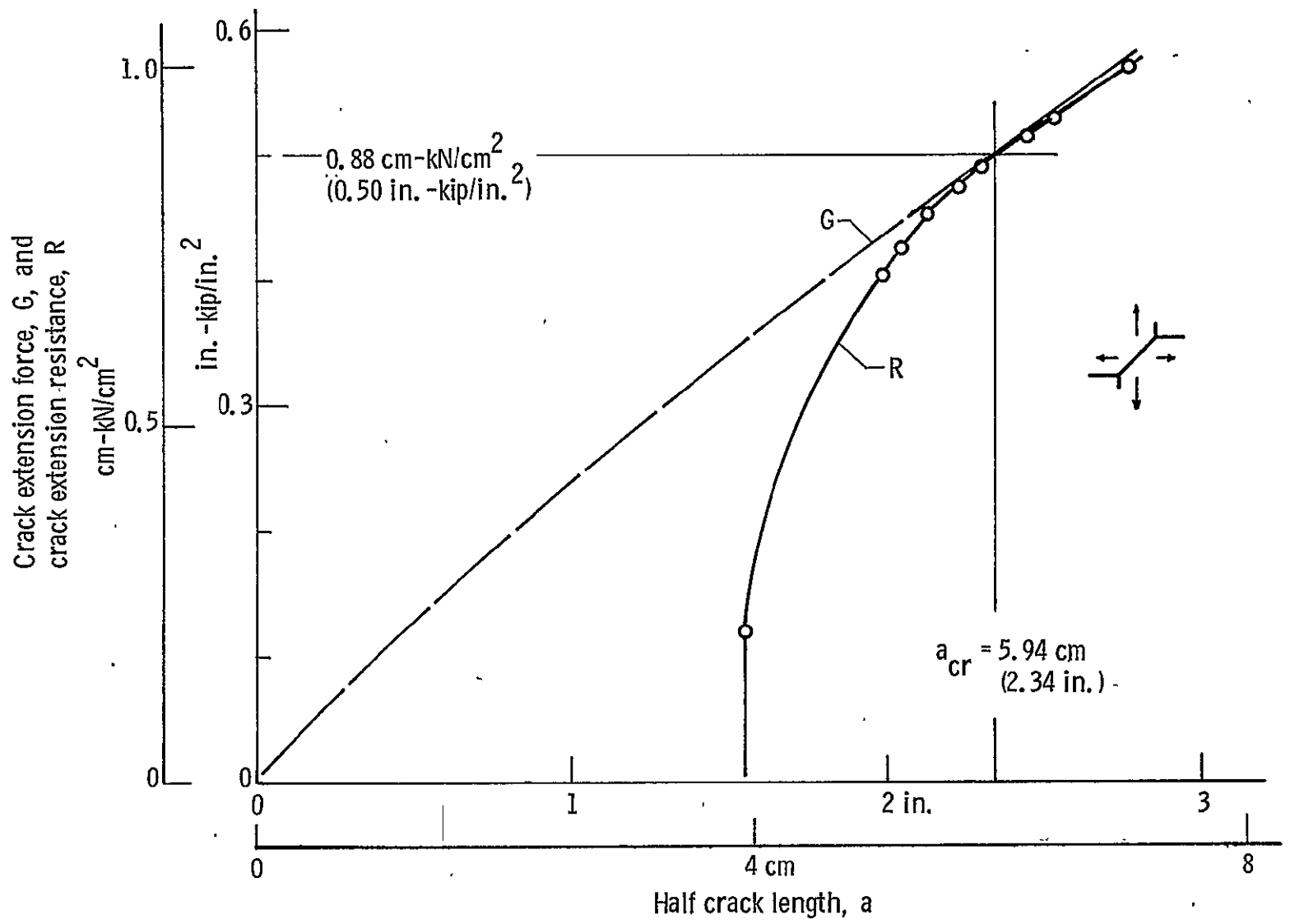
Figure 34. – R curve for SN-18.
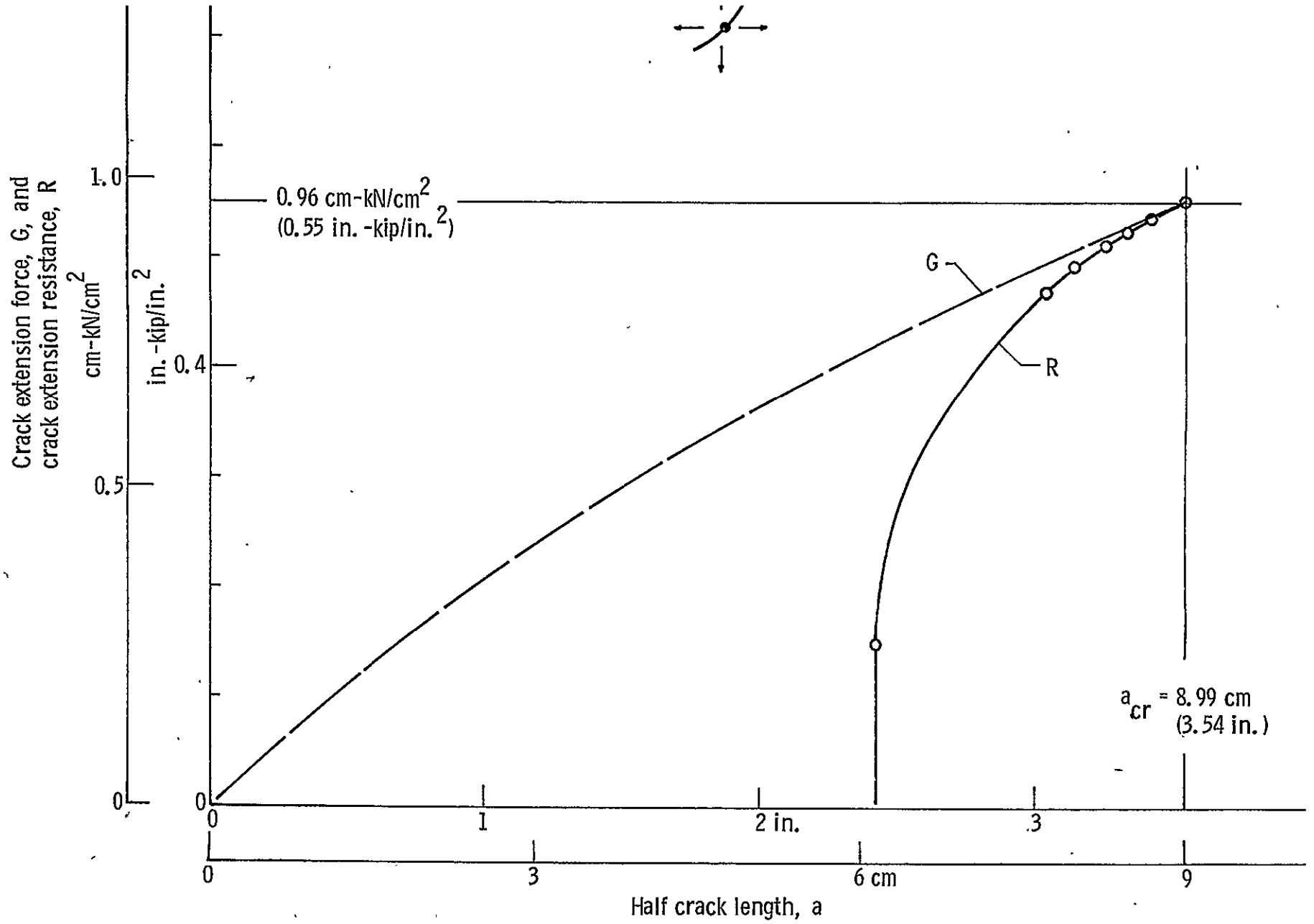
Figure 35. — R curve for SN-5.

Figure 36. – R curve for SN-6, arc-crack analysis.

dimensional arc crack. Figure 37 analyzes the same experiment using Holston's analysis. Again, differences between predicted critical G and critical crack length are small. Figures 39 and 40 present two analyses of sample SN-12. In this case, there is considerable difference between critical G and predicted critical crack length, but it is important to note that this sample was loaded in pure shear, meaning that the vertical load was compressive. Sample SN-12 failed by buckling rather than by crack propagation, making the R curves in figures 39 and 40 subject to question. Each of the remaining R curves was computed based on a single analysis described in the previous section.

R curve results are summarized in table VI, where they are categorized according to the alloy, material thickness, direction of crack growth relative to final rolling direction, and the ratio of mode I to mode II stress intensity that actually occurred in the experiment. In some experiments, data necessary to construct an R curve were not available. In these cases, values of critical G listed in table VI were computed from an estimate of the load at fracture.

Specimens SN-7 and 9 failed in rapid fracture while cyclic stress was being applied. In these cases, the load at fracture was recorded on the last cycle before failure, and the crack length at failure was estimated from the last recorded crack lengths before failure. Specimens SN-23 and 26 were rising-load tests and showed little subcritical crack growth. In both cases, the load at fracture was recorded. For SN-23, three frames of motion picture data are available from which critical crack length was estimated. The loading tab broke off SN-26 before fracture, so the estimated G value is well below the appropriate critical G.

Table VI gives values for net section normal and shear stress. Several experiments were conducted with the fracture direction 45° from the final rolling direction, and the loading was pure mode II, or the ratio K_I/K_{II} was approximately 0.4. In these tests, the failure was nearly flat and in the original plane of the crack. Note that net section shear stress is well above the expected shearing yield stress of approximately 0.6 times the tensile yield stress, so it must be concluded that these specimens (SN-11, 17, 18, 24, 25, 26) failed by net section yielding. Note that in some cases there is wide variation in the value of G_{cr} within a given alloy/thickness category. For a given alloy, it is expected that the following parameters should affect the critical value of G:

1) Material thickness - Material thickness influences the constraint at the crack tip and thus the amount of plastic deformation that can take place during the fracture process;

2) Crack growth direction - The direction in which the crack propagates relative to the rolling direction of the material
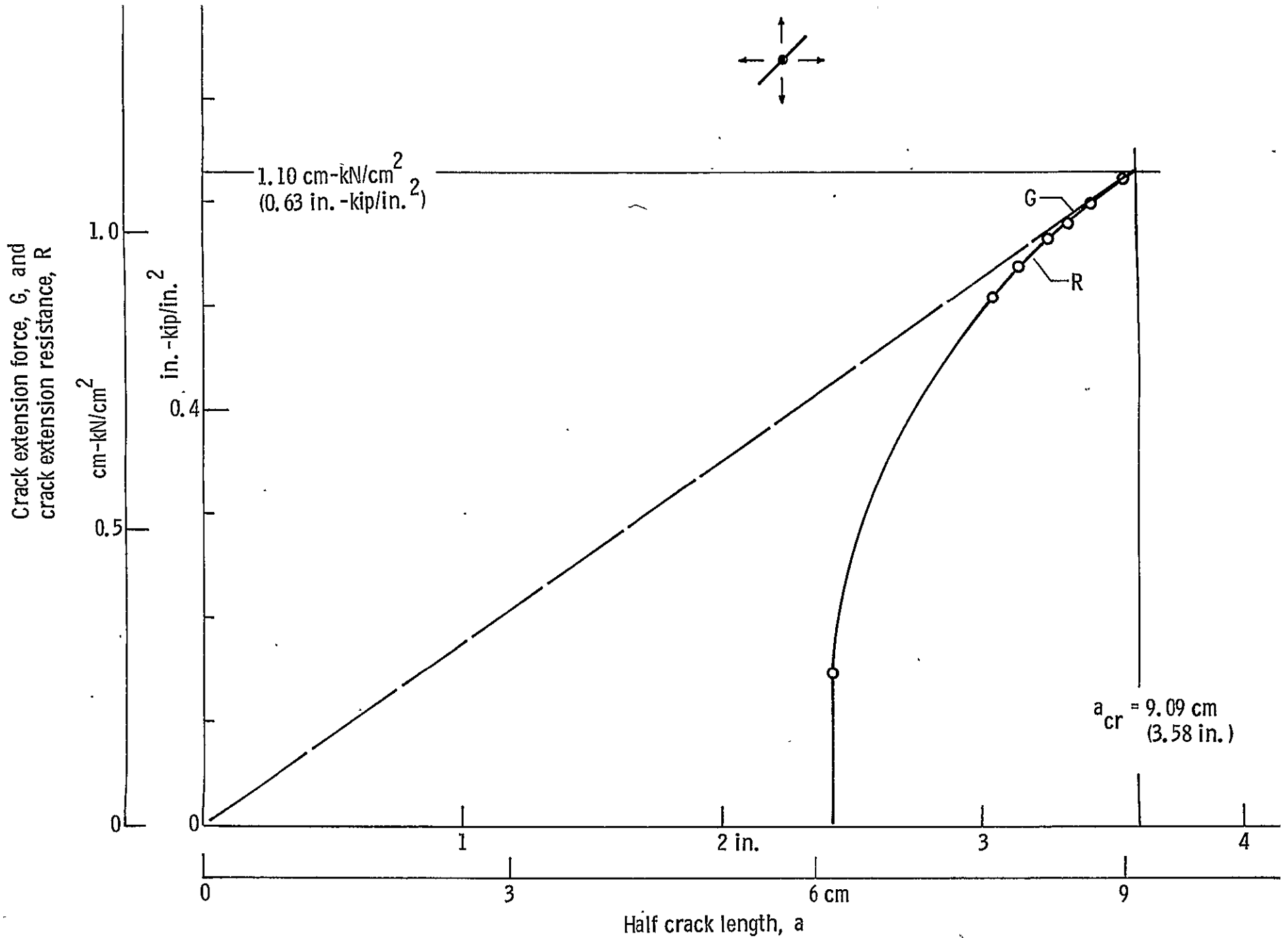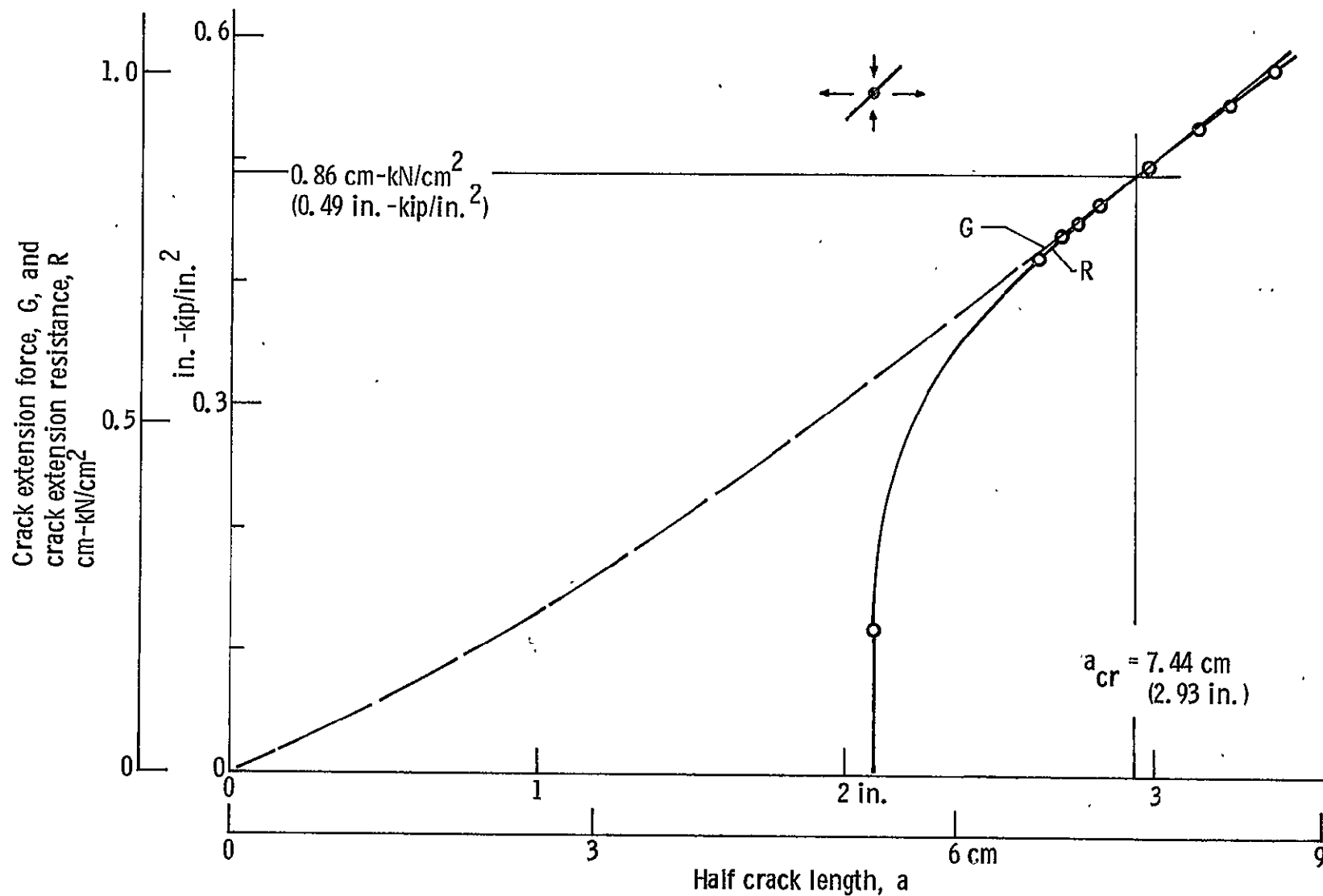
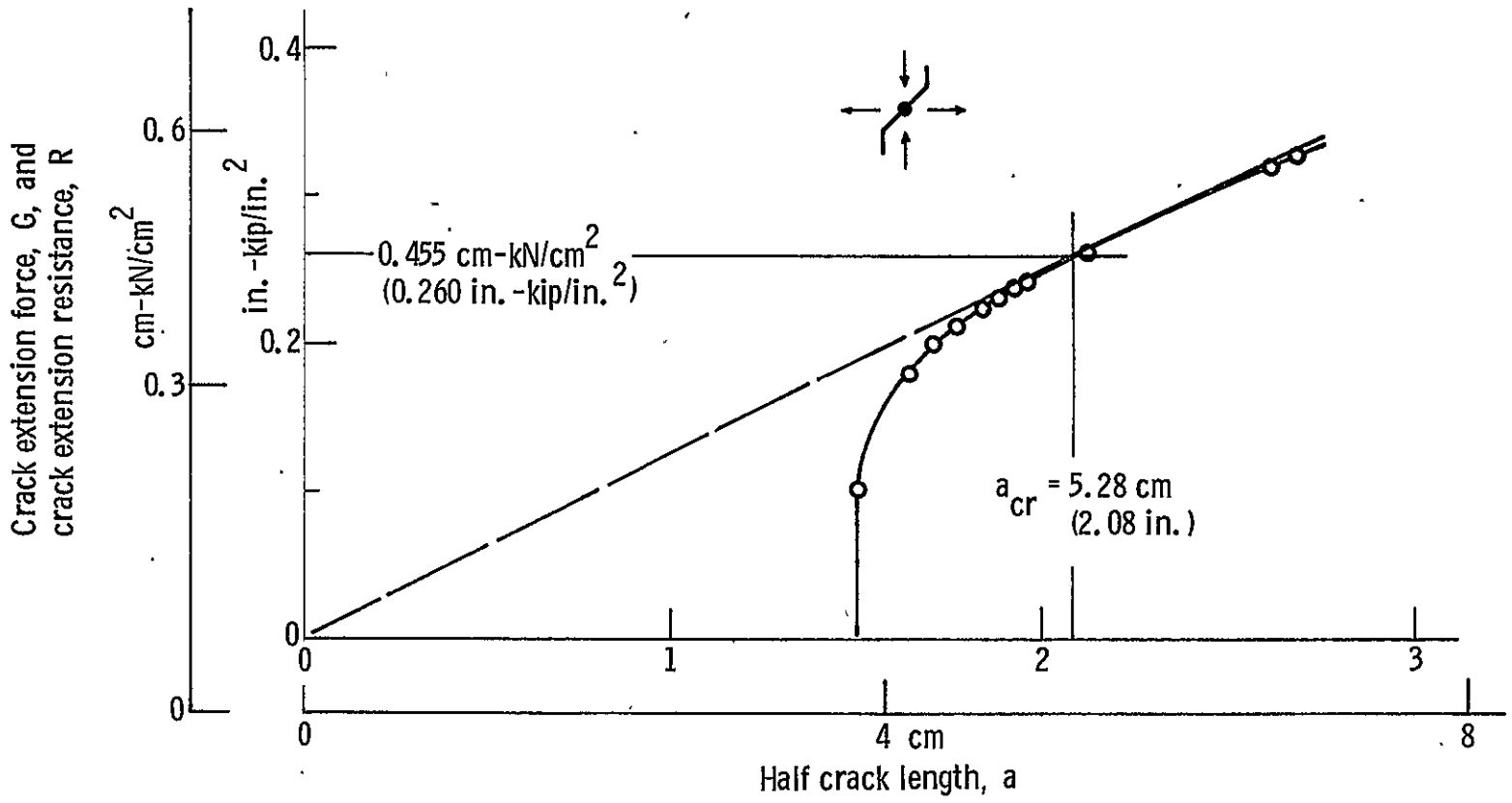Figure 37. – R curve for SN-6, Holston analysis.

Figure 38. - R curve for SN-11.

Figure 39. – R curve for SN-12, Iida analysis.
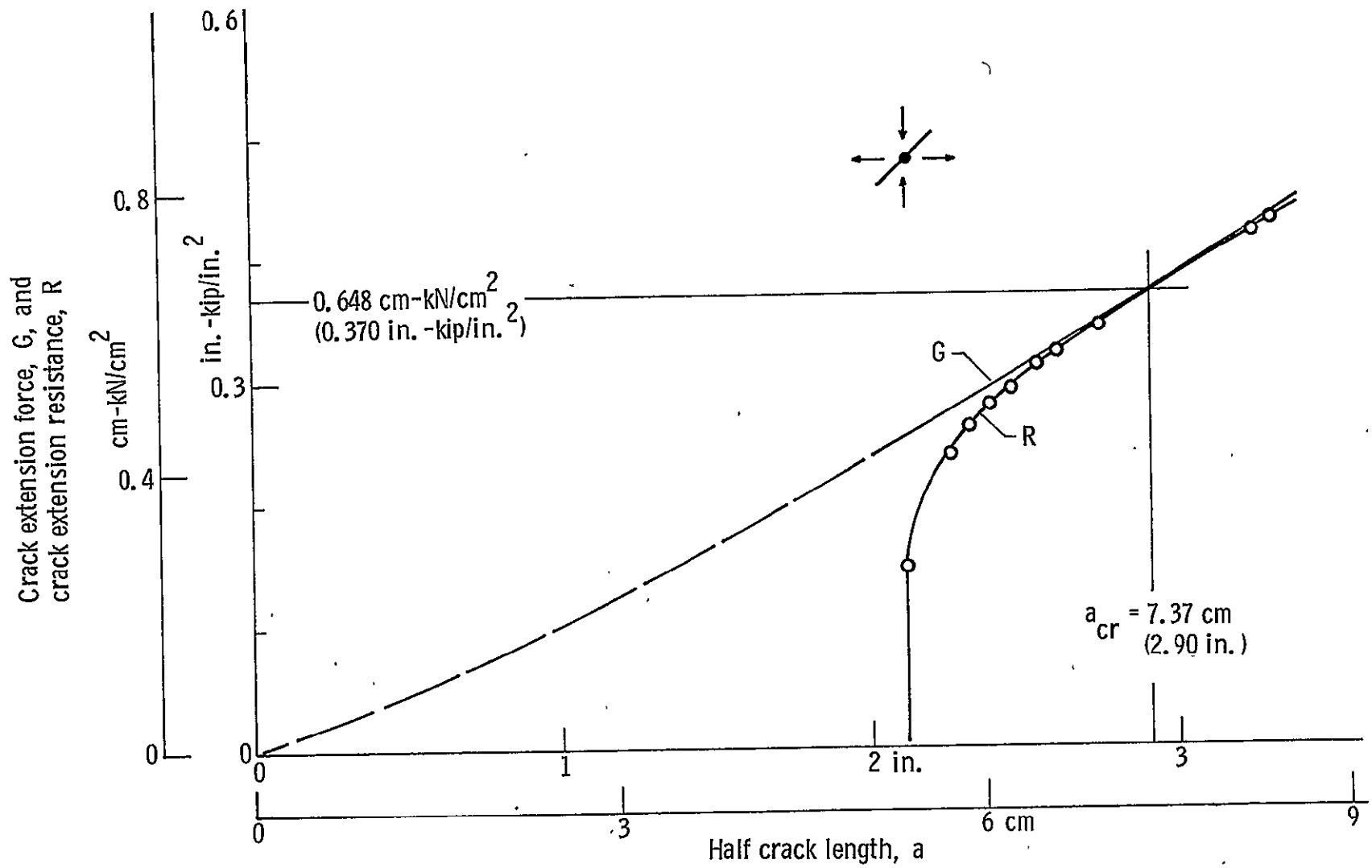
Figure 40. — R curve for SN-12, Holston analysis.

TABLE VI. - R CURVE SUMMARY

Specimen no.	Material	Crack growth direction related to final rolling direction	K_{Iu}		K_{IIu}		$\dfrac{K_{Iu}}{K_{IIu}}$	a_{cr}	
			kN-cm$^{1/2}$/cm^2	ksi-in.$^{1/2}$	kN-cm$^{1/2}$/cm^2	ksi-in.$^{1/2}$		cm	in.
SN-5	2219	Parallel	83.51	76.00	4.62	4.20	18.1	5.94	2.34
SN-6	t=0.64cm	Either	83.80	76.26	21.17	19.27	4.0	8.99	3.54
SN-11	or	45 deg	29.97	27.27	77.79	70.79	0.4	7.44	2.93
SN-12	t=0.25 in.	Perpendicular	59.45	54.10	14.39	13.10	4.1	5.28	2.08
SN-2	2215	Parallel	53.07	48.30	2.57	2.34	20.6	6.65	2.62
SN-4	t=1.55 cm	Parallel	54.17	49.30	2.97	2.70	18.3	6.05	2.38
SN-17	or	45 deg	27.10	24.66	68.97	62.77	0.4	6.48	2.55
SN-18	t=0.61 in.	45 deg	-----	-----	85.27	77.60	Pure K_{II}	7.87	3.10
SN-7	7075	Parallel	57.14	52.00	1.52	1.38	37.7	13.11*	5.16*
SN-9	t=1.27 cm	Parallel	51.10	46.50	1.79	1.63	28.5	11.07*	4.36*
SN-14	or	Perpendicular	102.38	93.17	1.87	1.70	54.8	4.67	1.84
SN-15	t=0.50 in.	45 deg	72.85	66.30	-----	-----	Pure K_I	6.05	2.38
SN-16		Perpendicular	76.92	70.00	22.42	20.40	3.4	5.08	2.00
SN-23		Parallel	47.47	43.20	20.00	18.20	2.4	4.42	1.74
SN-24		45 deg	-----	-----	95.61	87.01	Pure K_{II}	8.00	3.15
SN-25		45 deg	-----	-----	95.21	86.65	Pure K_{II}	8.26	3.25
SN-26		45 deg	>28.08	>25.55	>68.14	>62.01	0.4	>5.74	>2.26

Specimen no.	G_{cr}		Nominal values of						Comments
	kN-cm cm^2	kip-in. in.^{2}	Net section Normal stress		Net section Shear stress		Yield Stress		
			kN/cm^2	ksi	kN/cm^2	ksi	kN/cm^2	ksi	
SN-5	0.88	0.50	NA	NA	NA	NA	38	55	--
SN-6	0.96	0.55	NA	NA	NA	NA	38	55	Arc crack
SN-11	0.86	0.49	NA	16.3	27.3	39.6	38	55	---
SN-12	0.46	0.26	11.2	NA	NA	NA	38	55	Buckled
SN-2	0.35	0.20	NA	NA	NA	NA	38	55	--
SN-4	0.37	0.21	NA	NA	NA	NA	38	55	--
SN-17	0.68	0.39	10.6	15.4	25.6	37.1	38	55	---
SN-18	0.89	0.51	≈0	≈0	29.4	42.6	38	55	---
SN-7	0.40	0.23	NA	NA	NA	NA	45	65	No R curve
SN-9	0.33	0.19	NA	NA	NA	NA	45	65	No R curve
SN-14	1.33	0.76	NA	NA	NA	NA	45	65	--
SN-15	0.75	0.43	2.81	40.7	≈0	≈0	45	65	---
SN-16	0.81	0.46	NA	NA	NA	NA	45	65	---
SN-23	0.33	0.19	NA	NA	NA	NA	45	65	No R curve
SN-24	1.16	0.66	≈0	≈0	33.3	48.3	45	65	---
SN-25	1.14	0.65	≈0	≈0	33.0	47.8	45	65	---
SN-26	>0.68	>0.39	11.2	16.2	25.4	36.9	45	65	No R curve

*Extrapolated.

66

Figure 41. - R curve for SN-14.

Figure 42. – R curve for SN-15.

Figure 43. – R curve for SN-16.

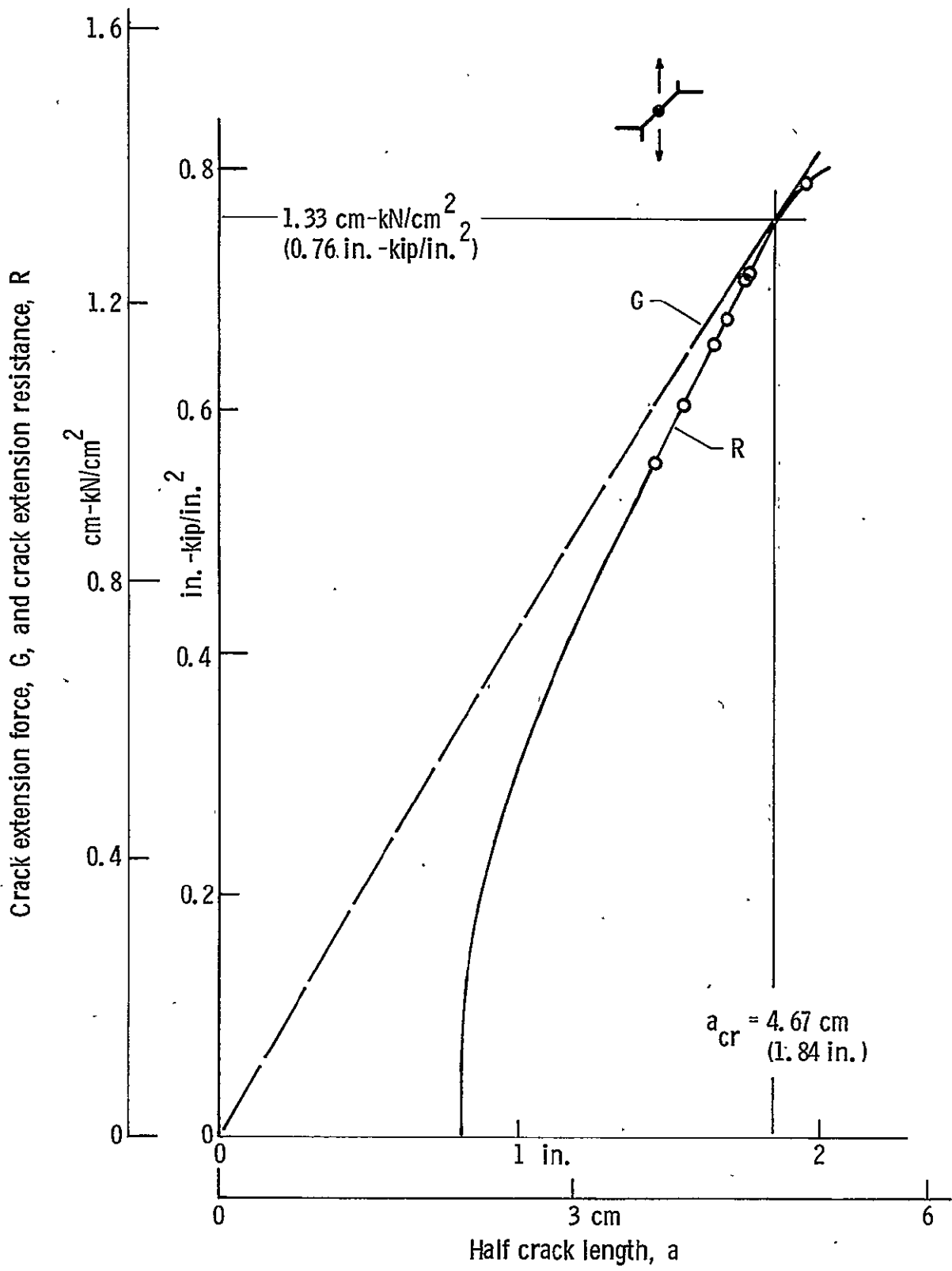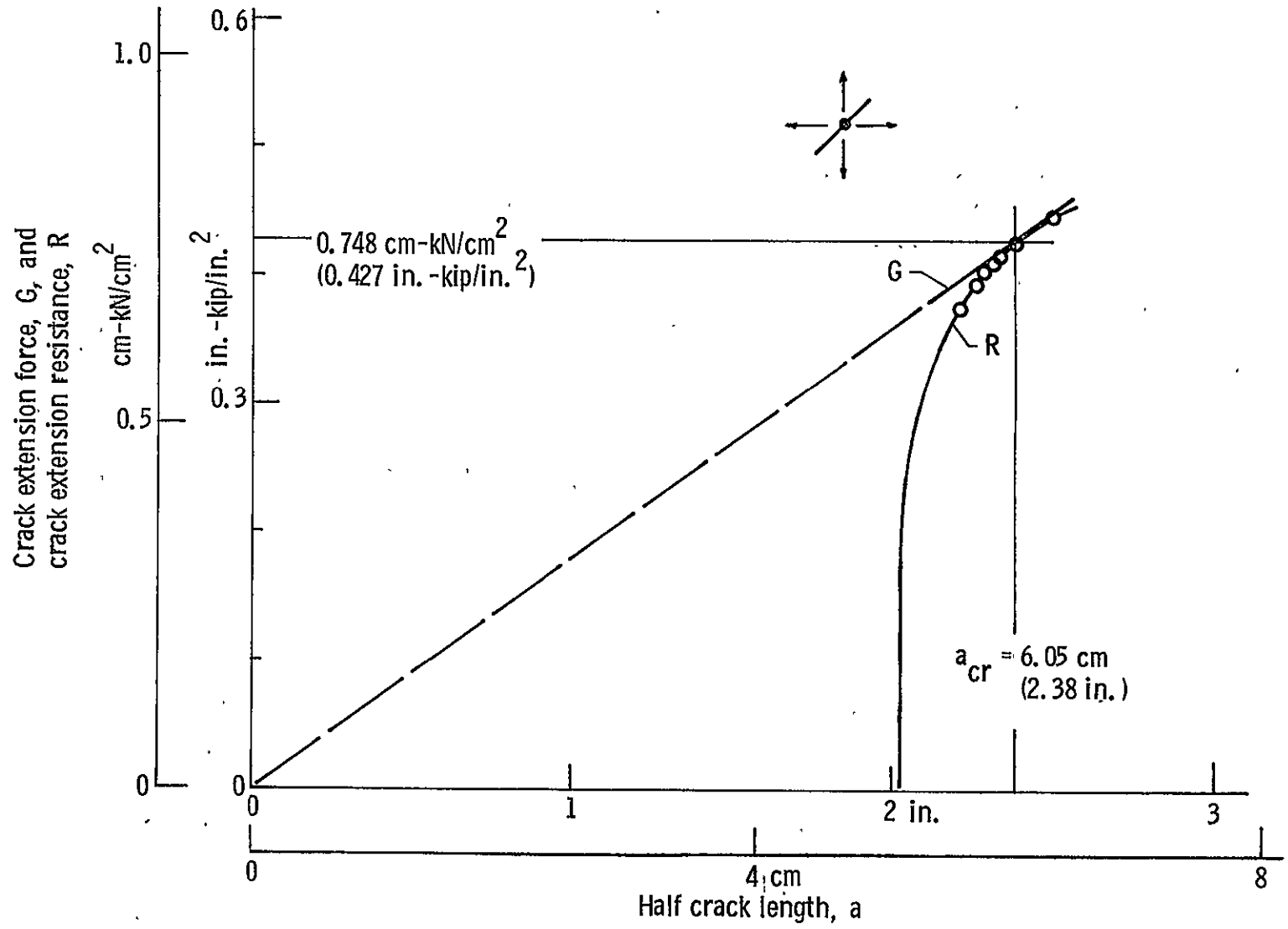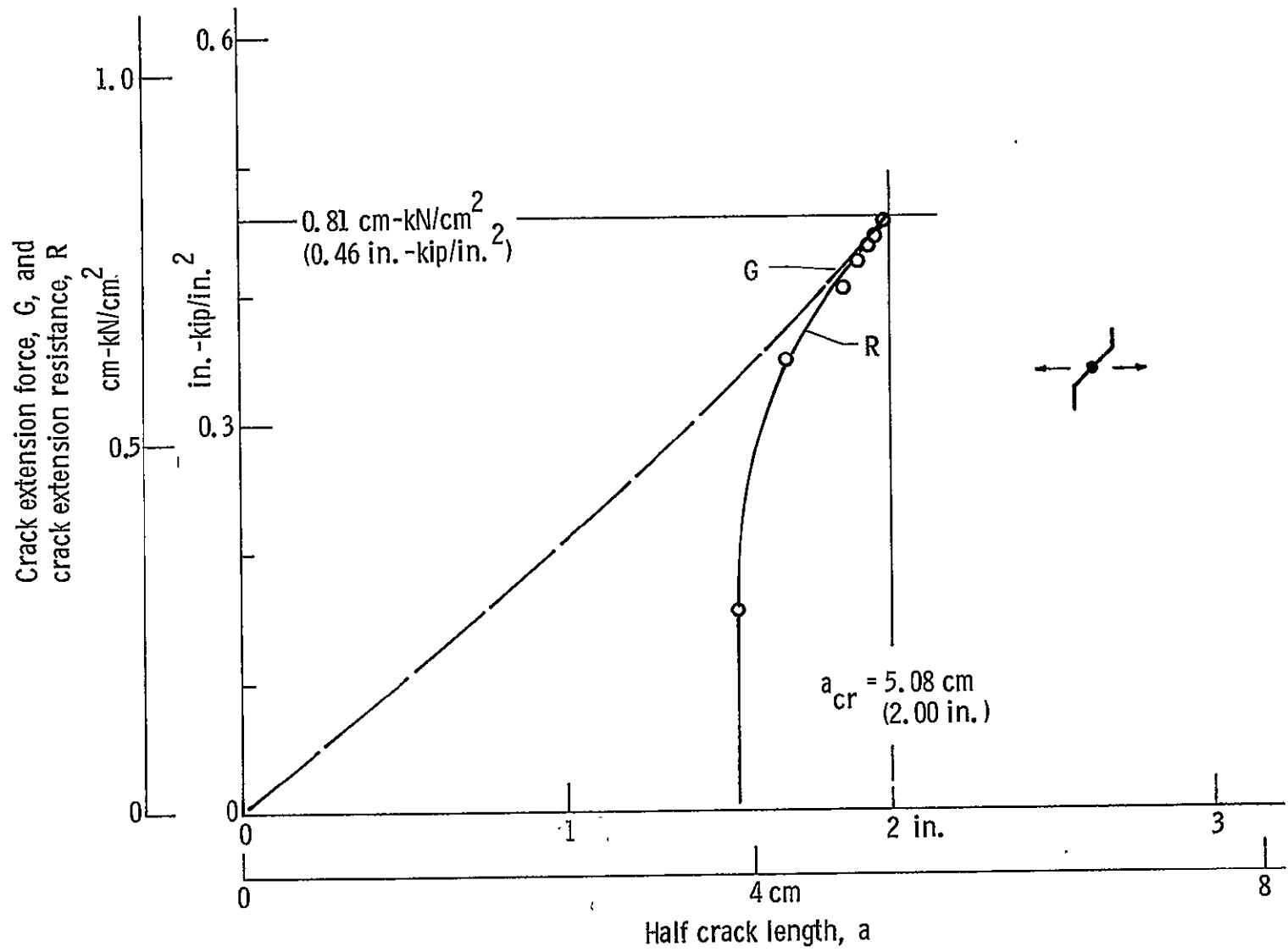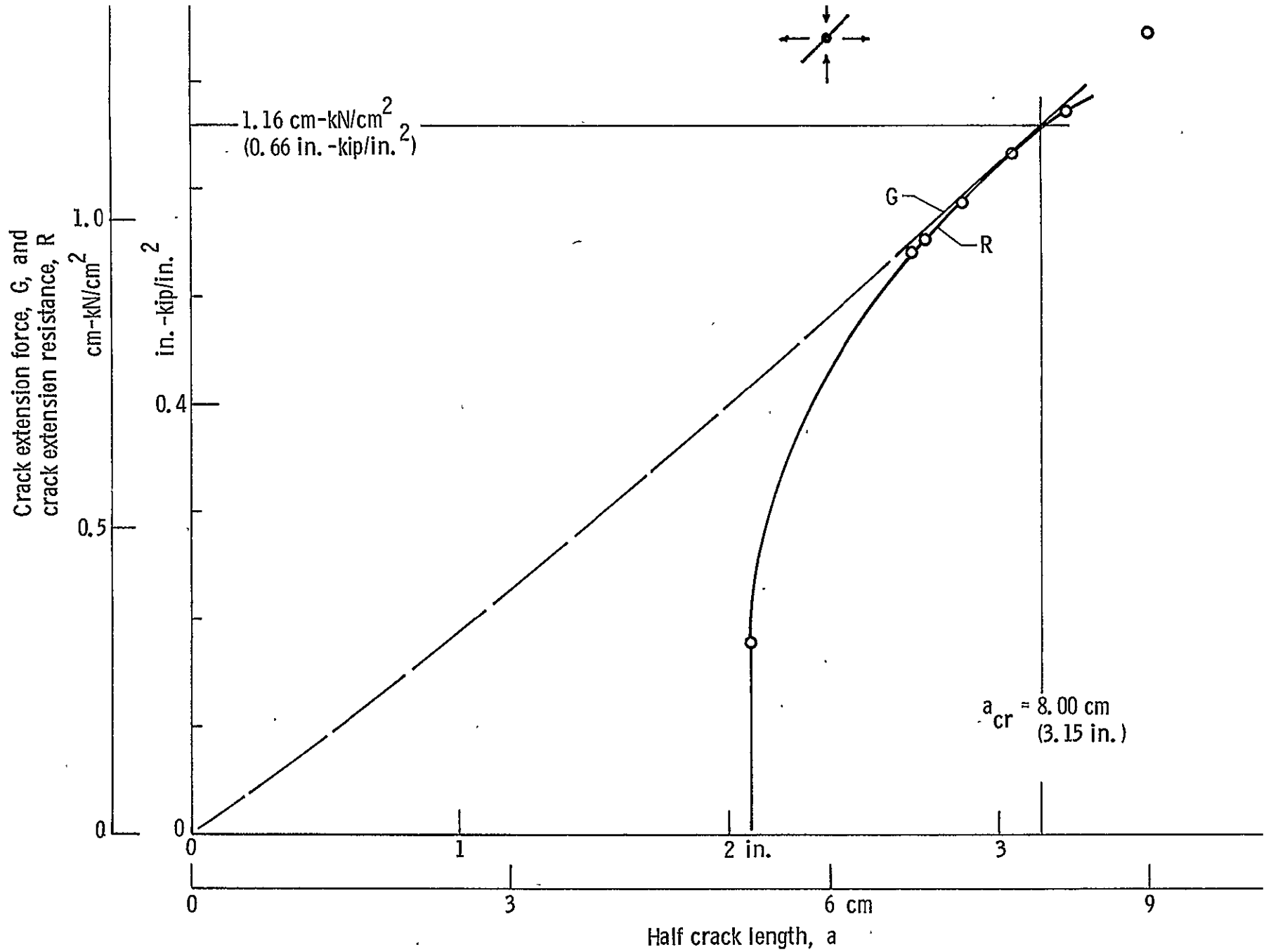Figure 44. – R curve for SN-24.
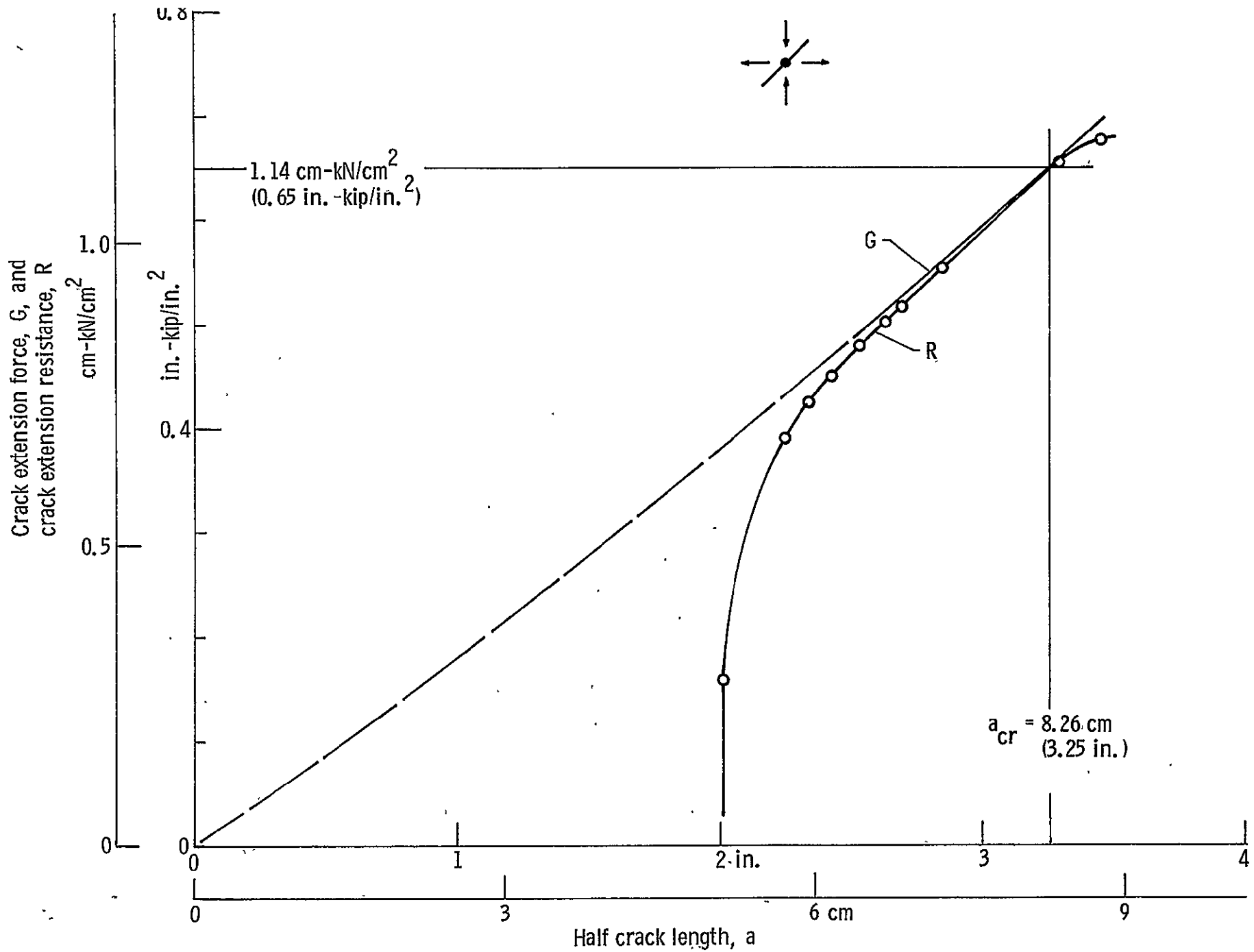
Figure 45. - R curve for SN-25.

might be expected to influence the critical value of G because of differences in material properties with respect to direction relative to rolling direction;

3) Ratio of K_I to K_{II} – This ratio should have some effect on the critical value of G because it is expected that development of plasticity is different in mode I than in mode II.

To gain some physical insight into the effects of plasticity in mode I and mode II, it is instructive to examine the plastic zone dimensions predicted by use of Dugdale-type strip models. The following expressions taken from reference 12 represent the estimated plastic zone dimensions for a condition of pure modes I and II:

$$L_I = \frac{\pi}{8}\left(K_I/\sigma_{ys}\right)^2 \qquad [25]$$

$$L_{II} = \frac{\pi}{2}\left(K_{II}/\sigma_{ys}\right)^2 \qquad [26]$$

where L refers to the plastic zone dimension. Note that, for a given level of K for pure mode I or II, the plastic zone dimension for pure mode II is estimated to be four times greater than that for pure mode I. This implies that there should be greater plastic energy to overcome in initiating fracture for pure mode II than for pure mode I. One therefore concludes that, as the loading condition traverses from pure mode I through conditions of mixed-mode loading toward pure mode II, the energy of fracture, or G_{cr}, might be expected to increase.

The effect of thickness on critical values of G has been long recognized for conditions of pure mode I. As material thickness decreases, the amount of constraint at the crack tip also decreases, thus allowing plastic deformation to increase. The result is an increase in the critical value of G as thickness decreases.

Figures 46, 47, and 48 are plots of the critical value of G determined from the R curve plotted against the angle θ defined by

$$\theta = \arctan\left(K_{Iu}/K_{IIu}\right) \qquad [27]$$

where the subscript u indicates fracture.

In these figures, data points are annotated to indicate the direction of crack propagation relative to the final rolling direction of the specimen being tested. Figure 46 presents the result for tests of 1.55-cm (0.61-in.) thick 2219. Note that the variation in the critical value of G with K_I/K_{II} is in the direction predicted above, and there appears to be little separation of the data with respect to the crack growth directions present. In figure 47, the results are presented for 0.64-cm (0.25-in.) thick 2219. In this case, the variation seen in figure 46 is not evident. The G_{cr} shown was computed assuming flat cracks. However, examination of the

Figure 46. – Effect of mixed-mode ratio, 2219 1.55-cm (0.61-in.) thick.
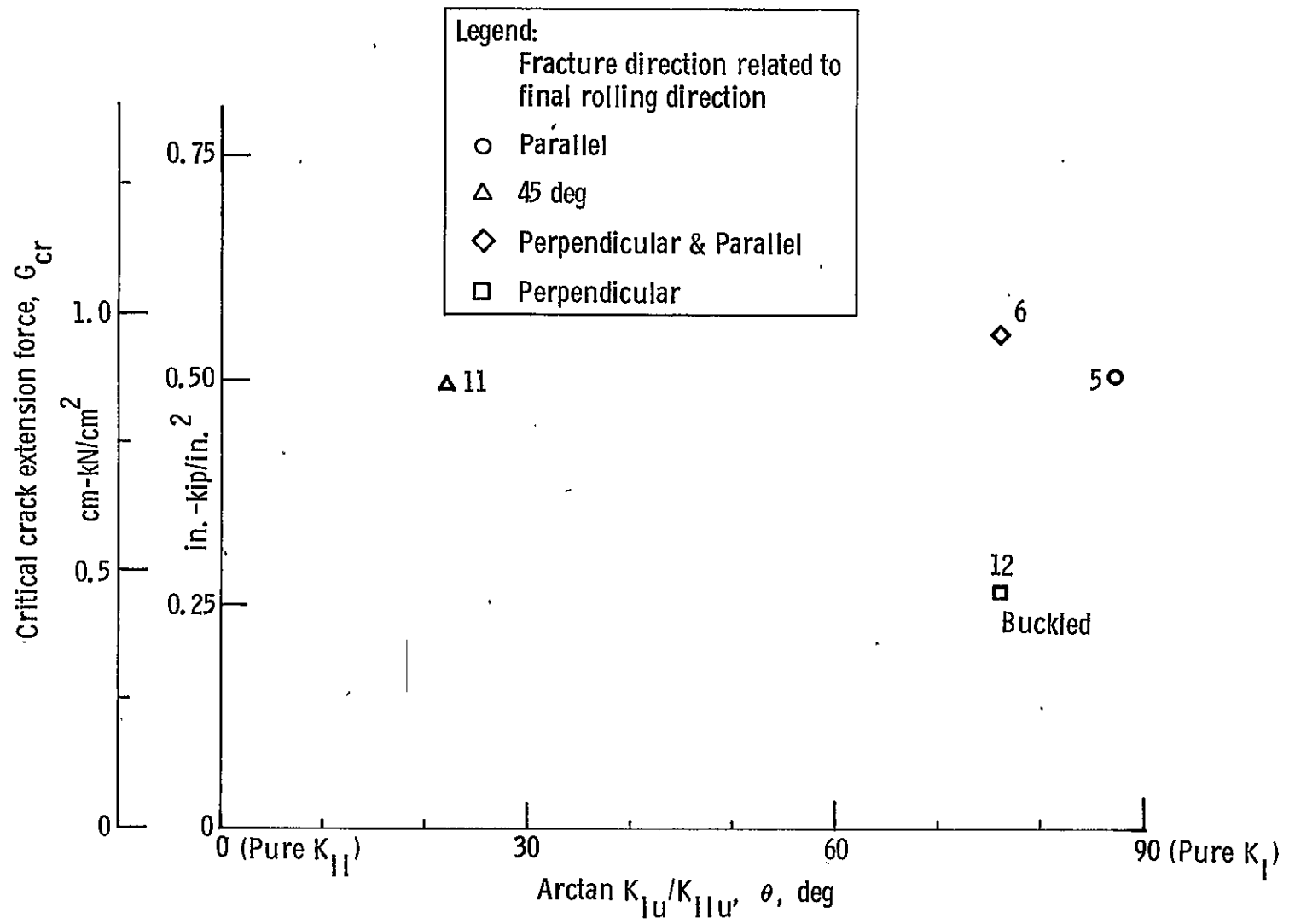
Figure 47. – Effect of mixed-mode ratio, 2219 0.64-cm (0.25-in.) thick.
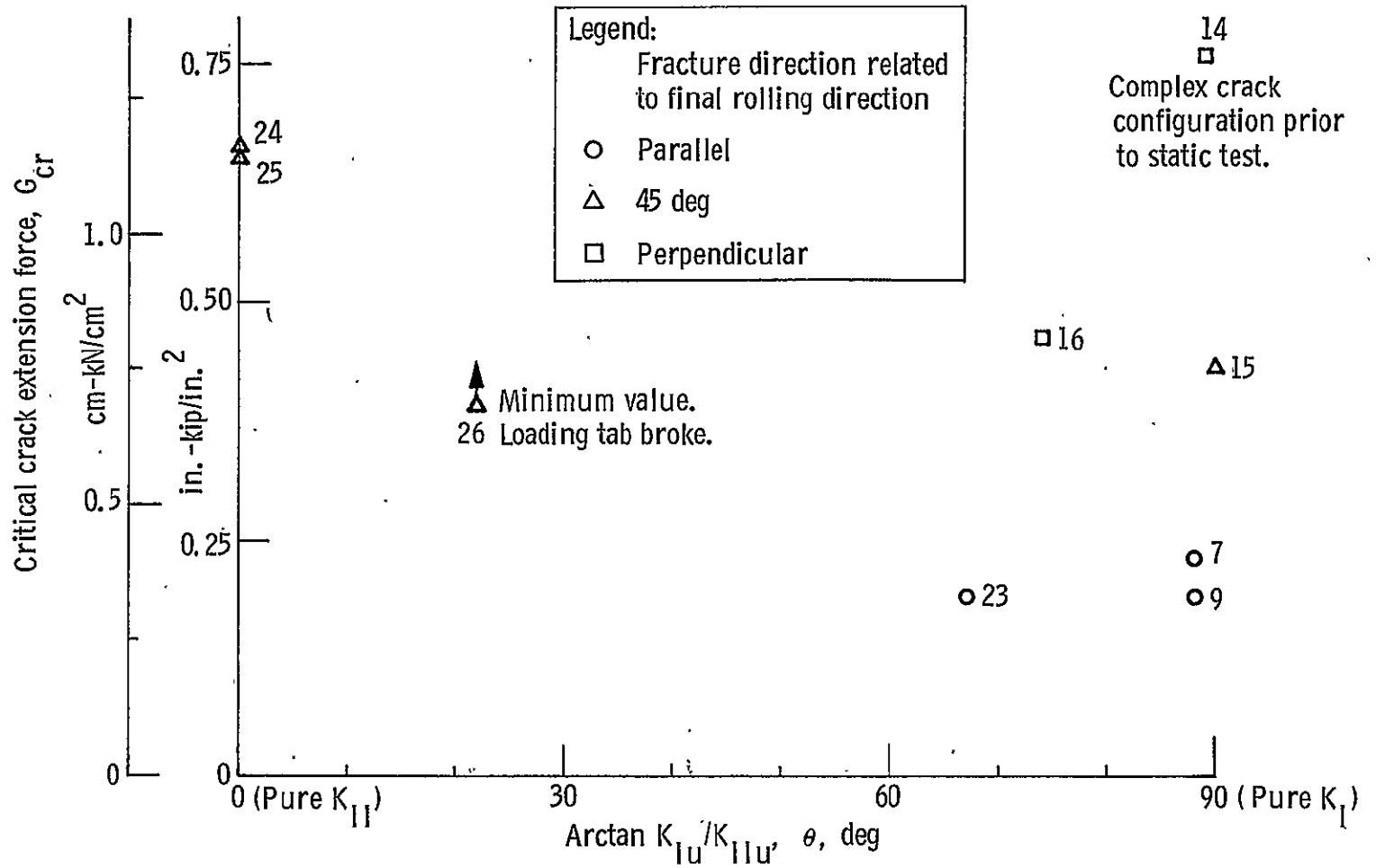
Figure 48. – Effect of mixed-mode ratio, 7075 1.27-cm (0.50-in.) thick.

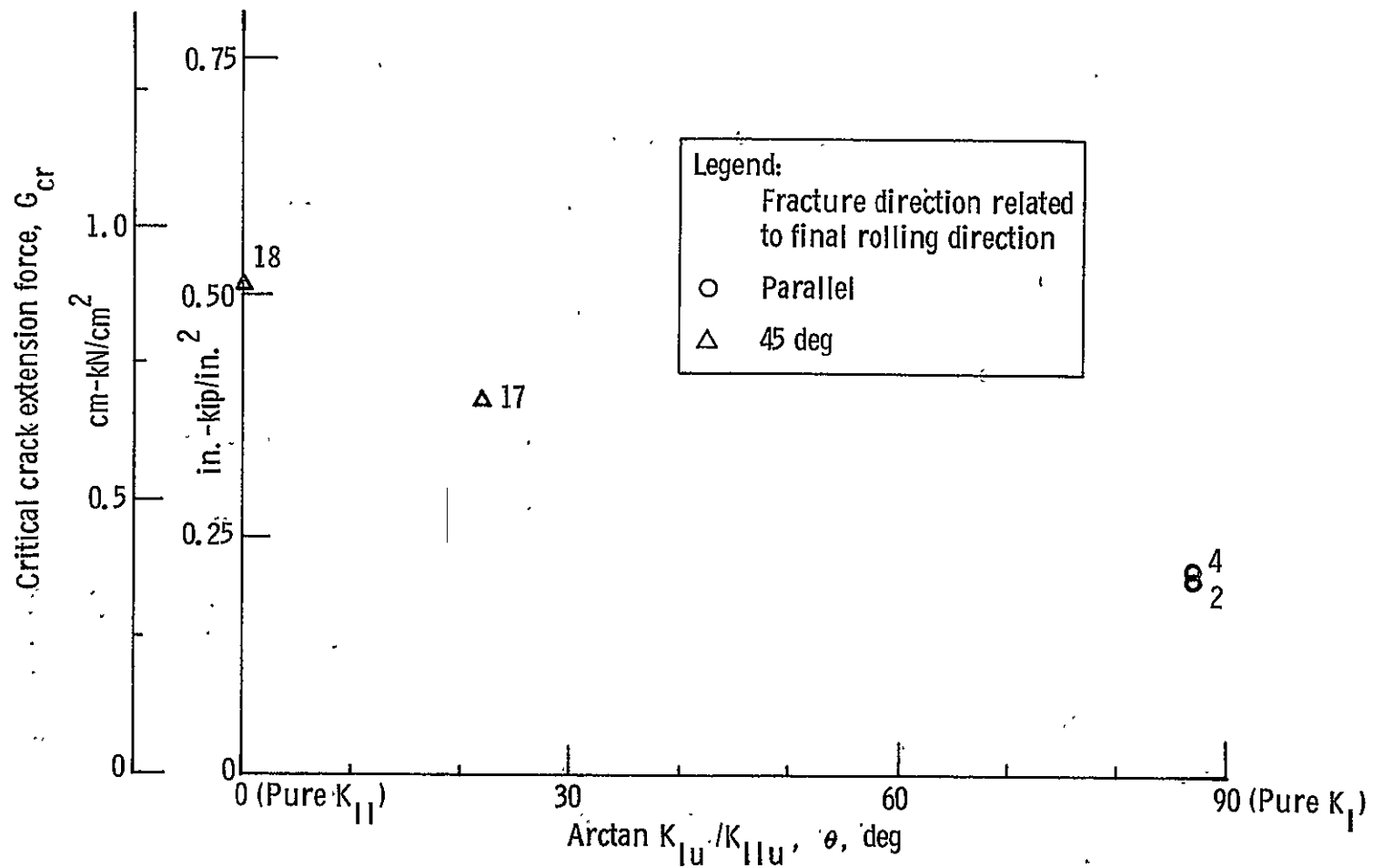specimens in the area of a_{cr} as determined from the R curves in figures 35 and 36 showed that the cracks had twisted approximately 45°. A better estimate of G_{cr} for SN-5 and 6 taking account of the rotated crack and resulting presence of mode III would be about 60% of the values shown in figure 47. Since the interaction diagrams in the next section involve only K_I and K_{II}, consideration of K_{III} and crack rotation were ignored. Furthermore, specimens SN-5 and 6 were the only ones exhibiting this behavior. Figure 48 is a similar plot for the 1.27-cm (0.50-in.) thick 7075. In this case, the proper trend with respect to angle θ is seen for tests in which crack growth direction was 45° to the final rolling direction. However, for cases in which crack growth was perpendicular to the final rolling direction, the variation is not consistent with the model described earlier. Also, data for the parallel propagation direction are nearly horizontal and do not support or contradict the proposed model. In figure 48, note the legend corresponding to the data point for specimen SN-26. This specimen did not undergo a rapid fracture; rather, the tab broke off the specimen at a G level of about 0.7 kN-cm/cm^2 as indicated in the figure. The data point is included in a way that indicates that G for that experiment would have been a value greater than 0.7.

One can conclude from these results that the critical value of G for pure mode II loading situations generally exceeds the critical value of G for pure mode I loading situations; and that the critical value of G for intermediate conditions of mixed-mode I and II loading lies between the two extremes. This statement is generally supported by the data; however, the 7075 data for perpendicular crack growth direction are not in agreement and results shown in figures 47 and 48 for parallel crack growth direction are inconclusive with respect to this point.

The R curves described in this section could have been plotted in terms of S in the strain energy density theory instead of G as used here. This was done for one specimen, SN-17, and the plots are shown in figure 33. Since there was almost no difference in the determination of a_{cr}, and because there was little difference to be expected theoretically, as described in the state-of-the-art review, analyses using S were not done.

Interaction Diagrams

Figures 49, 50, and 51 are plots of all static fracture data obtained in this program in the format of an interaction diagram. There is significant scatter in the data when plotted this way. However, if one separates these data according to crack growth direction relative to the final rolling direction of the specimen, one finds a tendency for the data to be stratified with respect
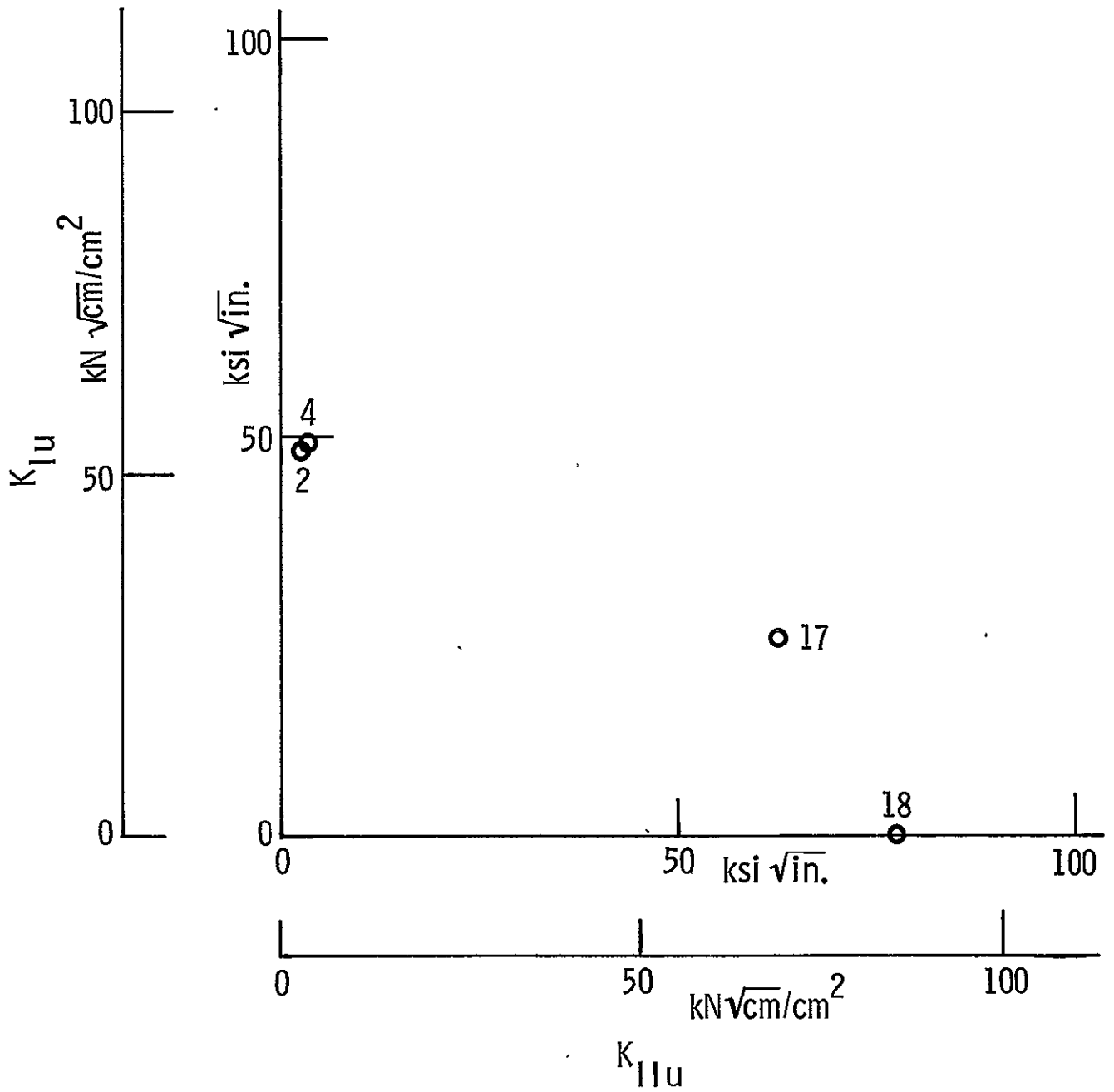
Figure 49. — Modes I and II interaction, 2219 1.55-cm (0.61-in.) thick.
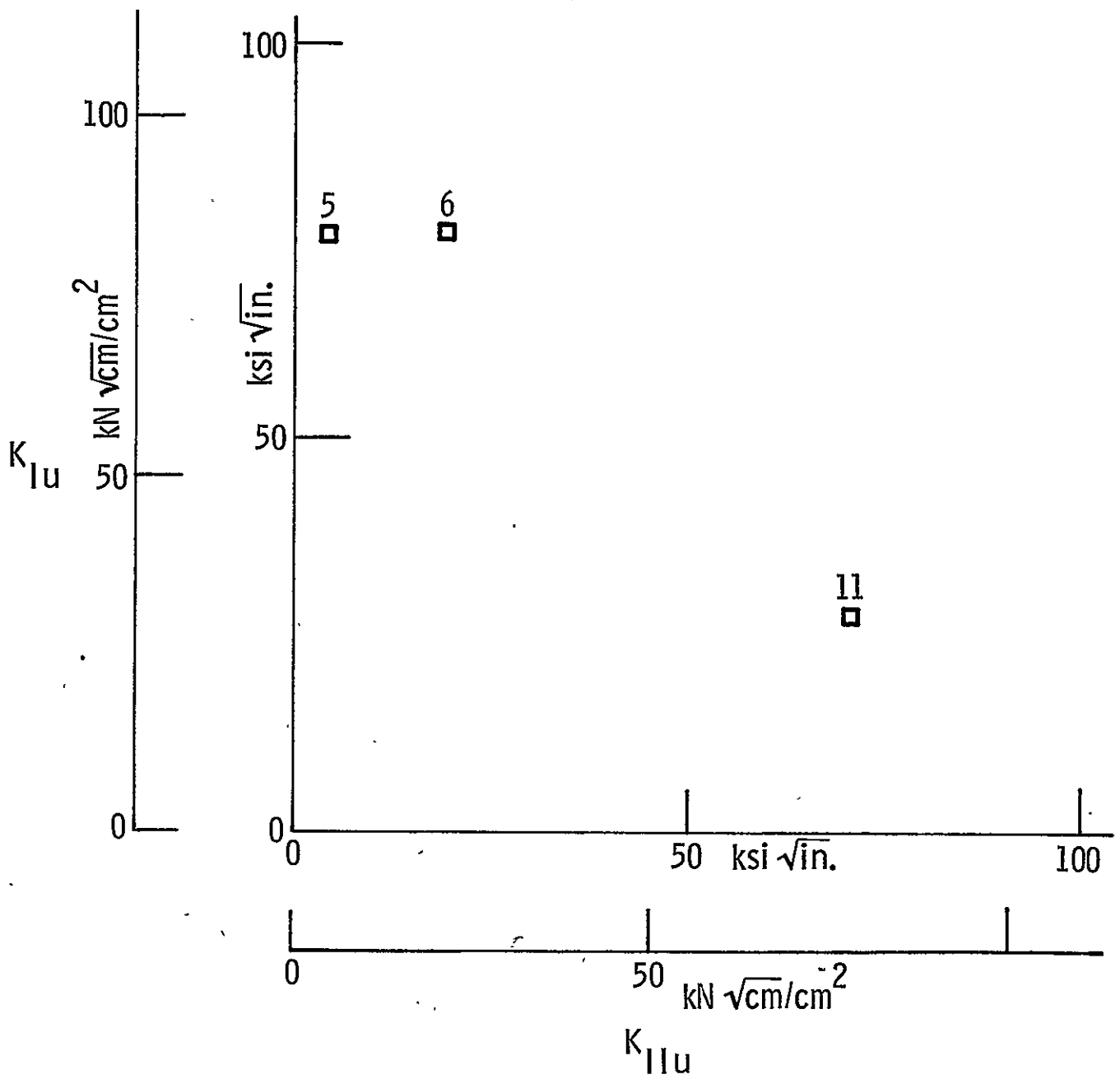
Figure 50. – Modes I and II interaction, 2219 0.63-cm (0.25-in.) thick.
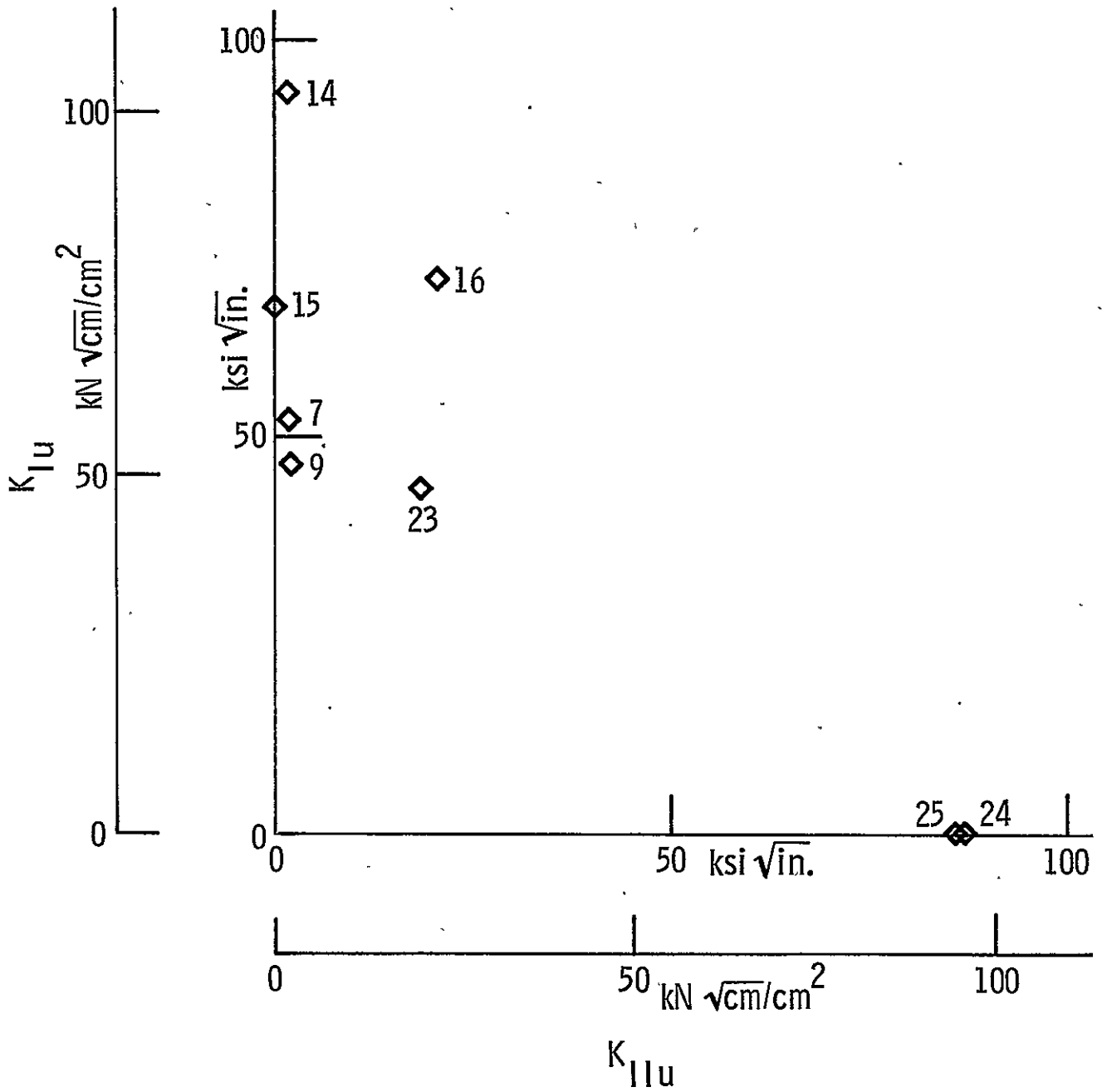
Figure 51. — Modes I and II interaction, 7075 1.27-cm (0.50-in.) thick.

to crack growth direction. To normalize the data, several critical stress intensity values from these figures were selected to represent critical K values for each group of material thicknesses and crack growth directions relative to final rolling direction. Critical stress intensity values selected are summarized in Table VII. Table VIII presents a series of K_c data from reference 15 for the same materials in different thicknesses. Note that K_I numbers selected here are consistent with other data on these materials.

Figure 52 is a normalized plot of data that were first presented in figures 49, 50, and 51. Data in these figures were categorized according to crack growth direction and were normalized using the appropriate K_{Ic} value taken from Table VII. In figure 52, note that normalizing in this way significantly reduces data scatter. Also note that there is a significant degree of interaction evident in these data, and the interaction is nearly as severe as the straight-line interaction noted by Shah (ref. 1) and Liu (ref. 4). Further note that the critical value if K_{II} is significantly greater than that of K_I. Figure 52 includes plots of predicted failure envelopes according to the various failure theories described in the state-of-the-art section. Values from the data show greater capability for combined mode stress intensities than the theories predicted for high proportions of shear stress intensity. However, in this region, net section stress exceeded yield stress in shear, as noted before. For small proportions of shear stress intensity, there is good correlation between data and theories.

Figure 53 is an interaction diagram in which the K_I axis has been normalized according to the appropriate values of K_{Ic} taken from Table VII, and the K_{II} axis has been normalized according to the values of K_{IIc} taken from Table VII. A further decrease in data scatter is seen but it is somewhat artificial because of the high degree of normalization.

The critical shear intensity, K_{IIc}, tends to be greather than K_{Ic} for the series of experiments conducted, and there is significant interaction between modes I and II. Further, it was found that the various theories of fracture correlate well with the data for low proportions of shear but underestimate stress intensities at fracture for high proportions of shear. It must be recognized that, in these experiments, a significant degree of plasticity influences the fracture process under high proportions of shear, and that the theories of fracture described only apply to conditions of brittle fracture.

TABLE VII. - PURE MODE CRITICAL STRESS INTENSITIES, THIS PROGRAM

| Material | Thickness | | K_{Ic} | | | | | | K_{IIc} | |
| | cm | in. | Parallel | | 45 deg | | Perpendicular | | $\frac{kN\text{-}cm^{1/2}}{cm^2}$ | $ksi\text{-}in.^{1/2}$ |
			$\frac{kN\text{-}cm^{1/2}}{cm^2}$	$ksi\text{-}in.^{1/2}$	$\frac{kN\text{-}cm^{1/2}}{cm^2}$	$ksi\text{-}in.^{1/2}$	$\frac{kN\text{-}cm^{1/2}}{cm^2}$	$ksi\text{-}in.^{1/2}$		
2219-T87	0.64	0.25	85.7	78	85.7	78	NA	NA	119.8*	109*
2219-T87	1.55	0.61	53.8	49	53.8	49	NA	NA	85.7	78
7075-T7351	1.27	0.50	51.6	47	72.5	66	89.0	81	95.6	87

*Estimated

NA = not available.

TABLE VIII. - VALUES FROM DAMAGE-TOLERANT DESIGN
HANDBOOK (ref. 15)

| Material | Thickness | | K_c | |
	cm	in.	$\frac{kN\text{-}cm^{1/2}}{cm^2}$	$ksi\text{-}in.^{1/2}$
2219-T87	0.152	0.060	84.6 - 86.8	77-79
2219-T87	0.254	0.100	82.4 - 115.4	75-105
2219-T87	3.175	1.250	39.6 - 49.4	36-45
7075-T6	0.102	0.040	57.1 - 75.8	52-69
7075-T6	0.127	0.050	63.7 - 78.0	58-71
7075-T651	3.505	1.380	22.0 - 33.0	20-30
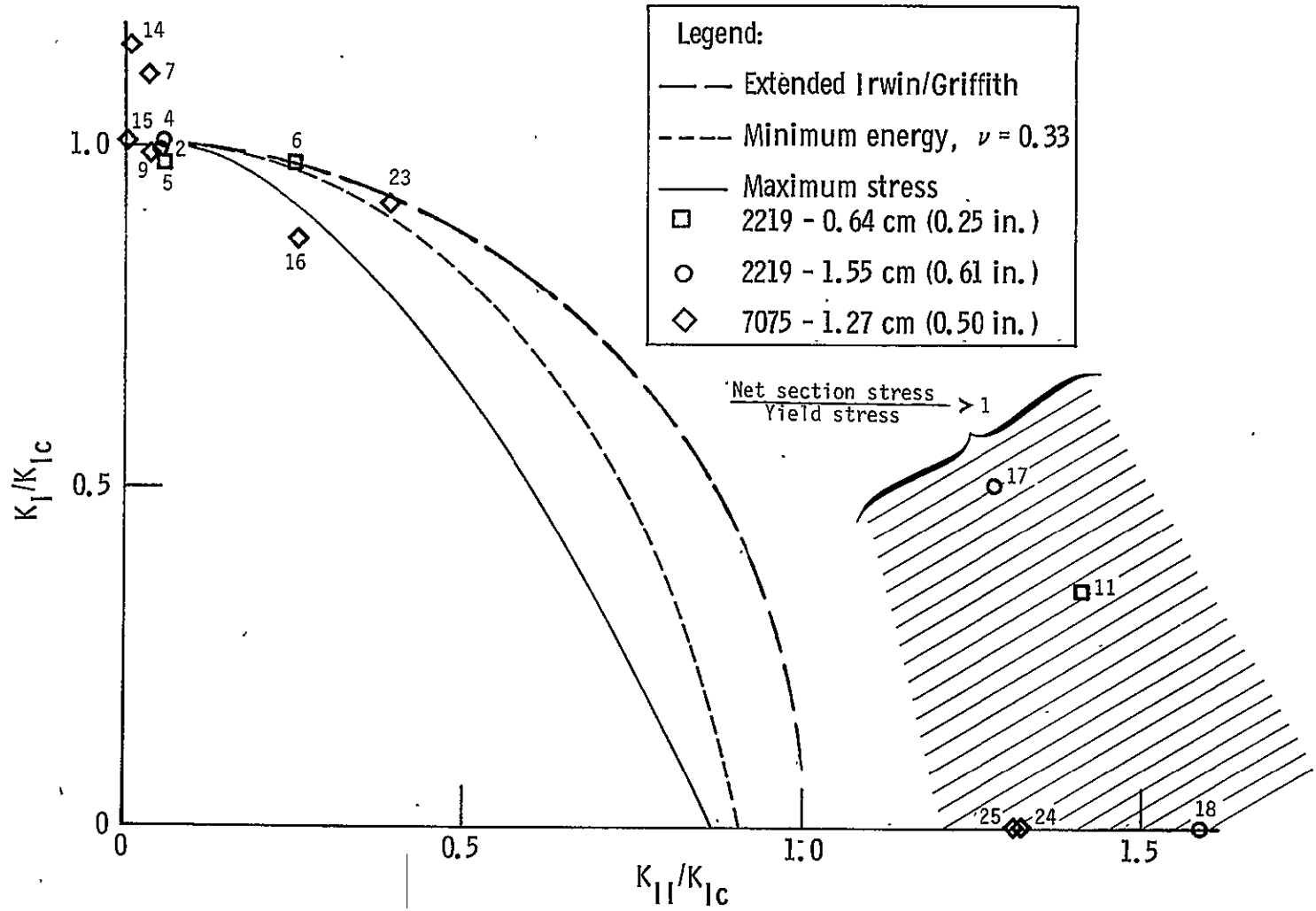
Figure 52. - Stress intensity interaction normalized to K_{Ic}.
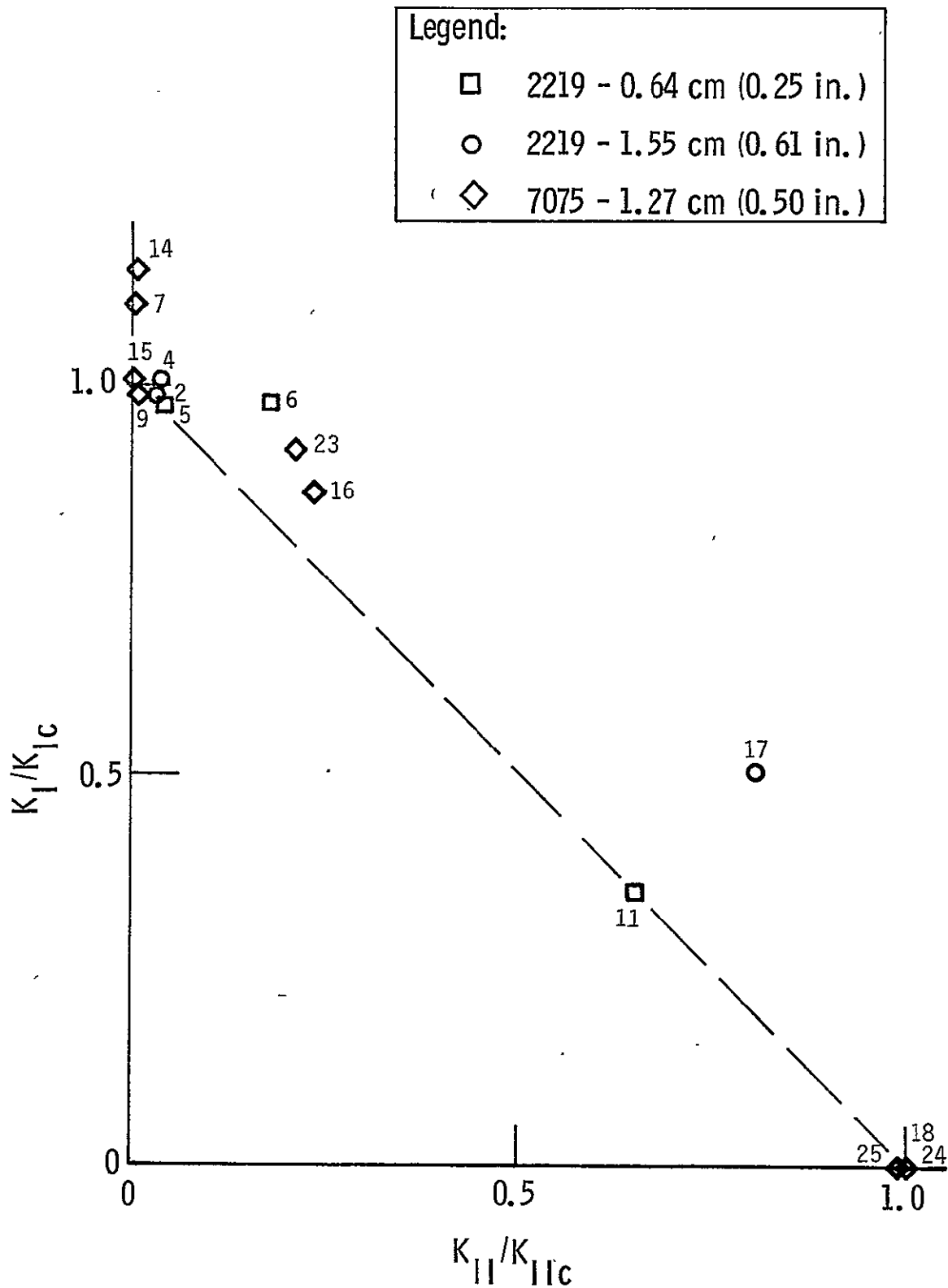
Figure 53. — Stress intensity interaction normalized to K_{Ic} and K_{IIc}.

A number of fatigure studies were conducted for which crack length was recorded as a function of number of cycles and loading. Figure 24 presented diagrams that describe variation with time of vertical and horizontal loads applied to cracked specimens. The first part of each cycle in figure 24 is referred to as part ①; the second is referred to as part ②. In these fatigue experiments, the initial precrack was oriented 45° to the vertical and horizontal axes. However, in most tests, crack branching occurred as soon as mixed-mode cycling with reversed shear commenced. Branching occurred in such a way that one branch grew predominantly normal to the vertical loading; the other grew predominantly normal to the horizontal loading. This meant that, on a given crack tip, if applied loading produced predominantely mode I with some mode II on one part of the cycle, then almost no stress intensity of either kind was produced during the other part of the cycle.

Because there was some degree of mixed-mode loading, fatigue data were analyzed in the following way. It was decided to characterize crack growth in terms of ΔG instead of the usual ΔK. ΔG quantities were computed for parts ① and ② of the cycle using the following expressions:

$$\Delta G_{①,②} = \frac{1 - \upsilon^2}{E} \left[\left(K_I^2 + K_{II}^2 \right)_{max} - \left(K_I^2 + K_{II}^2 \right)_{min} \right]_{①,②} \quad [28]$$

Next, it was assumed that a fatigue law of the type

$$da/dN = C_f \left(\Delta K_I \right)^n \quad [29]$$

could be extended to mixed-mode situations by replacing the term ΔK_I with the equivalent relationship in terms of ΔG given by

$$da/dN = C \left(\frac{E}{1 - \upsilon^2} \right)^{n/2} \left(\Delta G \right)^{n/2} \quad [30]$$

Next, it was considered that crack growth occurs during both parts of the cycle plotted in figure 24. Accordingly, crack growth rate is assumed to contain contribution due to both parts ① and ② of the cycle and is expressed as

$$da/dN = C \left(\frac{E}{1 - \upsilon^2} \right)^{n/2} \left[\left(\Delta G_① \right)^{n/2} + \left(\Delta G_② \right)^{n/2} \right] \quad [31]$$

which may be rewritten in the form

$$da/dN = C \left(\frac{E}{1 - \upsilon^2} \right)^{n/2} \cdot \Delta G_①^{n/2} \left[1 + \left(\frac{\Delta G_②}{\Delta G_①} \right)^{n/2} \right] \quad [32]$$

The next step in the analysis is to recognize that the ratio of $\Delta G_{\textcircled{2}}$ to $\Delta G_{\textcircled{1}}$ is a small number and may be neglected compared to unity.

Based on the foregoing analyses and series of assumptions, it is concluded that the mixed-mode fatigue data obtained in this program should correlate with an expression having the form

$$da/dN = C \left(\frac{E}{1 - \upsilon^2}\right)^{n/2} \left(\Delta G_{\textcircled{1}}\right)^{n/2} \qquad [33]$$

where parameters n and C may be taken from mode I fatigue data obtained in previous experiments. The foregoing discussion presents a way in which crack growth data may be interpreted in terms of ΔG for mixed-mode situations. Equations of a type other than that of equation 29 could have been used as a basis for the discussion as well, with replacement for ΔK made in terms of ΔG in a similar manner. For example, in the following discussion, some comparisons are made with Forman's (ref. 16) equation presented in terms of ΔG instead of ΔK.

Figures 54 through 59 present fatigue data from this study for 2219 aluminum in the form of plots of ΔG versus $\Delta a/\Delta N$. The figures also show plots of Forman's equation evaluated for 2219 aluminum in mode I fatigue tests. Data from this study involving fatigue crack growth under mixed-mode loading conditions were found to agree very well with the Forman equation when it is interpreted in terms of ΔG as described above.

Figure 60 through 63 are plots of ΔG versus $\Delta a/\Delta N$ for 7075 aluminum. These data are compared to Colliprist data (ref. 17)* for the same material subjected to mode I fatigue loading. Very good ageement is found between the mixed-mode fatigue data from this program so analyzed and data based on Collipriest's mode I fatigue studies for the slower growth rates.

In the upper ranges of $\Delta a/\Delta N$, data from this program consistently fell below Collipriest's pure mode I data. The difference cannot be attributed to the presence of mode II effects because there was very little mode II loading in the latter stages of the tests. It is more likely attributable to differences in specimen dimensions and shape and/or stress levels relative to yielding under which crack growth was fostered.

It is also interesting that in figure 63 the growth rate for SN-27 was always faster than predicted by Collipriest. In SN-27, the crack was grown under essentially pure K_I conditions except

---

*Collipriest's curve was not used. A curve was fitted through Collipriest's data points in the range $\Delta a/\Delta N$ covered by the tests on this program.

that a compressive load applied parallel to the crack growth direction on every cycle was equal in magnitude to the tensile load. Apparently this compression had considerable effect on growth rate, although no theoretical treatment takes such loading into account.

It is concluded from these results that the method presented here for analyzing mixed-mode fatigue data is reasonably correct for the experiments conducted. However, it is also recognized that the amount of mode II loading present in these fatigure experiments should not be expected to have a highly significant effect on the results.

Figure 54. – Crack growth rate for SN-1.

Figure 55. — Crack growth rate for SN-2.

Figure 56. – Crack growth rate for SN-3.
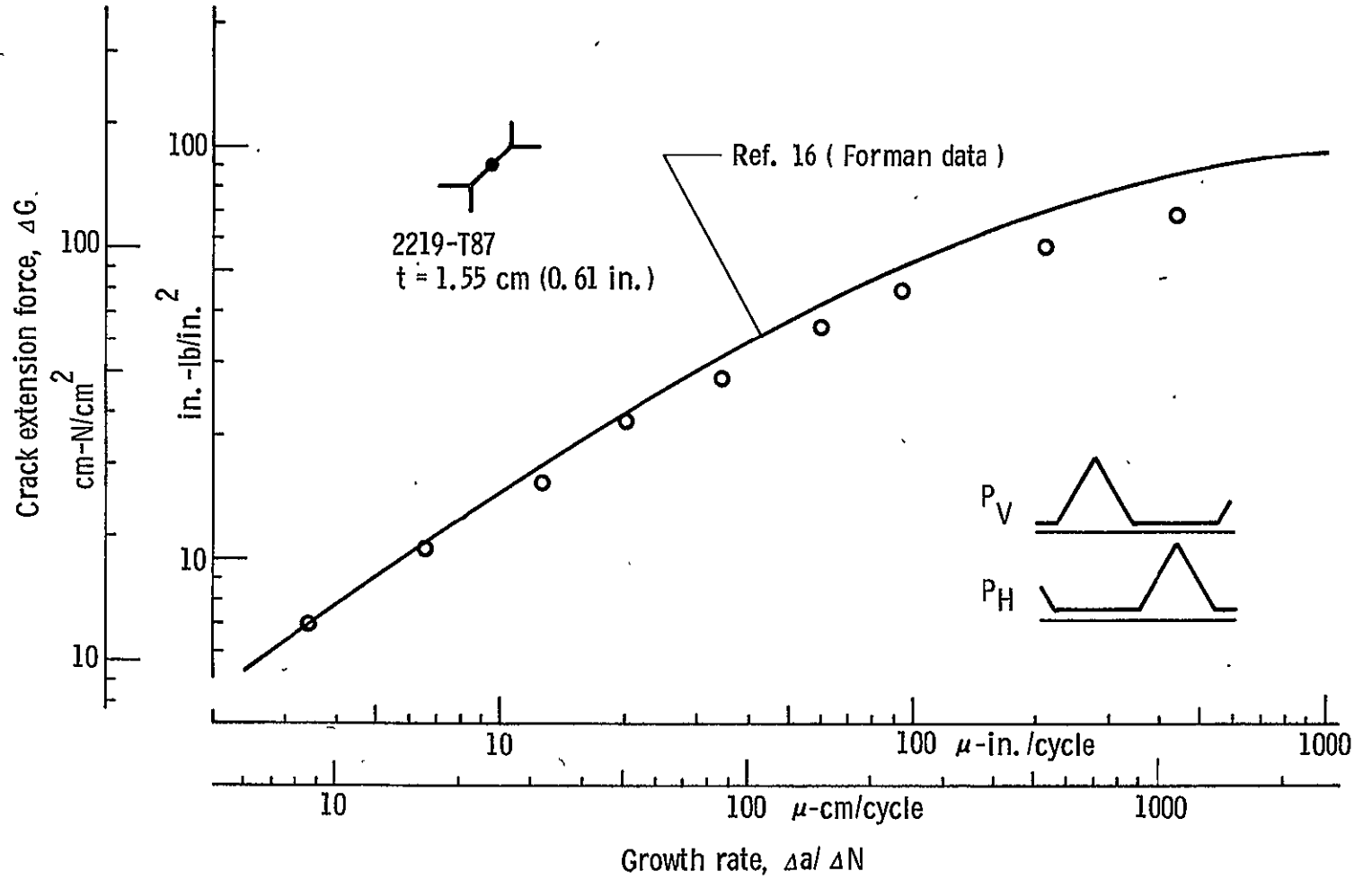
Figure 57. – Crack growth rate for SN-4.
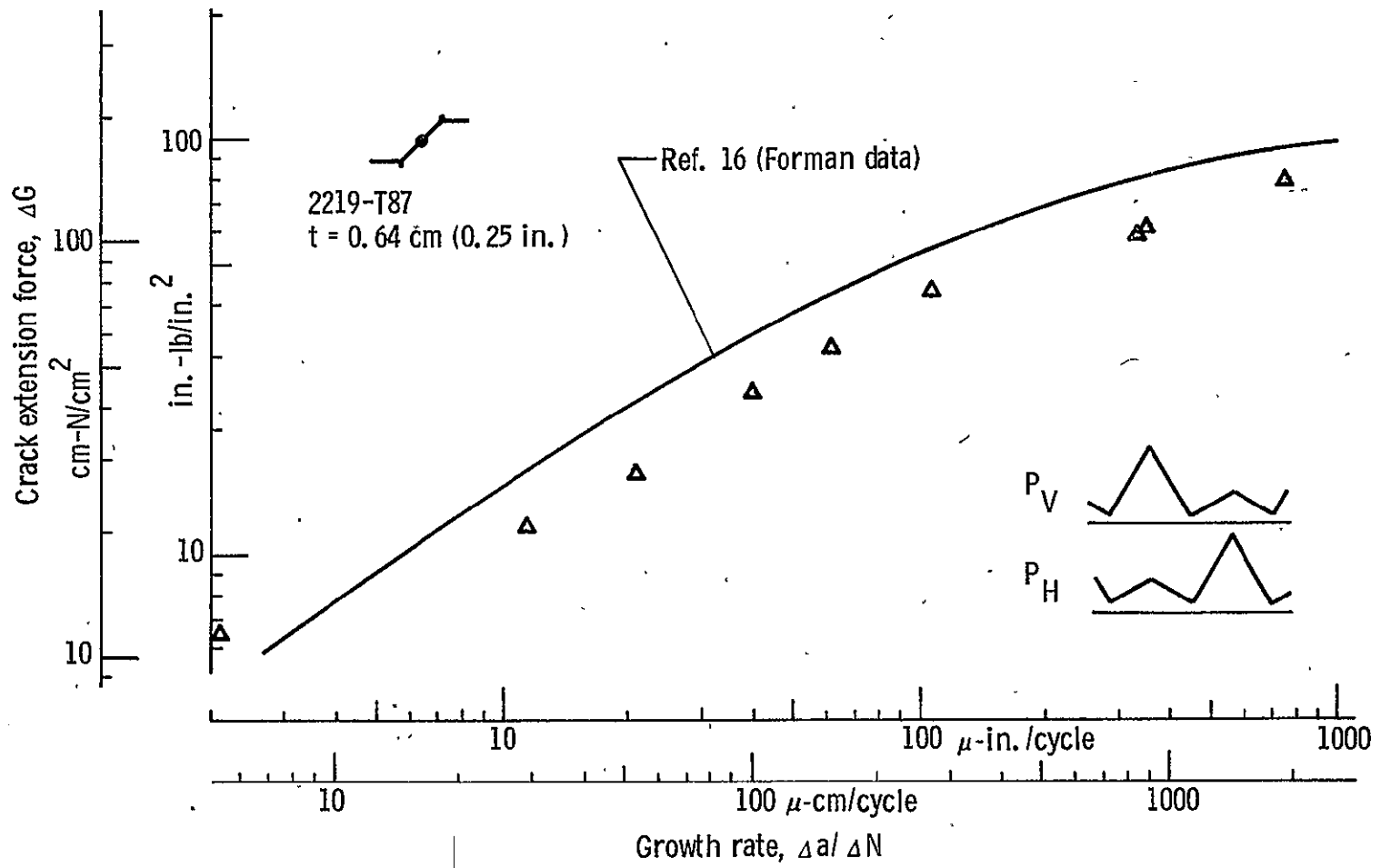
Figure 58. — Crack growth rate for SN-5.
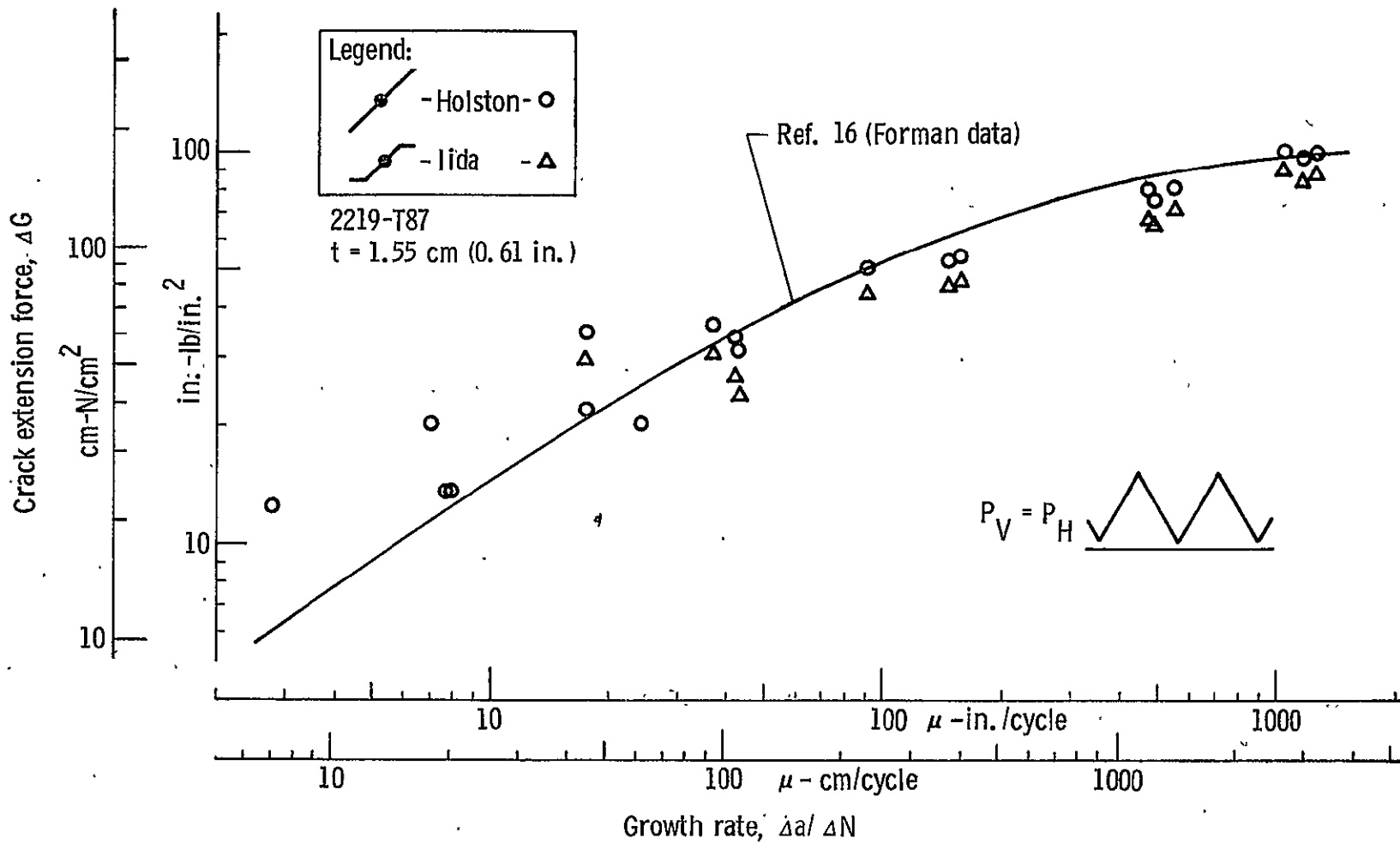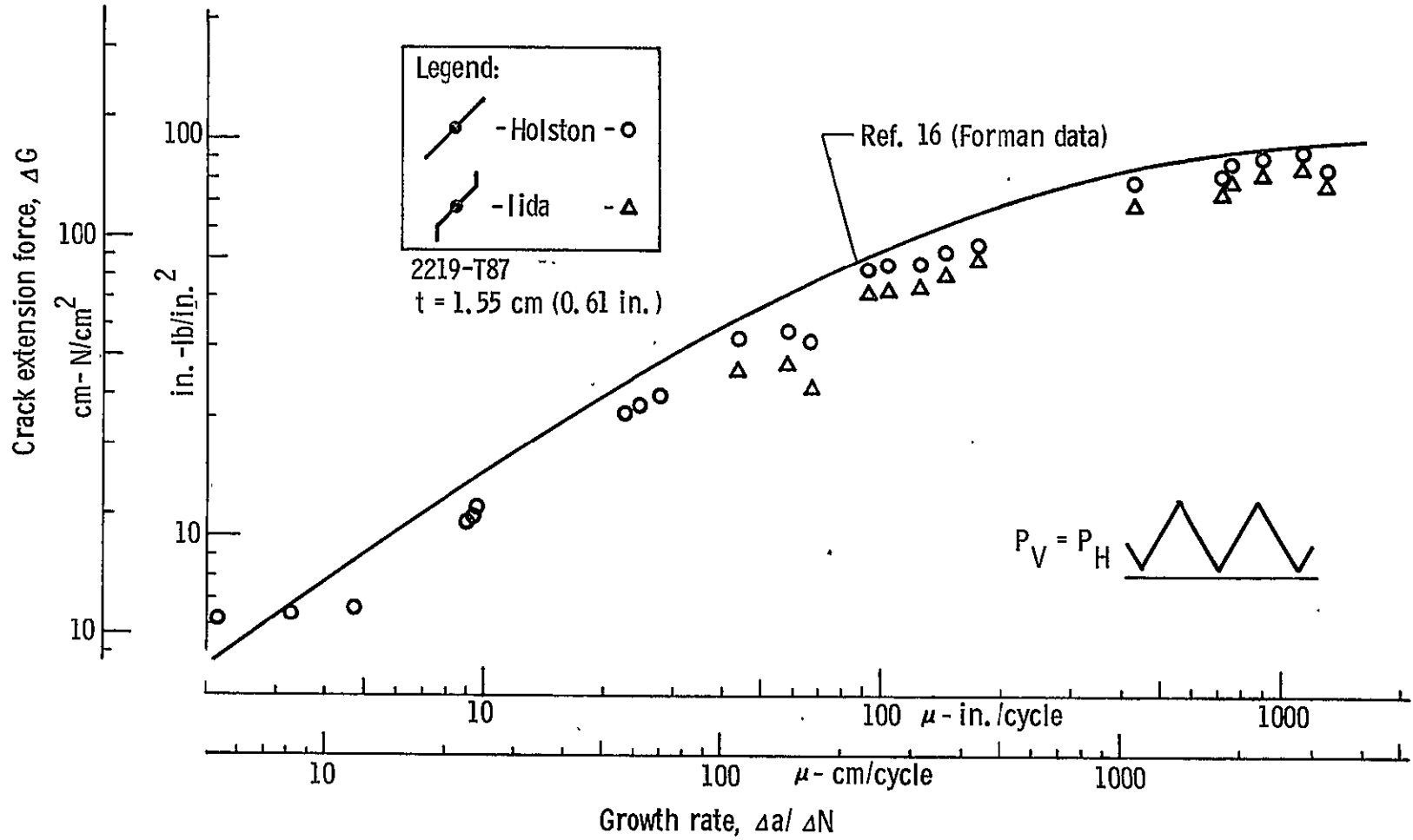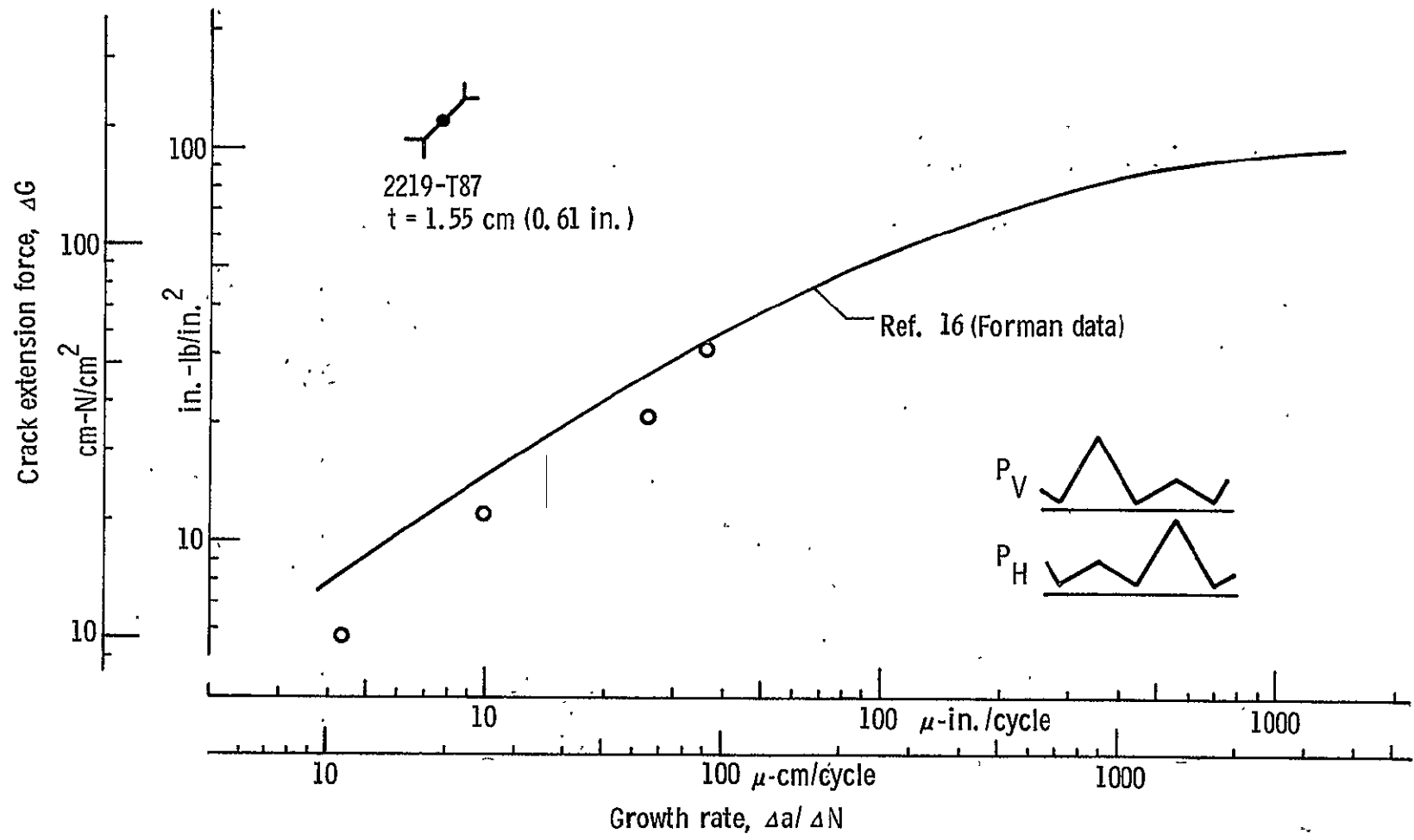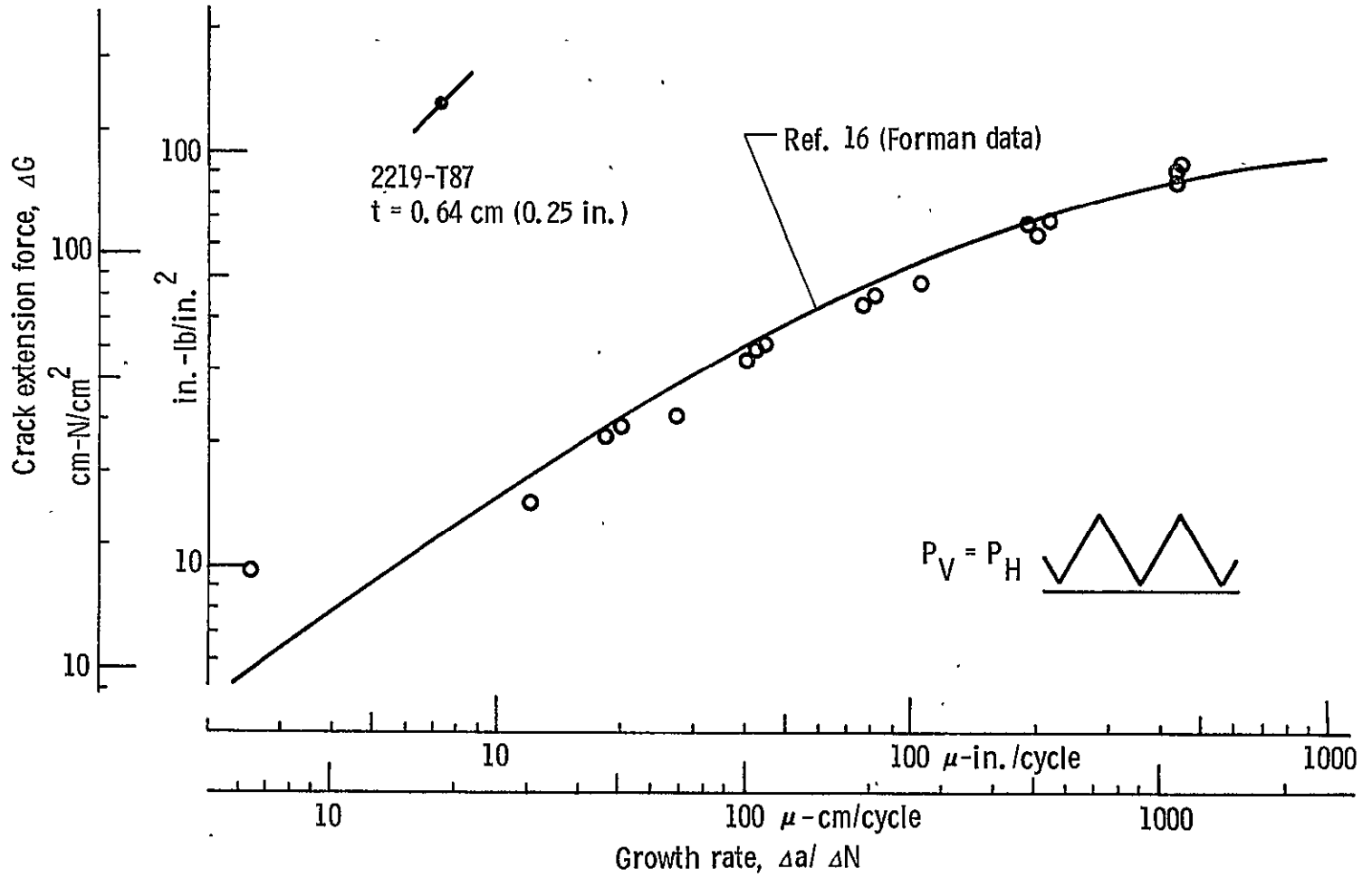
Figure 59. — Crack growth rate for SN-6.
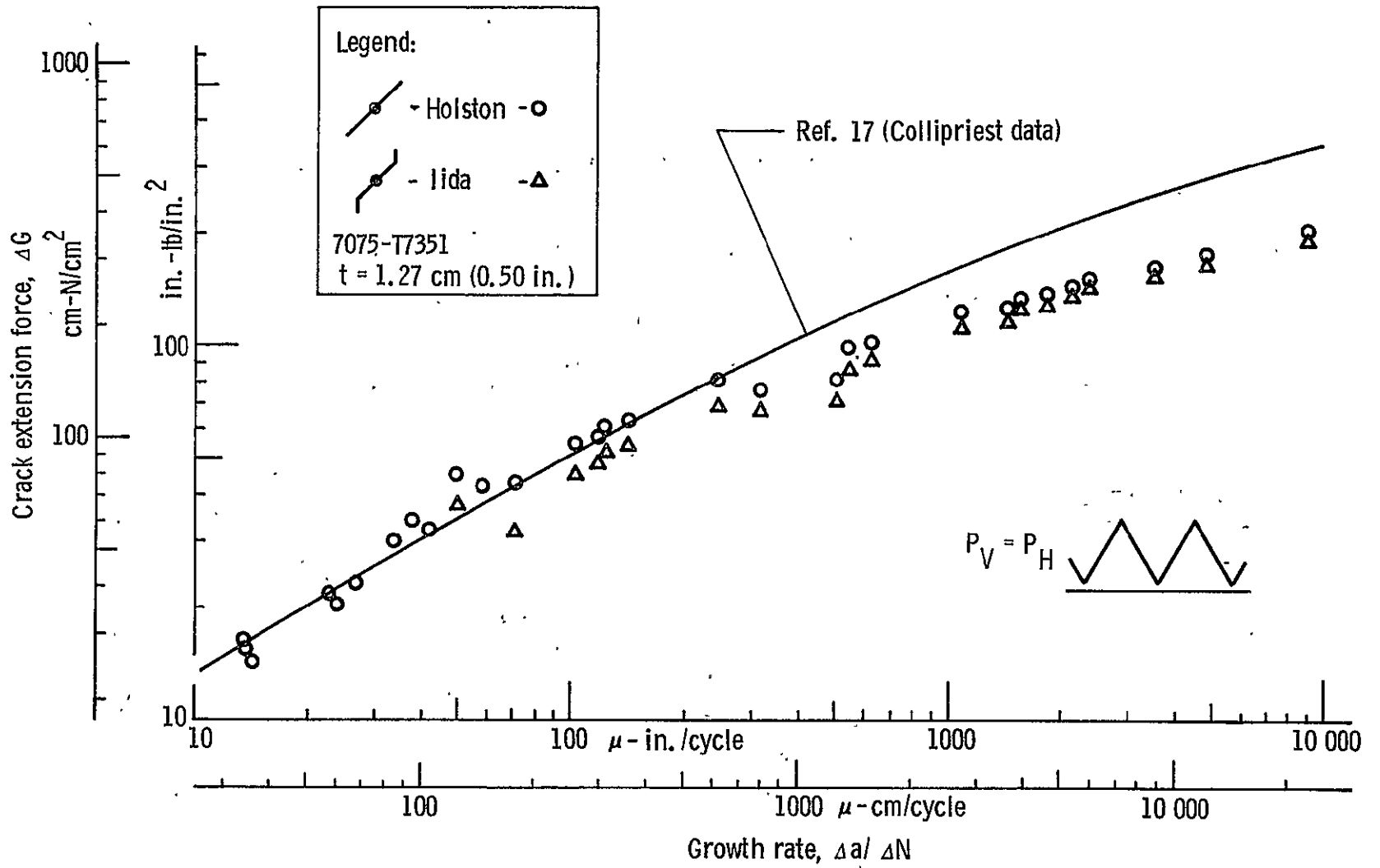
Figure 60. – Crack growth rate for SN-7.
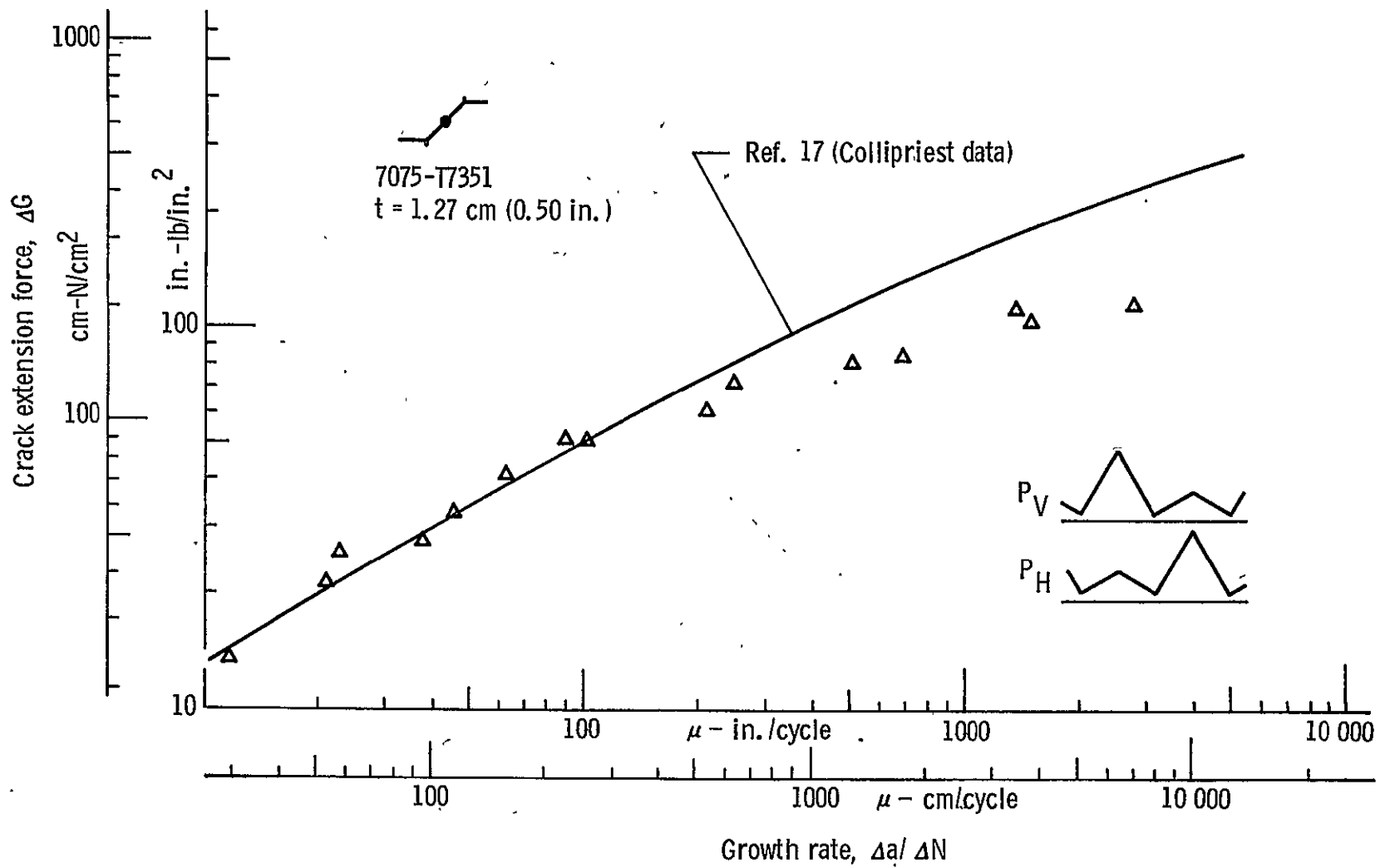
Figure 61. – Crack growth rate for SN-8.
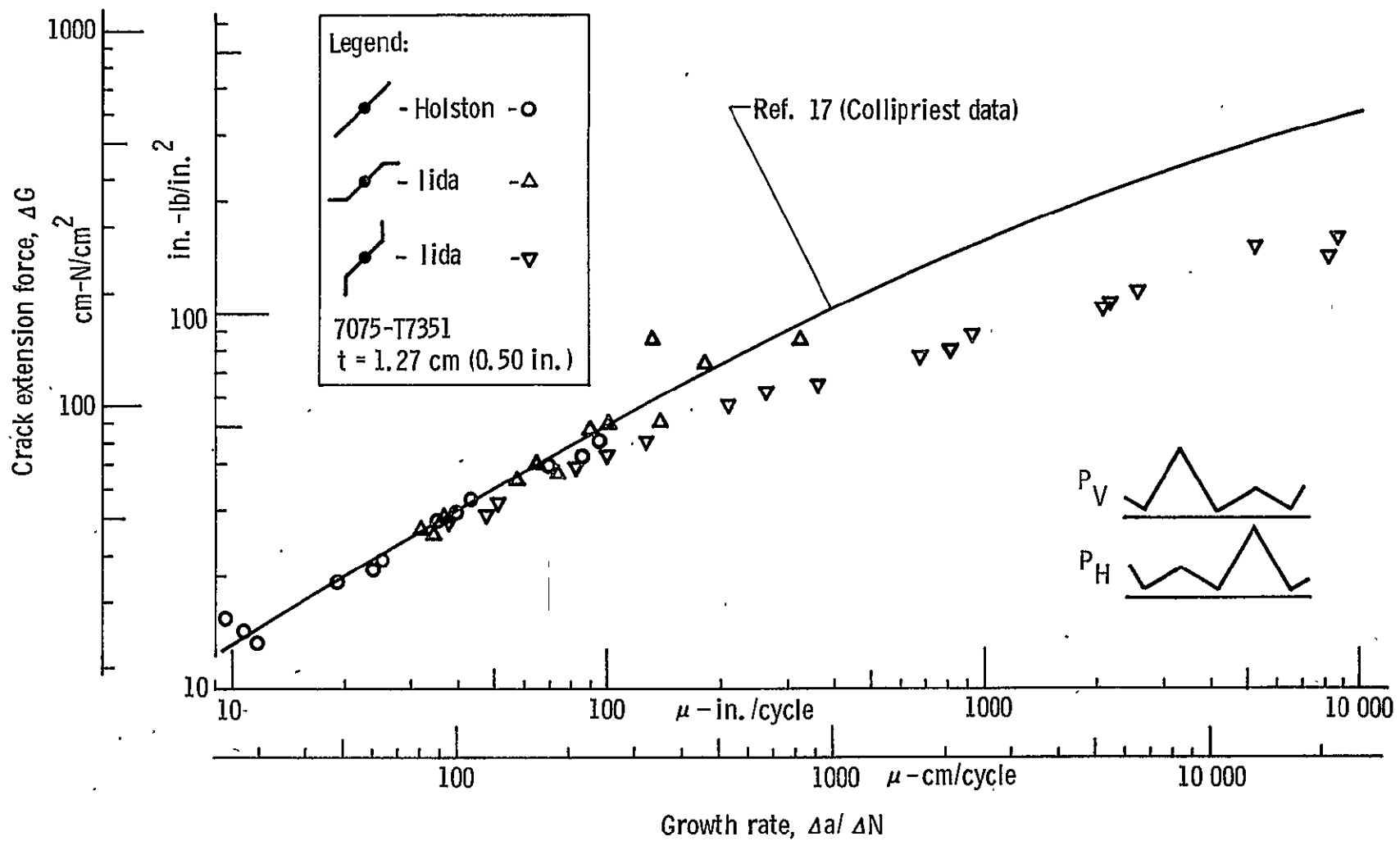
Figure 62. – Crack growth rate for SN-9.
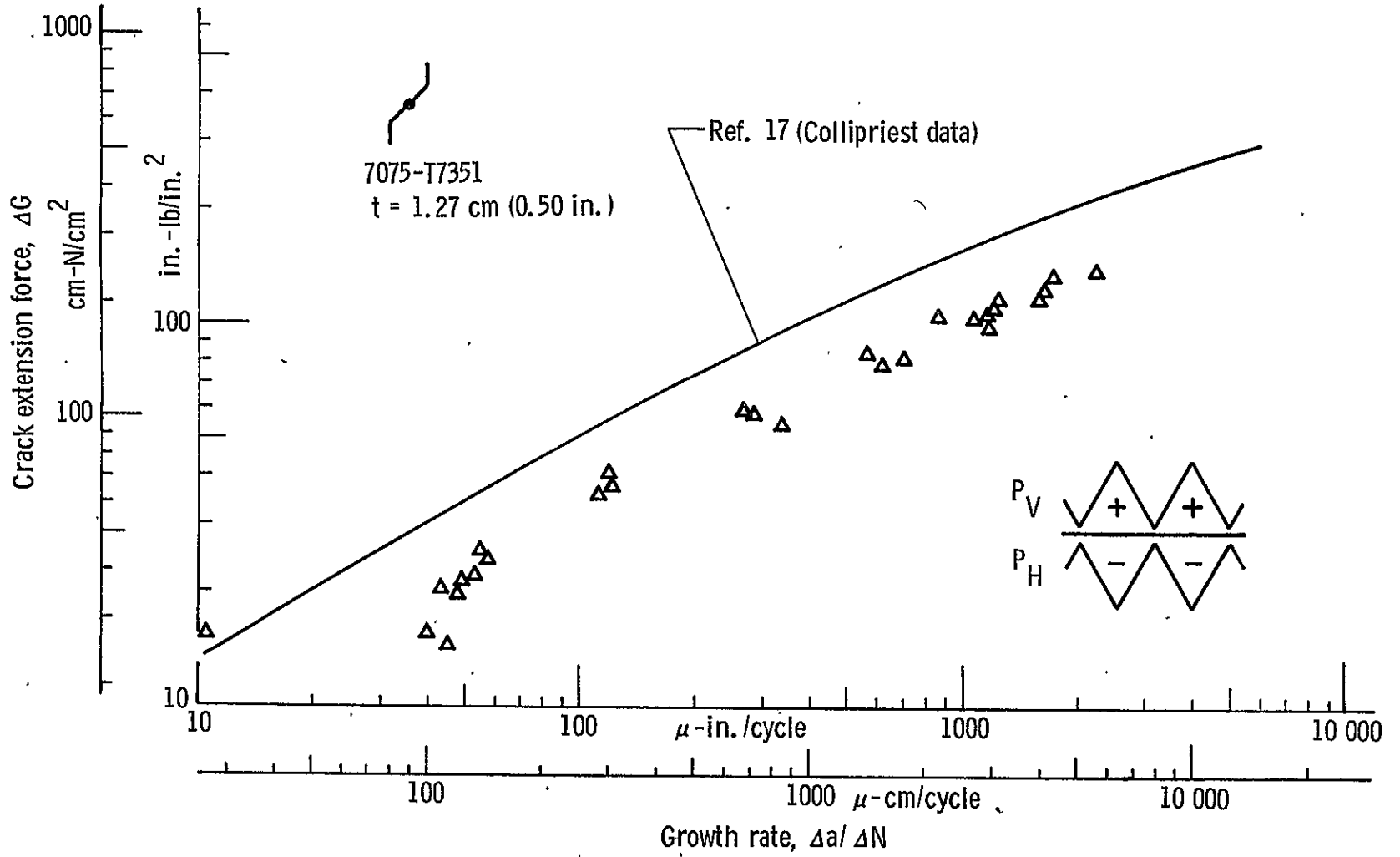
Figure 63. - Crack growth rate for SN-27.

Figures 64 through 73 show compliance data. Both analytical and experimental results are given for comparison. These results were not used in any other calculation; crack lengths were measured directly, and stress intensities were calculated using measured loads and crack lengths. Compliance data were used to monitor tests and provided a direct comparison between test and analysis.

Test data points shown were obtained by dividing measured COD and CSD by $\frac{1}{2}\left(P_V + P_H\right)$ and $\frac{1}{2}\left(P_V - P_H\right)$ respectively, except in cases of single-mode loading. In cases of pure mode I loading (SN-1, 2, 6, 7), $P_V = P_H$, and CSD should be zero as long as the specimen is symmetric. Thus, shearing compliance, $2(CSD)/\left(P_V - P_H\right)$, is indeterminate (0/0). For these cases, the ratio CSD/COD is shown along with opening compliance. Deviation of this ratio from zero indicates asymmetry of the specimen and/or deviation of loading from pure $P_V = P_H$ (see section on experiment observations and primary data). For pure mode II (SN-27), $P_V = -P_H$, and COD should be zero. The ratio COD/CSD is shown along with shearing compliance. Analytical results were obtained from the following expressions (see Appendix A for development):

$$COD = \frac{4\left(1 - \upsilon^2\right)a}{E}\ \frac{1}{2}\left(\sigma_V + \sigma_H\right)\tilde{v} \qquad [34]$$

$$CSD = \frac{4\left(1 - \upsilon^2\right)a}{E}\ \frac{1}{2}\left(\sigma_V - \sigma_H\right)\tilde{u} \qquad [35]$$

with $\qquad \sigma_V = P_V/20t$ and $\sigma_H = P_H/20t$ (customary units)

or $\qquad \sigma_V = P_V/50.8t$ and $\sigma_H = P_H/50.8t$ (SI units)

where t denotes thickness and 50.8 or 20 is the length used in normalizing analytical results. Theoretical compliances are shown by heavy lines, and the extent of the lines indicates range of applicability. Analytical results are shown where the crack remained straight or branched with equal branches. For other configurations (Z, unequal branches, or curved cracks), analytical expressions for stress intensities are available, but not for crack displacements.

These figures show general agreement between tests and analyses. The correlation deteriorated as the cracks grew into configurations different from those idealized in the analyses. In cases of single-mode loading, pure K_I, or pure K_{II}, the other crack displacement should have been zero. The figures show some small values. As explained above, these may have been due to asymmetry or bending of the specimen, small differences in the loads on each axis, and/or possible gage-holder mounting problems.
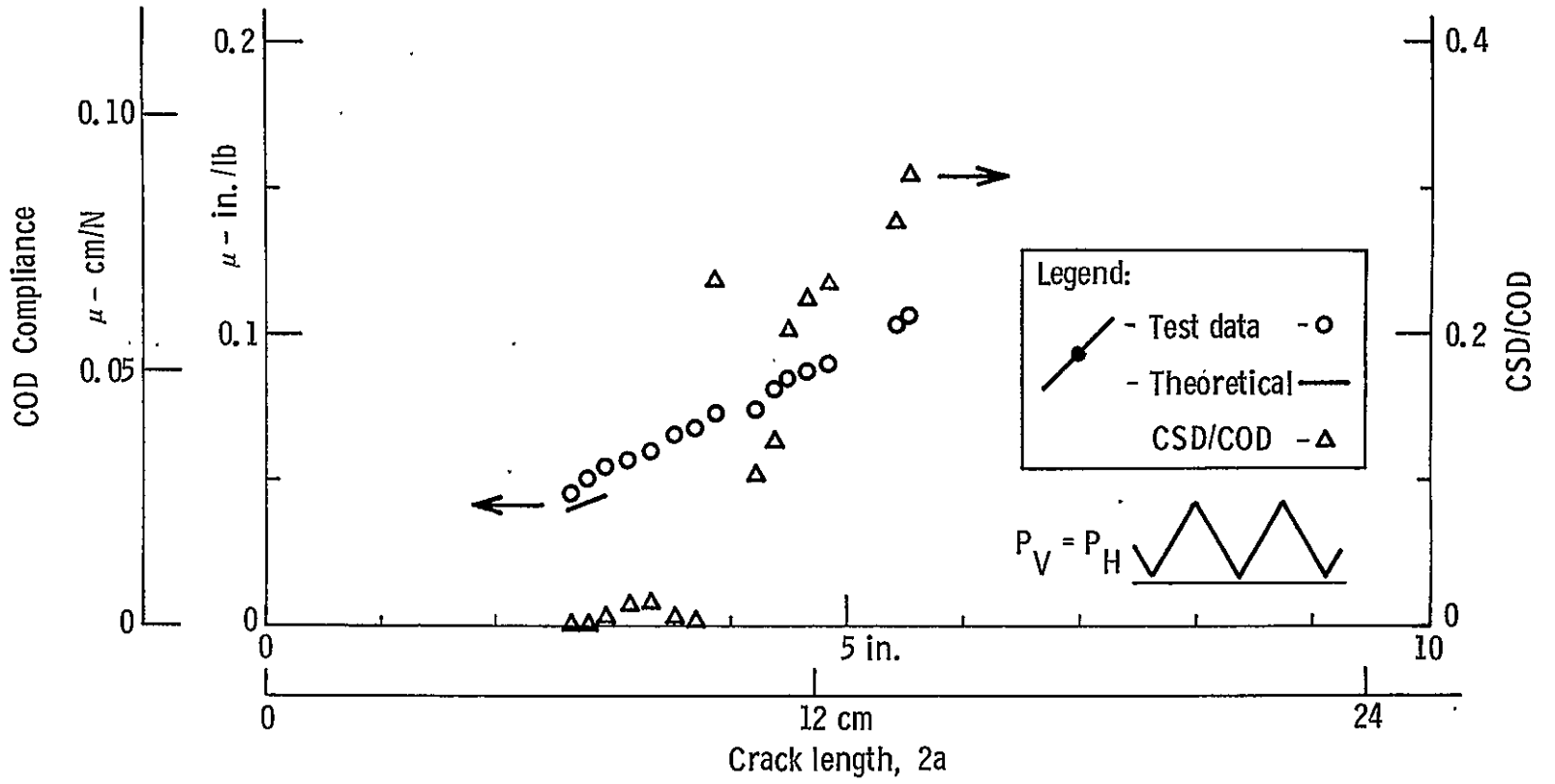
Figure 64. – Compliance for SN-1.
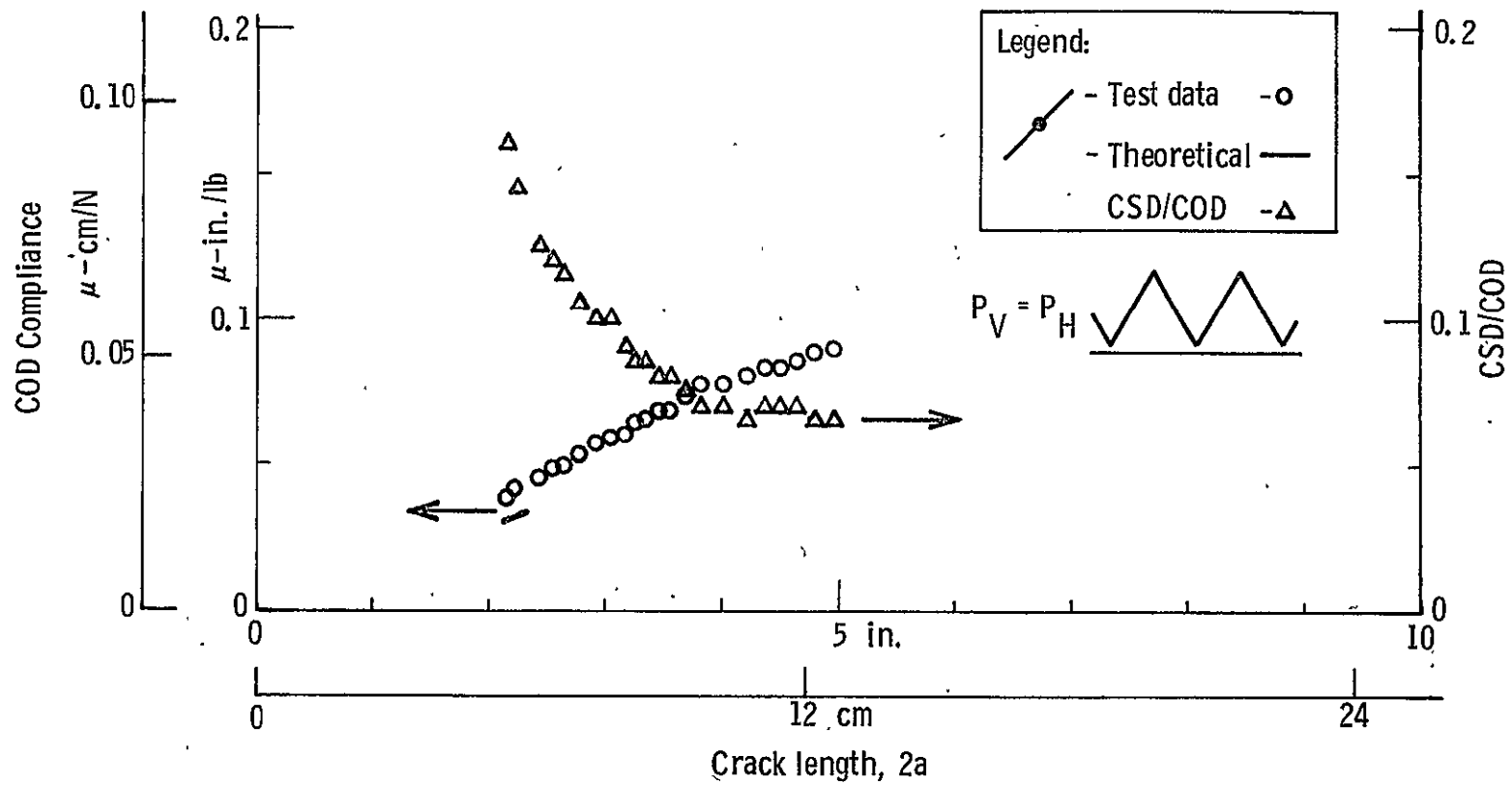
Figure 65. – Compliance for SN-2.
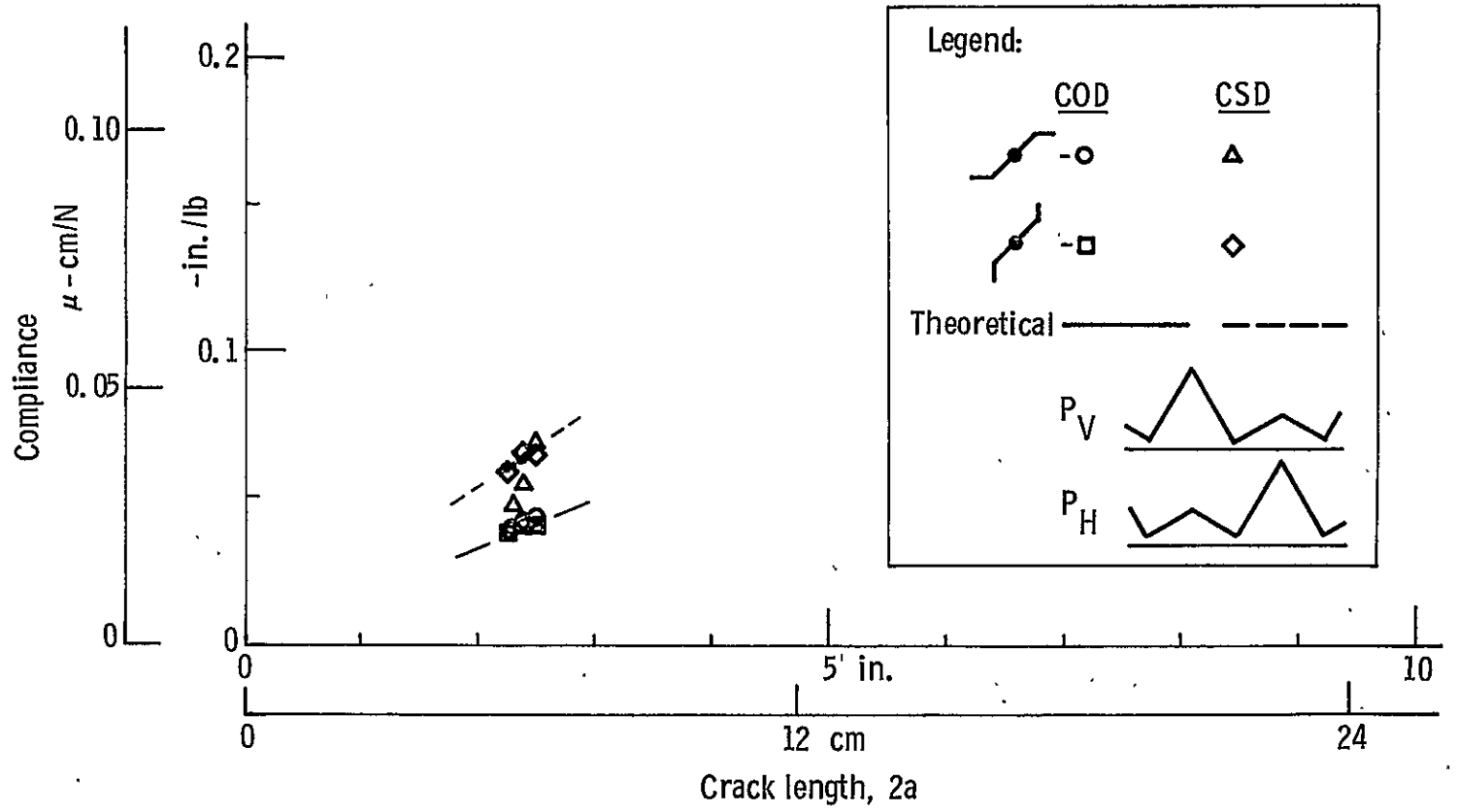
Figure 66. - Compliance for SN-3.
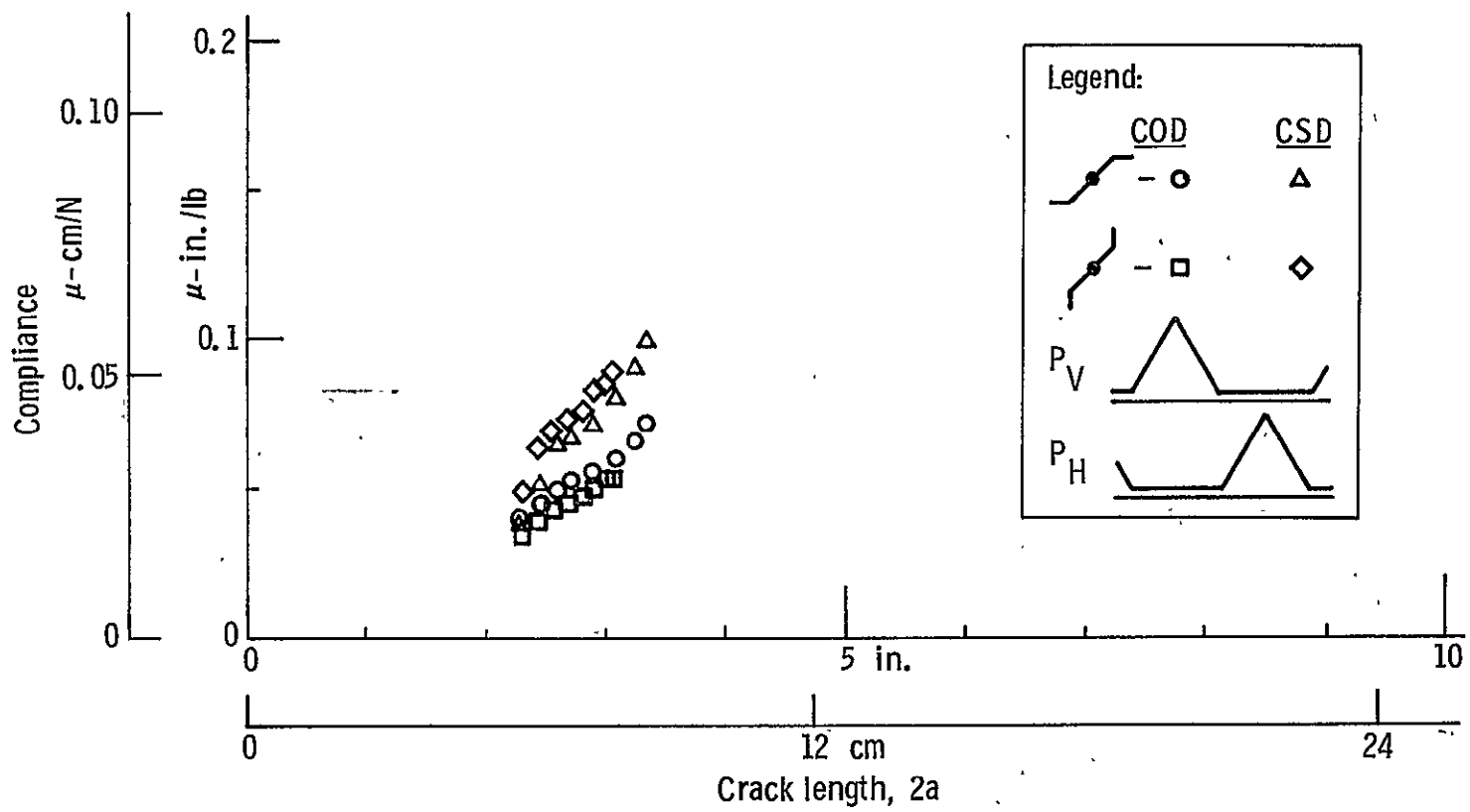
Figure 67. - Compliance for SN-4.
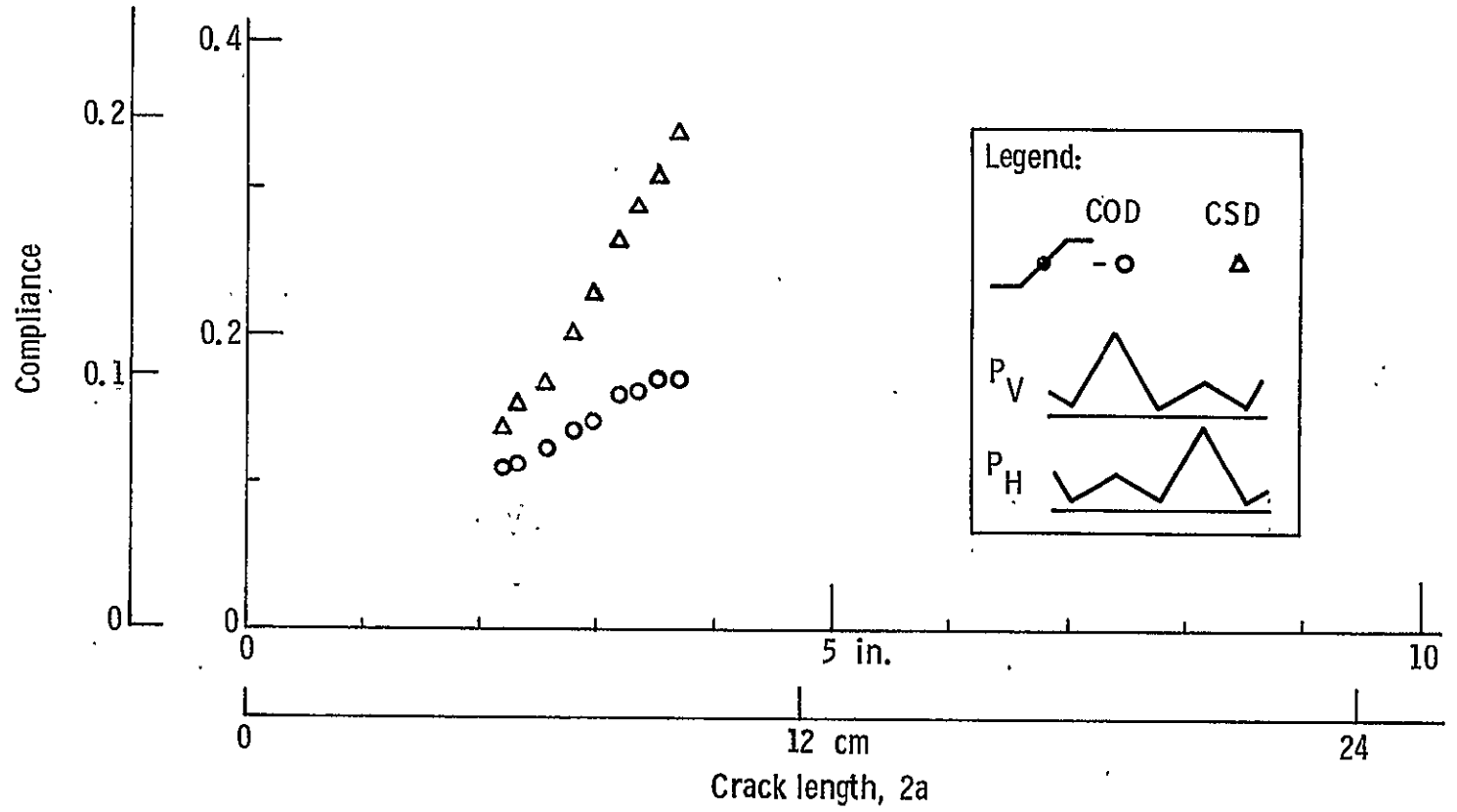
Figure 68. - Compliance for SN-5.
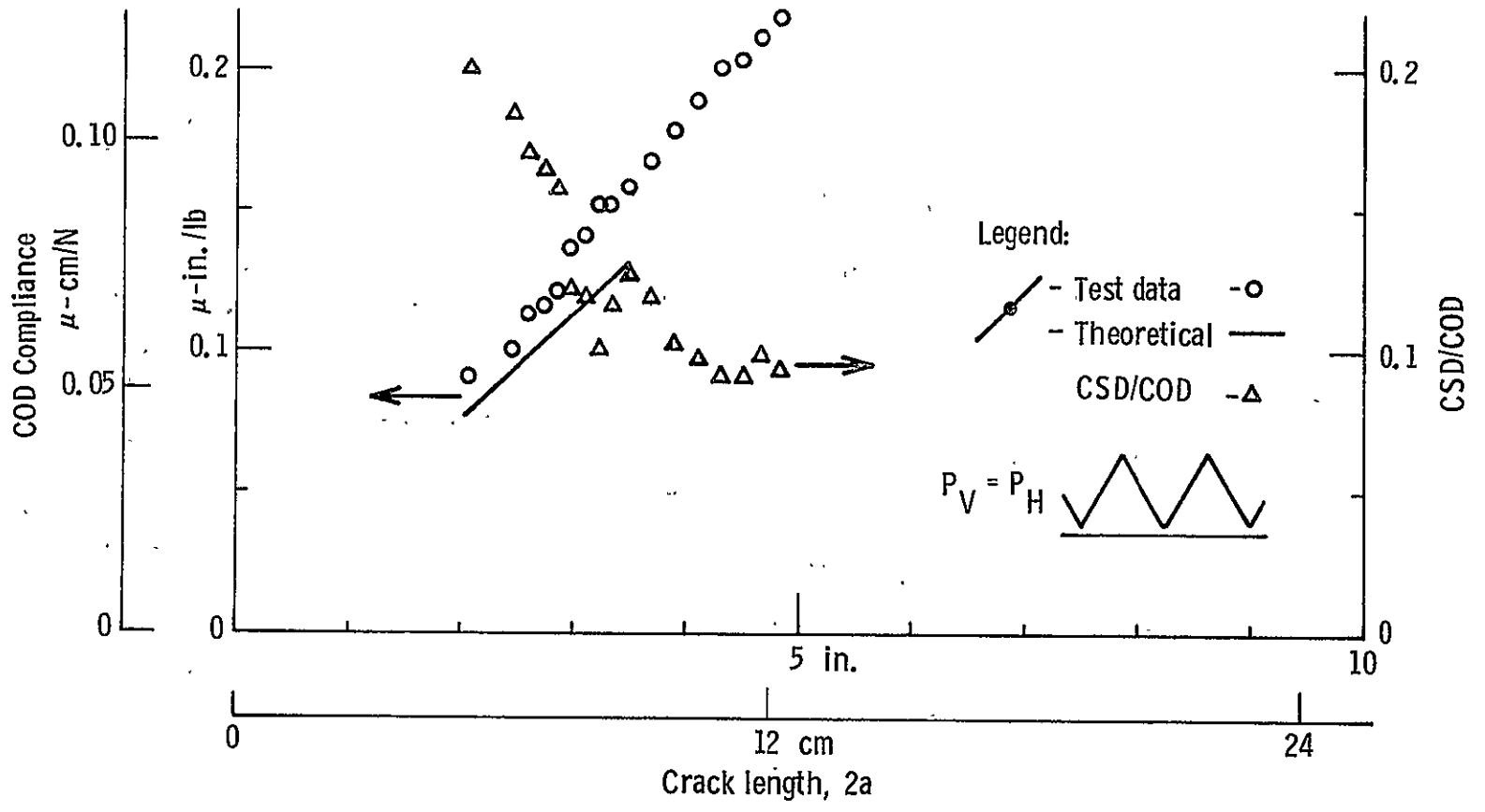
Figure 69. – Compliance for SN-6.
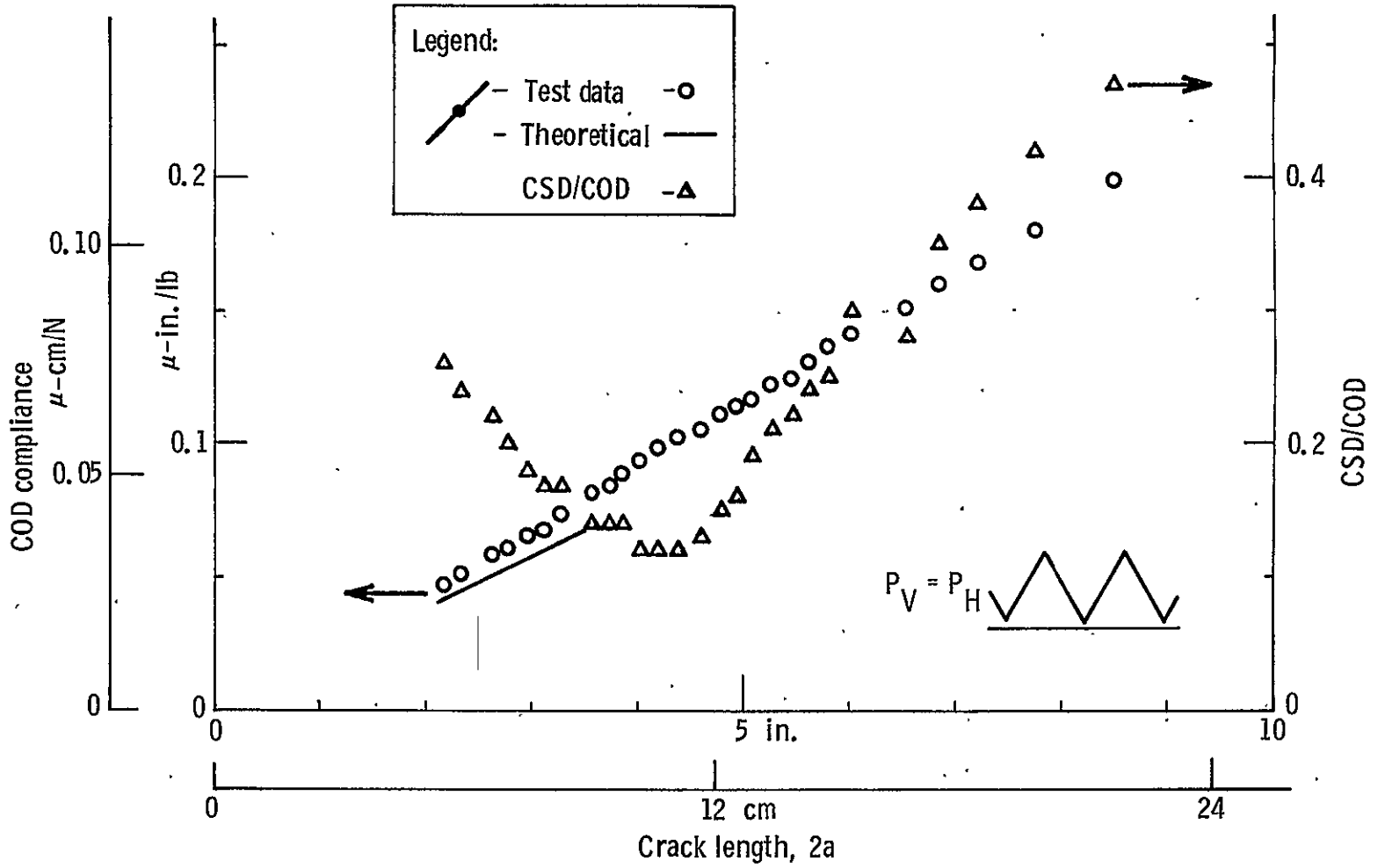
Figure 70. - Compliance for SN-7.
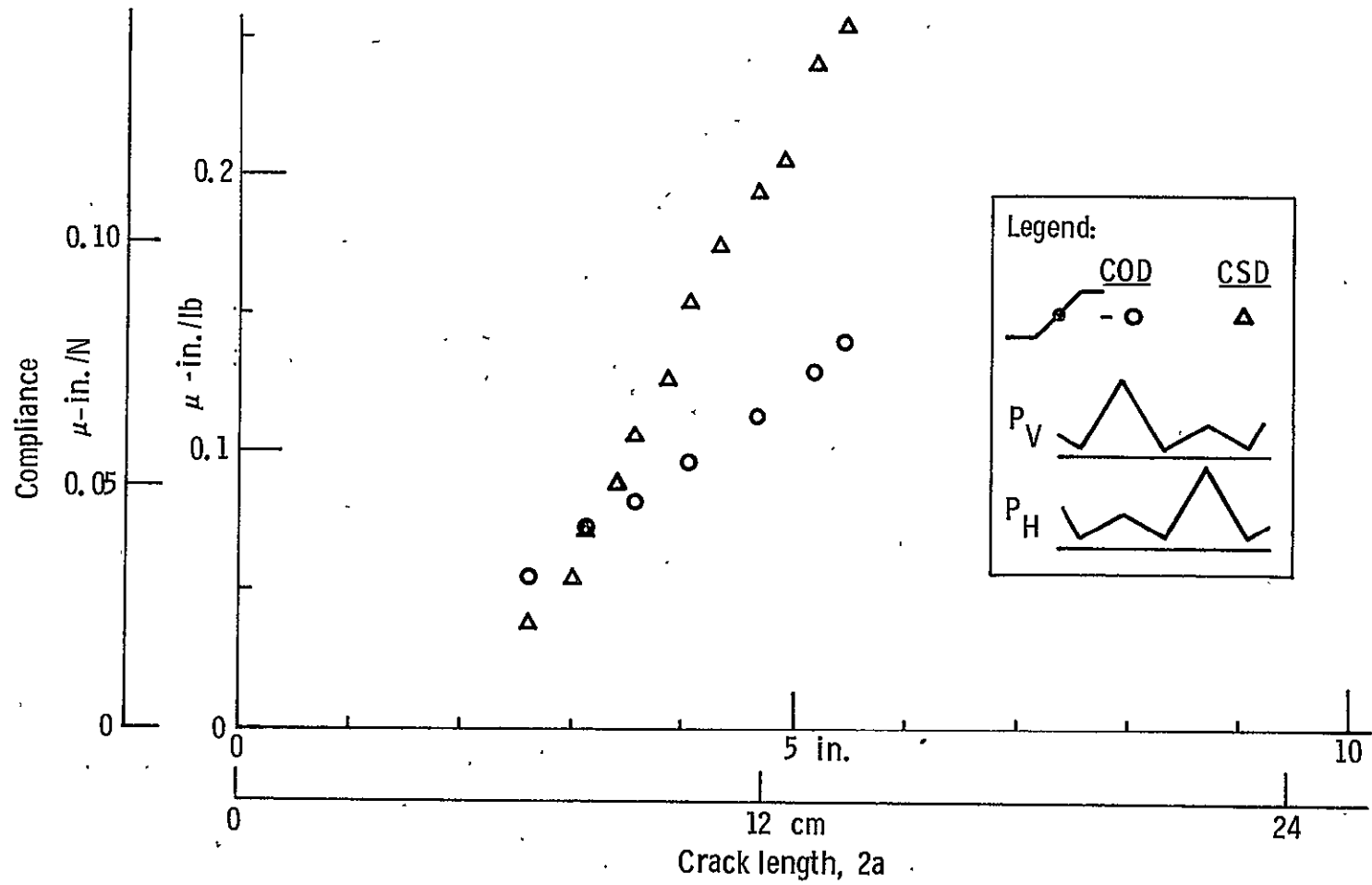
Figure 71. – Compliance for SN-8.
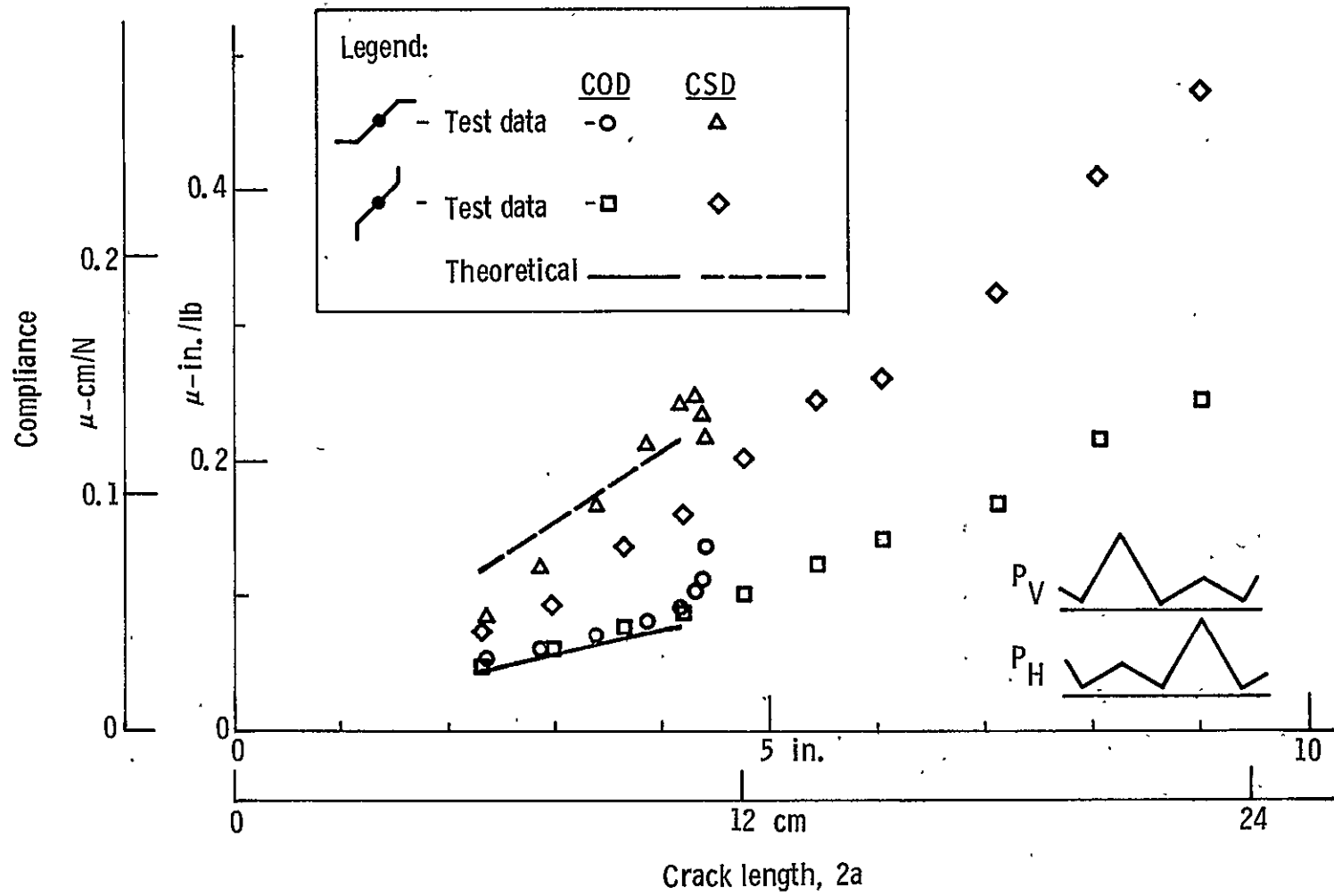
Figure 72. – Compliance for SN-9.
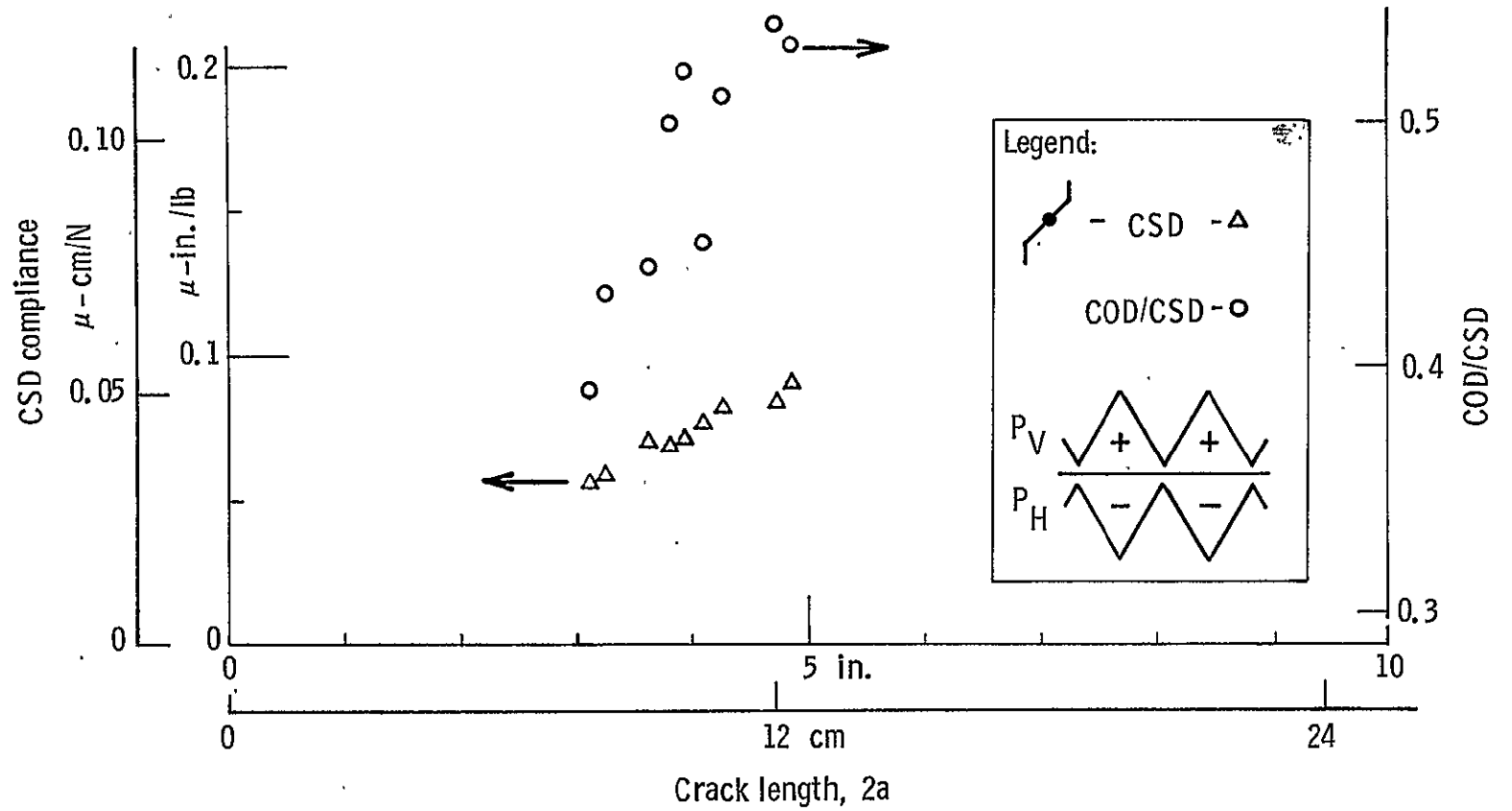
Figure 73. – Compliance for SN-27.

CONCLUSIONS

To develop crack-growth and fracture toughness data under mixed mode conditions, an experimental investigation was undertaken involving, in the main, room-temperature cyclic and static tests of flawed 91x91-cm (36x36-in.) aluminum plates. General conclusions that we believe are supported by the test results are set forth in this section.

During cyclic testing, it was impossible to maintain a high proportion of shear-mode deformation on the cracks. The cracks always branched when the shear was reversed on each cycle, resulting in crack fronts with very little K_{II}. When the shear was not reversed on each cycle, the cracks simply grew in an orientation that again resulted in almost no K_{II} at the tip. When there was no shear, the cracks turned to follow the final rolling direction of the material. When cracks branched, the branch parallel to the final rolling direction eventually grew faster.

Mixed-mode crack-growth rate data were analyzed in terms of energy release rate, G, taken as a function of both K_I and K_{II}, versus growth rate. Test results compare reasonably well with single-mode data from Forman and Collipriest, when their data are handled in the same fashion, keeping in mind that the shear component of G was relatively small. There was no noticeable difference in the effectiveness of the analyses used on crack growth data. Even though straight and branched cracks were analyzed using Holston factors, while Z-shaped cracks were analyzed using Iida factors, there was not an abrupt change in computed quantities derived from the test data when the cracks changed configuration and the analytical approach was correspondingly changed. In fact, in transition ranges, for example when cracks turned, the various approaches gave nearly the same computed values of K or G.

Measured crack opening and crack shear displacement agreed well with the straight and branched crack analyses over the range of applicability, that is, while the cracks were straight or the branches grew equally, and when significant displacements were expected from the load scheme applied. However, there was measurable opening and shear displacements when theoretically they should have been zero, suggesting that there were deviations from ideal conditions of specimen shape, load application, and gage mounting.

Under static loading to fracture, straight 45° cracks remained straight when the shear stress intensity exceeded the normal stress intensity at the crack tip. Thus, we were able to obtain fracture under pure shear. When applied shear was less than the normal

stress, the crack grew, or turned to become, perpendicular to the direction of higher load. When the loads on each axis were equal, the crack turned parallel to the final rolling direction. If the crack was branched before the static test, the branch perpendicular to the higher load was the one that grew to instability. When static loading of equal magnitude on each axis was applied to a curved crack, the crack grew to instability without further change in direction.

It was shown theoretically that there is little difference in the prediction of fracture behavior between the maximum tangential stress theory $\left(\sigma_{\theta\theta}\right)$, minimum-strain energy density theory (S), and an extension to the theory based on energy release rate (G). Therefore, all data were reduced in terms of G because it was simpler. In the range near pure K_I, the experimental G values fell both inside and outside the theories. Values of G_{cr} for pure K_{II} were approximately 50% higher than G_{cr} for pure K_I, which is contrary to the three theories mentioned above. However, the net section stresses were well above the shear yield stress when fracture occurred with high shear. For the 7075 alloy, values of G_{cr} were also affected by the relation between flaw growth direction and final rolling direction of the material. This dependence was not found in the 2219 alloy. For both, there was very strong interaction between the normal and shear mode stress intensities, with a large reduction in K_I resulting from the application of K_{II}. Again however, the conclusion must be tempered by the fact that fracture under conditions of high K_{II} occurred when the net section stresses were well within the inelastic region.

Choice of the Maltese cross specimen shape for this investigation served the program well. This configuration permits any combination of stress intensities from pure K_I through pure K_{II} with a 45° flaw orientation. The straight-crack analysis of reference 10 showed that stress intensities are nearly constant for a range of crack lengths. Branched crack results given in Appendix A show similar behavior. These analytical results were obtained via a special crack-tip finite element that properly accounts for both singularities. Resulting stress intensities are applicable for any thickness, Young's modulus, and loading combination for geometrically similar specimens.

In addition, the checkout procedure on the test machine revealed that the area of strain uniformity (±10%) under biaxial load in the center of an unflawed specimen extended for about five times the original 5-cm (2-in.) crack length, so that flaws grew into regions of constant strain.

APPENDIX A

ANALYSIS OF TEST SPECIMENS

I. INTRODUCTION

The test specimens shown in Figure 1 were analyzed to determine stress intensity factors and crack displacements. Stress intensity factors are used in studying flaw growth and fracture. Crack displacements may be compared with experimental measured values to provide a correlation between the analysis and test. The analysis considered specimen plane geometry and thickness, material elastic properties, flaw length, and combined loads. The main results are presented in the form of graphs for normalized stress intensity factors and crack displacements versus flaw length.

In performing the analysis, the finite element method was used to account for the irregular shape of the specimen boundary. A conventional element was used for most of the model and a special element used to model the region around the crack tip. This special element is required to properly treat the singularities occurring at the crack tip. The effects of flaw length were treated by making different finite element models for different flaw lengths.

Several features of the analysis method and specimen geometry permitted simplification of the modeling and generalization of the results. Symmetry of the specimen permitted modeling only one fourth of it. Linearity of the analysis with respect to specimen thickness, Young's modulus, and loads permitted scaling of these parameters. Finally, through the use of superposition any combination of loads may be treated from two fundamental cases. These features are discussed further in subsequent sections.

The main results from this analysis are given in the form of graphs showing normalized stress intensity factors and crack displacements versus flaw length. These results are applicable to other geometrically similar specimens for any thickness, Young's modulus, and all load combination.

II. SCALING

Before proceeding with scaling, consider the relative stiffnesses of the grip plates and test specimens. The grip plates will be used repeatedly and they must remain in tolerance with an infinite fatigue life. Thus they will be designed to low stress levels and will be very stiff relative to the test specimen.

Consequently, the grips were not modeled in the finite element analysis and a uniform displacement was applied to the specimen to simulate the grip plates. The load associated with the uniform displacement was determined from the analysis.

Two types of elements were used in the finite element models. Most of the specimen was modeled with constant strain triangular elements. This element is given in many text books on finite element analysis, such as Reference 1, and its stiffness matrix is linear in element thickness and Young's modulus,

$$\left[K \right] = h E \left[f \left(x_i, y_i, \nu, \tilde{\nu} \right) \right] \tag{1}$$

where h, E, ν are thickness, Young's modulus, and Poisson's ratio, respectively, x_i and y_i are node point coordinates, and

$$\tilde{\nu} = \nu \quad \text{for plane strain,}$$

$$\tilde{\nu} = \frac{\nu}{1 + \nu} \quad \text{for plane stress.} \tag{2}$$

The region around the crack tip was modeled with a special finite element, Reference 2. This element is based on Williams eigenfunction expansion of an airy type stress function about the crack tip. It is circular in shape, applicable to K_I (opening), K_{II} (in plane sliding), and $K_I + K_{II}$ modes of deformation, and contains the proper singularities. Generalized coordinates were used in the development and higher order terms from the expansions included. Compatibility of displacements at node points of adjacent conventional elements was ensured by using the Lagrange multiplier method in a constrained minimization. The stiffness matrix for this element is linear in Young's modulus and thickness also

$$\left[K \right] = h \, E \left[f(\nu, \tilde{\nu}) \right] \tag{3}$$

where the element geometrical parameter (element radius, r_e) is contained in the generalized coordinates. Stress intensity factors are given by

$$K_I = -2^{3/2} \frac{E}{2(1 + \nu)} \sqrt{\frac{\pi}{r_e}} \, \tilde{a}_1$$

$$K_{II} = 2^{3/2} \frac{E}{2(1 + \nu)} \sqrt{\frac{\pi}{r_e}} \, \tilde{b}_1 \tag{4}$$

where $\tilde{a}_1$ and $\tilde{b}_1$ are generalized coordinates. Now consider the question of scaling of stress intensity factors with Young's modulus and thickness. Suppose two finite element models were assembled from the above elements. The equations for these models

would be

$$\{F\}_1 = [K]_1 \{\delta\}_1 \qquad \{F\}_2 = [K]_2 \{\delta\}_2 \qquad (5)$$

where the subscripts denote the two models. Now each model stiffness matrix is linear in Young's modulus and thickness, since it was assembled from linear elements. Thus if the models have the same plane geometry and restraint, then their stiffness matrices are related as follows

$$\frac{1}{E_2 h_2} [K]_2 = \frac{1}{E_1 h_1} [K]_1 \qquad \text{or} \qquad [K]_2 = \frac{E_2 h_2}{E_1 h_1} [K]_1 = \propto [K]_1 \qquad (6)$$

If the node point loads are proportional, then

$$\{F\}_2 = \beta \{F\}_1 \qquad (7)$$

The solution for the second model is

$$\{\delta\}_2 = [K]_2^{-1} \{F\}_2 \qquad (8)$$

and (6) shows that

$$[K]_2^{-1} = \frac{1}{\propto} [K]_1^{-1} \qquad (9)$$

Substituting (9) and (7) into (8) gives

$$\{\delta\}_2 = \frac{\beta}{\propto} \{\delta\}_1 \qquad (10)$$

Equations 4 show that stress intensity factors for each model are proportional to Young's modulus and generalized displacements. Combining this with (10) gives

$$\begin{Bmatrix} K_I \\ K_{II} \end{Bmatrix}_2 = \frac{E_2}{E_1} \frac{\beta}{\propto} \begin{Bmatrix} K_I \\ K_{II} \end{Bmatrix}_1 = \frac{h_1}{h_2} \beta \begin{Bmatrix} K_I \\ K_{II} \end{Bmatrix}_1 \qquad (11)$$

Thus, stress intensity factors for all test specimens may be obtained by scaling results from a single model. In scaling, Young's modulus, specimen thickness and loads

are scaled. All other features must be equal. These include plane geometry (specimen including flaw length), Poisson's ratio, and type of plane analysis (plane stress or plane strain).

Scaling relationships for stresses and strains throughout the specimen may be developed. Strains are proportional to node point displacements and stresses are linear in Young's modulus and strains. Combining these with (10) gives

$$\{\epsilon\}_2 = \frac{E_1 h_1}{E_2 h_2} \beta \{\epsilon\}_1$$

$$\{\sigma\}_2 = \frac{h_1}{h_2} \beta \{\sigma\}_1$$

(12)

III. SYMMETRY AND SUPERPOSITION

Both the straight crack and branched crack configurations (Figure 1) have two axes of symmetry along the diagonals of the specimens. Thus only one-fourth of the specimens need be modeled. Results for the remaining three-fourths of the specimens are obtained from symmetry relationships and results computed in the quarter model. These symmetry relationships are developed in this section.

Figure 2 shows the coordinate system. $P(r,\theta)$ is a generic point and $P^1(r,\theta+\pi)$ is its image point. The structure is periodic in the angular coordinate θ with period π. If the loading is also periodic, then the response will be periodic.

$$\mathcal{U}_r(r,\theta+\pi) = \mathcal{U}_r(r,\theta)$$

$$\mathcal{U}_\theta(r,\theta+\pi) = \mathcal{U}_\theta(r,\theta)$$

(13)

This reduces the modeling required by $\frac{1}{2}$.

Grip Plates

Specimen

(a) Straight Crack

(b) Branched Crack
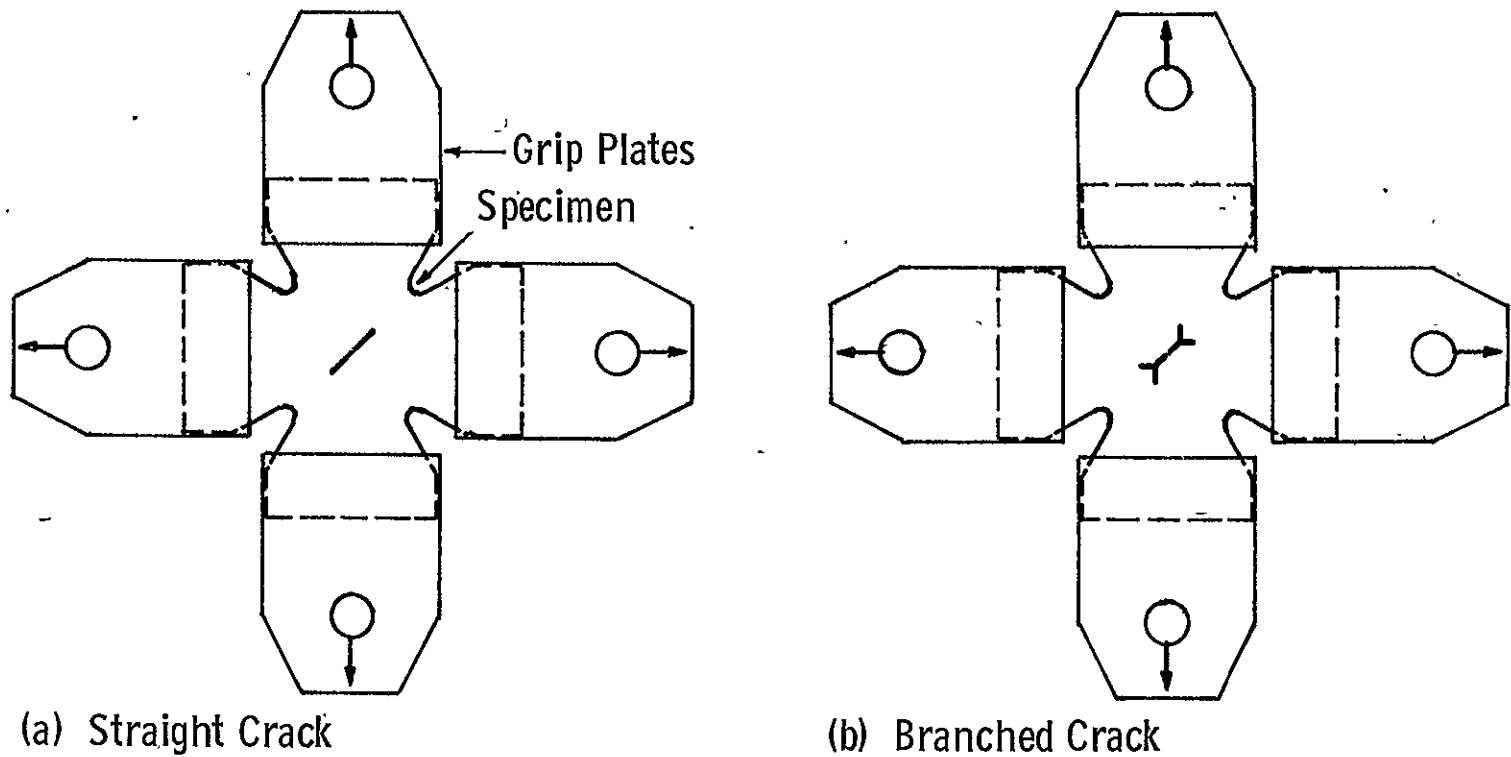
Figure A-1. — Test specimens.
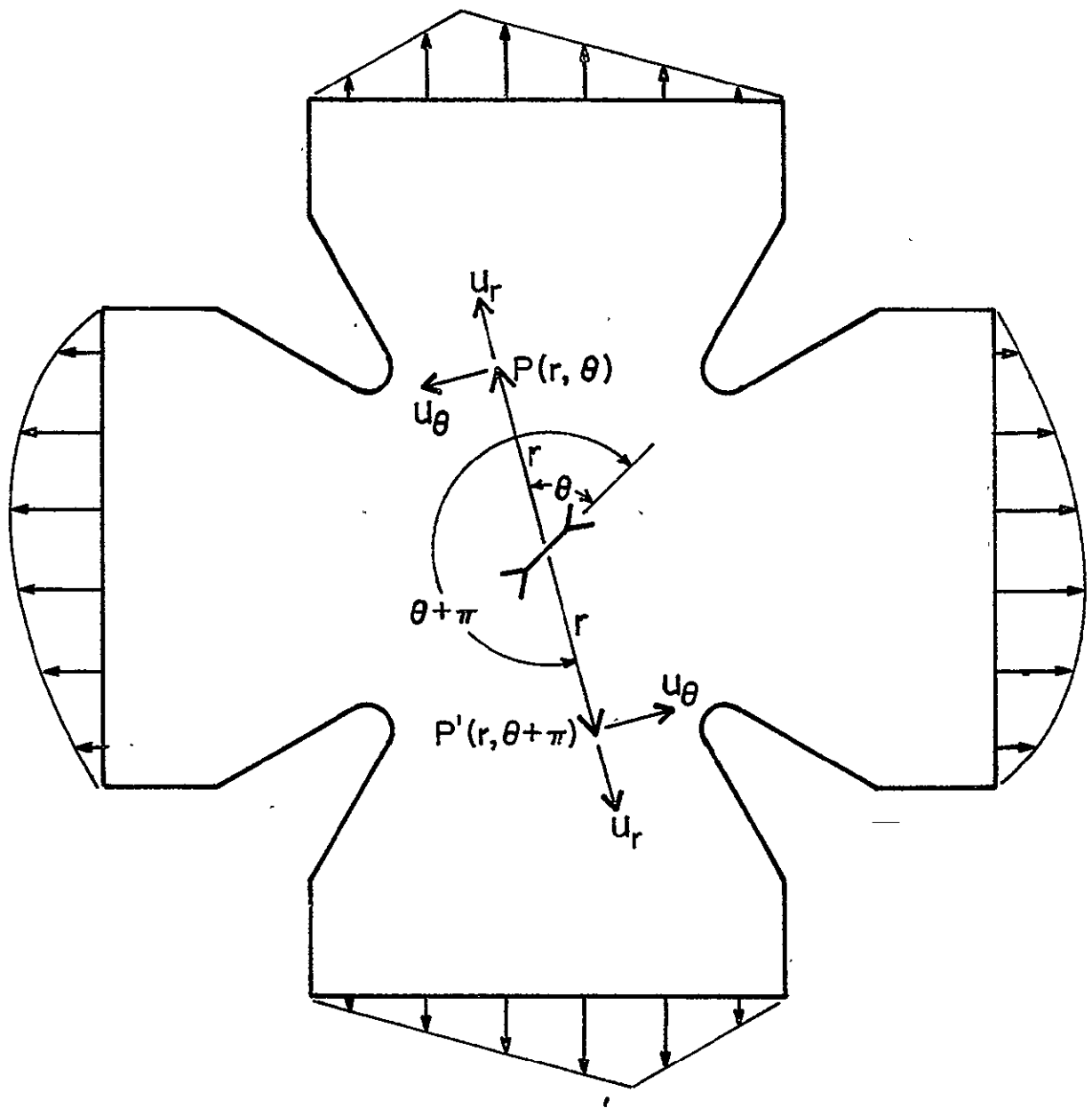
Figure A-2. — Polar coordinate system.

The structure is also symmetric about the line $\theta = 0, \pi$. Thus for symmetric loads, the response will be symmetric and for antisymmetric loads, it will be antisymmetric. Now any periodic loading can be decomposed into its symmetric and antisymmetric parts as shown in Figure 3. These two cases, symmetric and antisymmetric, may be treated separately and the results superposed since the analysis is linear in loadings. This provides another ½ reduction in the modeling. However, two different sets of boundary conditions on the quarter model must be treated corresponding to the symmetric and antisymmetric modes of deformation. Development of the required symmetry/antisymmetry relationships and boundary conditions is facilitated by considering several special load cases as follows.

For the first case consider the loading as shown in Figure 4 and denote this as case "a". Let $Q(r, -\theta)$ denote the image of $P(r, \theta)$ with respect to the line $\theta = 0$ and assume the displacements to be positive as shown. Now consider a load case obtained by folding case "a" along the line $\theta = 0, \pi$, as shown in Figure 5, and denote it case "b". Since the structure is symmetric with respect to this line, the displacements for case "b" are those of case "a" folded about the line as shown. Thus

$$\mu_r(P)_b = \mu_r(Q)_a \qquad \mu_\theta(P)_b = -\mu_\theta(Q)_a$$
$$\mu_r(Q)_b = \mu_r(P)_a \qquad \mu_\theta(Q)_b = -\mu_\theta(P)_a \qquad (14)$$

The third case is the superposition of cases "a" and "b" as shown in Figure 6. Displacements for this case are obtained by superimposing those of cases "a" and "b", thus,

| General | | Symmetric | | Antisymmetric |
| Loading | | Component | | Component |
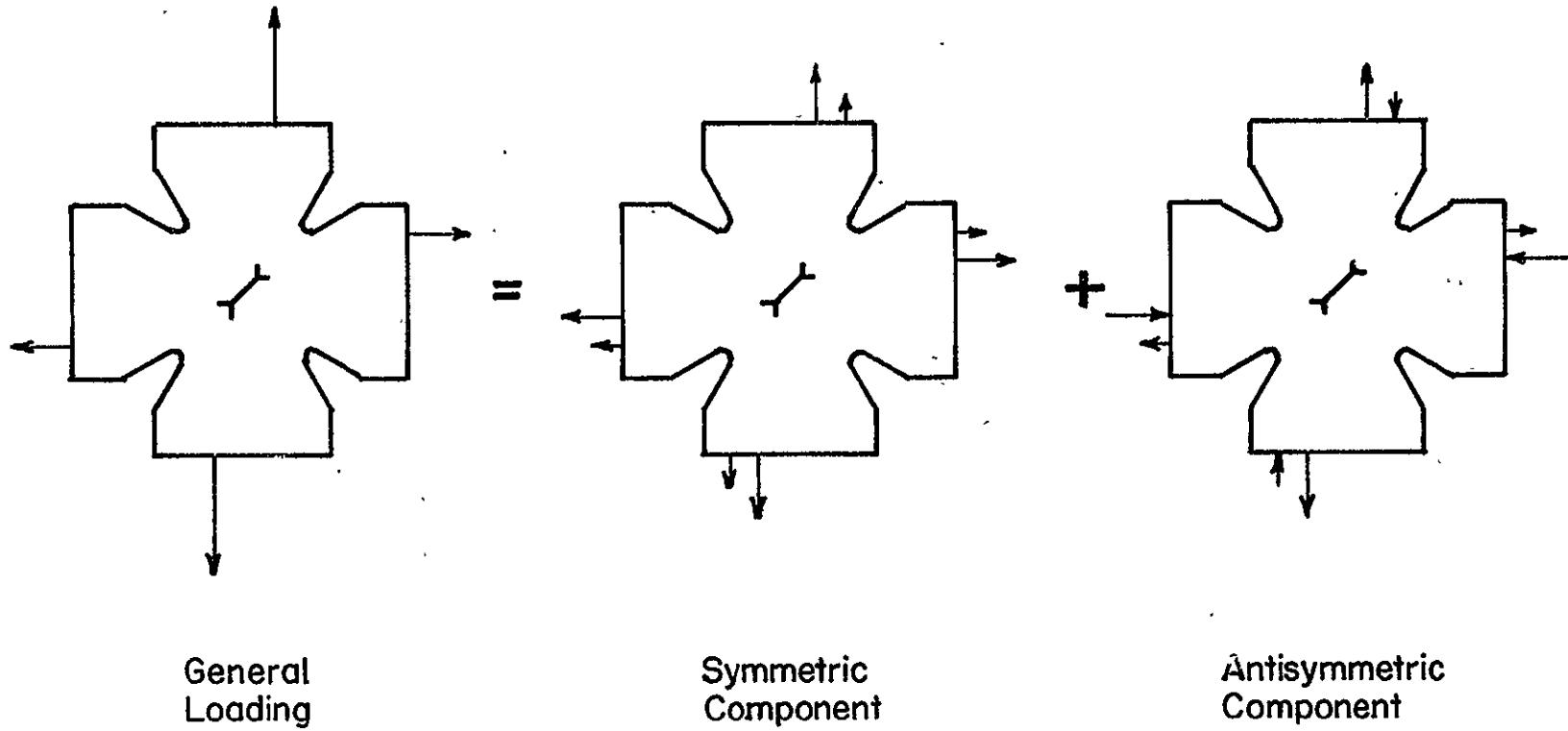
Figure A-3. — Decomposition of loads.
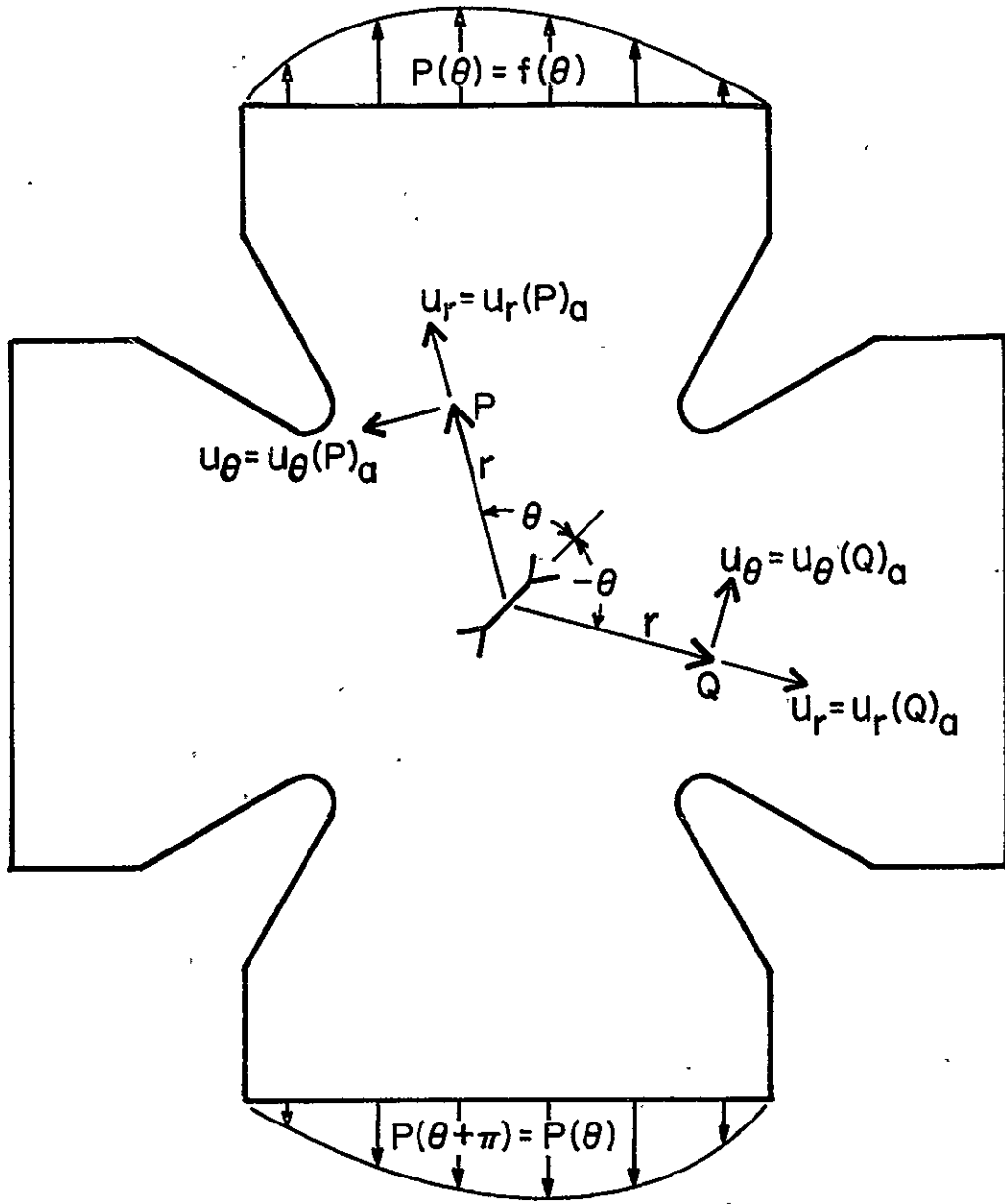
Figure A-4. — Load case a.
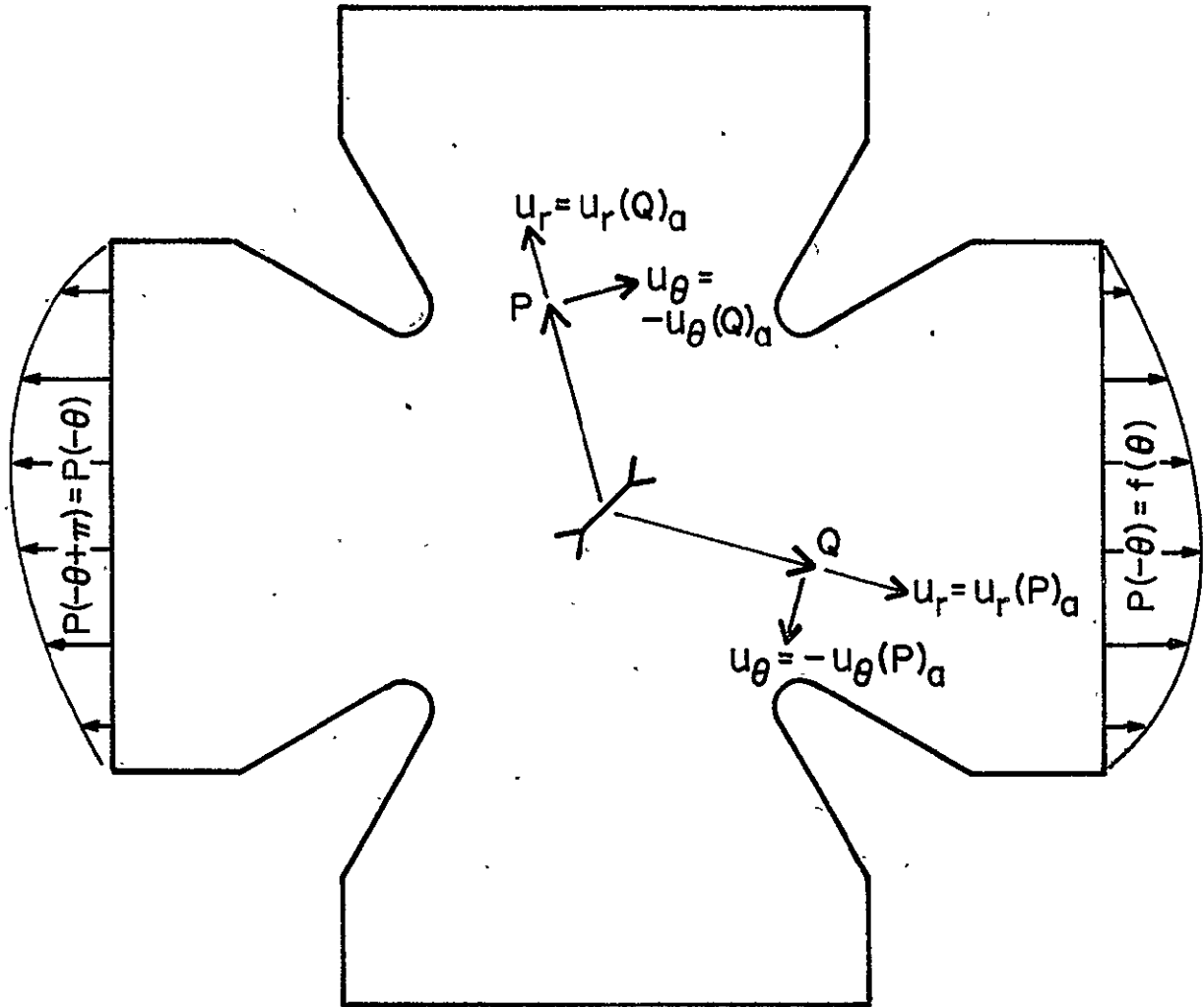
Figure A-5. — Load case b.
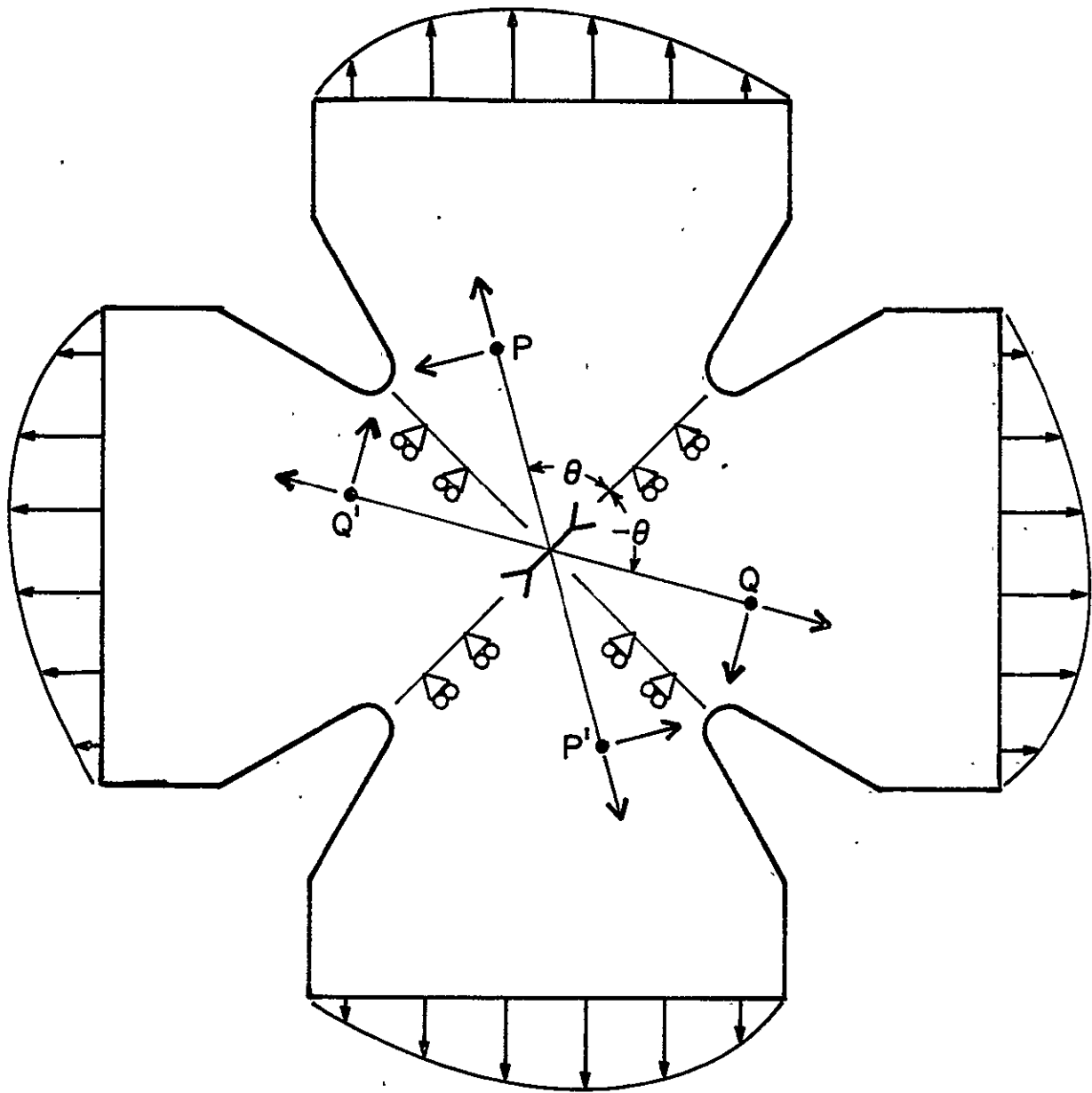
Figure A-6. – Load case a + b.

$$U_r^{(P)}{}_{a+b} = U_r^{(P)}{}_a + U_r^{(P)}{}_b$$

$$U_r^{(Q)}{}_{a+b} = U_r^{(Q)}{}_a + U_r^{(Q)}{}_b$$

$$U_\theta^{(P)}{}_{a+b} = U_\theta^{(P)}{}_a + U_\theta^{(P)}{}_b \tag{15}$$

$$U_\theta^{(Q)}{}_{a+b} = U_\theta^{(Q)}{}_a + U_\theta^{(Q)}{}_b$$

Substituting (14) into (15) gives

$$U_r^{(P)}{}_{a+b} = U_r^{(P)}{}_a + U_r^{(Q)}{}_a$$

$$U_r^{(Q)}{}_{a+b} = U_r^{(Q)}{}_a + U_r^{(P)}{}_a$$

$$U_\theta^{(P)}{}_{a+b} = U_\theta^{(P)}{}_a - U_\theta^{(Q)}{}_a \tag{16}$$

$$U_\theta^{(Q)}{}_{a+b} = U_\theta^{(Q)}{}_a - U_\theta^{(P)}{}_a$$

Equations 15 show that

$$U_r^{(Q)}{}_{a+b} = U_r^{(P)}{}_{a+b}$$

$$U_\theta^{(Q)}{}_{a+b} = -U_\theta^{(P)}{}_{a+b} \tag{17}$$

as is shown in Figure 6. Substitution of (13) into (17) gives

$$U_r^{(Q^1)}{}_{a+b} = U_r^{(P^1)}{}_{a+b}$$

$$U_\theta^{(Q^1)}{}_{a+b} = -U_\theta^{(P^1)}{}_{a+b} \tag{18}$$

as shown. Now $P(r,\theta)$ is a generic point and the other points, P^1, Q and Q', are images. Thus letting $\theta=0$ in (17) and (18) defines conditions along the line $\theta=0, \pi$. Similarily, setting $\theta = \pi/2$ defines conditions along $\theta = \pi/2, -\pi/2$ as shown in Figure 6. For the straight crack configuration, this loading gives pure opening stress intensity (K_I). In the branched crack configuration, both modes K_I and K_{II} are present, with their proportion dependent on branching angle and length.

The final load case is the superposition of case "a" with the negative of case "b" as shown in Figure 7. Thus superimposing displacements of case "a" with the negative of case "b" gives

$$U_r^{(P)}{}_{a-b} = U_r^{(P)}{}_a - U_r^{(P)}{}_b$$

$$U_r^{(Q)}{}_{a-b} = U_r^{(Q)}{}_a - U_r^{(Q)}{}_b$$

$$U_\theta^{(P)}{}_{a-b} = U_\theta^{(P)}{}_a - U_\theta^{(P)}{}_b \tag{19}$$

$$U_\theta^{(Q)}{}_{a-b} = U_\theta^{(Q)}{}_a - U_\theta^{(Q)}{}_b$$

Substituting (14) into (19) gives

$$U_r^{(P)}{}_{a-b} = U_r^{(P)}{}_a - U_r^{(Q)}{}_a$$

$$U_r^{(Q)}{}_{a-b} = U_r^{(Q)}{}_a - U_r^{(P)}{}_a$$

$$U_\theta^{(P)}{}_{a-b} = U_\theta^{(P)}{}_a + U_\theta^{(Q)}{}_a \tag{20}$$

$$U_\theta^{(Q)}{}_{a-b} = U_\theta^{(Q)}{}_a + U_\theta^{(P)}{}_a$$

Comparing equations 20 shows that

$$U_r^{(Q)}{}_{a-b} = -U_r^{(P)}{}_{a-b}$$

$$U_\theta^{(Q)}{}_{a-b} = U_\theta^{(P)}{}_{a-b} \tag{21}$$

as shown in Figure 7. Setting $\theta = 0$ and $\pi/2$ give conditions along the diagonals as shown. For the straight crack configuration, this loading gives pure shearing stress intensity (K_{II}). The branched crack gives a mixed mode $(K_I$ and $K_{II})$ with different proportion than the previous case, in general.

126
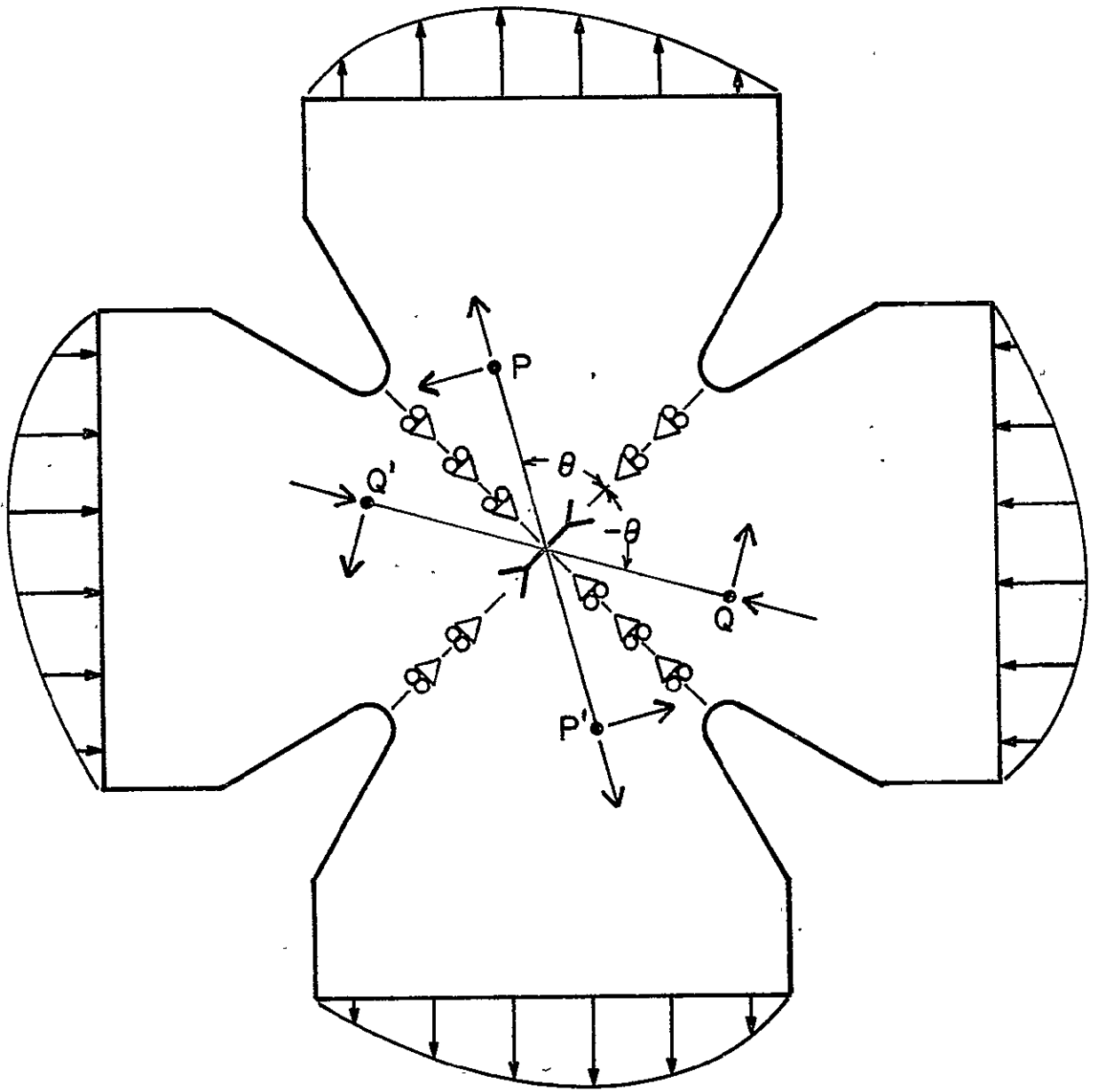
Figure A-7. - Load case a - b.

Thus a ¼ model of the specimen along with superposition and scaling will

provide answers for the complete specimen, all thicknesses and Young's moduli,

under any load combination.

Now consider the question of rigid body motion and restraint. In the pre-

ceeding discussion, it was implicitly assumed that no rigid body motion was

present. Three rigid body modes are possible in a plane problem; two translations

and a rotation. For the case "a + b", sufficient restraint is provided by the

symmetry conditions to prevent all three rigid body motions as is shown in

Figure 6. In the case "a - b" symmetry conditions prevent both translations but a

rigid body rotation about the origin would be possible as shown in Figure 7. This

rotation may be prevented by restraining an additional node point or within the

crack tip element as it contains all three rigid body modes explicitly. In this

study a uniform displacement was imposed at the interface with the grip plates,

thus restraining all rigid body modes.

The final item to be discussed in this section is the relationship of stresses,

strains, and stress intensities in the remaining three-fourths of the specimen to those

in the quarter model. In order to avoid confusion, assume that the upper quarter of

the specimen, $0 \leq \theta \leq \pi/2$, has been modeled and the two sets of boundary conditions,

corresponding to the fundamental cases "a + b" and "a - b", analyzed. Thus all answers

will be given explicitly for the first quadrant.

In the following, it is convenient to use a cartesian coordinate system as shown

in Figure 8. Displacements in this system are related to those in the polar system via

$$\mathcal{U}_r = \mathcal{U}_x \cos \theta + \mathcal{U}_y \sin \theta$$
$$\mathcal{U}_\theta = \mathcal{U}_y \cos \theta - \mathcal{U}_x \sin \theta$$

(22)

128
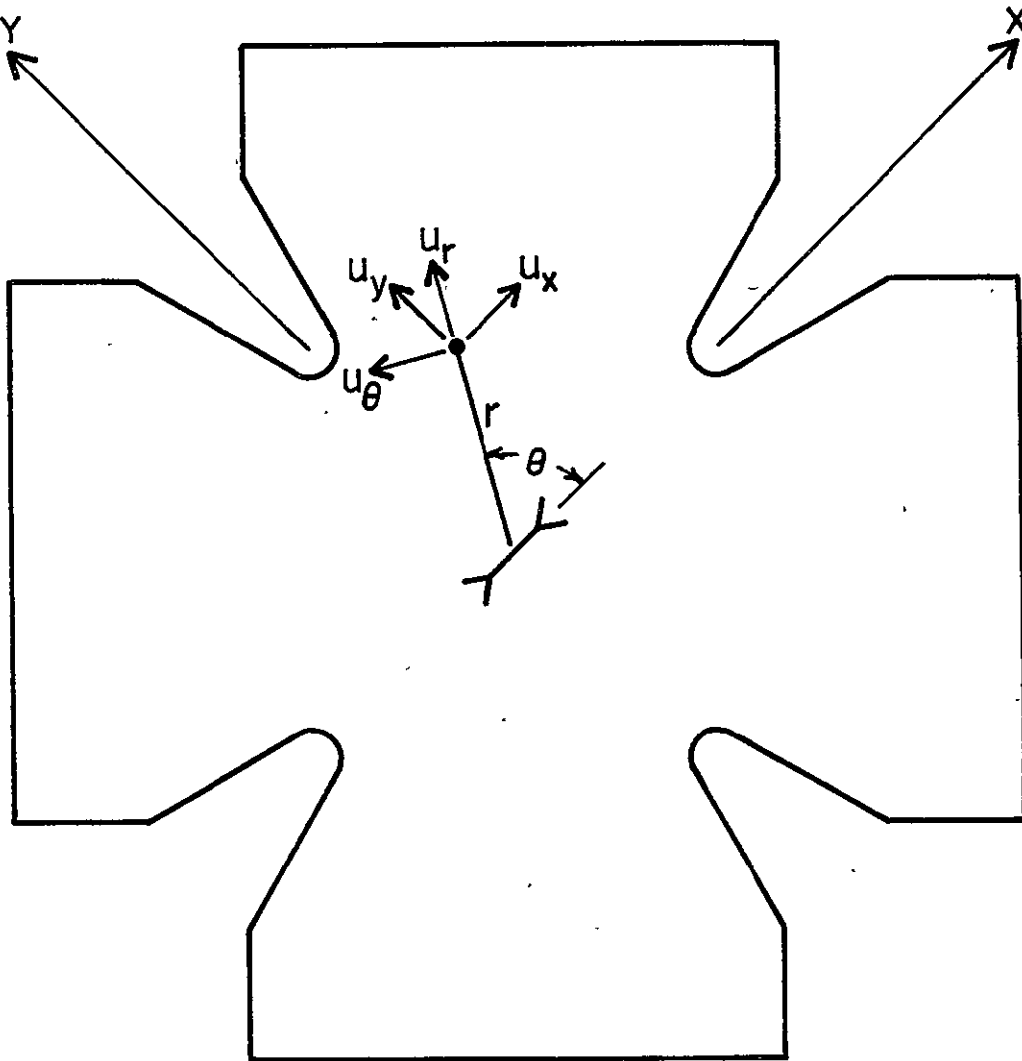
Figure A-8. — Cartesian coordinate system.

Applying these transformations to equations 13 shows that

$$\mathcal{U}_x(r, \theta + \pi) = -\mathcal{U}_x(r, \theta) \tag{23}$$

$$\mathcal{U}_y(r, \theta + \pi) = -\mathcal{U}_y(r, \theta)$$

If one now introduces a second cartesian system that is rotated by π from the first then the displacements of the two points in their own systems are equal. Thus stresses and strains are also equal. Now stresses and strains are second order tensors and the transformation associated with the π rotation, or inversion of axes, is an identity transformation, thus stresses and strains are equal when expressed in either system.

$$\in_{xx}(r, \theta + \pi) = \in_{xx}(r, \theta)$$

$$\in_{yy}(r, \theta + \pi) = \in_{yy}(r, \theta)$$

$$\in_{xy}(r, \theta + \pi) = \in_{xy}(r, \theta)$$

$$\tag{24}$$

$$\sigma_{xx}(r, \theta + \pi) = \sigma_{xx}(r, \theta)$$

$$\sigma_{yy}(r, \theta + \pi) = \sigma_{yy}(r, \theta)$$

$$\sigma_{xy}(r, \theta + \pi) = \sigma_{xy}(r, \theta)$$

Since stresses are equal, stress intensities are necessarily equal also

$$K_i(r, \theta + \pi) = K_i(r, \theta) \tag{25}$$

These results may be expressed with the point designations used earlier as

$$\begin{aligned} \{\in(P^1)\} &= \{\in(P)\} & \{\in(Q^1)\} &= \{\in(Q)\} \\ \{\sigma(P^1)\} &= \{\sigma(P)\} & \{\sigma(Q^1)\} &= \{\sigma(Q)\} \\ \{K(P^1)\} &= \{K(P)\} & \{K(Q^1)\} &= \{K(Q)\} \end{aligned} \tag{26}$$

where $\{\in(P)\}$ denotes the column vector of strains evaluated at point "P", etc.

Thus the response in quadrants 2 and 3 is identical to that in 4 and 1 respectively for all loadings and they (2 and 3) need no further discussion.

In considering quadrants 1 and 4, it is necessary to treat the two fundamental load cases separately. Consider the case "a + b" first. Transforming equations 17 via equations 22 shows that

$$
\begin{aligned}
\mathcal{U}_x(Q)_{a+b} &= \mathcal{U}_x(P)_{a+b} \\
\mathcal{U}_y(Q)_{a+b} &= -\mathcal{U}_y(P)_{a+b}
\end{aligned}
\tag{27}
$$

Hence a second cartesian system obtained by inverting the "y" axis in the reference system will render the points equal in their individual systems. The tensor transformation between this pair of coordinate systems produces a sign change on shearing terms, thus

$$
\left\{ \begin{array}{c} \epsilon_{xx}(Q) \\ \epsilon_{yy}(Q) \\ \epsilon_{xy}(Q) \end{array} \right\}_{a+b}
=
\begin{bmatrix} 1 & 0 & 0 \\ 0 & 1 & 0 \\ 0 & 0 & -1 \end{bmatrix}
\left\{ \begin{array}{c} \epsilon_{xx}(P) \\ \epsilon_{yy}(P) \\ \epsilon_{xy}(P) \end{array} \right\}_{a+b}
\tag{28}
$$

and the same relationship is applicable for stresses. Now K_I and K_{II} are related to normal and shearing stresses respectively, thus

$$
\left\{ \begin{array}{c} K_I(Q) \\ K_{II}(Q) \end{array} \right\}_{a+b}
=
\begin{bmatrix} 1 & 0 \\ 0 & -1 \end{bmatrix}
\left\{ \begin{array}{c} K_I(P) \\ K_{II}(P) \end{array} \right\}_{a+b}
\tag{29}
$$

For the case "a - b" transforming equations 21 gives.

$$
\begin{aligned}
\mathcal{U}_x(Q)_{a-b} &= -\mathcal{U}_x(P)_{a-b} \\
\mathcal{U}_y(Q)_{a-b} &= \mathcal{U}_y(P)_{a-b}
\end{aligned}
\tag{30}
$$

hence inversion of the "x" axis will make the points equal in their own system. The transformation between these two systems changes the sign of normal stresses, thus

$$
\begin{Bmatrix} \epsilon_{xx}(Q) \\ \epsilon_{yy}(Q) \\ \epsilon_{xy}(Q) \end{Bmatrix}_{a-b} = \begin{bmatrix} -1 & 0 & 0 \\ 0 & -1 & 0 \\ 0 & 0 & 1 \end{bmatrix} \begin{Bmatrix} \epsilon_{xx}(P) \\ \epsilon_{yy}(P) \\ \epsilon_{xy}(P) \end{Bmatrix}_{a-b}
$$

(31)

and

$$
\begin{Bmatrix} K_I(Q) \\ K_{II}(Q) \end{Bmatrix}_{a-b} = \begin{bmatrix} -1 & 0 \\ 0 & 1 \end{bmatrix} \begin{Bmatrix} K_I(P) \\ K_{II}(P) \end{Bmatrix}_{a-b}
$$

(32)

IV. TYPICAL FINITE ELEMENT MODELS

Figures 9 and 10 show typical finite element models for the straight and branched crack configurations. In both specimen configurations, the region $0 \leq \theta \leq \pi/2$ was chosen for modeling. The center of the crack is located at the origin. In Figure 9 the crack extends to the center of the semicircle. In Figure 10 it follows the "x" axis to the point shown and then follows a straight path to the center of the circle. The semicircular and circular regions are those occupied by the special crack tip elements. Half an element is used in the straight crack quarter model since the specimen is symmetric. Constant strain triangular elements were used in modeling the remaining region with small elements near the corner cuts for stress concentrations.

A uniform displacement was applied at locations corresponding to the bolt holes to simulate rigid grip plates. Loads required to produce these displacements were determined from the analysis and used in normalizing results. Several different models were analyzed to investigate the effects of flow length and branching angle.

ANGLES THI = -90.00 DEGREES TH2 = -45.00 DEGREES TH3 = -90.00 DEGREES
PLOT NO. 1
BIAXIAL IRON CROSS TEST
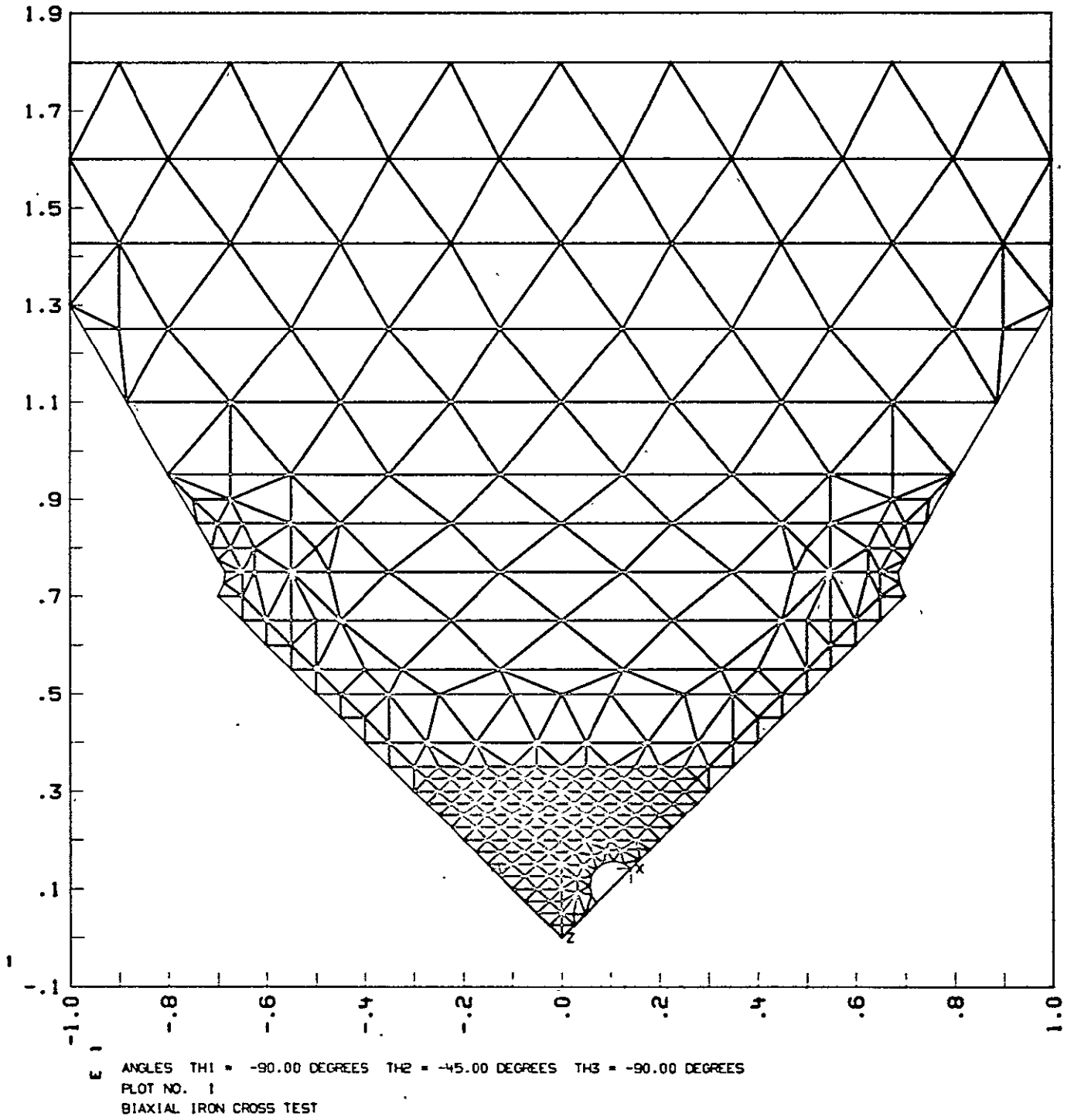
Figure A-9. — Typical finite-element model, straight crack.

ANGLES TH1 = 90.00 DEGREES TH2 = 90.00 DEGREES TH3 = 90.00 DEGREES
PLOT NO. 1
BIAXIAL IRON CROSS TEST
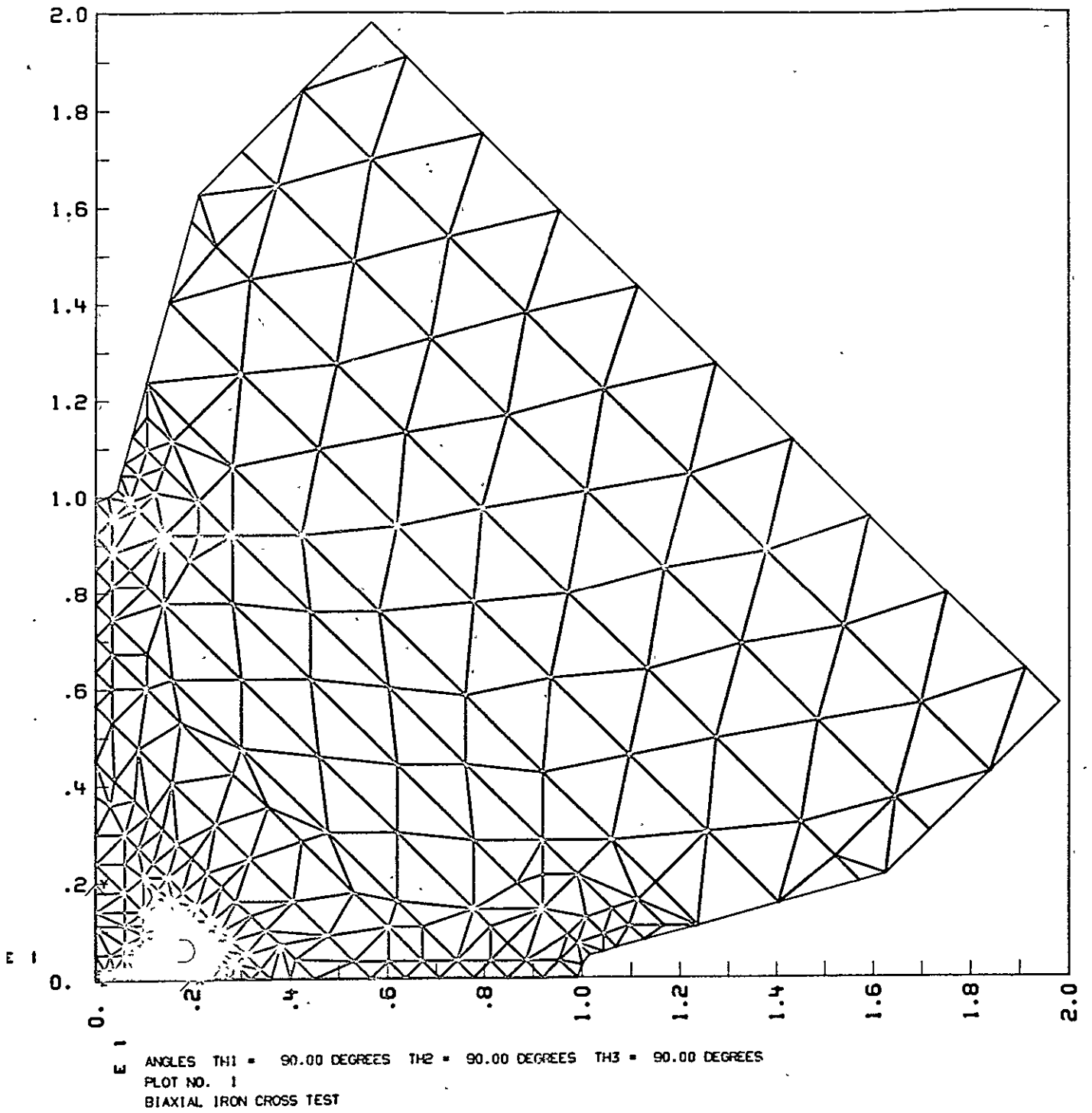
Figure A-10. – Typical finite-element model, branched crack.

V. NUMERICAL RESULTS

Normalized stress intensity factors and crack center displacements are shown in Figures 11-14. All calculations are for the case of plane strain ($\tilde{\nu} = \nu$) and $\tilde{\nu} = .33$ throughout. Normalized values were obtained by dividing the computed results by the corresponding value for an infinite plate in plane strain with a crack oriented at 45° from the applied loads and under the appropriate bi-axial loading ($a + b$ or $a - b$). For the branched crack cases the crack length used in normalizing was the sum of lengths as shown below.

$$a = a_1 + a_2$$
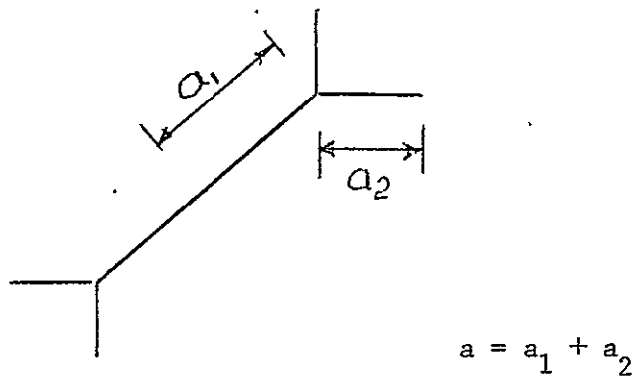
In referring to crack length, no dimensions are used. Any consistent dimensional system may be used throughout and the results will be applicable if the proportions of crack length to overall specimen geometry are maintained. For example, a crack length of two ($2a = 2$, $a = 1$) is applicable for a crack length equal to 1/10 of the grip plate width, which is shown to be twenty in Figure 9. The overall specimen geometry shown in Figures 9 and 10 was maintained throughout and the crack geometry varied.
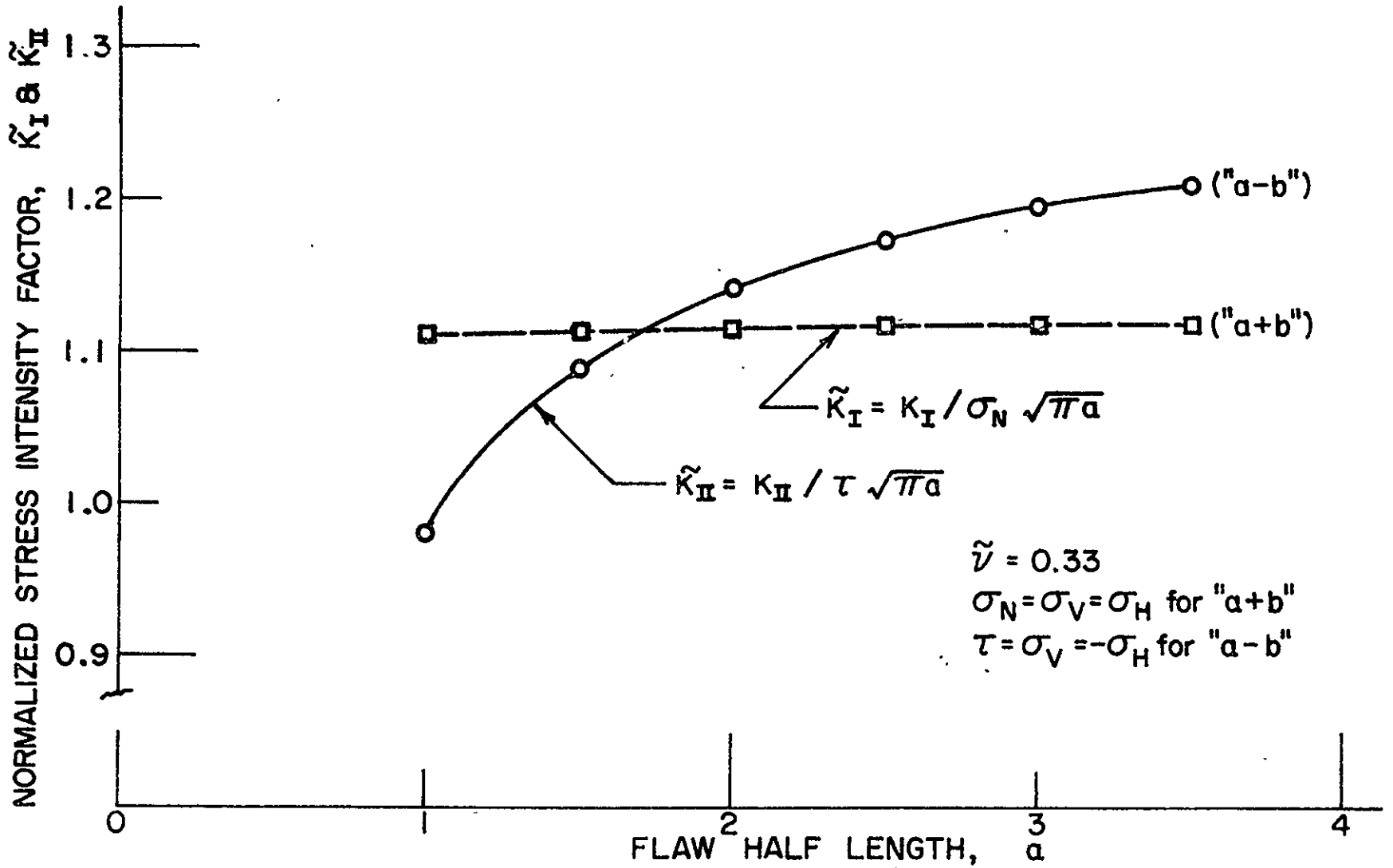
Figure A-11. – K_I and K_{II} for straight cracks.
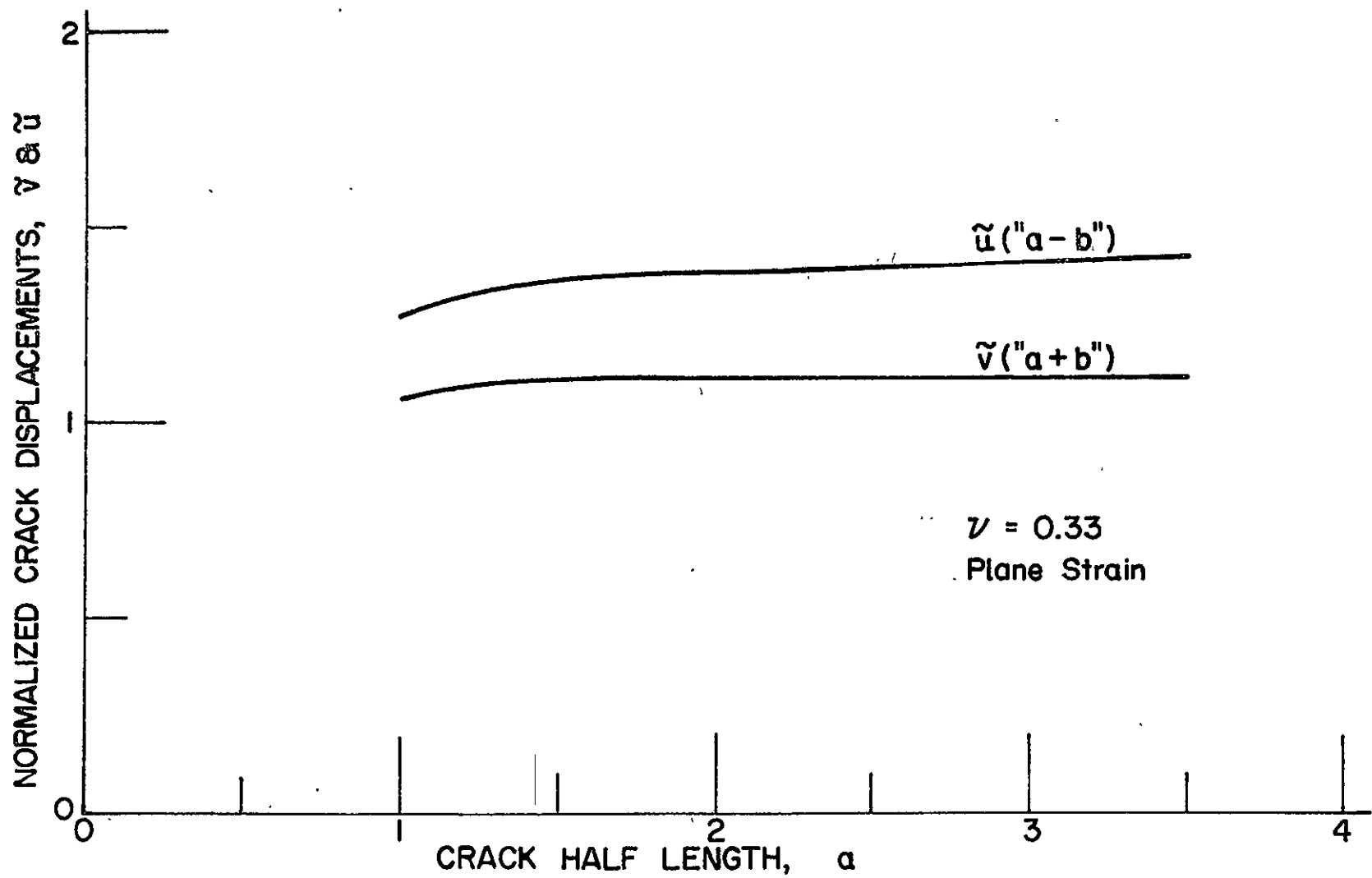
Figure A-12. — Crack displacements for straight cracks.
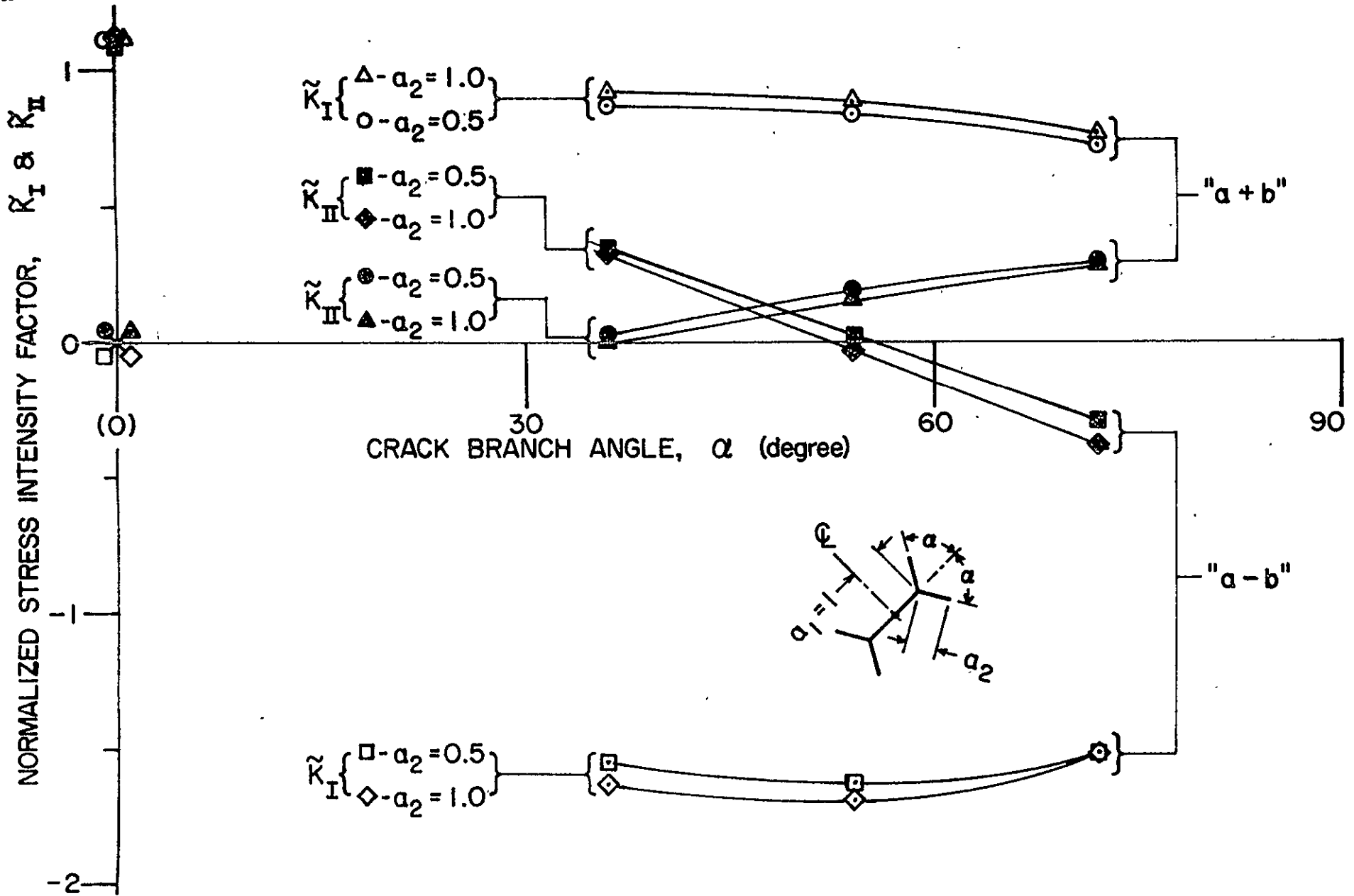
Figure A-13. – K_I and K_{II} for branched cracks.
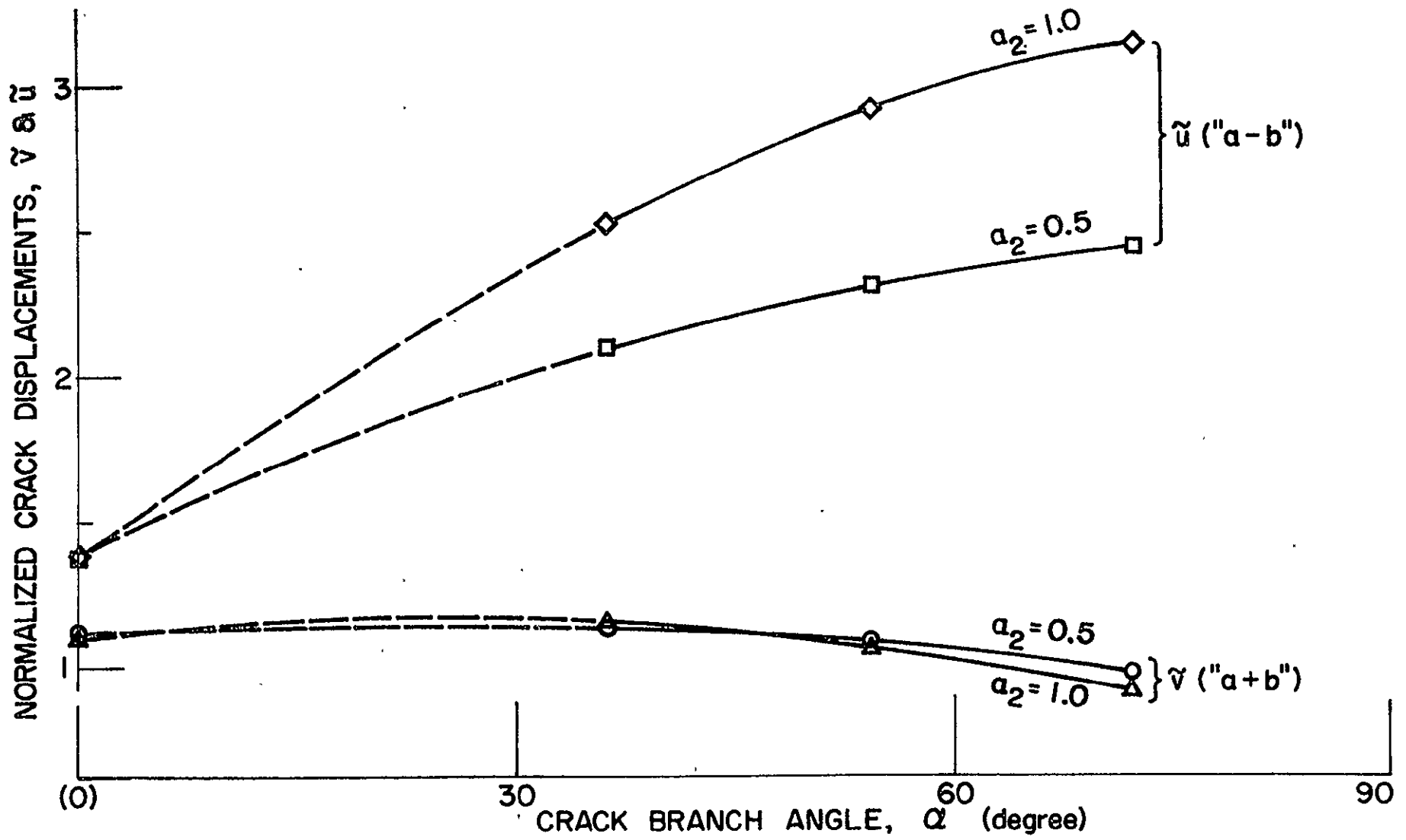
Figure A-14. – Crack displacements for branched cracks.

Stress intensity factors vs. flaw length for the straight crack are shown in Figure 11. For this configuration, the "a + b" load case produced pure K_I and crack opening. The "a - b" case gives pure K_{II} and crack shearing. It should be noted that "a + b" is hydrostatic tension and "a - b" is pure shear in the 45° orientation. This figure shows that K_I is essentially constant over the range considered and that K_{II} increases with increasing flaw length. Combining the scaling relationships discussed earlier with superposition and normalization leads to the following equations for stress intensities of straight cracks under any load combination,

$$K_I = \tfrac{1}{2}(\sigma_V + \sigma_H)\sqrt{\pi a}\ \ \widetilde{K}_1$$

$$K_{II} = \tfrac{1}{2}(\sigma_V - \sigma_H)\sqrt{\pi a}\ \ \widetilde{K}_{II}$$

(33)

where $\widetilde{K}_I$ and $\widetilde{K}_{II}$ are given by Figure 11 and σ_V, σ_H are average vertical and horizontal applied stresses associated with an uniform displacement of the grip plates.

Corresponding crack displacements are shown in Figure 12. They are also normalized to plane strain infinite plate values with $\nu = .33$. The displacements shown are for a point at the center of the crack and on the upper face; $r = 0^+$ and $\Theta = \pi/2$ in Figure 2 or $x = 0$ and $y = 0^+$ in Figure 8. $\widetilde{u}$ and $\widetilde{v}$ are normalized shearing and opening displacements respectively. These curves show that the normalized displacements increase slightly with increasing crack length. Crack opening displacements (COD) and crack shearing displacements (CSD) are twice these values as shown in the sketch below.
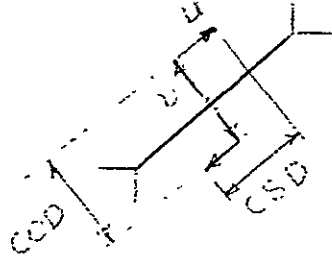
From superposition, symmetry, scaling and normalization, it follows that

$$COD = \frac{2(1-\nu^2)a}{E} (\sigma_V + \sigma_H) \tilde{v}$$

$$CSD = \frac{2(1-\nu^2)a}{E} (\sigma_V - \sigma_H) \tilde{u}$$

(34)

Similar results for the branched crack are shown in Figures 13 and 14. These results were also normalized to infinite plate values with the total crack length ($a = a_1 + a_2$) and main crack orientation (45° from applied loads). A single main crack length was investigated ($a_1 = 1$) with two branch lengths ($a_2 = .5$, 1) and three angles ($\alpha = 36^\circ$, 54°, 72°).

These curves show several interesting features. Both modes, K_I and K_{II}, are present in both the hydrostatic ("a + b") and shear ("a - b") loadings. Opening stress intensities are significantly larger than shearing intensities and the shear loading produces a large closing intensity. The branch length effect is nearly square root; as accounted for in the normalization. The effect of branch angle (α) is greater on K_{II} than K_I, however the K_{II} is smaller over the range studied. Straight crack results are also shown along the ordinate for reference but these points have not been connected as the two problems are basically different. Consideration of superposition, symmetry, scaling and normalization leads to equations for stress intensities as in the straight crack case. However both branches

141

must be treated here as they have different intensities. Let the branches be

denoted as shown below:
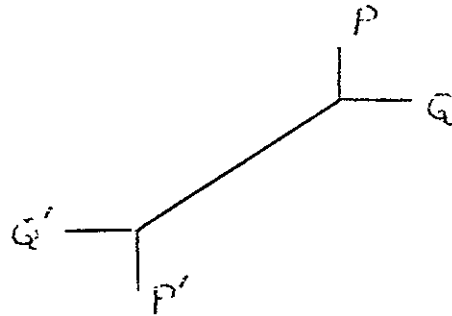
Intensities at P^1 and Q^1 will be equal to those at P and Q respectively, for any

loading, as shown by equation 13. Intensities at P and Q are given by

$$
\begin{Bmatrix} K_{I,P} \\ \hline K_{II,P} \\ \hline K_{I,Q} \\ \hline K_{II,Q} \end{Bmatrix} = \tfrac{1}{2}\sqrt{\pi a}
\left[\begin{array}{c|c|c}
\mathcal{T}_V + \mathcal{T}_H & \mathcal{T}_V - \mathcal{T}_H & \\
\hline
& \mathcal{T}_V + \mathcal{T}_H & \mathcal{T}_V - \mathcal{T}_H \\
\hline
\mathcal{T}_V + \mathcal{T}_H & -(\mathcal{T}_V - \mathcal{T}_H) & \\
\hline
& -(\mathcal{T}_V + \mathcal{T}_H) & \mathcal{T}_V - \mathcal{T}_H
\end{array}\right]
\begin{Bmatrix} K_{I,\,a+b} \\ K_{II,\,a+b} \\ \hline K_{I,\,a-b} \\ K_{II,\,a-b} \end{Bmatrix}
\qquad (35)
$$

were P and Q denote branches, "a + b" and "a - b" denote the basic load cases.

These equations show that the two branches have different intensities for any

general load condition.

Normalized crack displacements for branched cracks are shown in Figure 14. These curves show that opening displacements (V) are approximately equal to infinite plate values but shearing displacements are greater and they increase with increasing branch angle. Equations for COD and CSD are the same as for straight cracks, Equation 34, since the specimen is still symmetric.

These four sets of curves, Figures 11-14, are the main results from this analysis and they are applicable for any load combination, thickness, and Young's modulus. These curves along with Equations 33-35 permit calculation of stress intensity factors and crack displacements. In applying these results, the specimen configuration should be as shown in Figures 9 and 10, and the specimen should be sufficiently thick to produce plane strain with a material having a Poisson's ratio of .33. Several other results from the analysis are interesting and lead to a better understanding of the mixed mode problem.

Figure 15 shows normalized crack displacements for a straight crack under the hydrostatic loading ("a + b"). Computed results were normalized by the infinite plate value at the crack center. The opening center value is slightly greater than an infinite plate and the distribution is ellipsoidal like an infinite plate. Shearing displacements are very small over the entire crack length. Adjacent points on opposing crack faces have equal shearing displacements and equal but opposite opening displacements. Similar results for the shear loading ("a - b") are shown in Figure 16. These results are normalized by the infinite plate displacement parallel to the crack and at its center. In this case, displacements perpendicular to the crack are of the same magnitude as those parallel to the crack.

Adjacent points have the same perpendicular displacement and equal but opposite parallel (shearing) displacements. The shearing displacement distribution is ellipsoidal as is an infinite plate. Displacements for other crack lengths were similar to those shown here.

Crack displacements for a branched crack are shown schematically in Figures 17 and 18. The points labeled "A, B, C" are at the branch juncture. These are distinct points in the finite element model but they all have the same coordinates. Points "D, E" and "F, G" are similar and located where the crack intersects the special element. Crack tips are located at "P, Q" and their displacements are not shown in these figures. Figure 17 shows that the "a + b" loading produces opening of the main crack and both branches. Figure 18 shows sliding in the main crack, opening in the "Q" branch, and closing in the "P" branch. Closing is greatest between the points "A" and "C". This closing is consistent with the negative K_I shown in Figure 13. In the finite element model adjacent points on crack faces have the same coordinates and they are connected only via the elements; there is no direct connection across the crack faces. Thus the analysis permits them to overlap under load as shown on the "P" branch. This is physically impossible (impenetrability of matter), however several other things must be considered before deducing that contact will occur in a test. First the relative porportions of the two basic loadings ("a + b" and "a - b") must be considered for the loading applied (σ_V and σ_H). If opening from the "a + b" component exceeds closing from the "a - b" component then contact will not occur. Secondly, any residual opening such as from residual stresses, plasticity, finite width saw cuts, etc., must be considered as they were not included in the analysis.
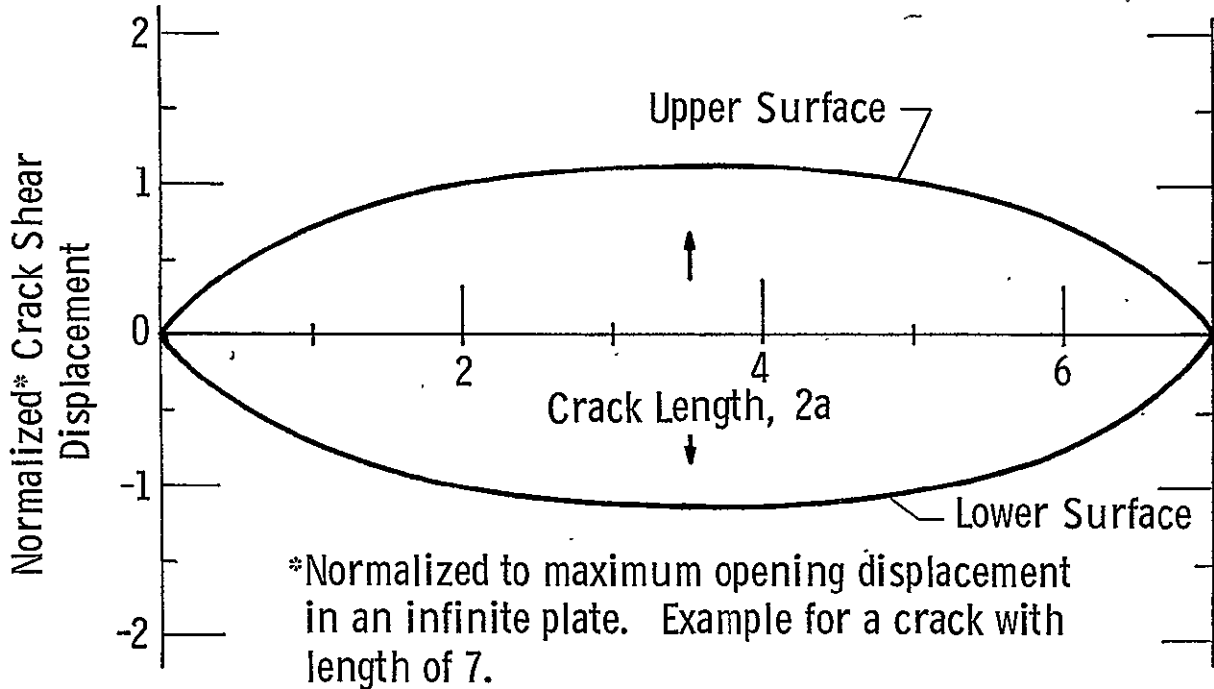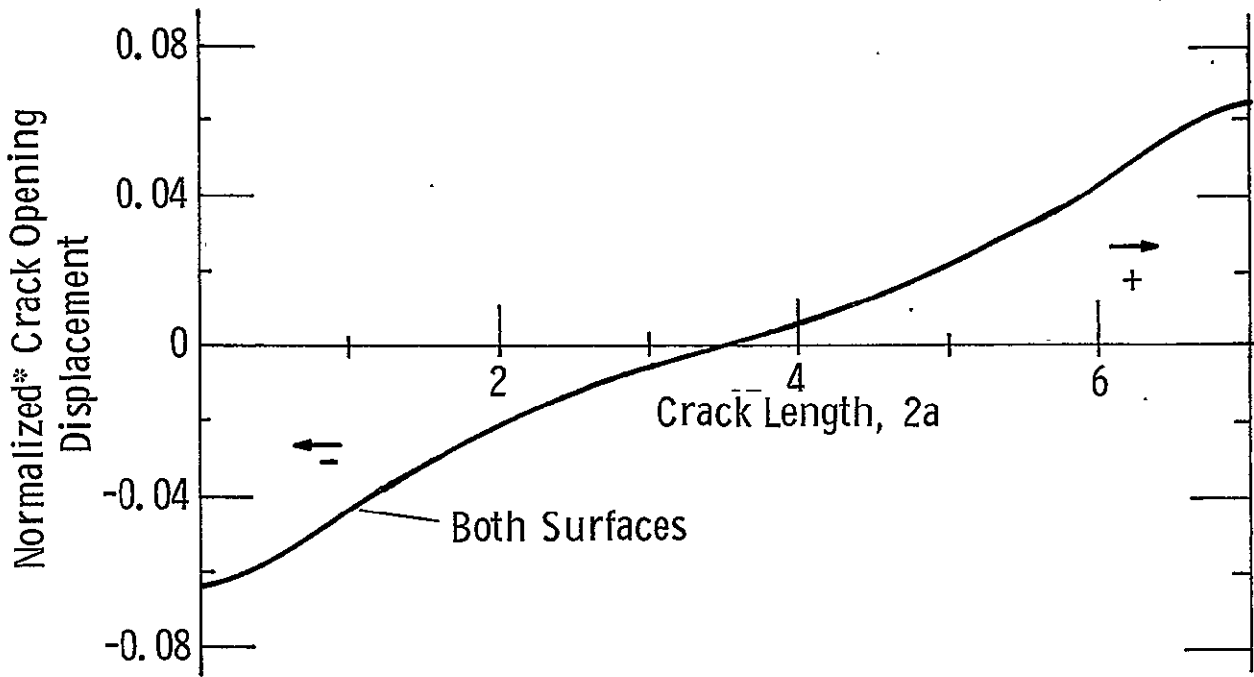
Figure 15   Crack Displacement Distribution For a Straight Crack,
"a + b" Loading
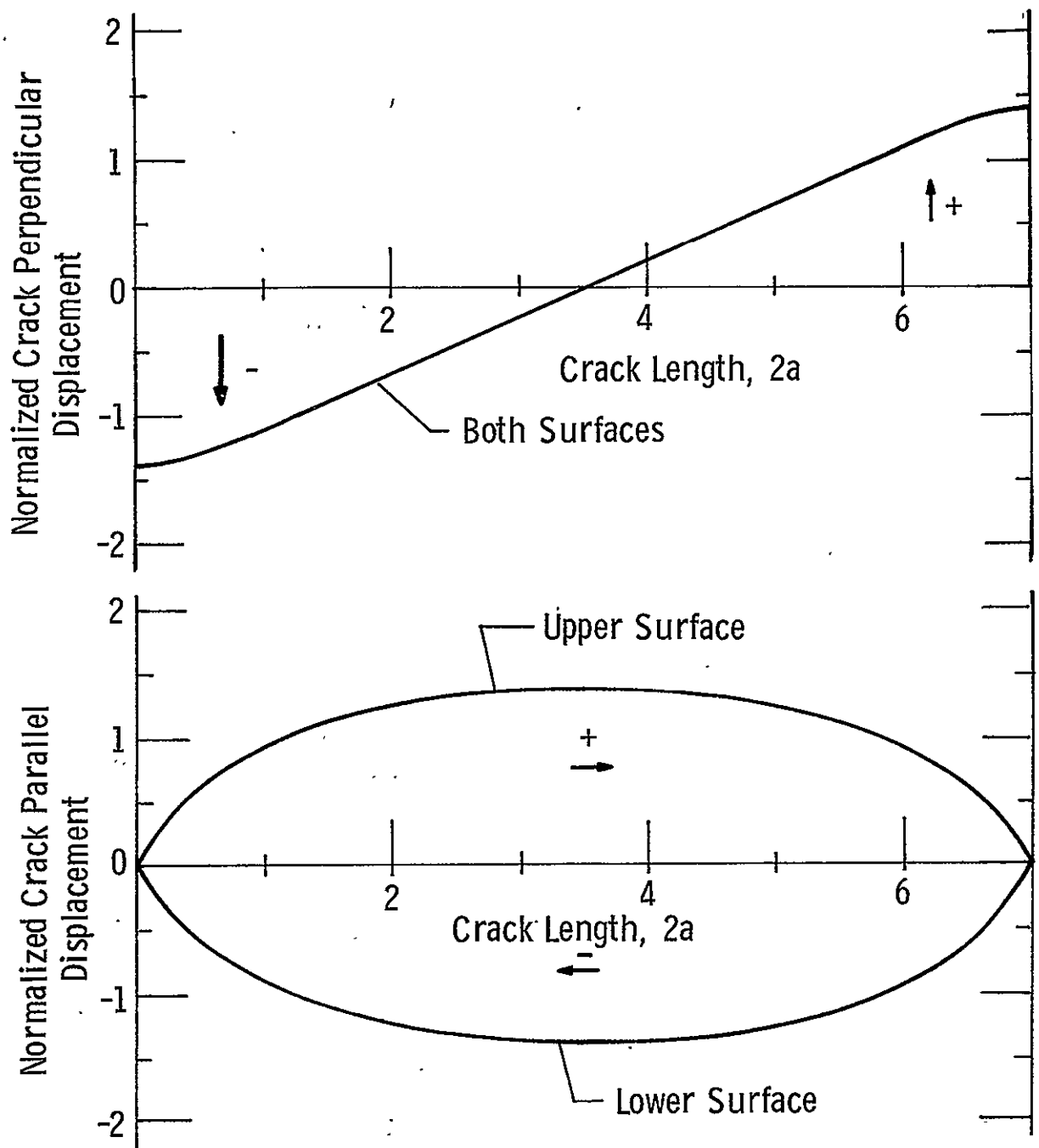
Figure 16   Crack Displacement Distribution For a Straight Crack,
"a → b" Loading
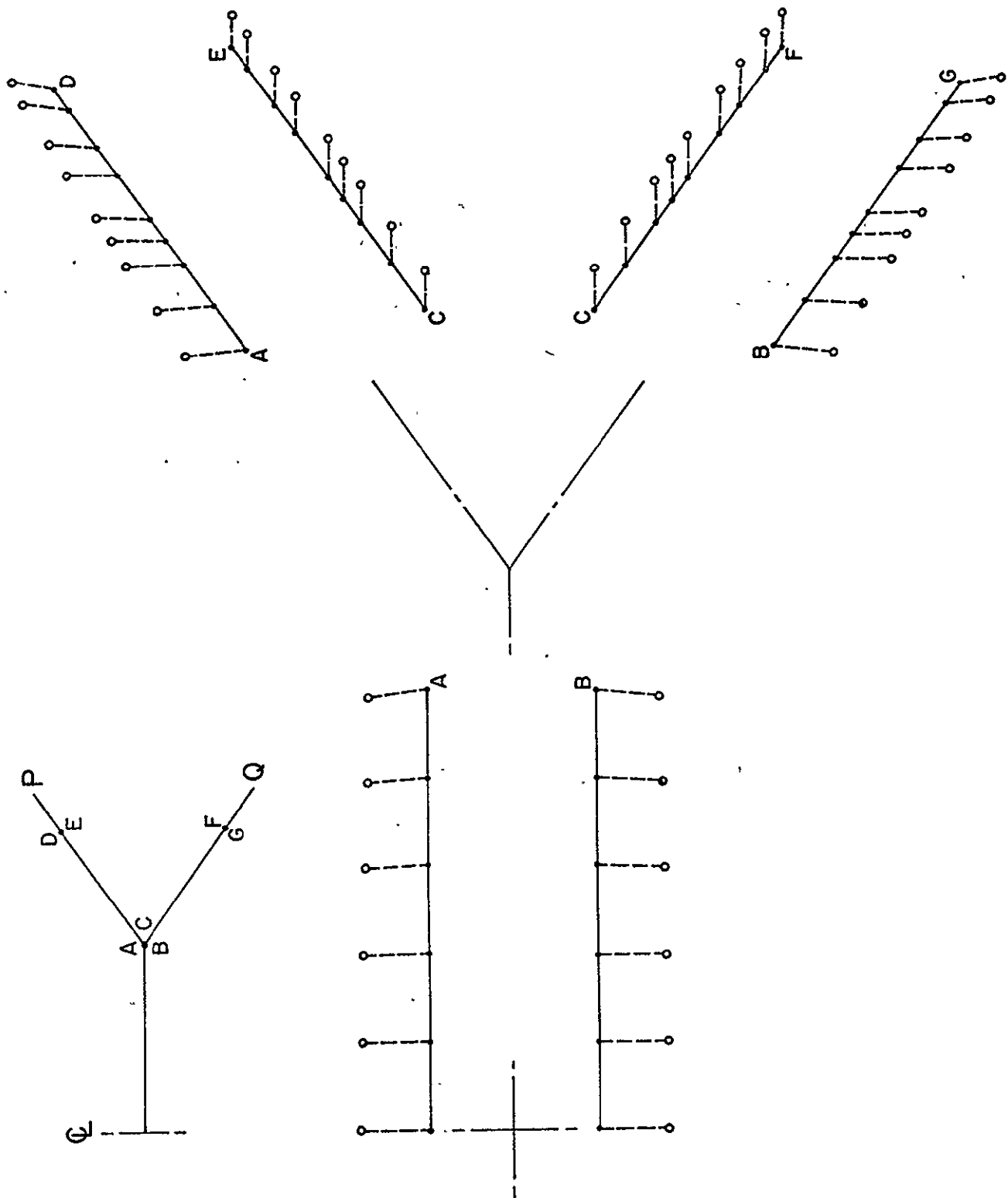
Figure 17   Crack Displacement Distribution For a Branched Crack, "a + b" Loading
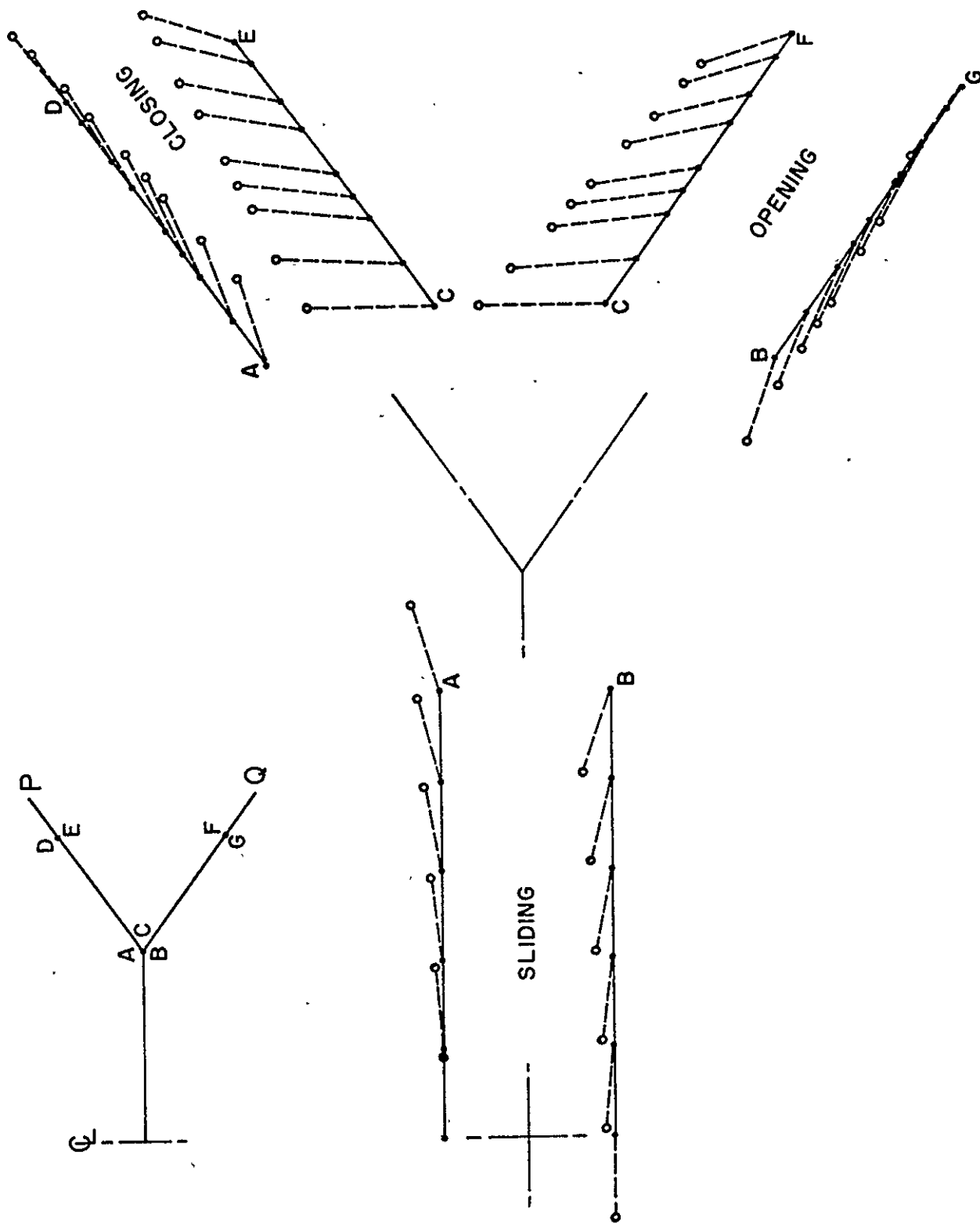
Figure 18 Crack Displacement Distribution For a Branched Crack,
"a - b" Loading

One model was reanalyzed under the assumption of plane stress to compare plane stress with plane strain. It was a straight crack configuration with a = 1.5 and the stress intensities are:

	K_I $\frac{}{a+b}$	K_{II} $\frac{}{a-b}$
Plane Stress	1.111	1.043
Plane Strain	1.115	1.088

Both sets of stress intensities are normalized to infinite plate plane strain values, thus they are directly comparable. The differences are very small and probably less than the accuracy of the analysis.

REFERENCES

1. Zienkiewicz, O. C., "The Finite Element Method in Engineering Science", McGraw-Hill, London, 1971.

2. Holston, A., Jr., "A Mixed Mode Crack Tip Finite Element", accepted for publication in International Journal of Fracture.

APPENDIX B
PRECRACKING STUDY AND PARAMETERS

PRECRACKING STUDY

Development trials were run to determine the relation between pressure level and crack growth for pressure-loaded flaws. Data from these trials are given in Table B-1. The development specimens were 15¼ x 8.9 x 1.14 cm (6 x 3½ x 0.450 in.) with the flaw parallel to the long direction. All specimens were cut from the same sheet of 2219-T87 material. A 0.635-cm (¼-in.) hole was drilled through the specimen and used as a starter for a 5-cm (2-in.) long saber saw cut. Notches were put in the ends of the cut with a sharpened saber saw blade. The notches were scored with a razor blade, each corner of the blade being used only once. Cycling pressure was supplied by the hydraulic system of an MTS machine at 7 cycles/ second. Two of the best examples from the development series are shown in Figures B-1 and B-2. The lightest areas are those of crack growth; the darkest are the original saw cut flaws and the saw cuts after cracking to permit breaking open of the specimens; the intermediate are the fracture areas.

SPECIMEN PRECRACKING

Based on the experience gained during the precracking development effort, initial values of pressure and number of cycles were established for the test specimens. However, in every instance of specimen precracking the precracker was opened several times to permit tracking of the progress of the sharpening. After the first few specimens, the precracking effort became somewhat routine and complete data sets were not kept. The available data on precracking the specimens is contained in Table B-2.

TABLE B-1. – PRECRACKING DEVELOPMENT TESTS

Specimen designation	Flaw orientation with respect to grain, deg	Razor blade scoring[a]	Maximum pressure[b]	Number of cycles	Flaw growth each end		Flaw growth character
					mm	mils	
A	0	0	B	3 200	0.25 – 1.91	10 – 75	Concentrated at one end. Uneven, out of plane.
B	0	B	A	100 000	0.38 – 1.91	15 – 75	Uneven at both ends, out of plane.
C	45	B	A	61 000	3.56 – 3.30	140 – 130	Uneven, out of plane.
D	45	0	B	60 000	3.81 – 0	150 – 0	In plane, one end only.
E	45	0	A	76 000	3.18 – 3.18	125 – 125	Out of plane.
1	45	0[c]	B	125 000	1.65 – 1.65	65 – 65	Out of plane and uneven.
2	45	0	B	10 000	0 – 0	0 – 0	No growth.
			A	52 000	2.28 – 1.78	90 – 70	Out of plane and uneven.
3	45	0	A	65 000	3.30 – 2.54	130 – 100	In plane.
4	45	0[d]	A	40 000	1.91 – 2.54	75 – 100	In plane one end, out of plane on other.
1A	45	B[d]	A	45 000	2.28 – 3.81	90 – 150	Out of plane and uneven.
2A	45	B[d]	A	25 000	4.06 – 3.81	160 – 150	Out of plane.
3A	45	B[d]	B	20 000	7.62 – 8.89	300 – 350	Even and in plane.
4A	45	B[d]	B	10 000	5.33 – 4.57	210 – 180	Even and in plane.
5A	45	B[d]	C	5 000	4.32 – 4.57	170 – 180	Even and in plane.

[a] 0 – One draw through each end; B – Two draws through each end, one from each side.

[b] A – 2070 N/cm^2 (3000 psi); B – 2400 N/cm^2 (3500 psi); C – 2750 N/cm^2 (4000 psi).

[c] Exacto blade.

[d] Resharpened saber saw blade.

Note: All specimens: 2219-T87, t – 1.14 cm (0.450 in.), cut from one sheet. Initial flaw length – 5 cm (2 in.), flaw cut with saber saw. End V-notches made with sharpened saber saw. Notches scored with razor blade. Cycle rate = 7 cycles/second.
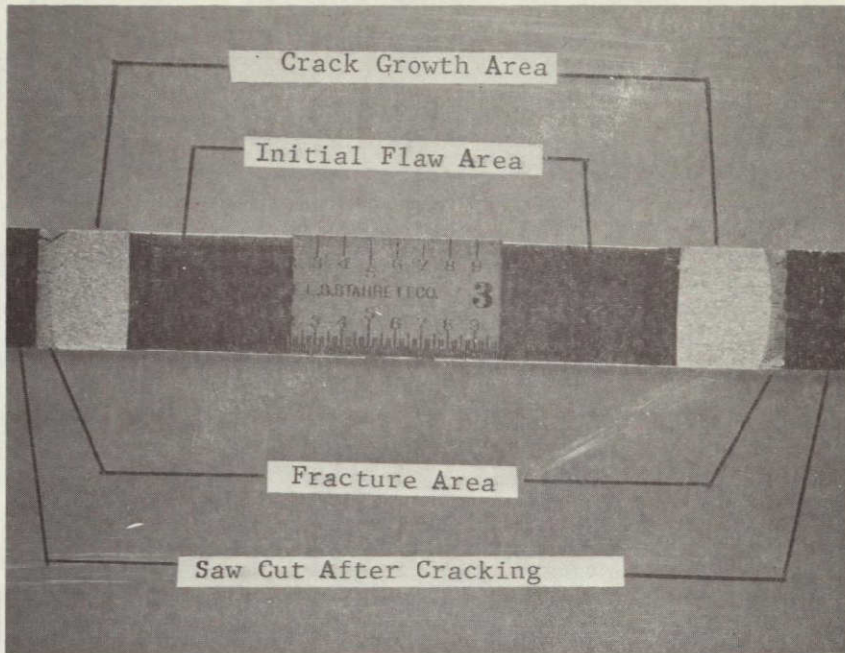
Figure B-1. – Precracking Development Specimen 3A,
2400 N/cm^2 (3500 psi), 20 000 Cycles.
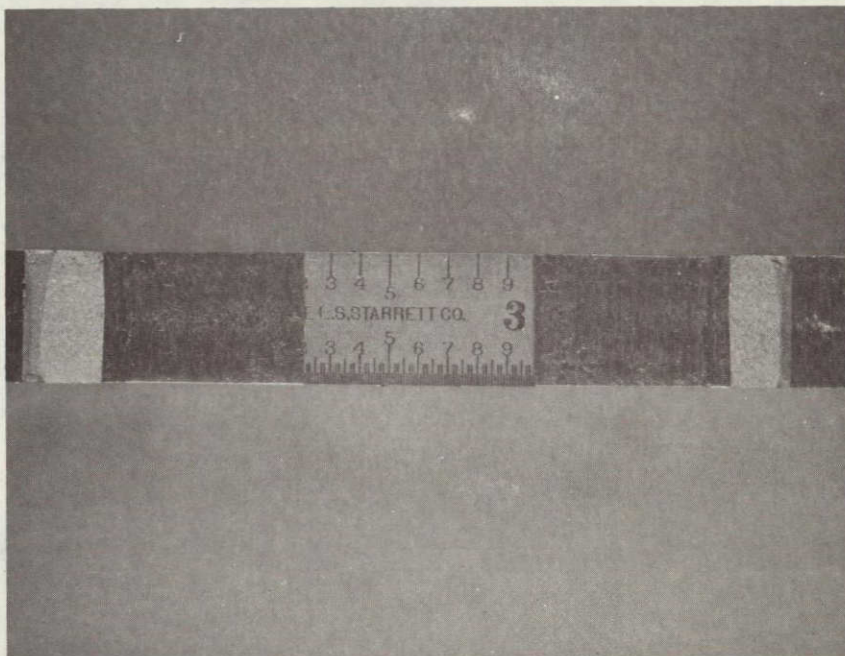
Figure B-2. – Precracking Development Specimen 4A,
2400 N/cm^2 (3500 psi), 10 000 Cycles.

TABLE B-2. – PRECRACKING PARAMETERS

Specimen number	Face	Precracking flaw growth				Average flaw length after sharpening		Precracking parameters		
		End A		End B				Cycles, thousands	Pressure	
		mm	mils	mm	mils	cm	in.		N/cm²	ksi
1	A	1.7	70	1.1	45	6.541	2.575	5.5	24.1	3.5
	B	1.0	40	1.7	70					
2	A	1.7	70	1.2	50	5.385	2.120	13	24.1	3.5
	B	2.0	80	1.2	50			1	27.6	4.0
3	A	1.8	75	1.7	70	5.469	2.153	5	27.6	4.0
	B	1.5	60	1.7	70			8	24.1	3.5
4	A	1.8	75	1.6	65	5.423	2.135	5	27.6	4.0
	B	1.6	65	1.6	65			4	24.1	3.5
5	A	1.2	50	1.7	70	5.283	2.080	6	22.1	3.2
	B	0.8	30	1.5	60					
6	A	1.8	75	1.0	40	4.928	1.940	5	22.1	3.2
	B	1.0	40	1.5	60					
7	A	3.2	130	5.6	230	5.166	2.034	135	22.1	3.2
	B	1.0	40	3.2	130			197.8		
8	A	1.8	75	1.5	60	6.375	2.510	112	34.5	5.0
	B	3.7	150	3.2	130					
9	A	2.5	100	3.4	140	5.474	2.155	50	34.5	5.0
	B	4.4	180	6.6	270					
11	A	1.7	70	1.6	65	10.60	4.175	8	24.1	3.5
	B	1.8	75	0.5	20			20	27.6	4.0
12	A	2.1	85	2.3	95	10.73	4.225	20	27.6	4.0
	B	2.5	100	2.1	85					
14	A	1.7	70	1.8	75	5.029	1.980	40	34.5	5.0
	B	2.9	120	2.6	105					
15	A	1.3	55	0.1	5	10.26	4.040	20	17.2	2.5
	B	1.5	60	1.3	55			60	24.8	3.6
16	A	4.2	170	3.9	160	10.92	4.300	25	24.8	3.6
	B	4.9	200	4.9	200					
17	A	2.0	80	2.7	110	10.49	4.130	14.6	27.6	4.0
	B	1.8	75	1.3	55					
18	A	1.2	50	0.6	25	10.34	4.070	6	22.4	3.3
	B	0.4	15	0.5	20			9	27.6	4.0
23	A	1.2	50	3.2	130	10.57	4.160	65	22.4	3.3
	B	3.3	135	2.5	100					
24	A	1.5	60	1.7	70	10.52	4.140	60	22.4	3.3
	B	0.2	10	0.1	5					
25	A	0.1	5	0.2	10	10.17	4.005	40	22.4	3.3
	B	2.3	95	1.3	55					
26	A	0.1	5	4.8	195	10.72	4.220	a	24.1	3.5
	B	4.0	165	1.5	60					
27	A	1.0	40	1.1	45	7.701	3.032	35	24.1	3.5
	B	0.1	5	0.2	10					

[a] No data.

154

APPENDIX C

MIXED-MODE SYSTEM CHECKOUT SUMMARY REPORT

Note: This appendix is a copy of a report prepared by the Denver
Division for Corporate Headquarters, Martin Marietta Corpo-
ration. The checkout was performed as part of the facility
procurement program of the Denver Division, and not as part
of the mixed-mode program. Calibration data in Figure C-1
are incorrect for the machine in the configuration ulti-
mately put into service.

I. System Operational Verification Objective: The objective of this phase of
the checkout procedure was to verify the functionality of the Mixed Mode
Test Machine and associated controls operating in concert with the 10^6 lb.
MTS machine and to develop operational procedures.

Results

Note: Paragraph numbers used below refer to the corresponding objective
       section in the Checkout and Acceptance Plan.

5.0 MMTM Uniaxial Checkout

5.1.1 Horizontal axis load carrying capability was demonstrated at 300 kips
in tension and 100 kips in compression. These loads exceed the load require-
ments for contracted testing which can be forseen. Strain measurements
obtained on the checkout specimen indicated that due to stress concentrations
in the specimen corner the maximum tensile load which could be carried on the
.3 inch thick 4340 steel specimen is approximately 140 kips rather than the
originally estimated 683 kips. The maximum compression load applied of 100
kips likewise exceeds the compressive load requirements of the Mixed Mode
Contract.

5.1.2 The MMTM "load cell" was calibrated for loads from -100 kips to
+300 kips. The resulting calibration data is shown in Figure 1.

5.1.3 The strain distribution resulting from MMTM loading only is shown
in Figure 3. Strain gage locations are shown in Figure 2.

5.1.4 The dynamic response of the MMTM to cyclic ramp loads from function
generator inputs was evaluated as a function of frequency at $\pm$ 25, $\pm$ 75
and $\pm$ 100 kips. It was determined that the maximum frequencies which
could be used were 1.0, 1.0, 0.9, and 0.5 Hz, respectively. The limiting
factor in each case being an apparent resonance of the hydraulic lines.

    Checkout of the computer controlled operation of the MMTM was per-
formed using the programmed load input shown in 2.1 of the checkout
plan. The cyclic rate used was 8 sec/cycle.

6.0   MMTM Support System - Final Check

    With the specimen pinned to both sides of the MMTM and the actuator
side of the MTS and the MMTM supported on the three support jacks the
MTS was cycled through $\pm$ .125 inch stroke at frequencies up to 1 Hz. The
strain gages monitored during this test essentially followed the cyclic
input (Figure 4) - indicating acceptability of the support system.
Inertia effect of transverse fixture during cycling of MTS machine intro-
duces only minimal bending strains in the specimen. A 1/8 inch stroke
at 1 cycle/sec, which is larger and faster than will ever be used, pro-
duced not over 700 psi stress at the most critical locations for detecting
in-plane bending.

7.0   MTS Checkout-Uniaxial

7.5.1; 7.5.2   The strain distribution due to uniaxial loading in the MTS axis was determined incrementally at ± 100 kips (Figure 5).

7.6   Cyclic functioning of the MTS was verified using function generator inputs.

7.7   Operation of the MTS system using computer control was verified using the load history shown in 2.1 of the checkout plan.

8.0   Biaxial System Checkout

Prior to proceeding with the programmed biaxial loading static biaxial loads were applied to evaluate strain distribution. The results of loading to ± 100 kips in 25 kip increments is shown in Figures 6a and b. The strain distribution in biaxial tension is uniform to less than ±5% along both axes up to 100 kips for a 9 inch diameter around the center of the specimen. In compression the strain distribution is uniform to within ±5% at loads up to 75 kip for a 9 inch diameter and within a 3½ inch diameter at 100 kip. This uniformity of strain is well within the acceptance limits.

The system was operated in the biaxial mode using computer control. The programmed load input was as shown in 2.1 of the checkout plan. Response of the system operating at 8 sec/cycle is shown in Figures 7a and 7b. In both figures the feedback from the load cells on each axis is shown. Both axes exhibit some looseness going through zero. At this cyclic rate it is acceptable since the peak load levels achieved are not affected. The figures also show the response of strain gages located inside a 4½ inch radius circle near the center of the specimen. Figure 7a shows the response of gages aligned with the MTS axis; Figure 7b those aligned with the MMTM axis. Two points with respect to the strain gages response should be noted: 1) In both cases the fidelity of the gage response reflects that of the load input and 2) The strains peaks agree with those predicted analytically.

The system was also operated at a cyclic rate of 4 sec/cycle (Figure 8). At this cyclic rate the feedback from the MMTM axis was distorted and load and strain peaks affected by reverberations in the system. It has been concluded that 4 sec/cycle is too fast to obtain meaningful test data.

Conclusions

1. The load carrying capability of the MMTM has been demonstrated to 300 kip which is more than adequate for the forseeable test usage.

2. The stress distribution in the specimen is extremely uniform under equal biaxial loads.

3. System functions as required under computer control input to both axes.

158

Excitation: 15.000 Volts

LOAD CELL CIRCUIT "L"

Excitation: 15.149 Volts

LOAD CELL CIRCUIT "R"
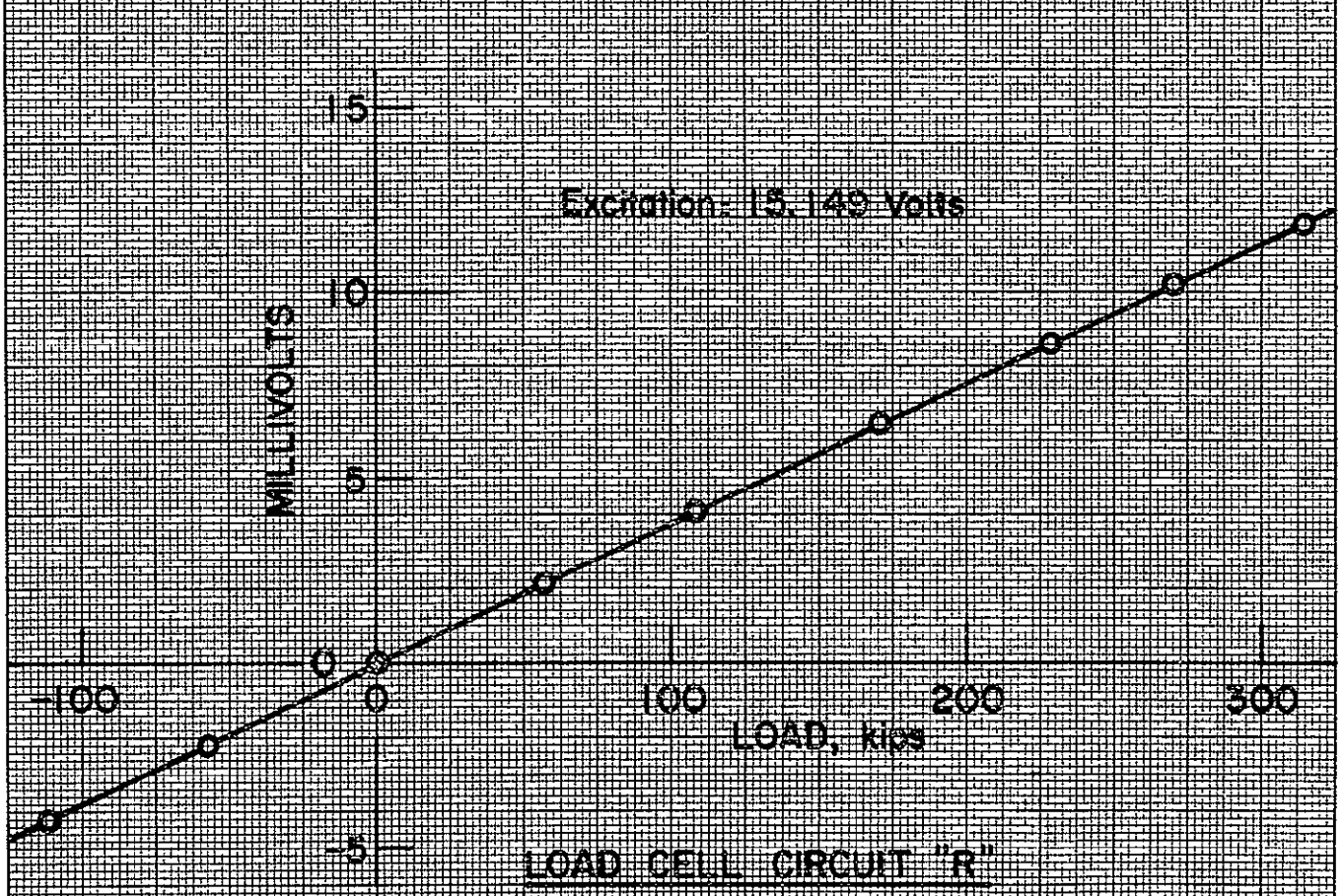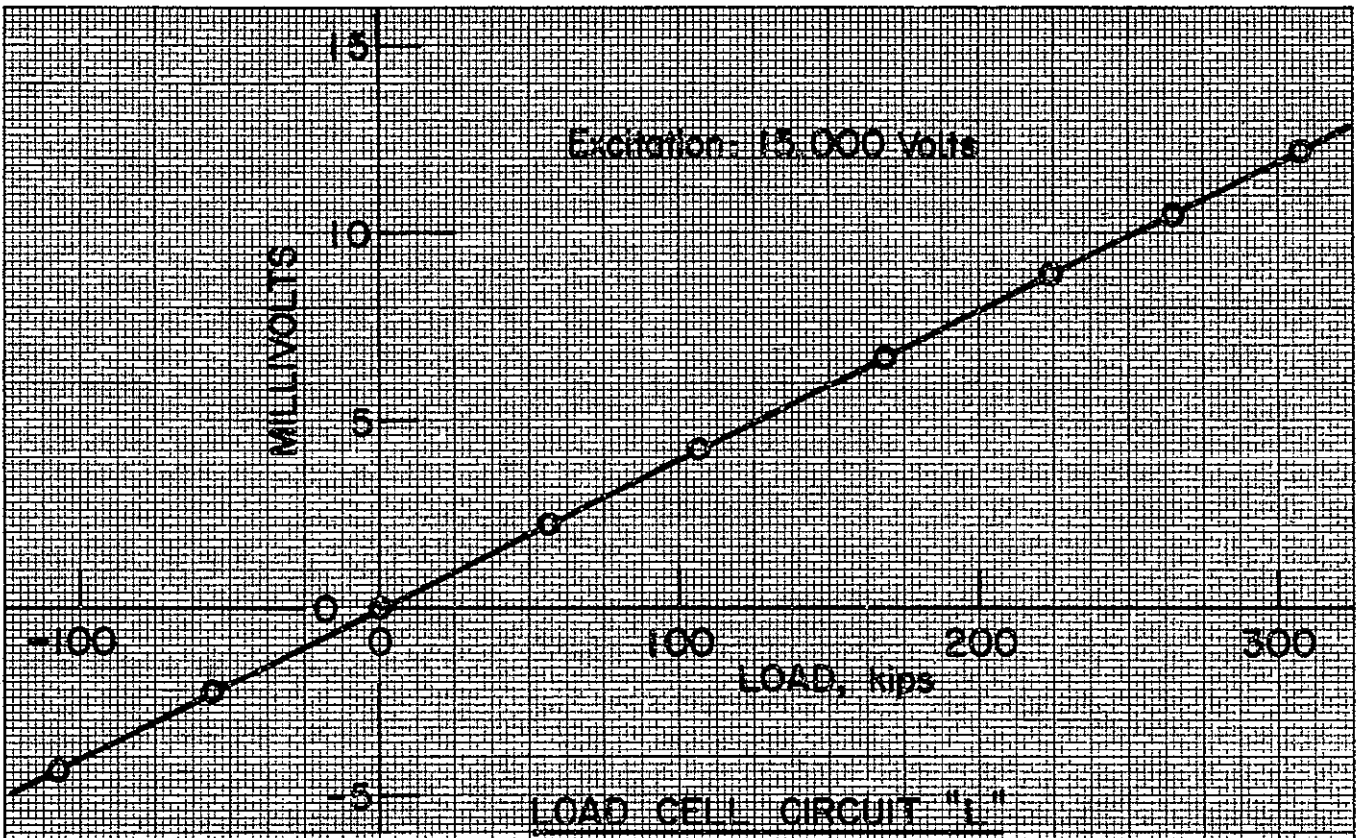
MMTM LOAD ROD CALIBRATION
Figure 1
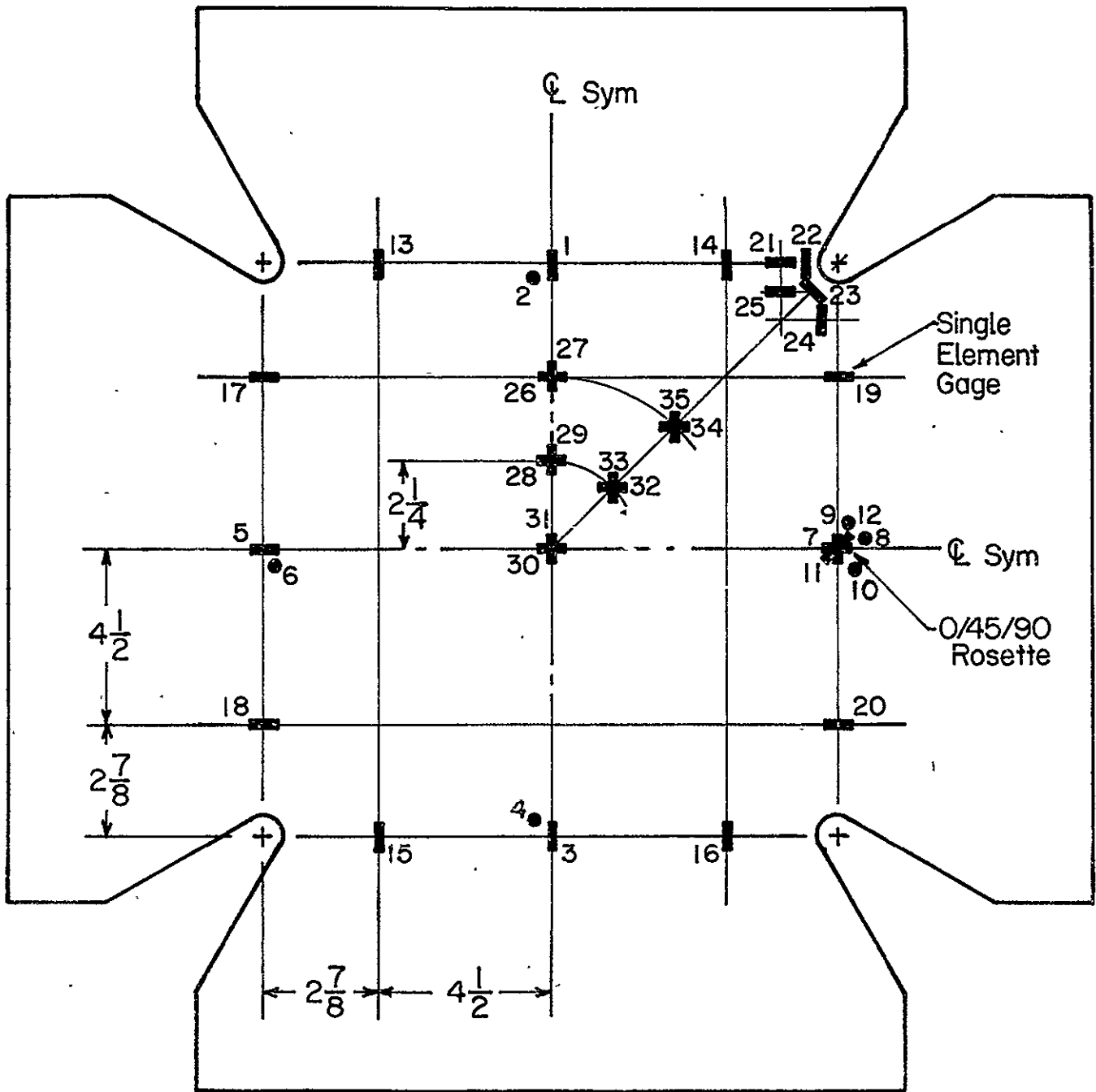
ONE INCH THICK ALUMINUM CHECKOUT SPECIMEN
Figure 2
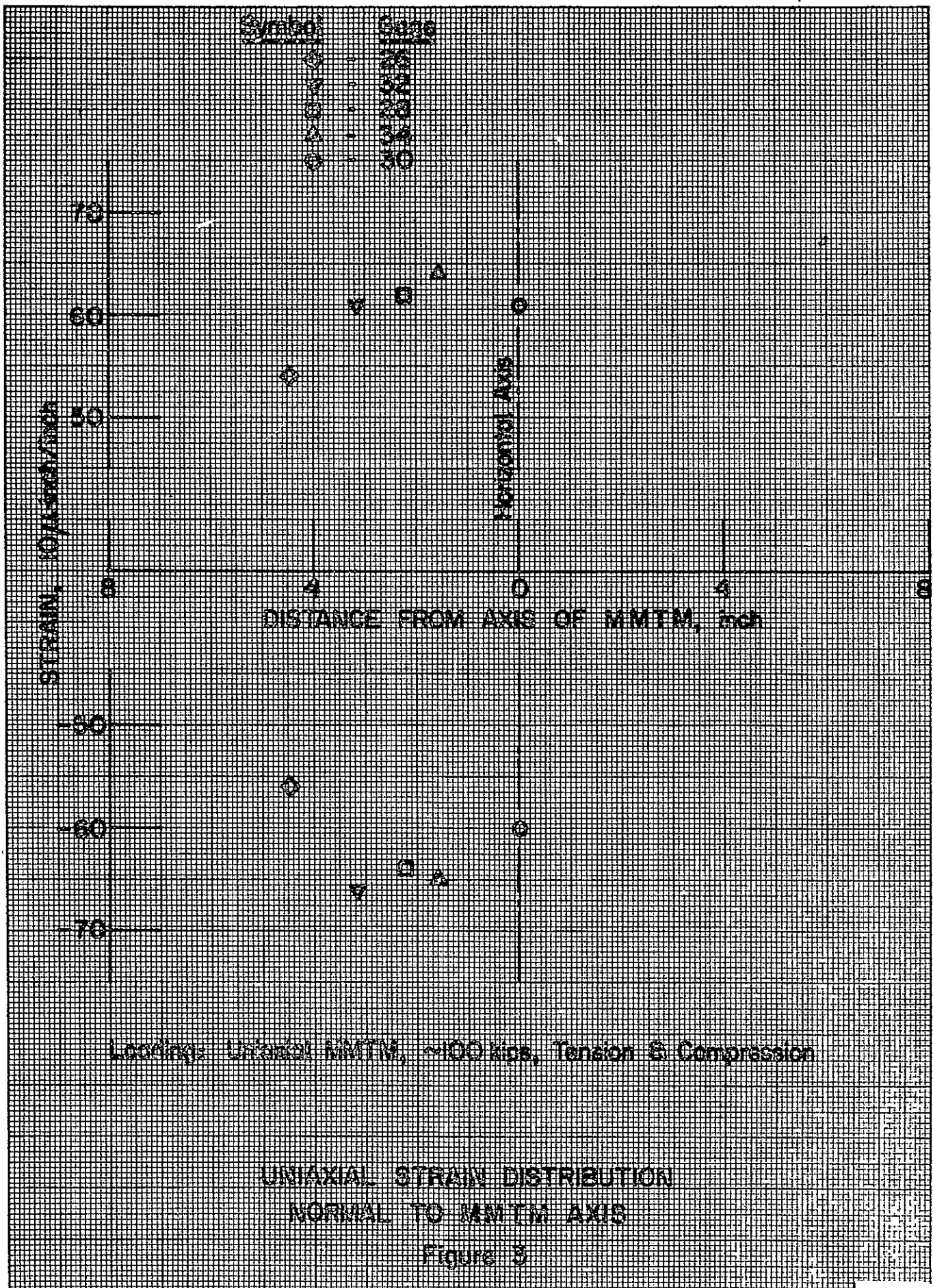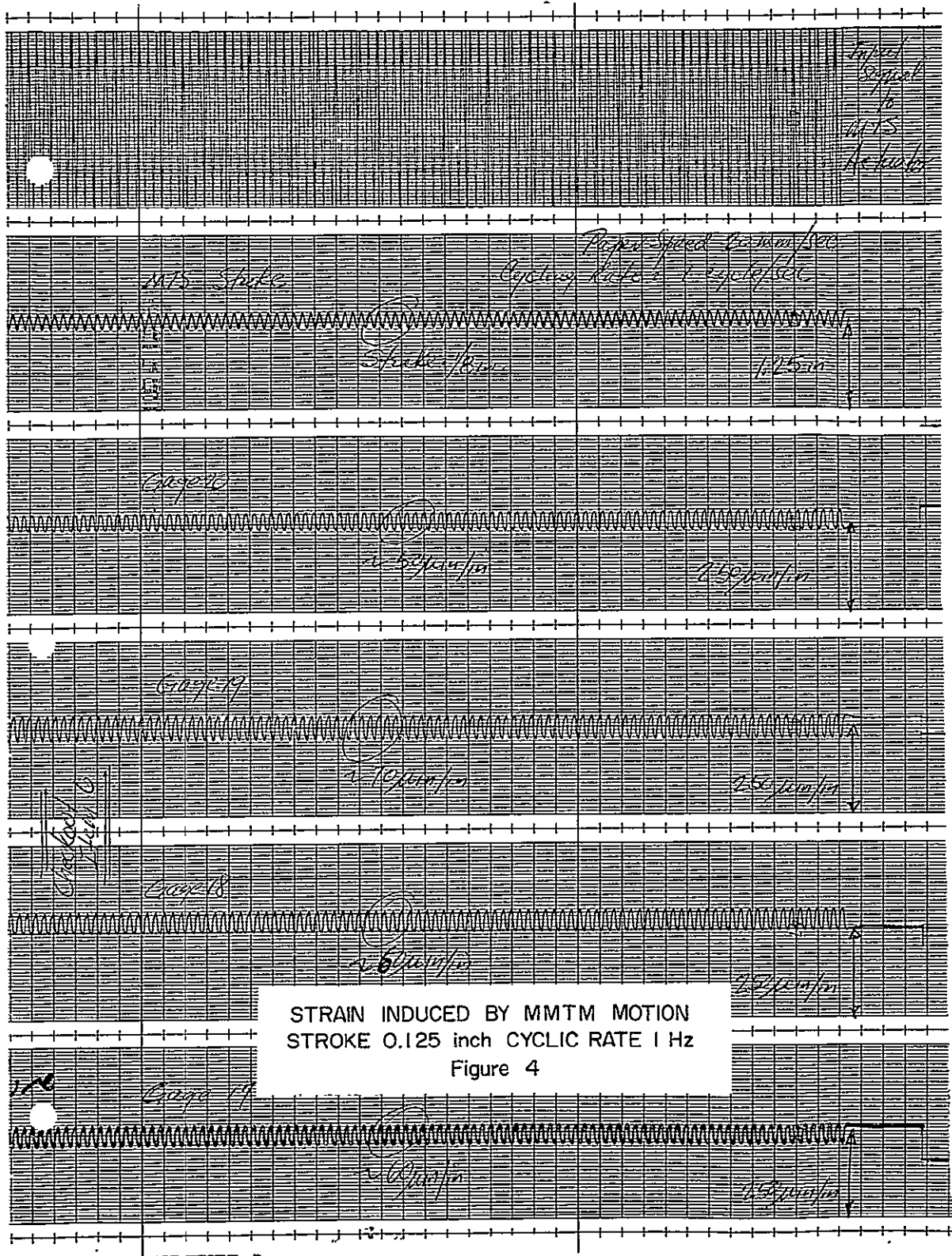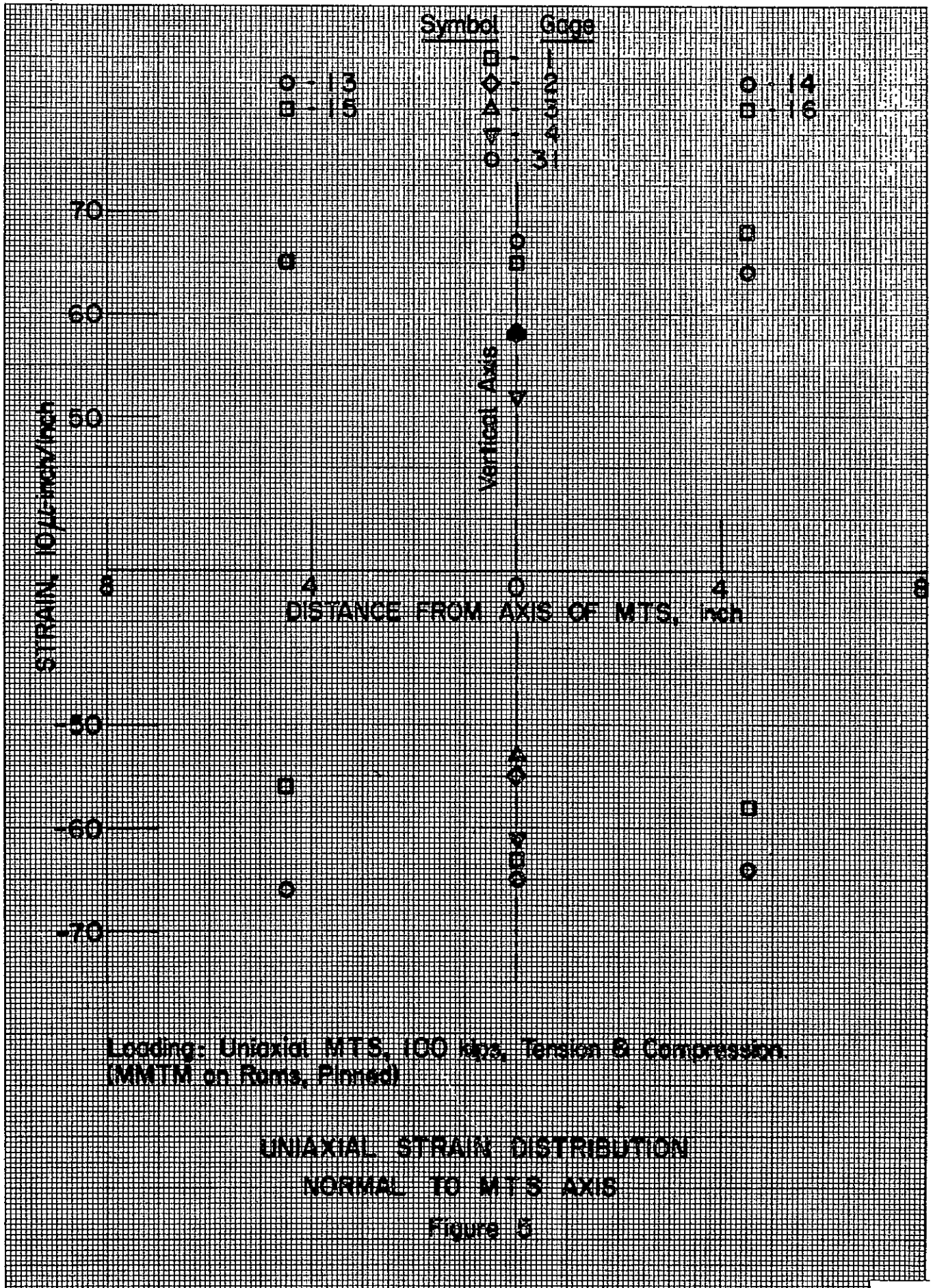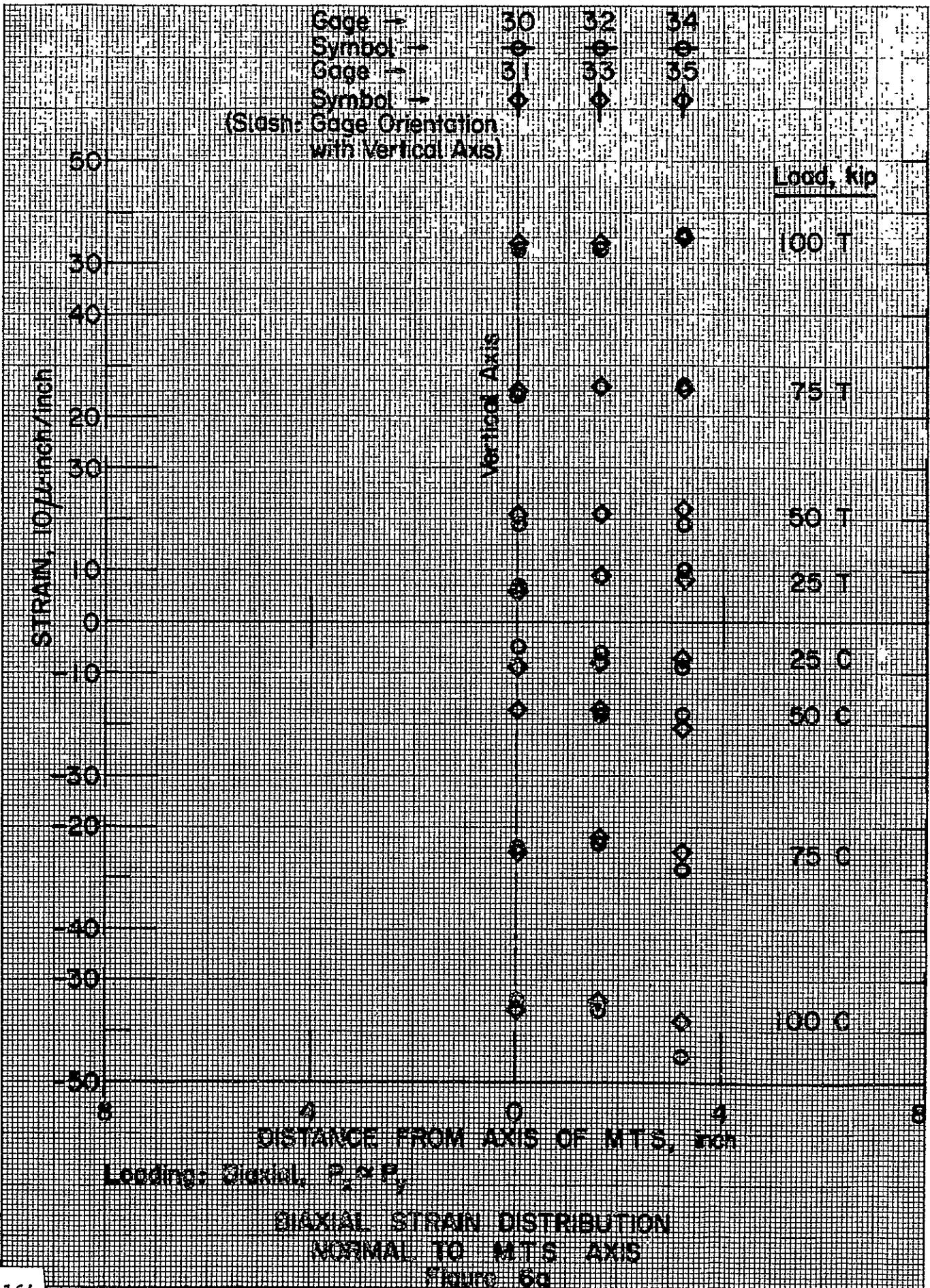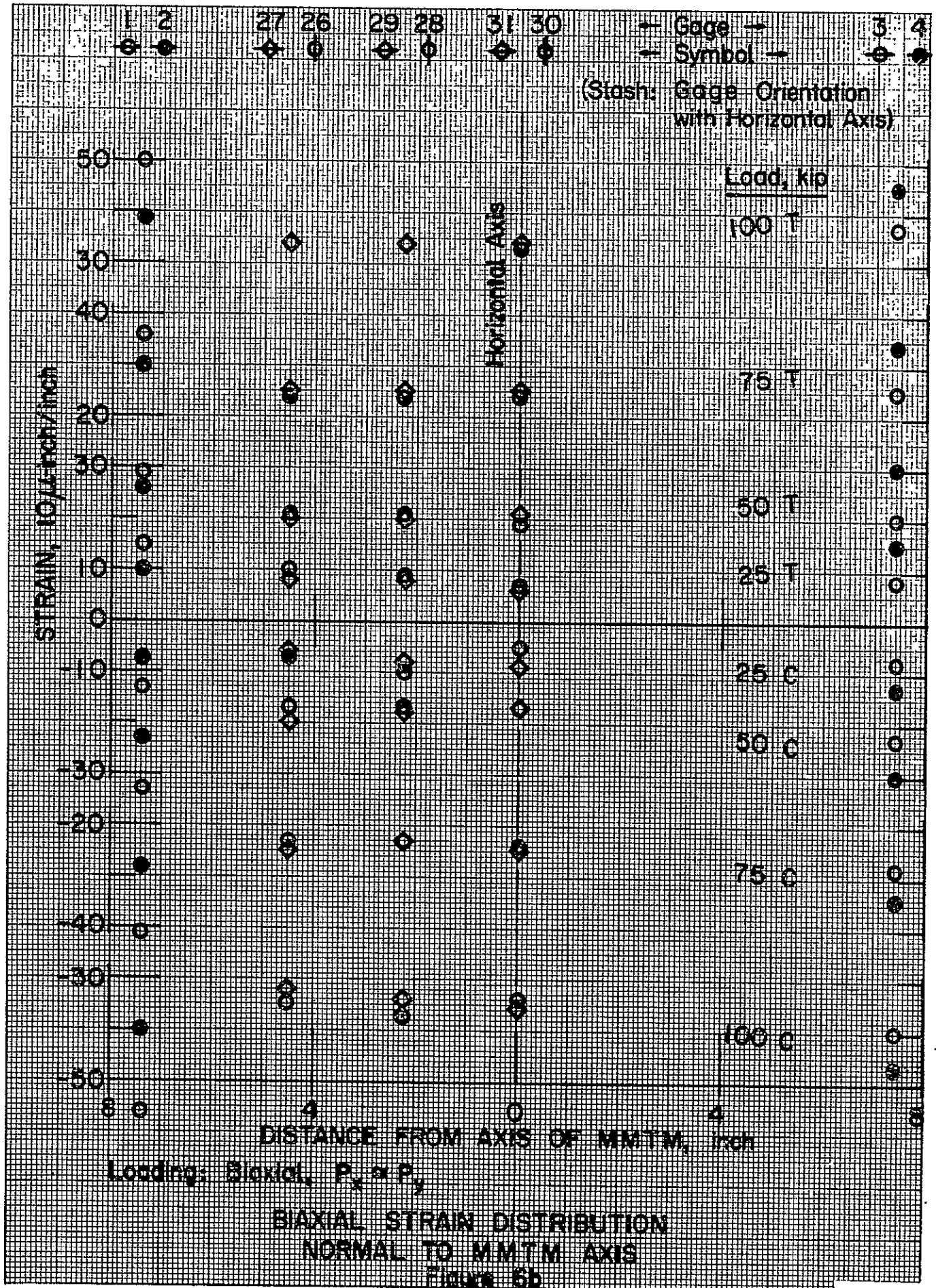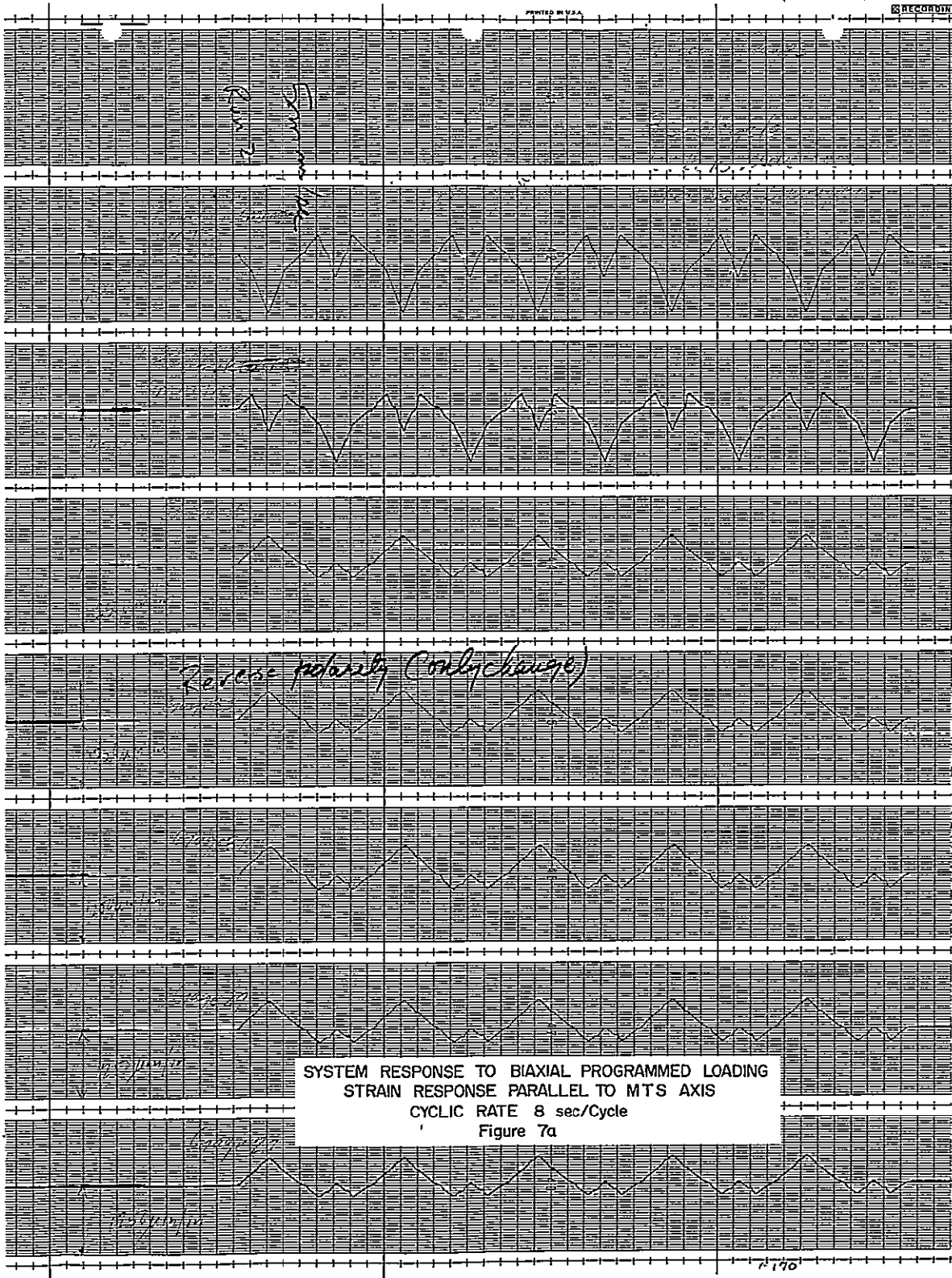
UNIAXIAL STRAIN DISTRIBUTION
NORMAL TO MMTM AXIS
Figure 9

STRAIN INDUCED BY MMTM MOTION
STROKE 0.125 inch CYCLIC RATE I Hz
Figure 4

UNIAXIAL STRAIN DISTRIBUTION
NORMAL TO M.T.S. AXIS

Figure 5

BIAXIAL STRAIN DISTRIBUTION
NORMAL TO MTS AXIS
Figure 6a

BIAXIAL STRAIN DISTRIBUTION
NORMAL TO MMTM AXIS
Figure 6b

SYSTEM RESPONSE TO BIAXIAL PROGRAMMED LOADING
STRAIN RESPONSE PARALLEL TO MTS AXIS
CYCLIC RATE 8 sec/Cycle
Figure 7a

SYSTEM RESPONSE TO BIAXIAL PROGRAMMED LOADING
STRAIN RESPONSE PARALLEL TO MMTM AXIS
CYCLIC RATE 8 sec/Cycle
Figure 7b

SYSTEM RESPONSE TO BIAXIAL PROGRAMMED LOADING
STRAIN RESPONSE PARALLEL TO MTS AXIS
CYCLIC RATE 4 sec/Cycle
Figure 8

168
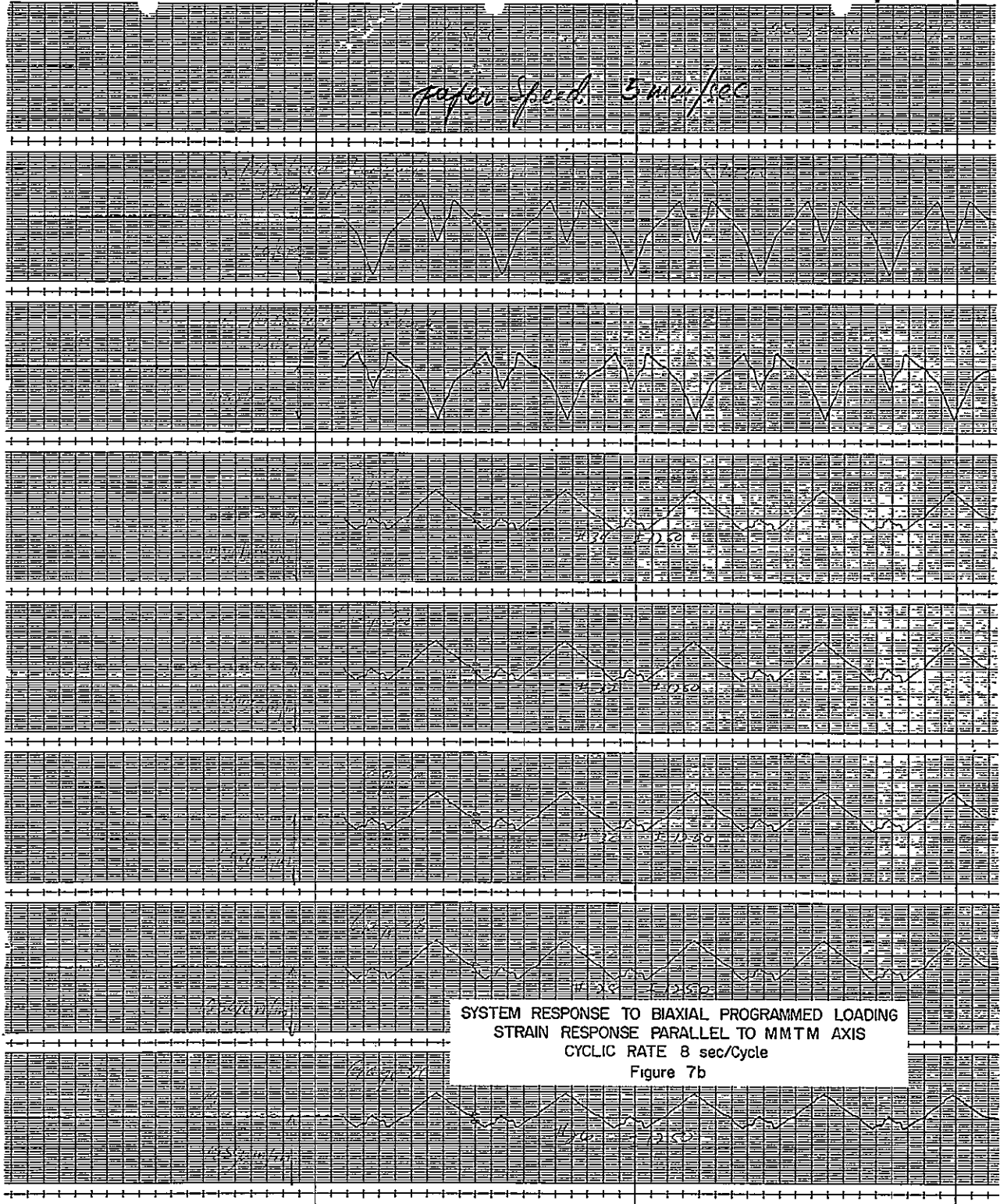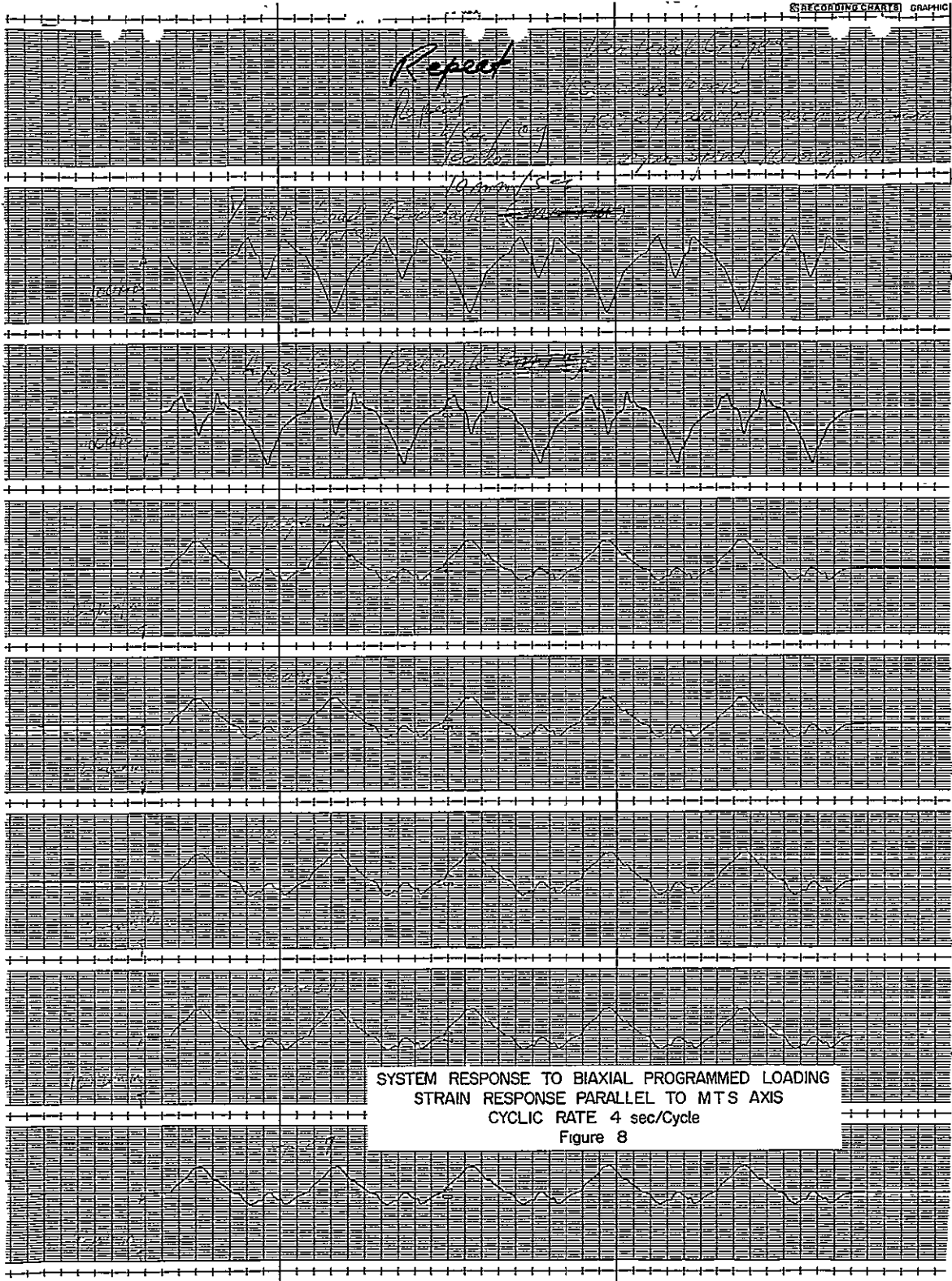
APPENDIX D

TABLES OF PRIMARY CYCLIC AND STATIC DATA

This appendix contains a description of the experimental response of each specimen and tables of the primary load and crack length data recorded during each test in the program. All lengths in the tables are actual crack lengths. Where projected crack lengths were required in the analyses, the crack lengths in the tables were transformed to the appropriate projected length.

SN-1. - This sample was subjected to approximately 1750 cycles of loading in the pure K_I mode, load type A (equal, synchronized loads on each axis). Load was applied at very low stress intensity values $\left(\text{less than 5500 kN cm}^{1/2}/\text{cm}^2 \text{ or 5000 psi-in.}^{1/2}\right)$ to check the operation of the recording equipment. Cycle testing of the specimen then began at a stress intensity level of approximately 11 000 kN cm$^{1/2}$/cm^2 $\left(10\ 000 \text{ psi-in.}^{1/2}\right)$, which corresponded to a maximum biaxial load of 289 kN (65 kips). The table for SN-1 in this appendix lists the subsequent loads, the number of cycles at each load level, and the resulting crack length. The crack did not grow straight. However, each increment of crack growth was measured as a straight line from the last position of the crack tip at which a measurement was taken. The values of crack length in the table are the average of the four values of crack growth measured at each end of the crack on each face of the specimen, added cumulatively to the original flaw length.

The 2673 cycles at 311-kN (70-kip) maximum load were applied during an effort to locate a noise on the horizontal axis that was causing a bump in the horizontal load feedback signal. The noise was localized to the bottom actuator on the transverse axis. Jamb nuts were installed on the actuator piston rod but the problem persisted throughout the program.

In the table, the 1102 cycles of loading at 405 kN (91 kips), primarily on the horizontal axis, was an attempt to cause the crack to turn back toward the 45-deg line. It appeared from the intersection of the crack leading edges with the specimen surfaces, that the attempt was successful. Subsequently, the "phase shifting" technique previously described was employed. However, the crack resumed its growth in the horizontal direction.

The static test performed after completion of cycling did not yield usable data. The crack under the top loading tab in the photographs in Appendix E was caused during specimen removal.

SN-2. - This sample was cyclically tested under load type A as a duplicate of SN-1. The maximum load imposed during the cyclic tests was 592 kN (133 kips). After cyclic testing, SN-2 was tested statically to fracture under equal biaxial loads. High-speed movies revealed that subcritical crack growth started at the upper end of the crack at approximately 594 kN (134 kips) and at the lower end at approximately 604 kN (136 kips). Fracture occurred at approximately 774 kN (174 kips) after subcritical growth of between 0.76 and 2.54 cm (0.3 and 1.0 in.), depending on which end of the flaw and which face of the specimen were considered. Turning the crack appears to have started at the very beginning of cyclic testing and continued until the cracks were parallel to the final rolling direction. This is the same phenomenon as observed in the test of SN-1.

SN-3. - This specimen was the first cyclically tested under the mixed-mode condition (load type B). Branching was immediately exhibited at both ends of the flaw and on both faces of the specimen. All legs of the flaw continued to grow until the test was stopped. The test was stopped during cyclic testing after approximately 22 700 cycles when there was sudden growth (3.8 to 5 cm or 1½ to 2 in.) of the horizontal legs of the cracks during one cycle of loading at the 489-kN (110-kip) load level. At the time this appeared to be a considerably premature failure. There was no further testing, cyclic or static.

SN-4. - This specimen was cyclically tested under load type C for approximately 32 000 cycles up to a maximum load of 569 kN (128 kips) then tested statically to failure. Failure occurred under static loading at 850 kN (191 kips) as evidenced by sudden growth of the cracks into the grips. Branching of the flaw appeared to start immediately on cyclic testing. There was considerable subcritical crack growth of the horizontal legs of the branched cracks during static testing. The static load was applied normal to the rolling direction. Due to operator error the load was not removed after failure but allowed to increase. At 889.6 kN (200 kips) the top loading tab of the specimen broke off. It was thus learned that the central portion of the specimens must be weakened by sufficient flaw growth (or longer initial flaws for the specimens to be tested only statically) to the point where fracture can occur there and not across the tab notches.

SN-5. - This sample was cyclically tested under load type B for approximately 43 100 cycles up to maximum loads of 265 kN (59.5 kips) on one axis and 113 kN (25.5 kips) on the other, then tested statically to failure. Failure occurred at 545 kN (122.6 kips) on the vertical axis with 230 kN (51.8 kips) on the horizontal axis. Branching of the flaw appeared to start immediately on cyclic testing. The branches parallel to the rolling direc-

tion grew much faster than those perpendicular to it during the cyclic test.

SN-6. - This specimen was cyclically tested under equal biaxial loads, load type A, for approximately 55 000 cycles up to a maximum load of 244 kN (54.8 kips). It was then tested statically to failure under equal biaxial loads. Failure occurred at about 513 kN (115.4 kips). Crack growth during cyclic testing was straight until a shear lip started forming on the lower end of the flaw. On one surface of the specimen, the crack remainted straight while on the other it curved sharply to the horizontal. At fracture the upper end of the flaw grew vertically while the lower end grew horizontally.

SN-7. - SN-7 was cyclically tested under equal biaxial loads for approximately 40 500 cycles up to a maximum load of 512 kN (115 kips). Fracture occurred at the 696th cycle at 512 kN (115 kips). The length of the crack at fracture is unknown because no movies were taken during cyclic testing. It was decided to test SN-7 cyclically to failure to obtain as complete a plot of ΔG versus $\Delta a / \Delta N$ as possible. The flaw turned parallel to the rolling direction soon after the beginning of cyclic testing and grew into the grips at fracture. The length of the crack at fracture has been estimated by extrapolating the compliance plot to the value of compliance measured on the last cycle, which was recorded on the oscillograph. The last cycle has been considered a static test in the data analysis.

SN-8. - SN-8 was cyclically tested under load type B for 23 673 cycles at which time one of the load tabs broke off. The maximum cyclic loads achieved were approximately 514 kN (115.5 kips) on one axis with 218 kN (49 kips) on the other. Though branching of the crack was apparent at the very beginning of cyclic loading, the vertical legs of the branches developed only slightly. Most crack growth took place in the horizontal direction, parallel to the rolling direction. Vertical crack growth has been ignored in the data analysis as insignificant.

SN-9. - This was essentially a retest of SN-8 except that the final rolling direction was oriented vertically instead of horizontally in the testing machine. SN-9 was loaded cyclically for approximately 39 306 cycles. It was taken to failure under cyclic loading to provide a good comparison with specimen SN-7. The maximum loads just prior to failure were approximately 503 kN (113 kips) on one axis with 224 kN (50 kips) on the other. The crack branched and, in the early portions of the test, the branches grew at about the same rate. However, the vertical branches started to grow faster about half way through the test and growth of the horizontal branches almost ceased. Fracture was characterized by sudden growth of the vertical branches into the grips.

The length of the crack at fracture has been estimated by extrapolating the crack growth rate from the oscillograph records. The last cycle has been considered a static test.

SN-11. – This specimen was tested statically with a compression load on the vertical axis equal to about 40% of the tension load on the horizontal axis (load type D). The initial flaw was approximately 10-cm (4-in.) long. Fracture occurred with 256-kN (57.6-kip) compression on the vertical axis and 615-kN (138.2- · kip) tension on the horizontal axis $\left(K_{II} / K_I = 2.6\right)$. There was some subcritical crack growth, starting at -153 kN (-34.4 kips) and 371 kN (83.4 kips) on the vertical and horizontal axes, respectively. Crack growth was straight from the ends of the flaw directly into the corners of the specimen. There was no shear lip or turning of the crack. In the photographs of Appendix E, note the permanent shear deformation at the hole used for mounting the biaxial COD gage holder.

SN-12. – SN-12 was tested statically with compression on the vertical axis numerically equal to the tension on the horizontal axis, resulting in pure shear on the 10-cm (4-in.) 45-deg flaw (load type E). Fracture occurred when the specimen buckled under the vertical compressive load in spite of the presence of the antibuckling plates. Simultaneously one of the loading tabs on the horizontal axis broke off. The fracture was vertical, perpendicular to the rolling direction, but also perpendicular to the tension load.

SN-14. – SN-14 was cyclically tested under load type ·B; however, the shear was not reversed on each cycle. Approximately 39 300 cycles were applied with the higher load, 245 kN (55 kips), always in the vertical direction, resulting in horizontal crack growth of about 0.76 cm (0.3 in.) off each end of the original flaw. Then the shear was reversed by putting the higher load of 245 kN (55 kips) on the horizontal axis while the vertical load was reduced to 89 kN (20 kips). No crack growth was noticed for about 60 500 cycles. The horizontal load was increased to 311 kN (70 kips) with the vertical load at 116 kN (26 kips) and vertical branches started to grow. On one side of the plate they grew from the ends of the original flaw. On the other side the top one grew from the original flaw but the bottom one grew from the end of the horizontal branch. Total cycles at the 311-kN (70-kip) level were approximately 24 500. The vertical branches had grown about 0.76 cm .(0.3 in.). The test was terminated and SN-14 was subsequently tested statically. It is interesting to note that once the horizontal branches were started, applying the high horizontal load did not induce vertical branches as it would have had the high load been alternated between ·the vertical and horizontal axes on each cycle. SN-14 was tested statically under a vertical tension load. Fracture occurred at 1468 kN (330 kips)

with the horizontal branches running toward the grips then turning parallel to the rolling direction. The fracture surface exhibited large shear lips.

SN-15. - This specimen was tested statically under equal biaxial loading $\left(\text{pure } K_I\right)$. The initial flaw was approximately 10-cm (4-in.) long. Fracture occurred at 965 to 968 kN (217.0 to 217.5 kips) on each axis after approximately 1.2 cm (0.5 in.) of subcritical crack growth at each end of the flaw. The crack turned toward the rolling direction but was still generally at 45 deg to the loading axis when the critical length was reached.

SN-16. - SN-16 was tested statically with loading only on the horizontal axis $\left(K_I / K_{II} = 1\right)$. Again, the initial flaw was approximately 10 cm (4 in.) long. Fracture occurred at 1108 kN (249 kips). The crack propagated normal to the tension load, and therefore normal to the rolling direction, but turned parallel to the rolling direction before entering the grips.

SN-17. - SN-17 was tested statically with a compression load on the vertical axis equal to about 40% of the tension load on the horizontal axis (load type D). The initial flaw was approximately 10-cm (4-in.) long. Fracture occurred with a 1486-kN (334-kip) tension on the horizontal axis and a 614-kN (138-kip) compression on the vertical axis $\left(K_{II} / K_I = 2.5\right)$. There was some subcritical crack growth. Crack growth was straight from the ends of the flaw directly into the corners of the specimen. There was no shear lip or turning of the crack. In the photographs (Appendix E), note the permanent shear displacement at the center hole.

SN-18. - SN-18 was tested statically with compression on the vertical axis numerically equal to the tension on the horizontal axis, resulting in pure shear on the 10-cm (4-in.) 45-deg flaw. Fracture occurred with $P_V = -1103$ kN (-248 kips) and $P_H = 1130$ kN (254 kips). There was some subcritical growth. Crack growth was straight into the corner notches. There were no shear lips.

SN-23. - SN-23 was tested statically with tension on the vertical axis and no load on the horizontal axis (load type C). If there had been no subcritical growth, this loading arrangement would have produced a K_I / K_{II} ratio = 1. However, the small amount of subcritical growth in the horizontal direction drastically changed the K_I / K_{II} ratio at failure. Fracture occurred

at P_V = 752 kN (169 kips). Subcritical growth had started at 690 kN (155 kips). In the photographs in Appendix E, the crack emanating from the lower left notch opened after the fracture. Since the fracture cracks ran into the grips, the specimen-grip assembly was still in one piece and vertical load was transmitted through the horizontal grip plates. Because the MTS testing machine was operated as a load-controlled device, it continued to apply load until the second crack resulted in excessive actuator travel. Specimen SN-23 should be compared with specimen SN-16. The only difference was that SN-23 had the load applied perpendicular to the rolling direction while the load was applied parallel to the rolling direction on SN-16.

SN-24 and SN-25. - These specimens were both tested statically with compression on the vertical axis numerically equal to the tension on the horizontal axis, resulting in pure shear on the flaws. The only difference between the tests was that the tension load was applied perpendicular to the rolling direction on SN-25 and parallel to the rolling direction on SN-24. However, there was little difference in the results. SN-24 failed at approximately 1027 kN (231 kips) and SN-25 at 1005 kN (226 kips). There was some subcritical growth. Crack growth in both tests was straight into the corners.

SN-26. - SN-26 was tested statically with a compression load on the vertical axis equal to about 40% of the tension load on the horizontal axis (load type D). The initial flaw was approximately 10-cm (4-in.) long. Fracture occurred with a 1281-kN (288-kip) tension on the horizontal axis and a 498-kN (112-kip) compression on the vertical axis $\left(K_{II}/K_I = 2.4 \right)$ when a loading tab on the horizontal axis broke off. There was some subcritical crack growth. Unfortunately, there is no load record to correlate with the small amount of crack growth that did take place. The tab failure initiated at a sharp flaw in one corner of the specimen that had gone unnoticed before the test. The data analysis presented earlier used the final crack length and maximum loads to compute a minimum G_{cr}.

SN-27. - SN-27 was tested cyclically under a compression load on the vertical axis equal to the tension load on the horizontal axis on every cycle (load type E). This loading was intended to produce a case of pure K_{II} without shear reversal. However, the crack immediately started to grow perpendicular to the tension load rather than in line with the 7.5-cm (3-in.) flaw, which meant that there was little shear on the crack tip but much tension. The cyclic testing was continued for a little more than 26,000 cycles until the crack grew into the grip areas. No static test was made since load would have been transferred

174

through the grip plates rather than through the fully cracked specimen. . In the photographs in Appendix E, the slant crack into the lower right corner was inadvertently caused when the specimen was being removed from the testing machine.

STATIC TEST CRACK GROWTH FOR SN-6

Vertical load, P_V		Horizontal load, P_H		Crack length, 2a	
kN	kip	kN	kip	cm	in.
297	66.8	307	69	6.15	2.42
495	111.2	508	114.2	7.67	3.02
499	112.2	512	115	7.98	3.14
504	113.4	513	115.4	8.26	3.25
504	113.4	515	115.8	8.46	3.33
506	113.8	516	116	8.69	3.42
508	114.2	517	116.2	8.99	3.54

STATIC TEST CRACK GROWTH FOR SN-11

Vertical load, P_V		Horizontal load, P_H		Crack length, 2a	
kN	kip	kN	kip	cm	in.
-153	-34.4	371	83.4	10.61	4.18
-236	-53	569	128	11.20	4.41
-246	-55.4	594	133.6	11.99	4.72
-252	-56.6	606	136.2	12.83	5.05
-254	-57	612	137.6	13.28	5.23
-255	-57.4	614	138	13.64	5.37
-255	-57.4	615	138.2	13.89	5.47
-252	-56.7	615	138.2	14.27	5.62
-252	-56.7	616	138.4	15.90	6.26
-252	-56.7	615	138.2	16.41	6.46
-252	-56.7	615	138.2	17.17	6.76

STATIC TEST CRACK GROWTH FOR SN-5

Vertical load, P_V		Horizontal load, P_H		Crack length, 2a	
kN	kip	kN	kip	cm	in.
323	72.7	138	31.0	9.37	3.69
399	89.8	172	38.6	9.63	3.79
426	95.8	188	42.2	9.96	3.92
466	104.8	197	44.2	10.46	4.12
491	110.4	207	46.6	10.62	4.18
512	115.2	215	48.4	11.20	4.41
527	118.4	222	49.8	11.63	4.58
535	120.2	225	50.6	11.91	4.69
539	121.2	227	51	12.12	4.77
542	121.8	229	51.4	12.32	4.85
544	122.2	229	51.4	12.70	5.00
544	122.2	229	51.4	12.83	5.05
545	122.6	230	51.6	13.18	5.19
545	122.6	230	51.6	13.89	5.47
545	122.6	230	51.6	14.33	5.64
545	122.6	230	51.8	15.52	6.11

STATIC TEST CRACK GROWTH FOR SN-4

Vertical load, P_V		Crack length, 2a	
kN	kip	cm	in.
---	-----	10.74	4.23
750	168.5	10.92	4.30
772	173.5	11.05	4.35
794	178.5	11.13	4.38
816	183.5	11.38	4.48
841	189	11.84	4.66
843	189.5	11.91	4.69
845	190	12.12	4.77
847	190.5	12.57	4.95
850	191	13.34	5.25
850	191	13.67	5.38
850	191	14.10	5.55
850	191	14.38	5.66
Note: $P_H = 0$.			

STATIC TEST CRACK GROWTH FOR SN-14

Vertical load, P_V		Crack length, 2a	
kN	kip	cm	in.
---	-----	7.52	2.96
1352	304	9.09	3.58
1443	324.5	9.50	3.74
1457	327.5	10.01	3.94
1457	327.5	10.29	4.05
1468	330	10.57	4.16
1468	330	10.62	4.18
1468	330	11.56	4.55
Note: $P_H = 0$.			

STATIC TEST CRACK GROWTH FOR SN-15

Vertical load, P_V		Horizontal load, P_H		Crack length, 2a	
kN	kip	kN	kip	cm	in.
---	-----	---	-----	10.26	4.04
892	200.5	894	201	11.02	4.34
930	209	930	209	11.30	4.45
952	214	956	215	11.46	4.51
959	215.5	963	216.5	11.58	4.56
963	216.5	965	217	11.71	4.61
965	217	965	217	11.81	4.65
965	217	967	217.5	12.07	4.75
965	217	967	217.5	12.67	4.99

STATIC TEST CRACK GROWTH FOR SN-16

Horizontal load,		Crack growth,	
kN	kip	cm	in.
761	171	10.92	4.30
1036	233	11.76	4.63
1061	238.5	12.62	4.97
1074	241.5	12.85	5.06
1079	242.5	13.03	5.13
1081	243	13.13	5.17
1085	244	13.26	5.22
Note: $P_V = 0$.			

STATIC TEST CRACK GROWTH FOR SN-12

Vertical load, P_V		Horizontal load, P_H		Crack length, 2a	
kN	kip	kN	kip	cm	in.
-316	-71	314	70.6	10.73	4.23
-385	-86.6	383	86	11.46	4.51
-396	-89	393	88.4	11.76	4.63
-402	-90.4	399	89.6	12.09	4.76
-405	-91	400	90	12.45	4.90
-405	-91	402	90.4	12.52	4.93
-406	-91.2	402	90.4	12.62	4.97
-407	-91.6	402	90.4	12.67	4.99
-407	-91.6	404	90.8	12.73	5.01
-409	-92	404	90.8	12.88	5.07
-409	-92	405	91	13.06	5.14
-410	-92.2	405	91	13.18	5.19
-410	-92.2	406	91.2	13.89	5.47
-411	-92.4	405	91	16.41	6.46
-411	-92.4	405	91	16.74	6.59

178

STATIC TEST CRACK GROWTH FOR SN-17

Vertical load, P_V		Horizontal load, P_H		Crack length, 2a	
kN	kip	kN	kip	cm	in.
----	------	----	-----	10.49	4.13
-558	-125.5	1350	303.5	11.23	4.42
-574	-129	1390	312.5	11.46	4.51
-583	-131	1421	319.5	11.84	4.66
-594	-133.5	1437	323	12.27	4.83
-592	-133	1443	324.5	12.47	4.91
-601	-135	1446	325	12.67	4.99
-601	-135	1448	325.5	12.80	5.04
-603	-135.5	1448	325.5	13.18	5.19

STATIC TEST CRACK GROWTH FOR SN-2

Vertical load, P_V		Horizontal load, P_H		Crack length, 2a	
kN	kip	kN	kip	cm	in.
594	133.5	603	135.5	12.55	4.94
676	152	688	154.6	12.73	5.01
697	156.6	707	159	12.85	5.06
709	159.4	719	161.6	12.98	5.11
726	163.2	737	165.6	13.26	5.22
738	166	747	168	13.36	5.26
743	167	754	169.4	13.44	5.29
758	170.4	766	172.2	13.61	5.36
762	171.4	773	173.8	13.84	5.45
768	172.6	776	174.5	14.05	5.53
770	173	778	174.8	14.30	5.63
772	173.6	778	174.8	14.55	5.73
772	173.6	781	175.6	15.54	6.12

STATIC TEST CRACK GROWTH FOR SN-18

Vertical load, P_V		Horizontal load, P_H		Crack length, 2a	
kN	kip	kN	kip	cm	in.
-676	-152	681	153	10.34	4.07
-1025	-230.5	1032	232	11.25	4.43
-1079	-242.5	1083	243.5	11.91	4.69
-1103	-248	1101	247.5	12.70	5.00
-1117	-251	1114	250.5	13.56	5.34
-1123	-252.5	1117	251	14.35	5.65
-1125	-253	1119	251.5	14.48	5.70
-1125	-253	1121	252	14.76	5.81
-1130	-254	1121	252	15.44	6.08
-1130	-254	1117	251	16.92	6.66
-1130	-254	1108	249	17.75	6.99

STATIC TEST CRACK GROWTH FOR SN-23

Vertical load, P_V		Crack length, 2a	
kN	kip	cm	in.
----	----	10.57	4.16
752	169	10.74	4.23
752	169	11.91	4.69
Note: $P_H = 0$.			

STATIC TEST CRACK GROWTH FOR SN-26

Vertical load, P_V		Horizontal load, P_H		Crack length, 2a	
kN	kip	kN	kips	cm	in.
-498	-112	1281	288	11.46	4.51
Note: The values above are those at the time a loading tab broke off.					

STATIC TEST CRACK GROWTH FOR SN-24

Vertical load, P_V		Horizontal load, P_H		Crack length, 2a	
kN	kip	kN	kip	cm	in.
−692	−155.5	692	155.5	10.52	4.14
−990	−222.5	994	223.5	11.40	4.49
−1010	−227	1014	228	12.04	4.74
−1028	−231	1023	230	12.67	4.99
−1028	−231	1025	230.5	12.90	5.08
−1032	−232	1025	230.5	13.28	5.23
−1034	−232.5	1025	230.5	13.56	5.34
−1034	−232.5	1023	230	13.82	5.44
−1036	−233	1023	230	14.50	5.71
−1036	−233	1021	229.5	15.47	6.09
−1036	−233	1008	226.5	16.48	6.49
−1036	−233	1008	226.5	18.01	7.09

STATIC TEST CRACK GROWTH FOR SN-25

Vertical load, P_V		Horizontal load, P_H		Crack length, 2a	
kN.	kip	kN	kip	cm	in.
−665	−149.5	665	149.5	10.19	4.01
−974	−219	976	219.5	11.38	4.48
−994	−223.5	992	223	11.84	4.66
−1001	−225	999	224.5	12.24	4.82
−1005	−226	1001	225	12.78	5.03
−1008	−226.5	1001	225	13.26	5.22
−1008	−226.5	999	224.5	13.59	5.35
−1010	−227	999	224.5	14.40	5.67
−1010	−227	996	224	16.64	6.55
	−227	974	219	17.45	6.87

LOADING SCHEDULE AND CRACK GROWTH FOR CYCLIC TEST OF SN-1

Nominal P_{max}, kN (kip)	Horizontal load, P_H, kN (kip)		Vertical load, P_V, kN (kip)		Increment of cycles, ΔN	Crack length, 2a	
	Max	Min	Max	Min		cm	in.
						$2a_i$ = 6.541	2.575
≤156 (<35)	---	---	--	--	1 740	6.566	2.585
289 (65)	294–300 (66.0–67.5)	18–27 (4.0–6.0)	289–294 (64.5–66.0)	29–33 (6.5–7.5)	7 756	6.777	2.668
					8 737	7.127	2.806
					8 255	7.462	2.938
347 (78)	348–360 (77.5–81.0)	29–44 (6.5–10.0)	347–351 (78.0–79.0)	33–40 (7.5–9.0)	2 481	7.653	3.013
					3 620	8.087	3.184
					5 383	8.588	3.381
405 (91)	409–414 (92.0–93.0)	33 (7.5)	400 (90.0)	44 (10.0)	2 417	9.129	3.594
					2 097	9.563	3.765
					882	------	----
311 (70)	302 (68.0)	22 (5.0)	307 (69.0)	40 (9.0)	2 673	------	----
408 (91)	403 (90.5)	56 (12.5)	47 (10.5)	47 (10.5)	1 102	9.959	3.921
408 (91)	408 (91.0)	42 (9.5)	403 (90.5)	42 (9.5)	2 395	10.44	4.110
463 (104)	466–472 (104.8–106.1)	41–48 (9.2–10.8)	460–463 (103.3–104.0)	42–45 (9.5–10.1)	1 059	10.90	4.291
					500	11.27	4.435
					404	11.59	4.564
534 (120)	540–542 (121.4–121.8)	43 (9.6)	530–536 (119.1–120.4)	39–40 (8.8–9.1)	209	12.10	4.765
					146	12.46	4.904
					203	13.01	5.121
565 (127)	576 (129.4–129.5)	45–47 (10.1–10.5)	560–562 (126.0–126.3)	36–39 (8.2–8.8)	105	13.65	5.373
					49	13.97	5.499
					50	14.21	5.596
				Total	52 263		

LOADING SCHEDULING AND CRACK GROWTH FOR CYCLIC TEST OF SN-2

Nominal P_{Max}, kN (kip)	Horizontal load, P_H, kN (kip)		Vertical load, P_V, kN (kip)		Increment of cycles, ΔN	Crack length, 2a	
	Max	Min	Max	Min		cm	in.
						$2a_i = 5.385$	2.120
222 (50)	227–234 (51.0–52.5)	20–27 (4.5–6.0)	220–225 (49.5–50.5)	24–27 (5.5–6.0)	6 561 11 000 12 030	5.458 5.644 5.928	2.149 2.222 2.334
289 (65)	282–285 (63.5–64.0)	27–31 6.0–7.0)	287–285 (64.5–64.0)	29–31 (6.5–7.0)	5 022 5 991 4 969	6.160 6.449 6.690	2.425 2.539 2.634
356 (80)	376–378 (84.5–85.0)	36–38 (8.0–8.5)	351–356 (79.0–80.0)	38–42 (8.5–9.5)	3 056 3 015 2 000	7.036 7.407 7.689	2.770 2.916 3.027
423 (95)	416–425 (93.5–95.5)	40–42 (9.0–9.5)	416–420 (93.5–94.5)	47–49 (10.5–11.0)	1 020 1 000 997	8.029 8.252 8.547	3.161 3.249 3.365
489 (110)	485–494 (109.0–111.0)	49–58 (11.0–13.0)	489–507 (110.0–114.0)	49–62 (11.0–14.0)	518 500 500 500 500	8.791 9.050 9.370 9.733 10.18	3.461 3.563 3.689 3.832 4.008
556 (125)	578–592 (130.0–133.0)	62–76 (14.0–17.0)	578–583 (130.0–131.0)	53–62 (12.0–14.0)	110 100 50 100 75 75	10.70 11.06 11.39 11.77 12.12 12.55	4.213 4.354 4.484 4.635 4.770 4.940
				Total	59 689		

LOADING SCHEDULE AND CRACK GROWTH FOR CYCLIC TEST OF SN-3

Nominal P_{Max}, kN (kip)	Horizontal load, P_H, kN (kip)			Vertical load, P_V, kN (kip)			Increment of cycles, ΔN	Crack length, 2a	
	High max	Low max	Min	High max	Low max	Min		Vertical crack	Horizontal crack
								cm	in.
								$2a_i = 5.469$	$2a_i = 2.153$
222 (50)	229–231 (51.5–52.0)	85–89 (19.0–20.0)	11–13 (2.5–3.0)	220–222 (49.5–50.0)	82–85 (18.5–19.0)	9 (2.0)	13 657	5.735 (2.258)	5.801 (2.284)
311 (70)	320 (72.0)	100–122 (22.5–27.5)	11 (2.5)	309–311 (69.5–70.0)	96–113 (21.5–25.5)	9–11 (2.0–2.5)	5 014	6.027 (2.373)	6.017 (2.369)
400 (90)	407 (91.5)	129–131 (29.0–29.5)	9–11 (2.0–2.5)	391–394 (88.0–88.5)	100–122 (22.5–27.5)	11–13 (2.5–3.0)	2 740	6.281 (2.473)	6.337 (2.495)
489 (110)	489 (110.0)	191 (43.0)	22 (5.0)	489 (110.0)	187 (42.0)	13 (3.0)	1 243	6.541 (2.575)	6.546 (2.577)
						Total	22 654		

LOADING SCHEDULE AND CRACK GROWTH FOR CYCLIC TEST OF SN-4

Nominal P_{Max}, kN (kip)	Horizontal load, P_H, kN (kip)		Vertical load, P_V, kN (kip)		Increment of cycles, ΔN	Crack length, 2a			
						Vertical crack		Horizontal crack	
	Max	Min	Max	Min		cm	in.	cm	in.
						$2a_i =$ 5.423	$2a_i =$ 2.135	$2a_i =$ 5.423	$2a_i =$ 2.135
111 (25)					85				
222 (50)	231–236 (52.0–53.0)	13–18 (3.0–4.0)	222–236 (50.0–53.0)	13–18 (3.0–4.0)	14 145	5.685	2.238	5.657	2.227
267 (60)	276 (62.0)	13 (3.0)	276 (62.0)	18 (4.0)	5 000	5.834	2.297	5.845	2.301
311 (70)	316–325 (71.0–73.0)	13 (3.0)	311–316 (70.0–71.0)	13 (3.0)	5 229	6.152	2.422	6.213	2.446
356 (80)	374 (84.0)	18 (4.0)	356 (80.0)	13 (3.0)	3 161	6.459	2.543	6.556	2.581
400 (90)	400 (90.0)	18 (4.0)	400 (90.0)	18 (4.0)	1 798	6.779	2.669	6.858	2.700
449 (100)	449 (101.0)	18 (4.0)	449 (100.0)	18 (4.0)	1 402	7.165	2.821	7.325	2.884
489 (110)	476 (107.0)	22 (5.0)	489 (110.0)	22 (5.0)	713	7.369	2.901	7.808	3.074
534 (120)	529 (119.0)	13 (3.0)	525 (118.0)	18 (4.0)	268	7.564	2.978	8.186	3.223
578 (130)	565 (127.0)	27 (6.0)	569 (128.0)	27 (6.0)	99	7.724	3.041	8.468	3.334
				Total	31 970				

LOADING SCHEDULE AND CRACK GROWTH FOR CYCLIC TEST OF SN-5

Nominal P_{Max}, kN (kip)	Horizontal load, P_H, kN (kip)			Vertical load, P_V, kN (kip)			Increment of cycles, ΔN	Crack length, 2a	
	High max	Low max	Min	High max	Low max	Min		Horizontal crack	Vertical crack
								cm (in.)	cm (in.)
								$2a_i = 5.283$ = (2.080)	$2a_i = 5.283$ = (2.080)
111 (25)	111-114 (25.0-25.6)	44-46 (10.0-10.4)	9-12 (2.0-2.8)	106-109 (23.8-24.6)	39-41 (8.8-9.3)	3-5 (0.6-1.2)	25 264	5.550 (2.185)	5.474 (2.155)
133 (30)	130-135 (29.2-30.4)	49-53 (11.0-12.0)	11-16 (2.4-3.6)	133-135 (30.0-30.4)	51-54 (11.4-12.2)	6-8 (1.4-1.8)	6 425	5.923 (2.332)	5.474 (2.155)
156 (35)	153-155 (34.4-34.8)	58-61 (13.0-13.7)	9-14 (2.0-3.1)	149-155 (33.6-34.9)	54-55 (12.2-12.4)	3-8 (0.6-1.8)	5 462	6.500 (2.559)	5.608 (2.208)
178 (40)	176 (39.6)	72 (16.2)	14 (3.2)	177 (39.8)	69 (15.6)	14 (3.2)	2 817	7.059 (2.779)	5.756 (2.266)
200 (45)	198 (44.4)	80 (18.0)	11 (2.4)	193 (43.4)	73 (16.4)	5 (1.2)	1 510	7.529 (2.964)	5.946 (2.341)
222 (50)	205 (46.0)	81 (18.2)	33 (7.4)	215 (48.4)	84 (18.8)	12 (2.6)	1 007	8.082 (3.182)	6.093 (2.399)
245 (55)	225 (50.6)	92 (20.6)	15 (3.4)	243 (54.6)	98 (22.0)	15 (3.4)	255	8.506 (3.349)	6.185 (2.435)
245 (55)	229 (51.4)	95 (21.4)	25 (5.6)	240 (54.0)	96 (21.6)	12 (2.8)	254	8.948 (3.523)	6.210 (2.445)
267 (60)	254 (57.0)	113 (25.5)	18 (4.0)	265 (59.5)	113 (25.5)	16 (3.5)	111	9.373 (3.690)	6.231 (2.453)
						Total	43 105		

LOADING SCHEDULE AND CRACK GROWTH FOR CYCLIC TEST OF SN-6

Nominal P_{Max}, kN (kip)	Horizontal load, P_H, kN (kip)		Vertical load, P_V, kN (kip)		Increment of cycles, ΔN	Crack length, 2a	
	Max	Min	Max	Min		cm	in.
						$2a_i = 4.928$	$2a_i = 1.940$
116 (26)	120 (27.0)	17 (3.8)	121 (27.2)	17 (3.8)	20 852	5.197	2.046
138 (31)	141 (31.6)	17 (3.8)	137 (30.8)	15 (3.4)	15 000	6.139	2.417
160 (36)	156 (35.0)	18 (4.0)	157 (35.2)	16 (3.6)	5 013	6.614	2.604
	155 (34.8)	18 (4.0)	157 (35.2)	13 (3.0)	2 917	6.914	2.722
	157 (35.2)	18 (4.0)	157 (35.4)	16 (3.6)	5 000	7.209	2.838
178 (40)	179 (40.2)	19 (4.2)	180 (40.4)	19 (4.2)	1 510	7.523	2.962
	180 (40.4)	20 (4.6)	181 (40.6)	21 (4.8)	1 500	7.851	3.091
	180 (40.4)	20 (4.6)	181 (40.6)	21 (4.8)	1 500	8.197	3.227
200 (45)	199 (44.8)	24 (5.4)	198 (44.6)	20 (4.4)	511	8.395	3.305
	200 (45.0)	24 (5.4)	198 (44.6)	20 (4.6)	1 000	8.654	3.407
	199 (44.8)	22 (5.0)	199 (44.8)	19 (4.2)	1 000	9.352	3.682
222 (50)	222 (49.8)	25 (5.6)	221 (49.6)	26 (5.8)	509	9.873	3.887
	222 (49.8)	25 (5.6)	218 (49.0)	23 (5.2)	500	10.36	4.080
	222 (50.0)	25 (5.6)	218 (49.0)	24 (5.4)	500	10.91	4.297
245 (55)	244 (54.8)	25 (5.6)	237 (53.2)	24 (5.4)	210	11.37	4.478
	242 (54.4)	25 (5.6)	244 (54.8)	28 (6.4)	200	11.82	4.652
	243 (54.6)	24 (5.4)	242 (54.4)	28 (6.2)	200	12.27	4.832
				Total	55 005		

LOADING SCHEDULE AND CRACK GROWTH FOR CYCLIC TEST OF SN-7

Nominal P_{Max}, kN (kip)	Horizontal load, P_H, kN (kip)		Vertical load, P_V, kN (kip)		Increment of cycles, ΔN	Crack length, 2a	
	Max	Min	Max	Min		cm	in.
						$2a_i = 5.166$	2.034
289 (65)	282 (63.5)	24 (5.5)	287 (64.5)	31 (7.0)	4 982	5.527	2.176
					5 000	5.878	2.314
					5 000	6.220	2.449
311 (70)	311 (70.0)	29 (6.5)	322 (72.5)	31 (7.0)	3 467	6.642	2.615
					3 500	7.046	2.774
					3 500	7.523	2.962
343 (77)	347 (78.0)	31 (7.0)	345 (84.5)	38 (8.5)	2 331	7.925	3.120
					2 000	8.351	3.288
					2 000	8.745	3.443
378 (85)	376 (84.5)	31 (7.0)	376 (84.5)	38 (8.5)	1 213	9.103	3.584
					1 200	9.535	3.754
					1 200	9.837	3.873
409 (92)	409 (92.0)	36 (8.0)	409 (92.0)	42 (9.5)	755	10.23	4.028
					750	10.68	4.205
					750	11.14	4.387
					750	11.68	4.600
445 (100)	440 (99.0)	44 (10.0)	445 (100.0)	44 (10.0)	306	12.17	4.791
					300	12.54	4.937
					300	12.92	5.088
476 (107)	472 (106.0)	49 (11.0)	476 (107.0)	49 (11.0)	155	13.36	5.259
					150	13.84	5.449
					150	14.31	5.633
512 (115)	507 (114.0)	58 (13.0)	512 (115.0)	53 (12.0)	80	14.75	5.805
					75	15.31	6.028
					75	15.91	6.264
					75	16.61	6.538
					75	17.42	6.860
					75	18.33	7.218
					75	19.70	7.757
					75	21.54	8.479
					75	24.98	9.833
Fracture	503 (113.0)		516 (116.0)		16	28.88[a]	------
			Total		40 455		11.37[a]

[a] Extrapolated from compliance data.

LOADING SCHEDULE AND CRACK GROWTH FOR CYCLIC TEST OF SN-8

Nominal P_{Max}, kN (kip)	Horizontal load, P_H, kN (kip)			Vertical load, P_V, kN (kip)			Increment of cycles, ΔN	Crack length, 2a			
								Horizontal crack		Vertical crack	
	High max	Low max	Min	High max	Low max	Min		cm	in.	cm	in.
								$2a_i = 6.375$	$2a_i = 2.510$		
289 (65)	287 (64.5)	111 (25.0)	16 (3.5)	276 (62.0)	107 (24.0)	18 (4.0)	346	6.584	2.592	Disregard	
289 (65)	285 (64.0)	107 (24.0)	11 (2.5)	276 (62.0)	105 (23.5)	13 (3.0)	6 525	6.965	2.742		
289 (65)	285 (64.0)	109 (24.5)	13 (3.0)	276 (62.0)	107 (24.0)	16 (3.5)	6 000	7.602	2.993		
320 (72)	311 (70.0)	122 (27.5)	16 (3.5)	314 (70.5)	129 (29.0)	24 (5.5)	3 006	7.950	3.130		
351 (79)	349 (78.5)	140 (31.5)	16 (3.5)	343 (77.0)	140 (31.5)	22 (5.0)	1 500	8.235	3.242		
383 (86)	378 (85.0)	156 (35.0)	20 (4.5)	365 (82.0)	151 (34.0)	22 (5.0)	1 500	8.580	3.378		
383 (86)	378 (85.0)	156 (35.0)	20 (4.5)	365 (82.0)	151 (34.0)	22 (5.0)	1 500	9.055	3.565		
414 (93)	413 (93.0)	169 (38.0)	36 (8.0)	427 (96.0)	182 (41.0)	36 (8.0)	750	9.444	3.718		
445 (100)	423 (95.0)	187 (42.0)	36 (8.0)	418 (94.0)	182 (41.0)	31 (7.0)	750	9.779	3.850		
476 (107)	458 (103.0)	185 (41.5)	44 (10.0)	445 (100.0)	189 (42.5)	33 (7.5)	514	10.33	4.065		
476 (107)	458 (103.0)	185 (41.5)	44 (10.0)	445 (100.0)	189 (42.5)	33 (7.5)	500	10.95	4.309		
507 (114)	485 (109.0)	205 (46.0)	49 (11.0)	478 (107.5)	205 (46.0)	33 (7.5)	350	11.83	4.659		
507 (114)	480 (108.0)	200 (45.0)	53 (12.0)	472 (106.0)	205 (46.0)	31 (7.0)	169	12.42	4.890		
538 (121)	514 (115.5)	222 (50.0)	47 (10.5)	505 (113.5)	222 (50.0)	40 (9.0)	100	13.17	5.185		
538 (121)	512 (115.0)	218 (49.0)	47 (10.5)	505 (113.5)	220 (49.5)	38 (8.5)	100	13.83	5.455		
538 (121)	------	------	------	------	------	------	63	14.73	5.798		
							Total 23 673				

Nominal P_{Max}, kN (kip)	Horizontal load, P_H, kN (kip)			Vertical load, P_V, kN (kip)			Increment of cycles, ΔN	Crack length, 2a	
	High max	Low max	Min	High max	Low max	Min		Horizontal crack cm (in.)	Vertical crack cm (in.)
								$2a_i = 5.474$ = (2.155)	$2a_i = 5.474$ = (2.155)
289 (65)	285 (64.0)	111 (25.0)	9 (2.0)	282 (63.5)	105 (23.5)	11 (2.5)	7 246	5.977 (2.353)	5.842 (2.300)
	285 (64.0)	113 (25.5)	13 (3.0)	282 (63.5)	107 (24.0)	13 (3.0)	6 000	6.327 (2.491)	6.142 (2.418)
	289 (65.0)	113 (25.5)	13 (3.0)	280 (63.0)	107 (24.0)	13 (3.0)	5 003	6.614 (2.604)	6.345 (2.498)
320 (72)	318 (71.5)	129 (29.0)	13 (3.0)	311 (70.0)	120 (27.0)	16 (3.5)	3 500	6.957 (2.739)	6.701 (2.638)
	318 (71.5)	129 (29.0)	16 (3.5)	311 (70.0)	120 (27.0)	16 (3.5)	2 842	7.239 (2.850)	7.084 (2.789)
	320 (72.0)	129 (29.0)	16 (3.5)	307 (69.0)	118 (26.5)	13 (3.0)	3 511	7.648 (3.011)	7.569 (2.980)
351 (79)	351 (79.0)	142 (32.0)	18 (4.0)	343 (77.0)	138 (31.0)	20 (4.5)	1 761	7.955 (3.132)	7.899 (3.110)
	349 (78.5)	142 (32.0)	16 (3.5)	338 (76.0)	136 (30.5)	16 (3.5)	1 750	8.242 (3.245)	8.319 (3.275)
	349 (78.5)	142 (32.0)	16 (3.5)	343 (77.0)	138 (31.0)	18 (4.0)	1 750	8.567 (3.373)	8.766 (3.451)
383 (86)	376 (84.5)	160 (36.0)	16 (3.5)	371 (83.5)	156 (35.0)	20 (4.5)	1 205	8.918 (3.511)	9.268 (3.649)
	378 (85.0)	160 (36.0)	16 (3.5)	369 (83.0)	156 (35.0)	20 (4.5)	1 200	9.365 (3.687)	9.868 (3.885)
	378 (85.0)	160 (36.0)	16 (3.5)	374 (84.0)	158 (35.5)	22 (5.0)	1 200	9.761 (3.843)	10.63 (4.185)
414 (93)	407 (91.5)	178 (40.0)	16 (3.5)	405 (91.0)	173 (39.0)	22 (5.0)	603	10.04 (3.951)	11.27 (4.436)
	407 (91.5)	180 (40.5)	18 (4.0)	403 (90.5)	173 (39.0)	22 (5.0)	600	10.35 (4.074)	12.07 (4.752)
	409 (92.0)	182 (41.0)	18 (4.0)	403 (90.5)	169 (38.0)	20 (4.5)	327	10.58 (4.164)	12.66 (4.985)
445 (100)	436 (98.0)	191 (43.0)	27 (6.0)	436 (98.0)	191 (43.0)	22 (5.0)	150	--------	13.18 (5.188)
	436 (98.0)	191 (43.0)	27 (6.0)	436 (98.0)	191 (43.0)	27 (6.0)	150	10.65 (4.192)	13.80 (5.431)
	445 (100.0)	196 (44.0)	31 (7.0)	436 (98.0)	191 (43.0)	27 (6.0)	150	--------	14.50 (5.707)
476 (107)	472 (106.0)	200 (45.0)	31 (7.0)	472 (106.0)	205 (46.0)	31 (7.0)	75	10.92 (4.300)	15.28 (6.017)
	472 (106.0)	200 (45.0)	31 (7.0)	472 (106.0)	209 (47.0)	31 (7.0)	75	--------	16.09 (6.335)
	472 (106.0)	200 (45.0)	27 (6.0)	463 (104.0)	200 (45.0)	22 (5.0)	80	--------	17.11 (6.735)
507 (114)	503 (113.0)	222 (50.0)	31 (7.0)	503 (113.0)	218 (49.0)	31 (7.0)	30	11.04 (4.348)	18.09 (7.123)
	503 (113.0)	222 (50.0)	31 (7.0)	498 (112.0)	218 (49.0)	31 (7.0)	30	--------	19.15 (7.538)
	503 (113.0)	218 (49.0)	31 (7.0)	498 (112.0)	218 (49.0)	31 (7.0)	30	11.13 (4.381)	20.46 (8.056)
	503 (113.0)	218 (49.0)	31 (7.0)	498 (112.0)	218 (49.0)	31 (7.0)	30	11.19 (4.406)	22.83 (8.989)
Fracture	485 (109)			205 (46.0)			8	--------	23.75[a] (9.35[a])
							Total 39 306		

[a] Extrapolated from crack growth rate.

LOADING SCHEDULE AND CRACK GROWTH FOR CYCLIC TEST OF SN-27

Nominal P_{Max}, kN (kip)	Horizontal load, P_H, kN (kip)		Vertical load, P_V, kN (kip)		Increment of cycles, ΔN	Crack length, 2a	
	Max	Min	Max	Min		cm	in.
						$2a_i = 7.701$	$2a_i = 3.032$
267 (60)	269 (60.5)	20 (4.5)	265 (59.5)	18 (4.0)	884	7.904	3.112
	267 (60.0)	20 (4.5)	258 (58.0)	20 (4.5)	5 481	8.197	3.227
	267 (60.0)	18 (4.0)	269 (60.5)	18 (4.0)	4 970	9.195	3.620
267 (60)	269 (60.5)	20 (4.5)	274 (61.5)	24 (5.5)	1 732	9.614	3.785
	267 (60.0)	18 (4.0)	265 (59.5)	20 (4.5)	1 597	9.962	3.922
	267 (60.0)	18 (4.0)	267 (60.0)	18 (4.0)	1.719	10.34	4.081
267 (60)	267 (60.0)	18 (4.0)	267 (60.0)	20 (4.5)	1 442	10.78	4.245
	271 (61.0)	18 (4.0)	267 (60.0)	18 (4.0)	1 788	11.30	4.447
	271 (61.0)	18 (4.0)	262 (59.0)	18 (4.0)	1 307	11.66	4.590
311 (70)	316 (71.0)	22 (5.0)	309 (69.5)	20 (4.5)	786	12.11	4.768
	318 (71.5)	24 (5.5)	311 (70.0)	22 (5.0)	895	12.66	4.983
	318 (71.5)	27 (6.0)	309 (69.5)	20 (4.5)	899	13.20	5.198
356 (80)	360 (81.0)	22 (5.0)	356 (80.0)	24 (5.5)	408	13.90	5.471
	363 (81.5)	22 (5.0)	354 (79.5)	22 (5.0)	354	14.40	5.671
	360 (81.0)	22 (5.0)	356 (80.0)	27 (6.0)	392	14.95	5.884
400 (90)	405 (91.0)	29 (6.5)	387 (87.0)	27 (6.0)	160	15.44	6.079
	407 (91.5)	27 (6.0)	387 (87.0)	27 (6.0)	150	15.98	6.290
	407 (91.5)	29 (6.5)	387 (87.0)	24 (5.5)	150	16.40	6.458
445 (100)	431 (97.0)	44 (10.0)	440 (99.0)	31 (7.0)	72	16.84	6.629
	436 (98.0)	44 (10.0)	436 (98.0)	31 (7.0)	60	17.16	6.757
	436 (98.0)	44 (10.0)	436 (98.0)	27 (6.0)	60	17.42	6.860
445 (100)	436 (98.0)	44 (10.0)	436 (98.0)	31 (7.0)	120	18.09	7.116
	436 (98.0)	44 (10.0)	436 (98.0)	36 (8.0)	120	18.81	7.404
	436 (98.0)	44 (10.0)	436 (98.0)	31 (7.0)	120	19.56	7.700

LOADING SCHEDULE AND CRACK GROWTH FOR CYCLIC TEST OF SN-27 (concl)

Nominal P_{Max}, kN (kip)	Horizontal load, P_H, kN (kip)		Vertical load, P_V, kN (kip)		Increment of cycles, ΔN	Crack length, 2a	
	Max	Min	Max	Min		cm	in.
445 (100)	436 (98.0)	44 (10.0)	436 (98.0)	31 (7.0)	120	20.53	8.083
	431 (97.0)	44 (10.0)	436 (98.0)	27 (6.0)	120	21.43	8.436
	436 (98.0)	44 (10.0)	436 (98.0)	27 (6.0)	120	22.57	8.886
445 (100)	436 (98.0)	44 (10.0)	436 (98.0)	27 (6.0)	120	23.93	9.421
	436 (98.0)	49 (11.0)	436 (98.0)	27 (6.0)	60	-----	-----
				Total	26 206		

APPENDIX E

PHOTOGRAPHS OF SPECIMENS AFTER TESTING

Note: This appendix contains photographs of all the specimens after testing, in numerical order.
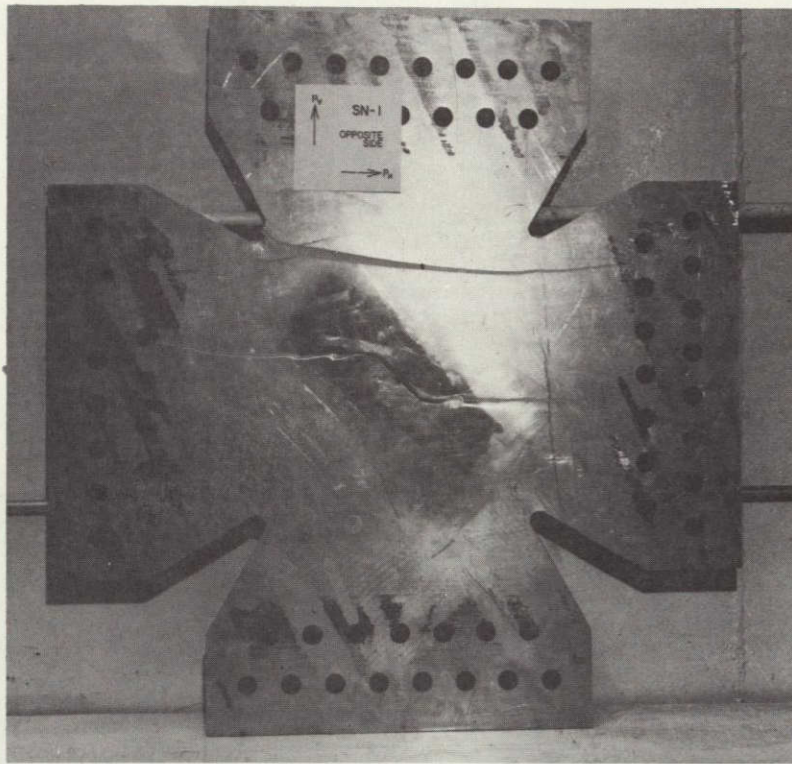
Figure 1. - SN-1 after Fracture, Console Side.
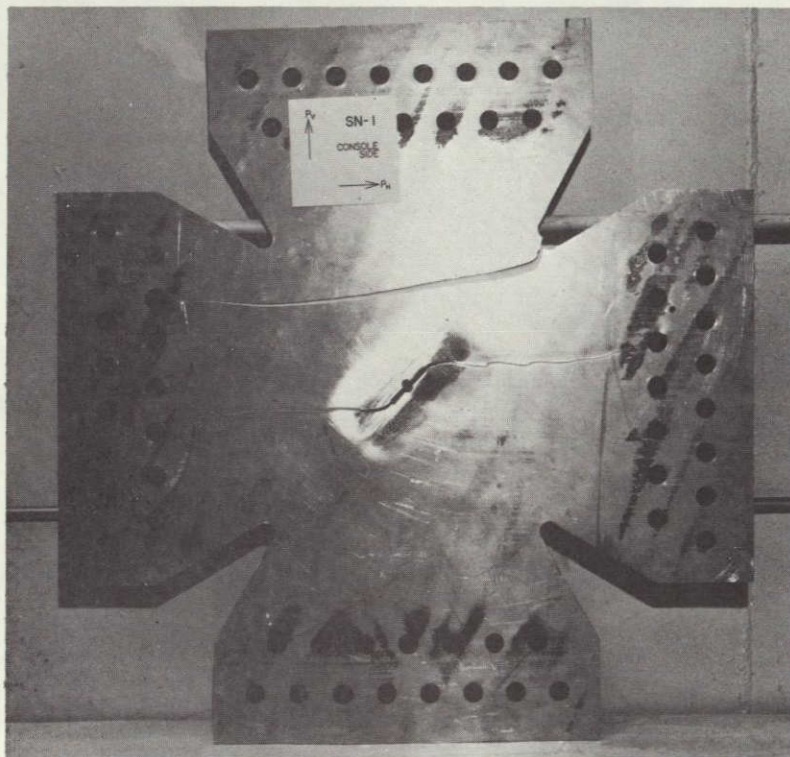
Figure 2. - SN-1 after Fracture, Opposite Side.

Figure 3. - Closeup of Console Side, SN-1.
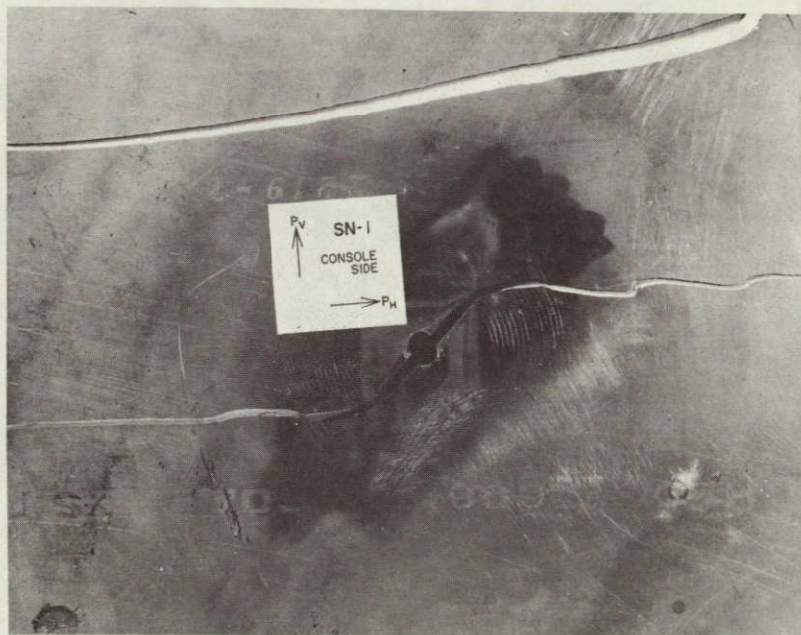
Figure 4. - Closeup of Opposite Side, SN-1.
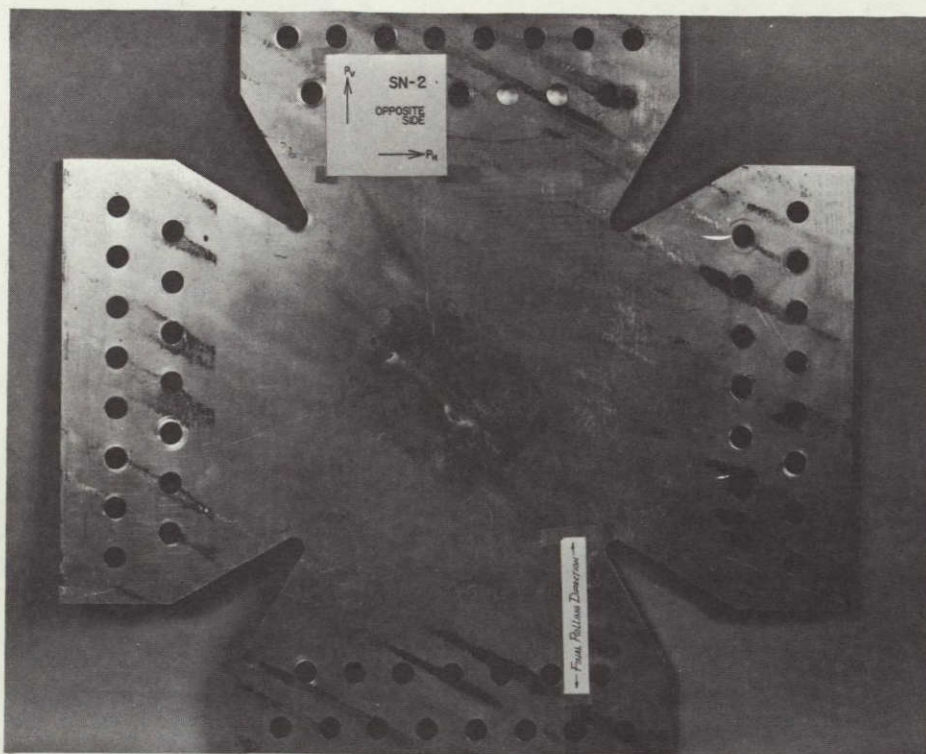
Figure 5. - Overall View of SN-2 after Testing, Console Side.
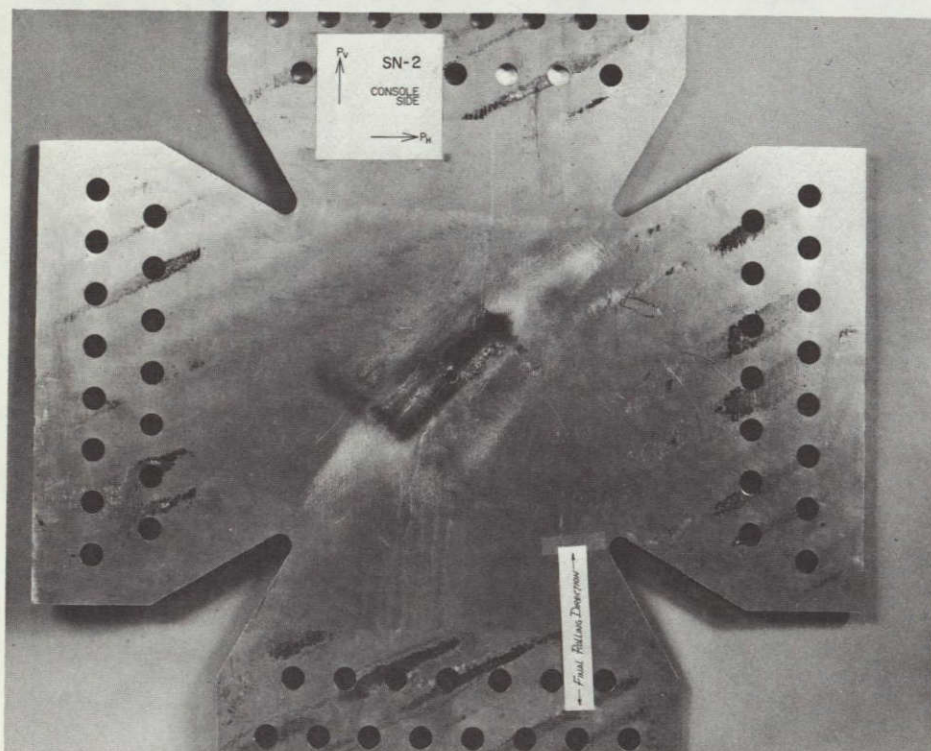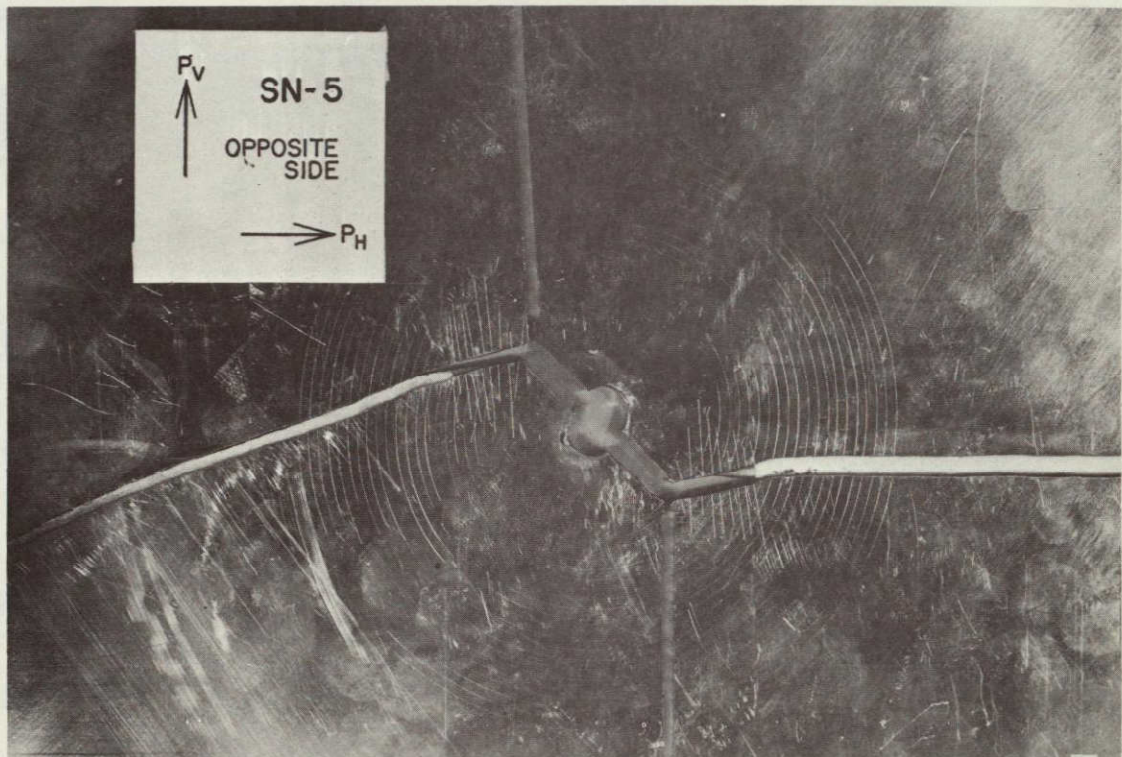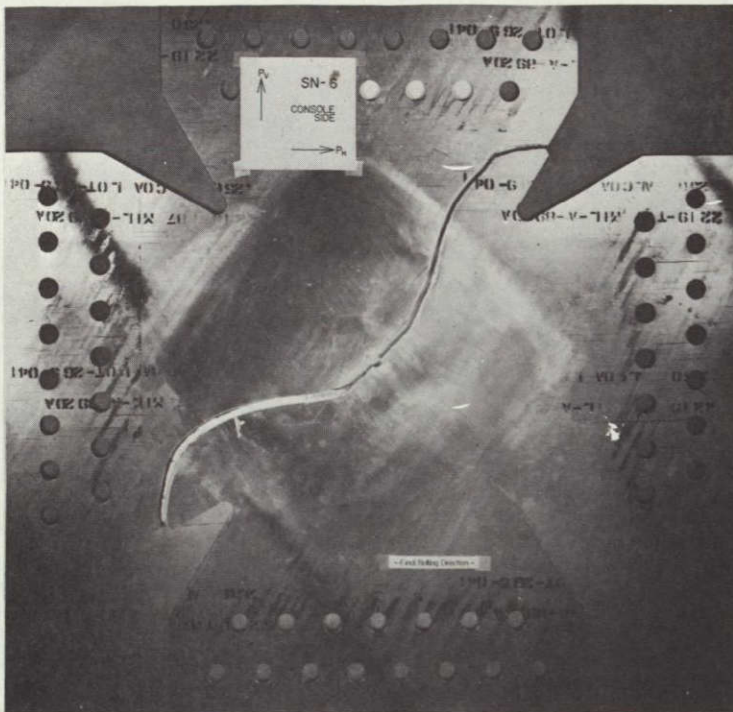

Figure 6. - Overall View of SN-2 after Testing, Opposite Side.
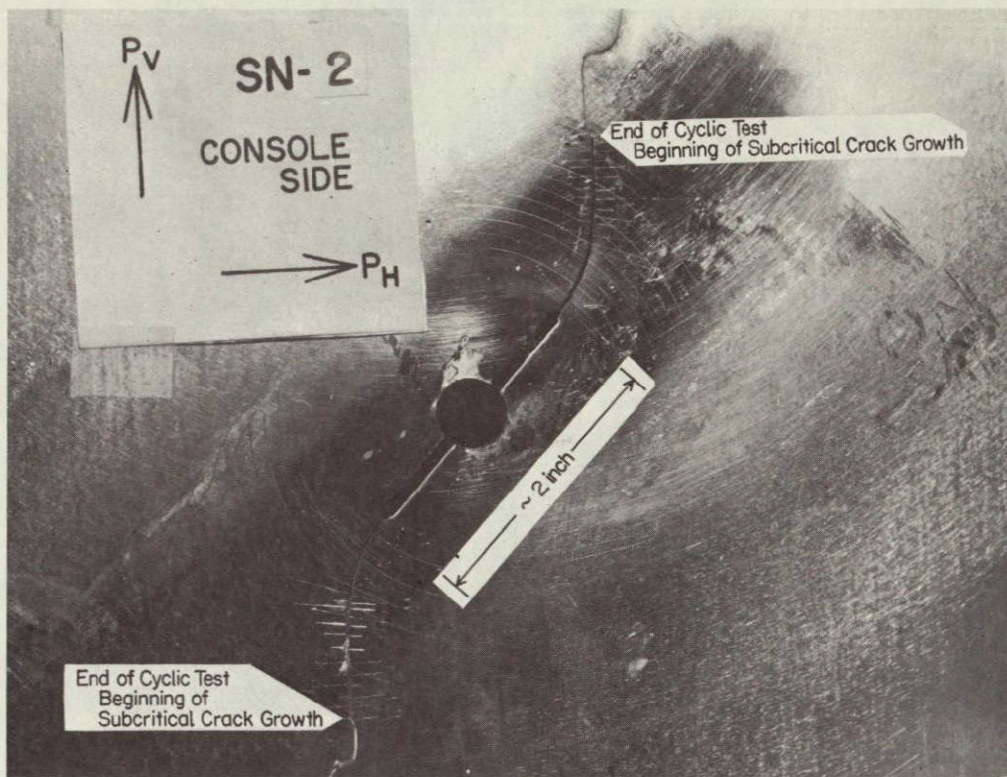
Figure 7. – Closeup View of SN-2 after Fracture, Console Side.
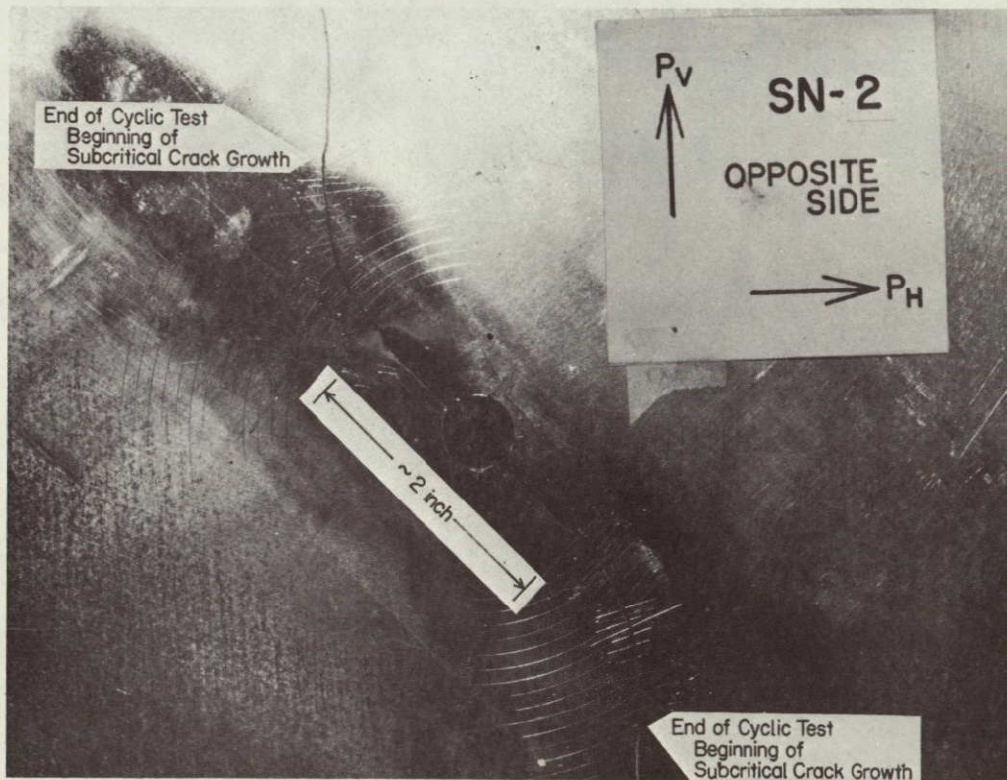
Figure 8. – Closeup View of SN-2 after Fracture, Opposite Side.
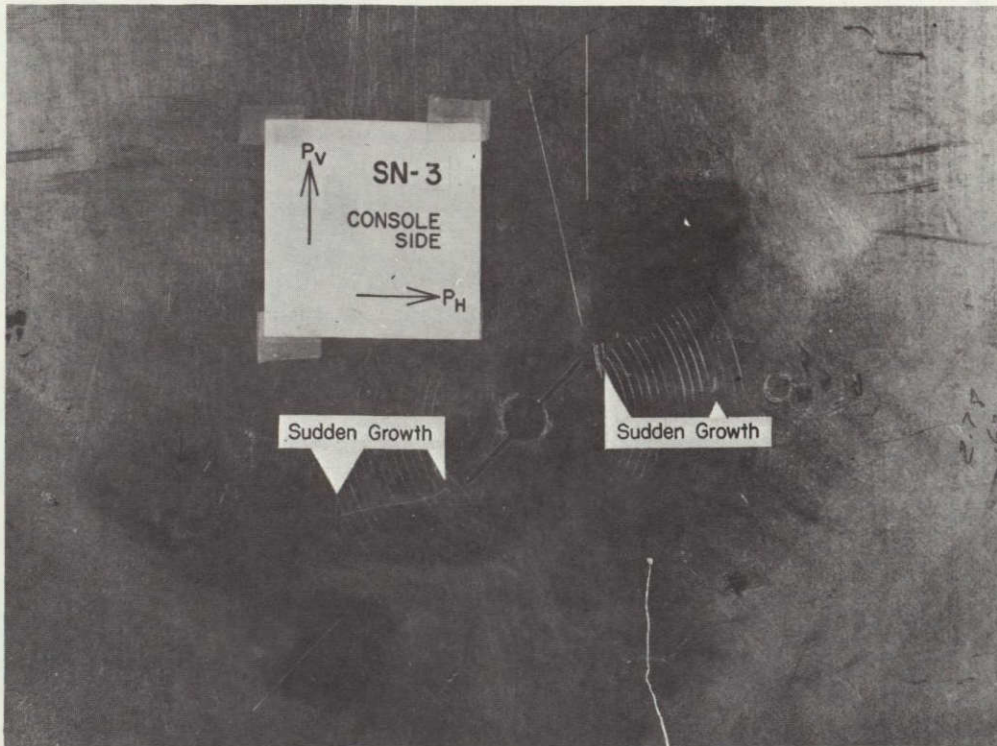
Figure 9. – Central Area of SN-3 after Testing, Console Side.
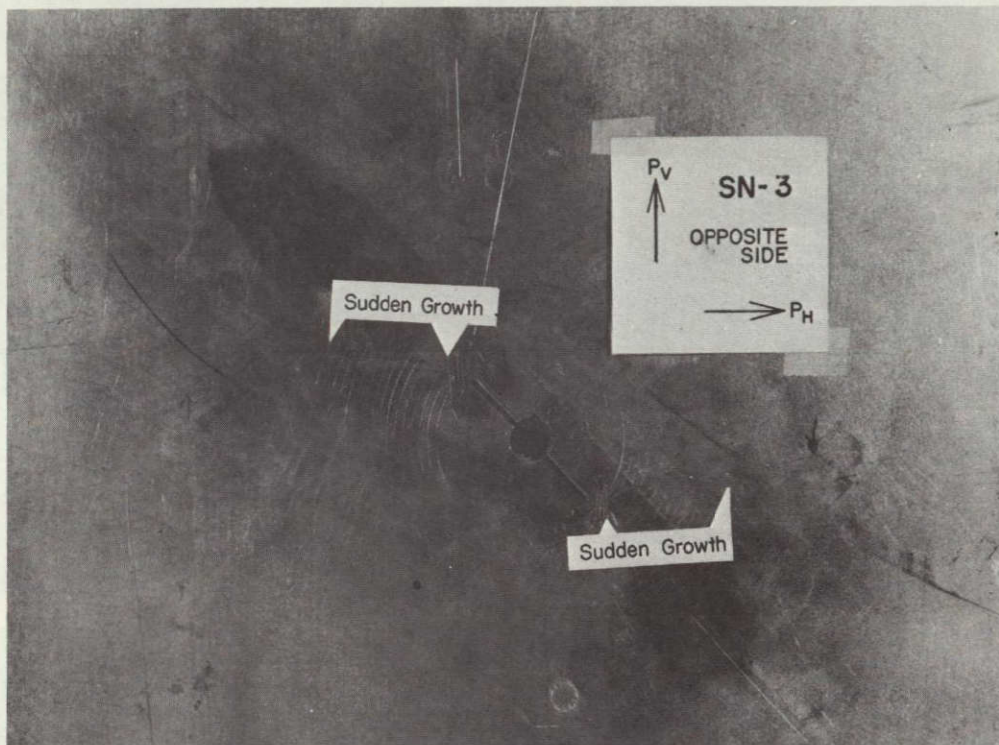
Figure 10. – Central Area of SN-3 after Testing, Opposite Side.
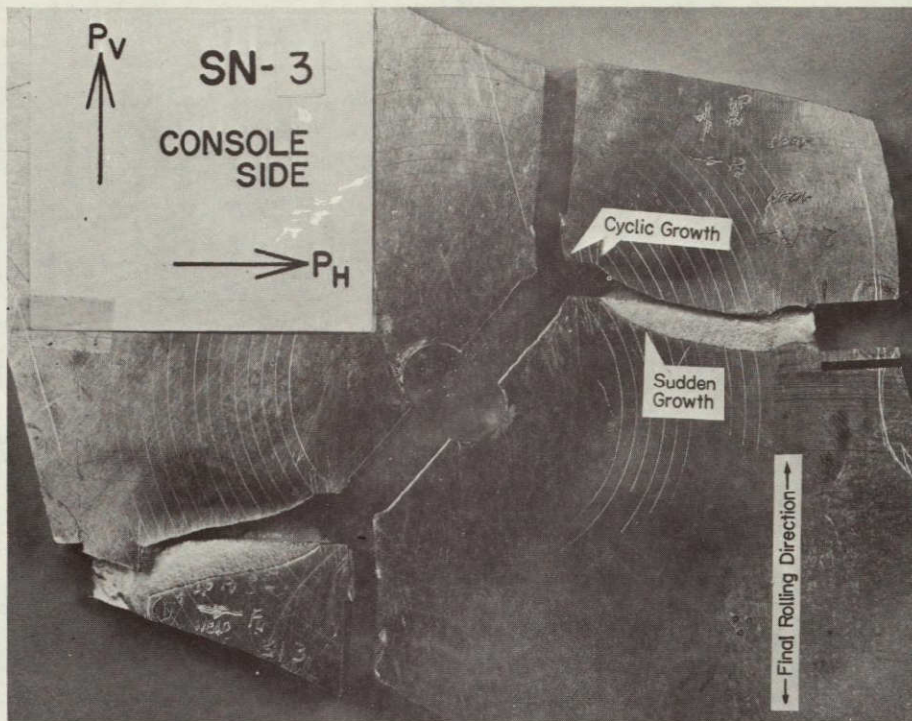
Figure 11. - Closeup of SN-3 after Testing, Console Side.
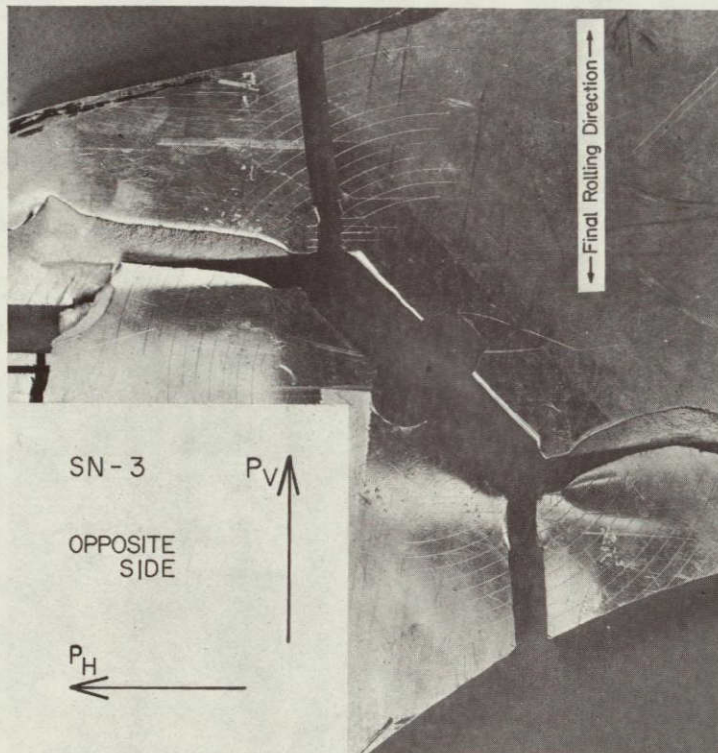
Figure 12. - Closeup of SN-3 after Testing,
Opposite Side.
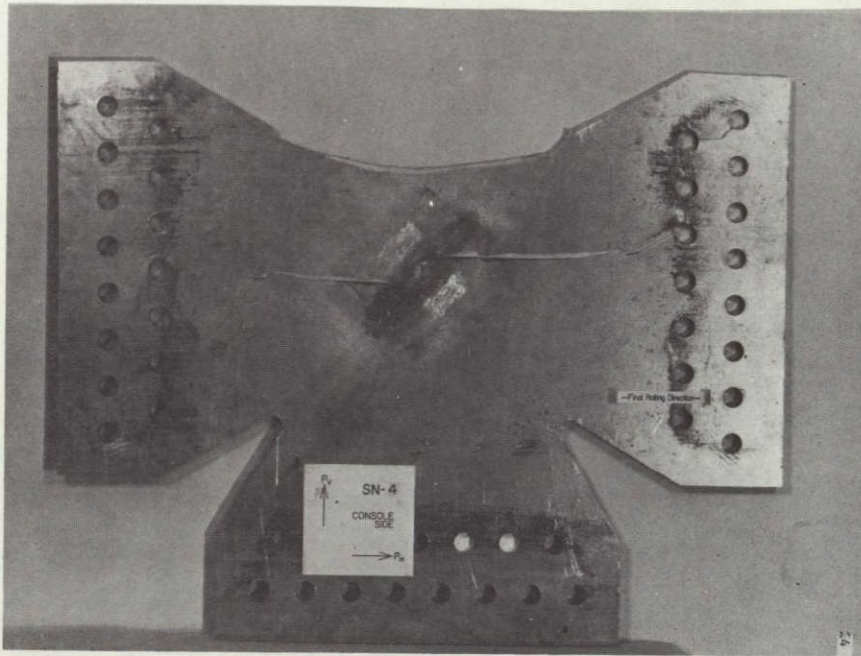
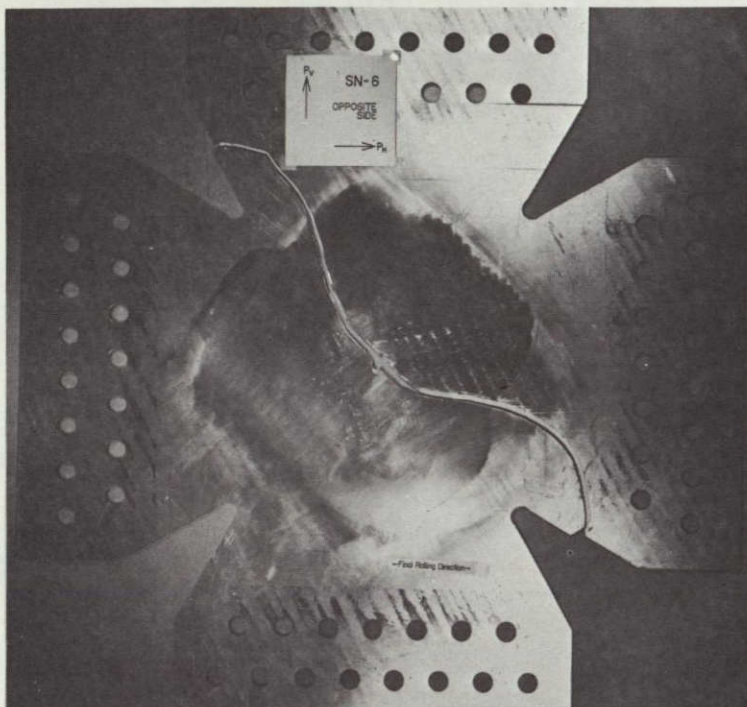Figure 13. - Overall View of SN-4 after Testing, Console Side.
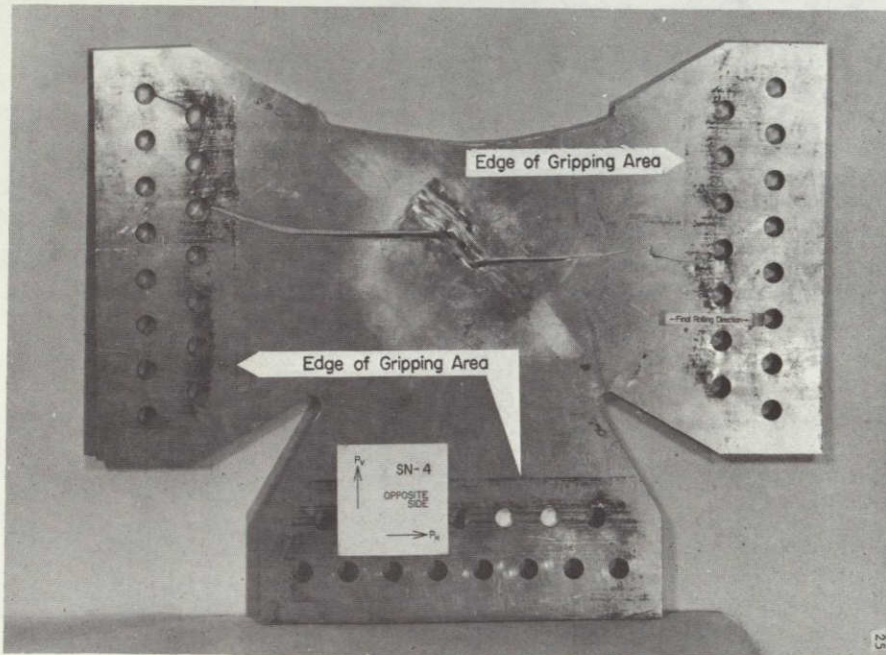
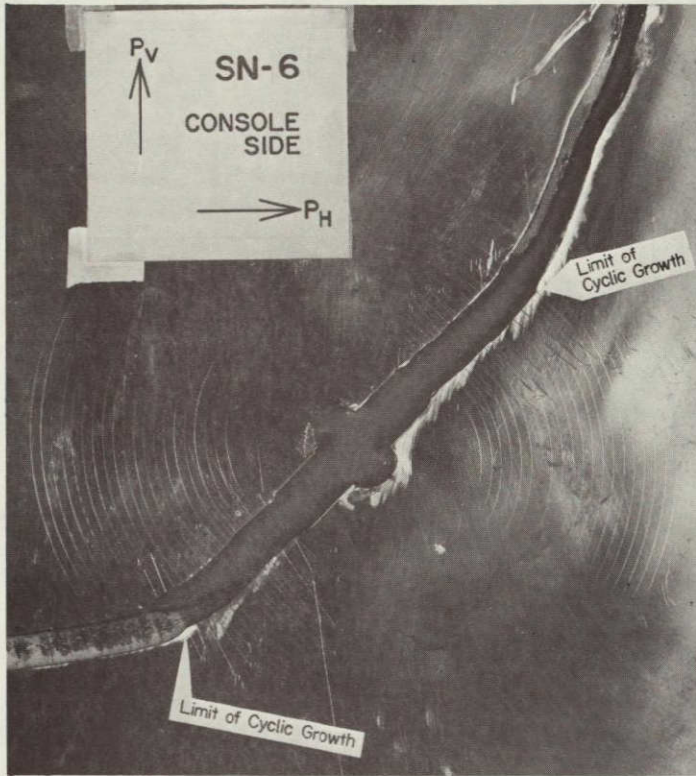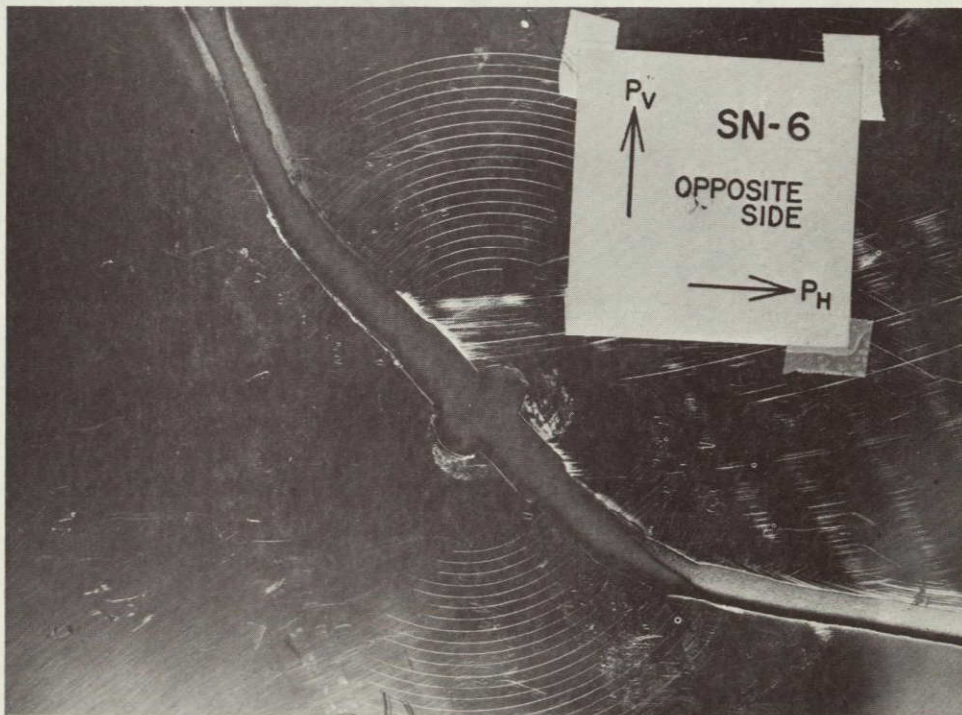Figure 14. - Overall View of SN-4 after Testing, Opposite Side.

200
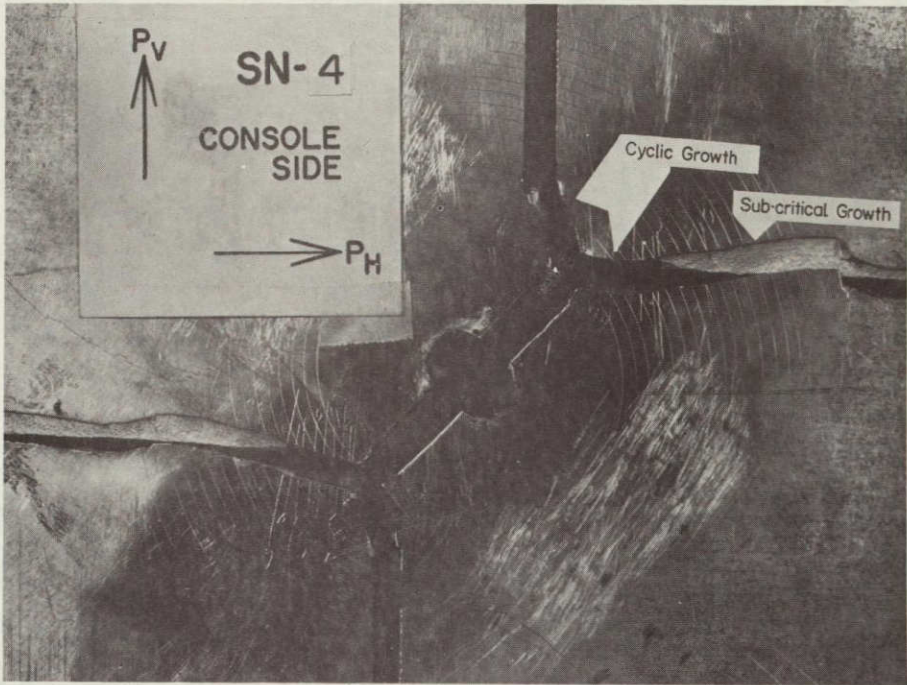
Figure 15. – Closeup of SN-4 after Testing, Console Side.
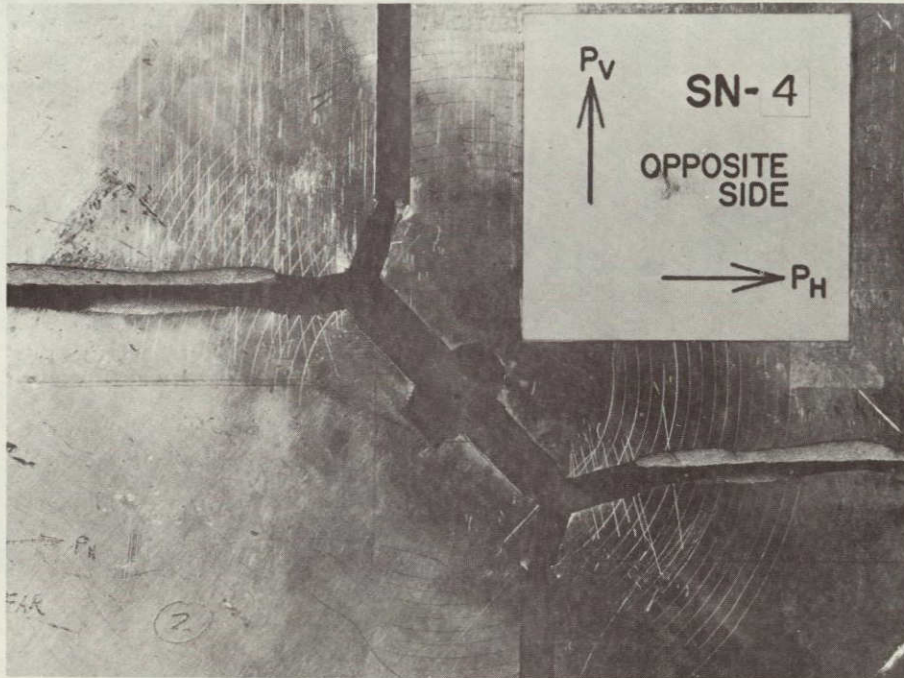
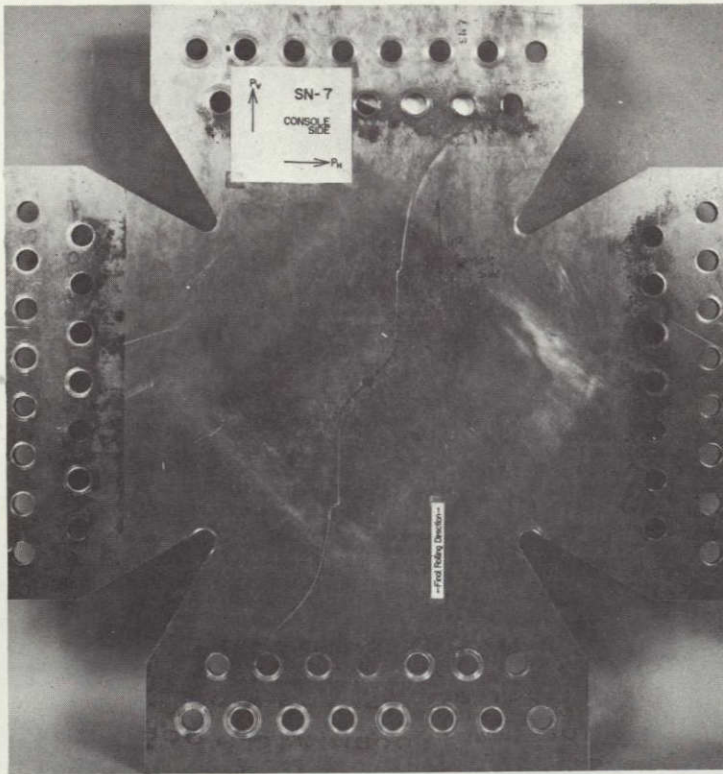Figure 16. – Closeup of SN-4 after Testing, Opposite Side.
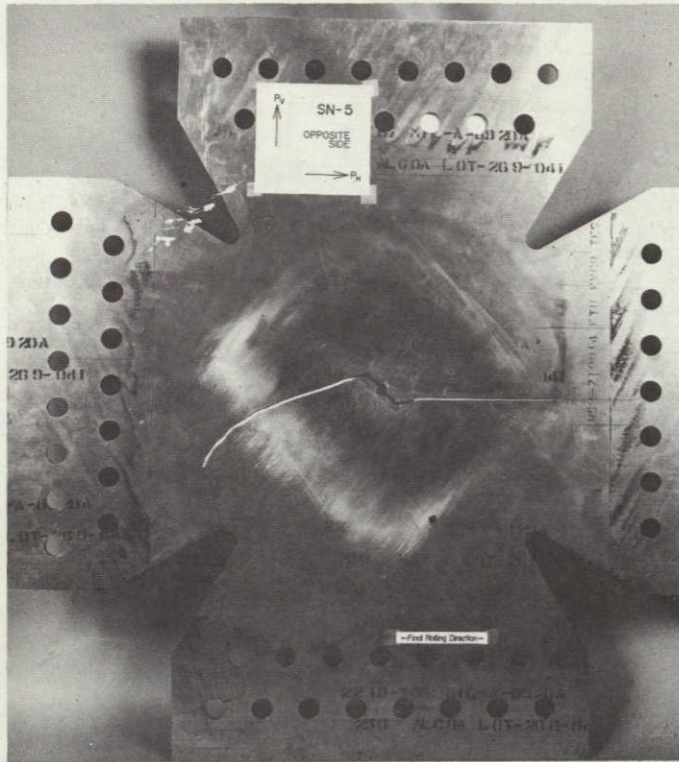
Figure 17. - Overall View of SN-5 after Testing,
Console Side.
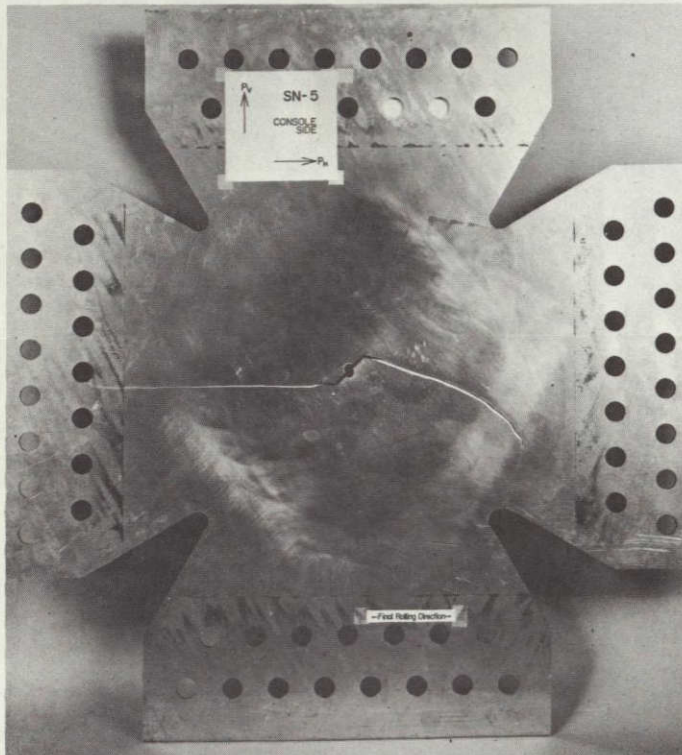
Figure 18. - Overall View of SN-5 after Testing,
Opposite Side.
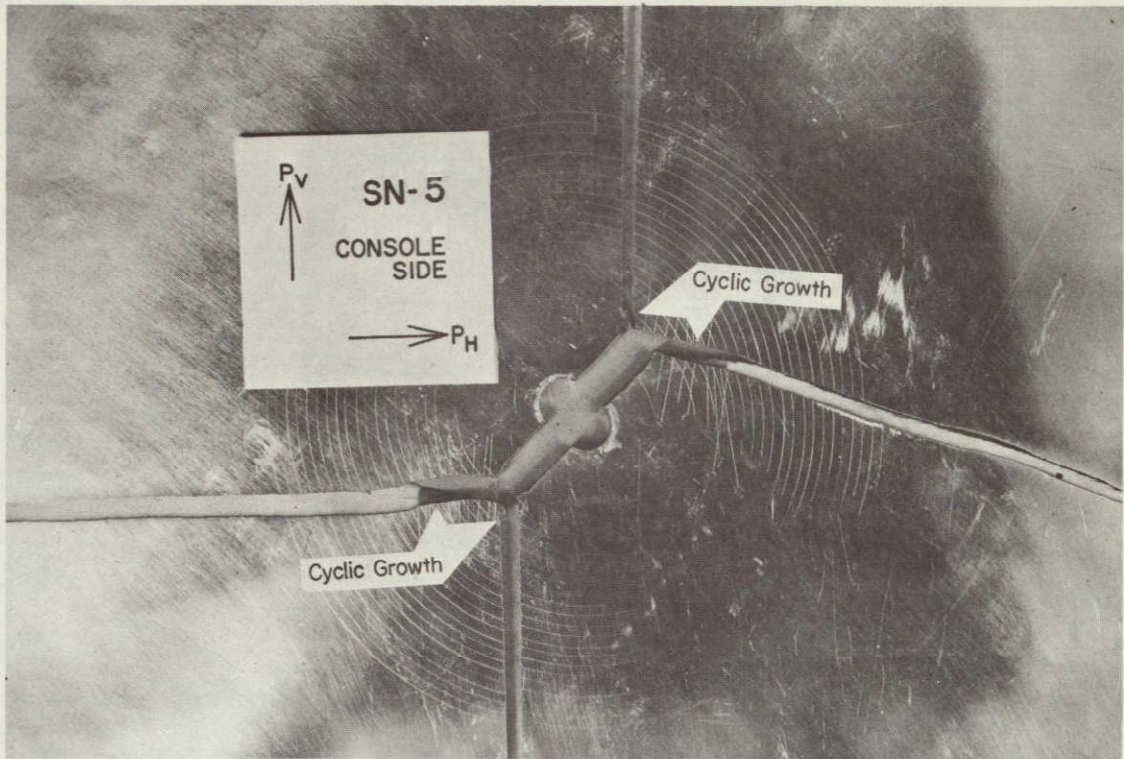
Figure 19. - Closeup of SN-5 after Cutting, Console Side.

Figure 20. - Closeup of SN-5 after Cutting, Opposite Side.

Figure 21. – Overall View of SN-6 after Testing,
Console Side.

Figure 22. – Overall View of SN-6 after Testing,
Opposite Side.

Figure 23. - Closeup of SN-6 after Testing,
Console Side.

Figure 24. - Closeup of SN-6 after Testing, Opposite Side.

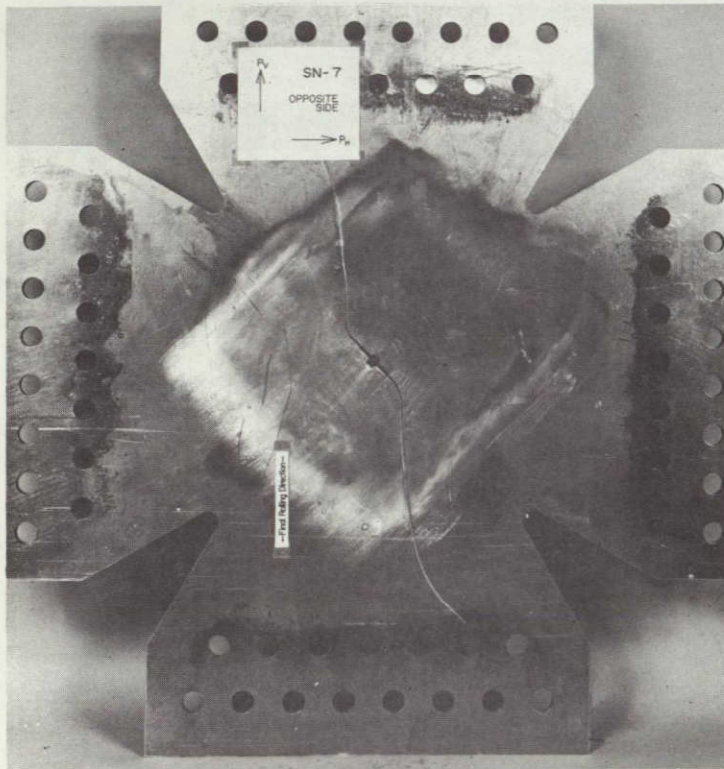Figure 25. - Overall View of SN-7 after Testing,
Console Side.

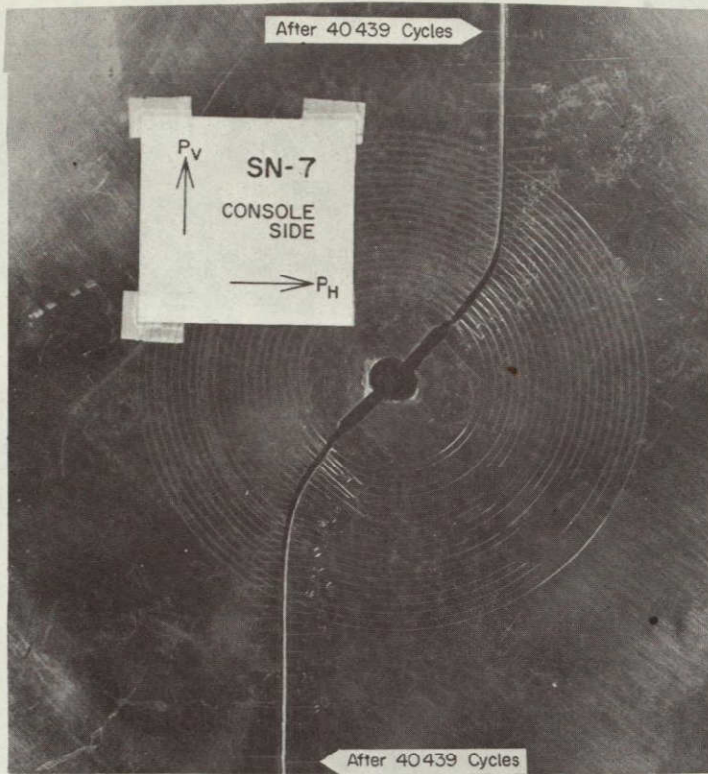Figure 26. - Overall View of SN-7 after Testing,
Opposite Side.

206

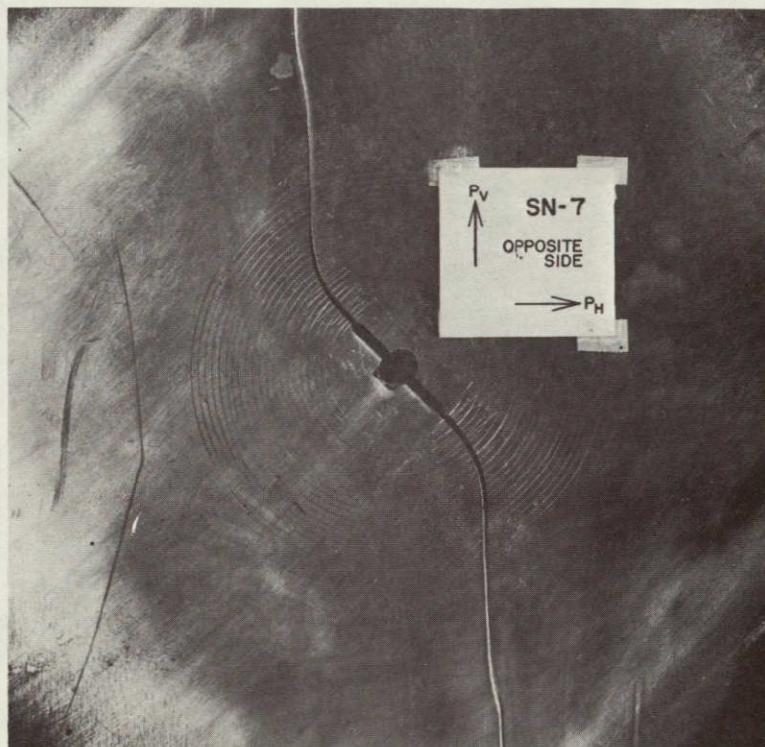Figure 27. - Closeup of SN-7 after Testing,
Console Side.

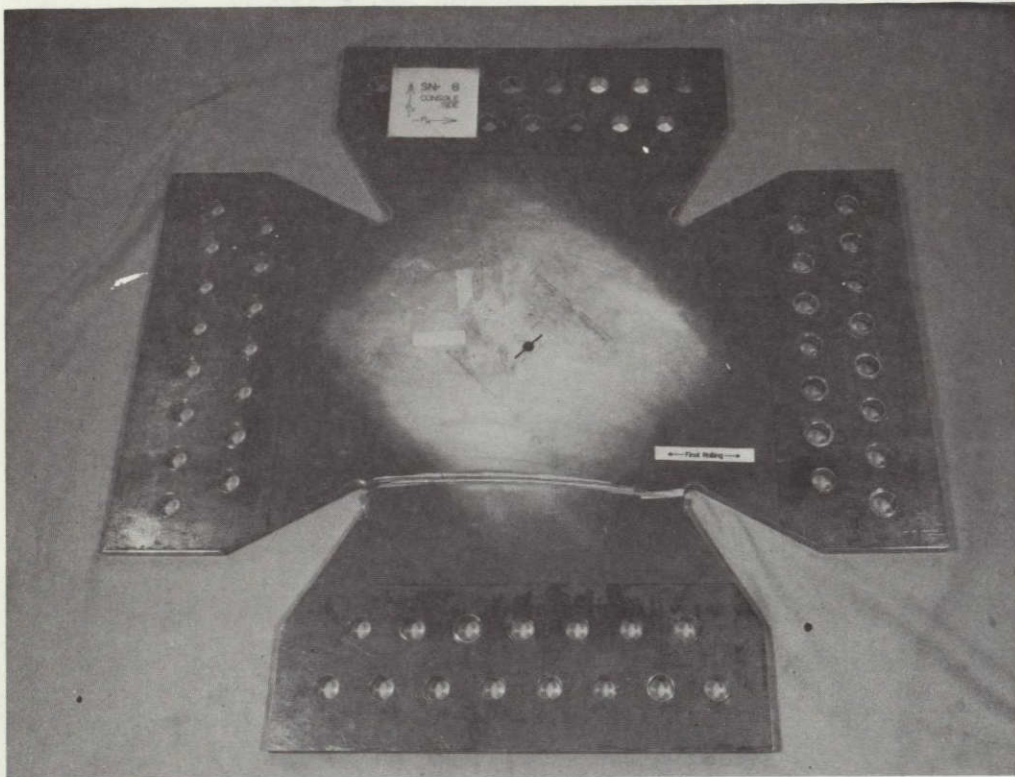Figure 28. - Closeup of SN-7 after Testing,
Opposite Side.

Figure 29. - Overall View of SN-8 after Testing.
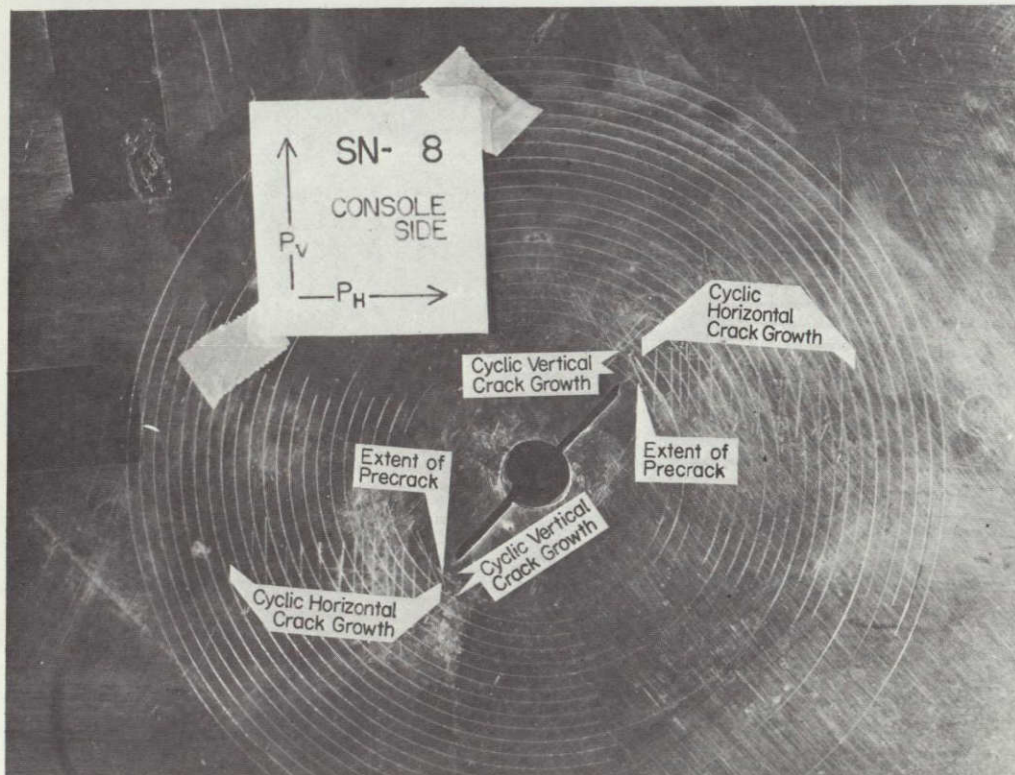

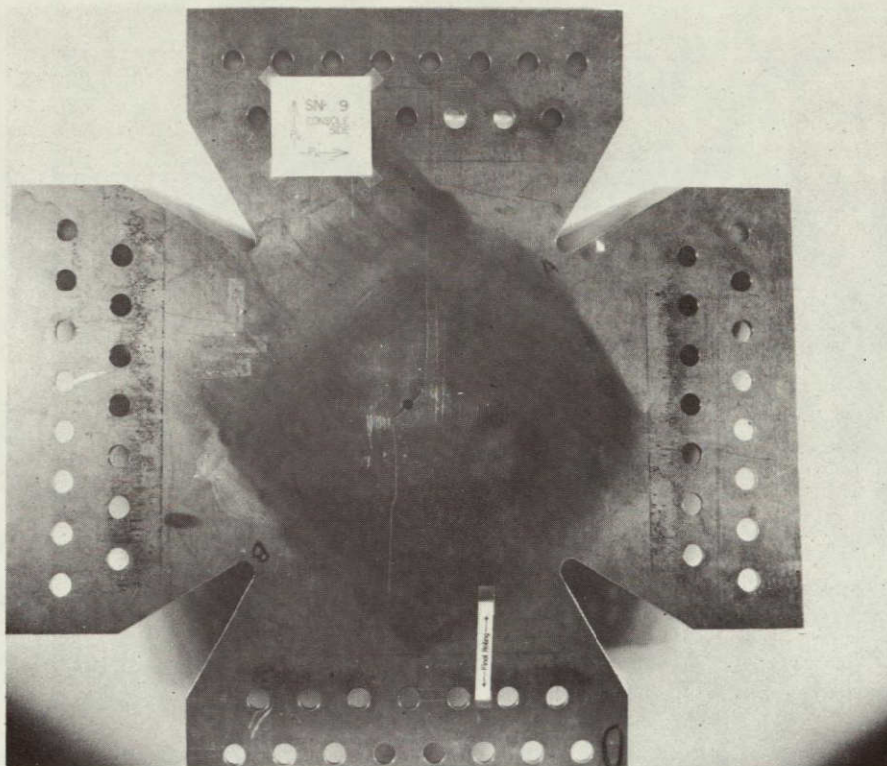Figure 30. - Central Portion of SN-8 after Testing.

Figure 31. – Overall View of SN-9 after Testing, Console Side.

Figure 32. – Overall View of SN-9 after Testing, Opposite Side.
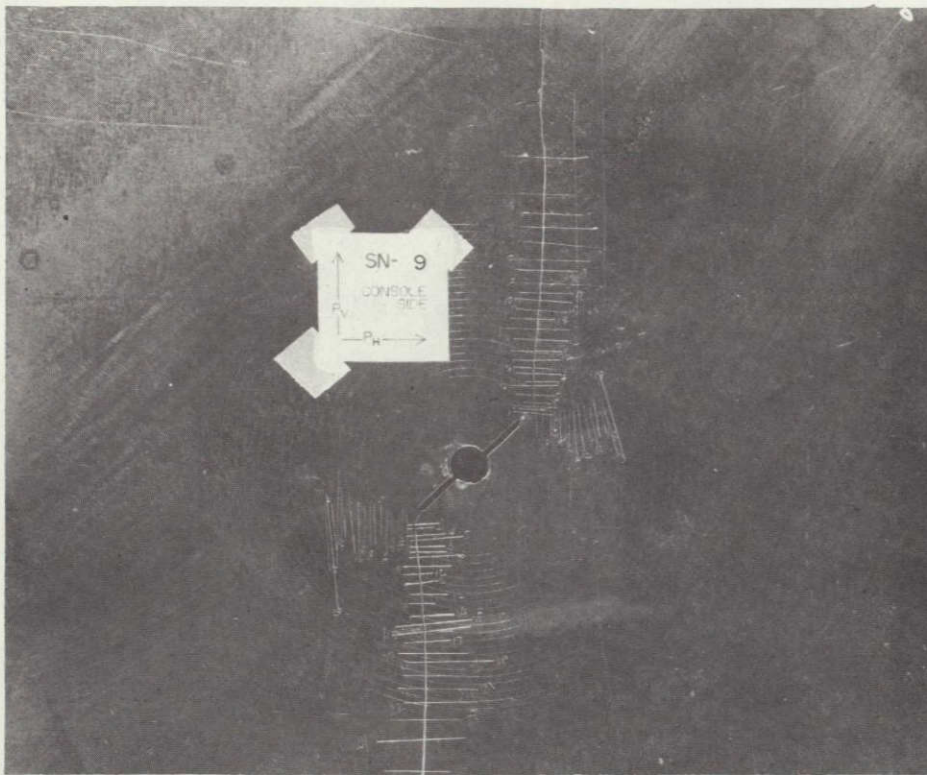
Figure 33. – Central Portion of SN-9 after Testing, Console Side.

Figure 34. – Central Portion of SN-9 after Testing, Opposite Side.
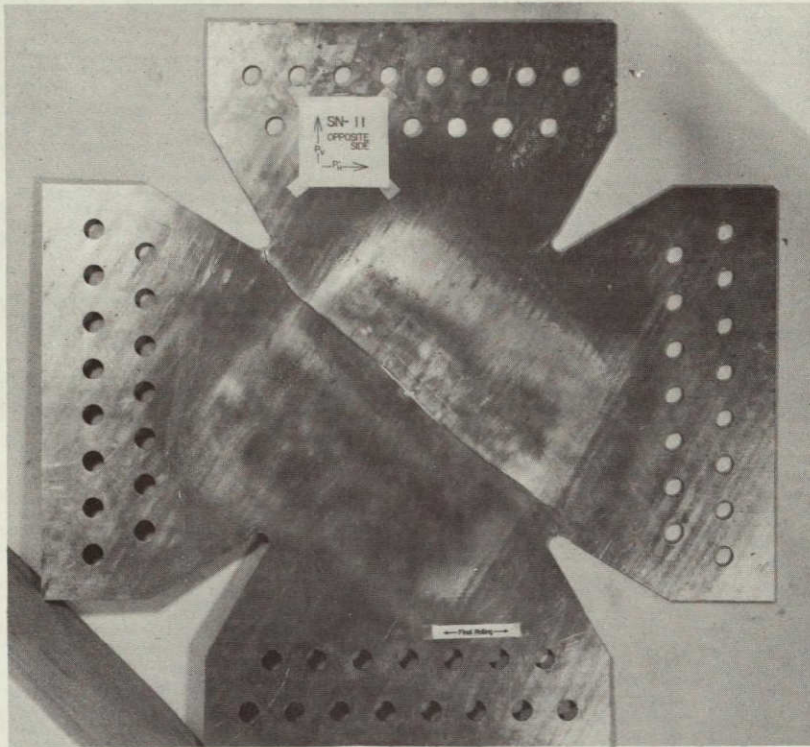
Figure 35. - SN-11 after Test.
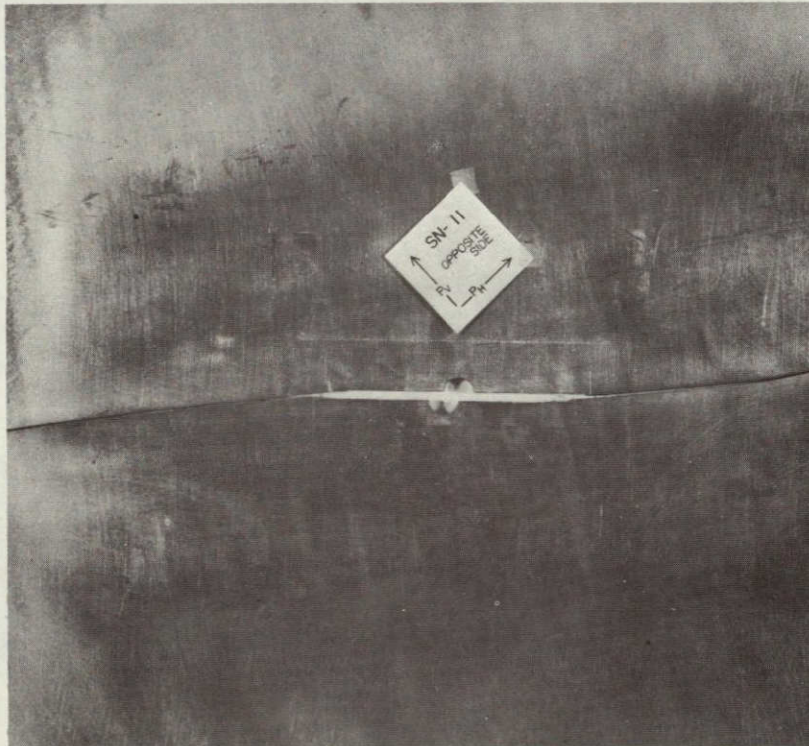
Figure 36. - Central Portion of SN-11 after Test.
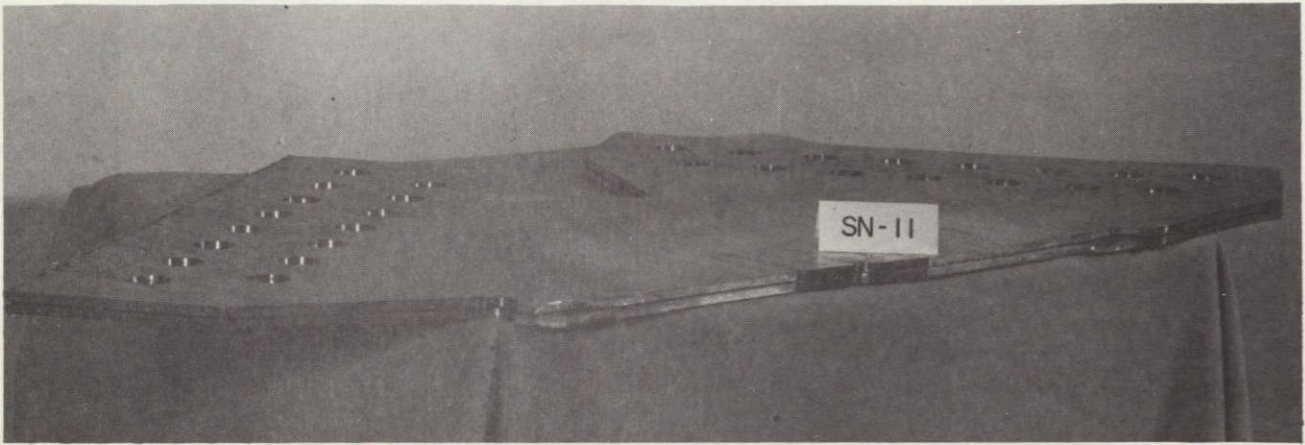
Figure 37. – Fracture Surface of SN–11.
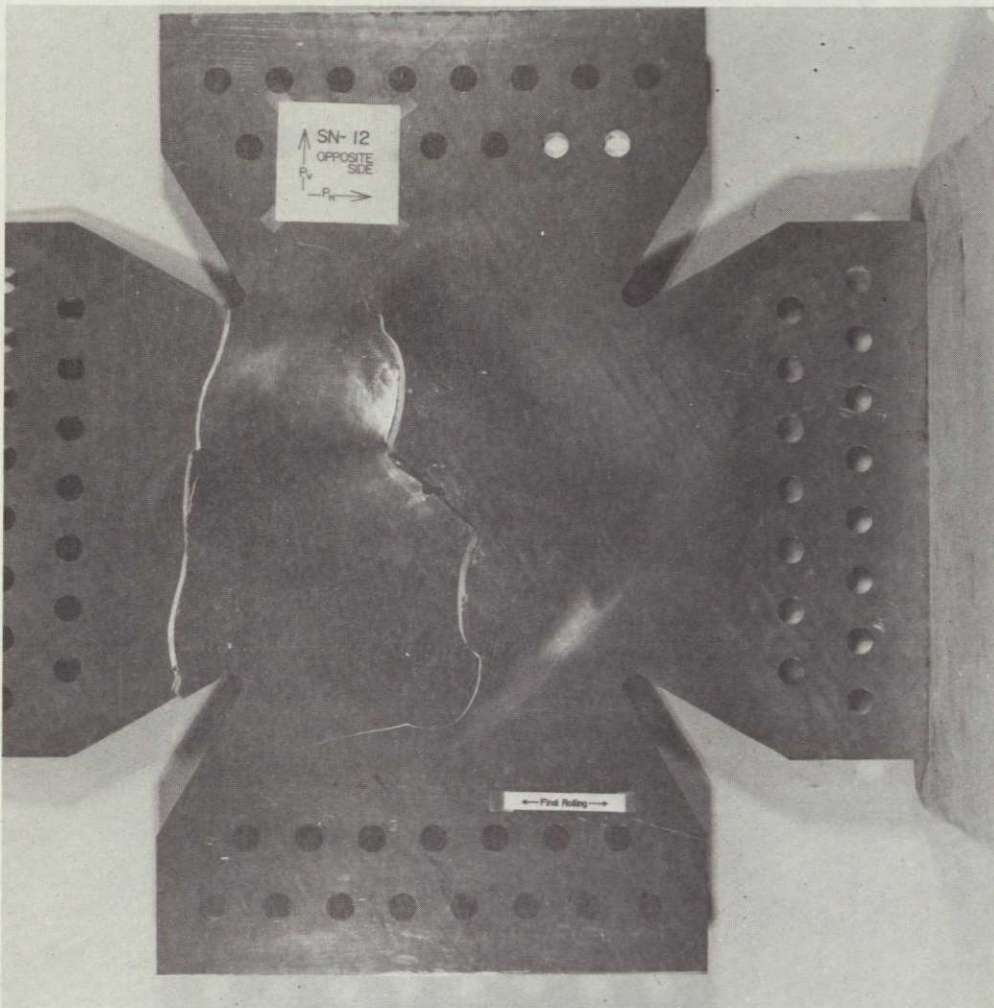
Figure 38. – SN–12 after Testing.

Figure 39. - Central Portion of SN-12
after Testing.
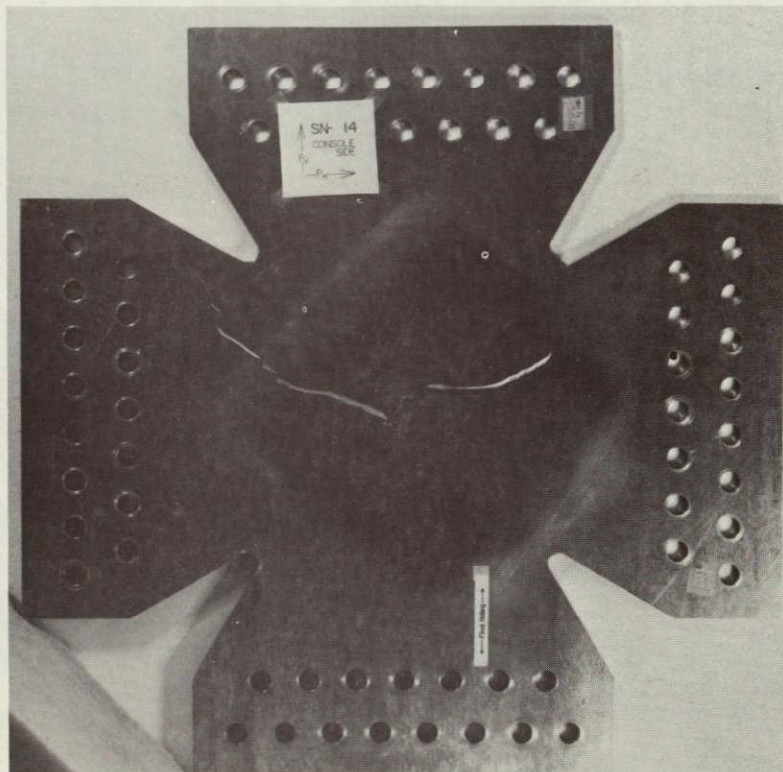
Figure 40. - SN-14 after Fracture Test.

213
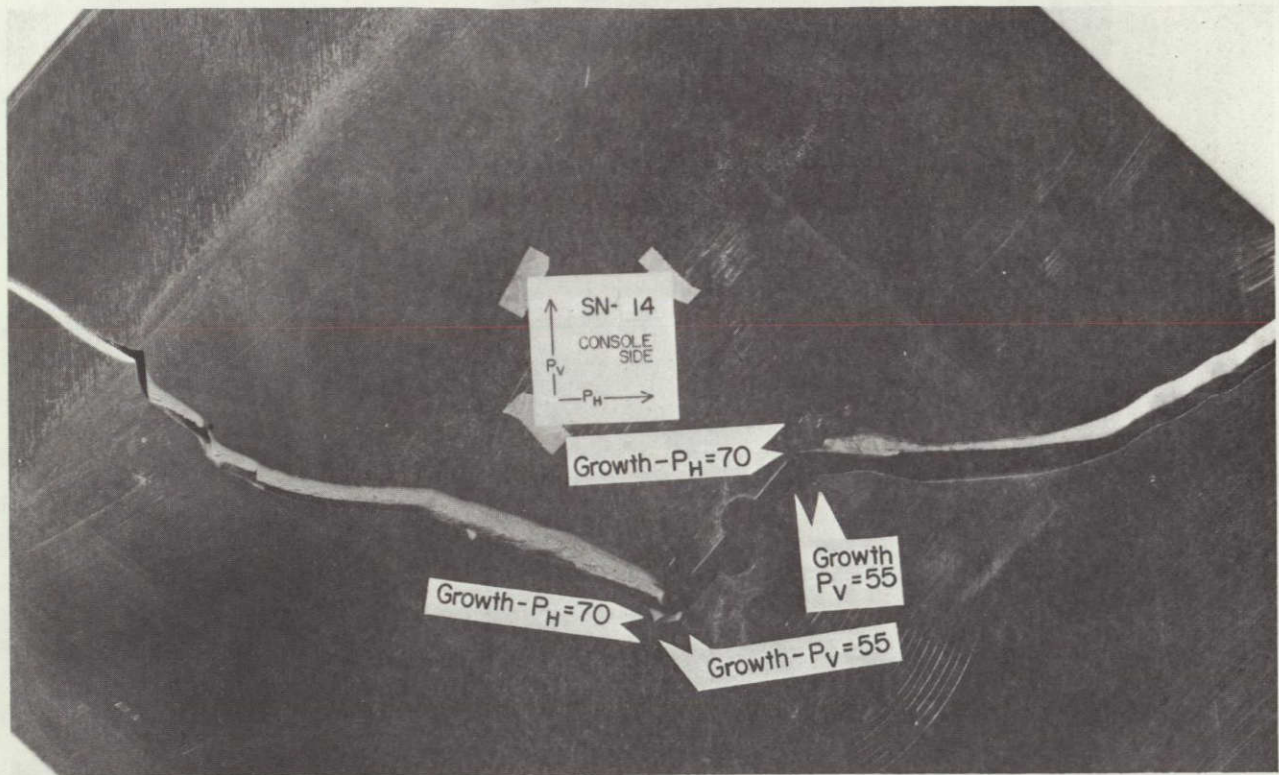
Figure 41. - Central Portion of SN-14 after Test, Console Side.
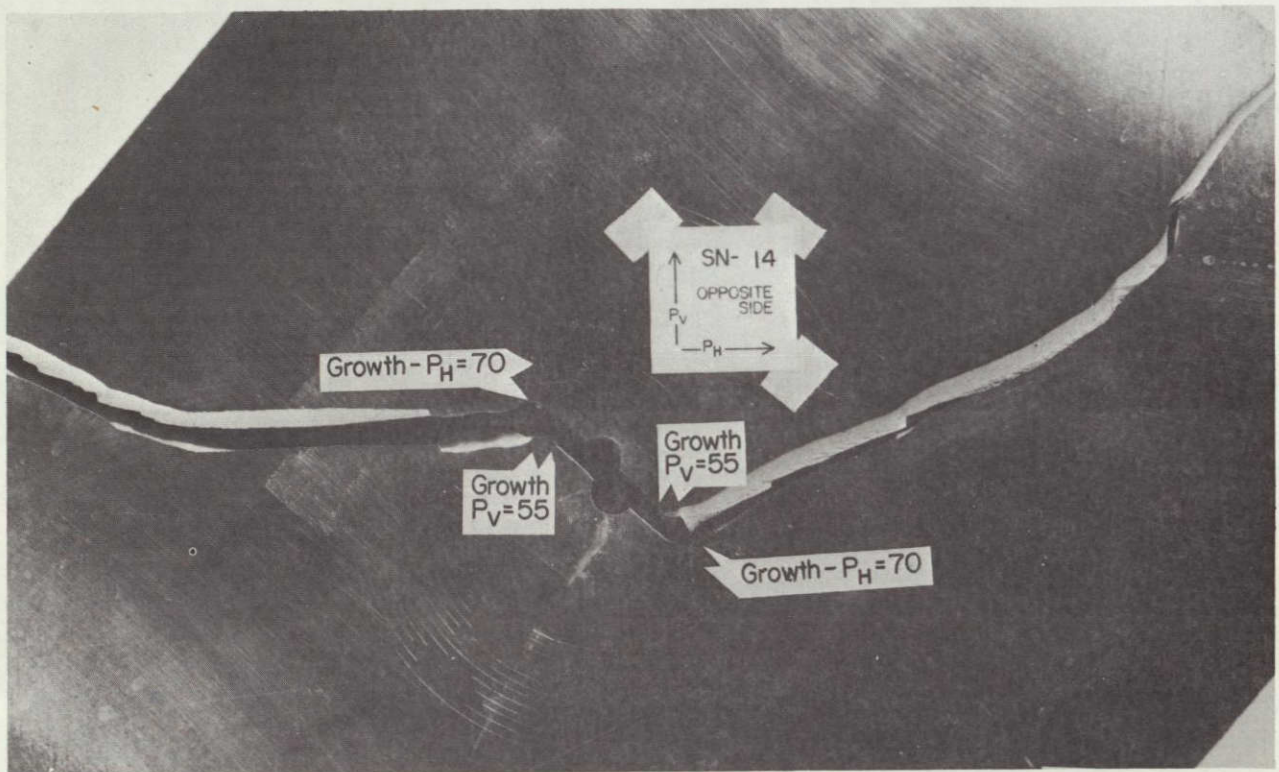
Figure 42. - Central Portion of SN-14 after Test, Opposite Side.
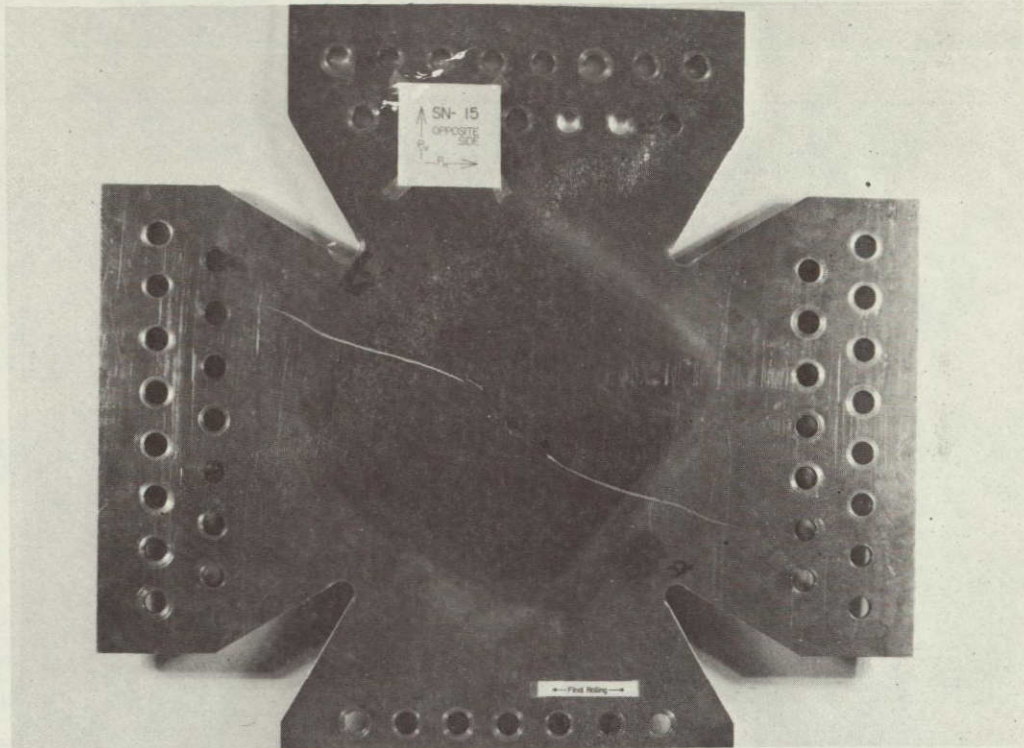
Figure 43. – Overall View of SN-15 after Testing.
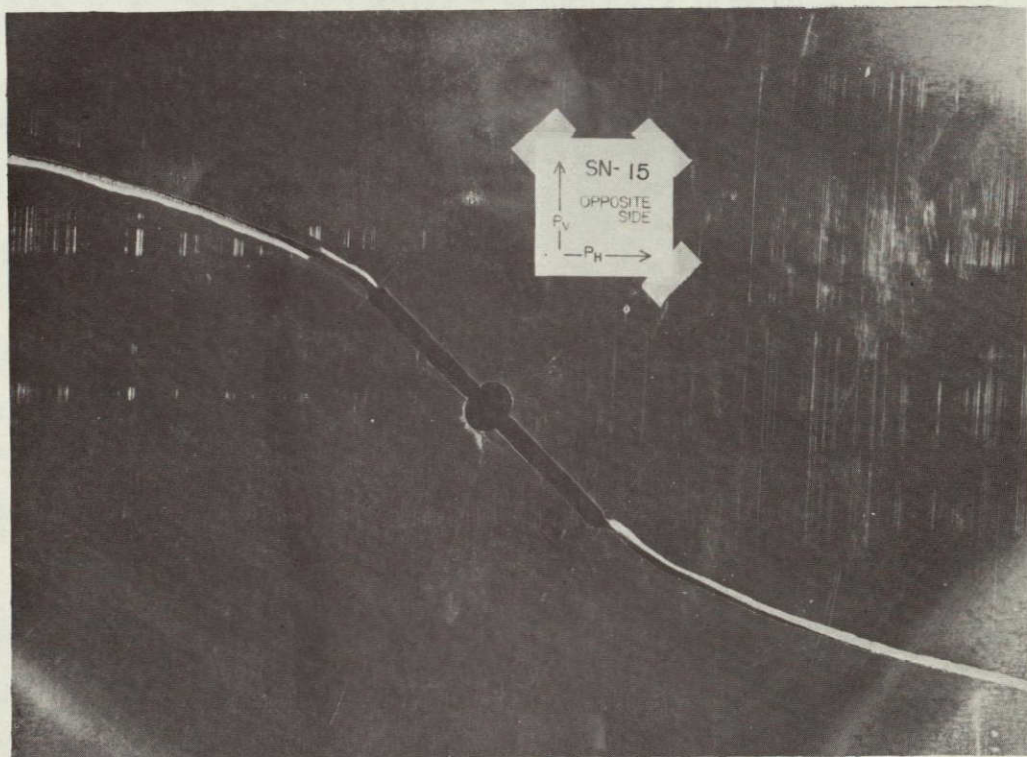
Figure 44. – Central Portion of SN-15 after Testing.
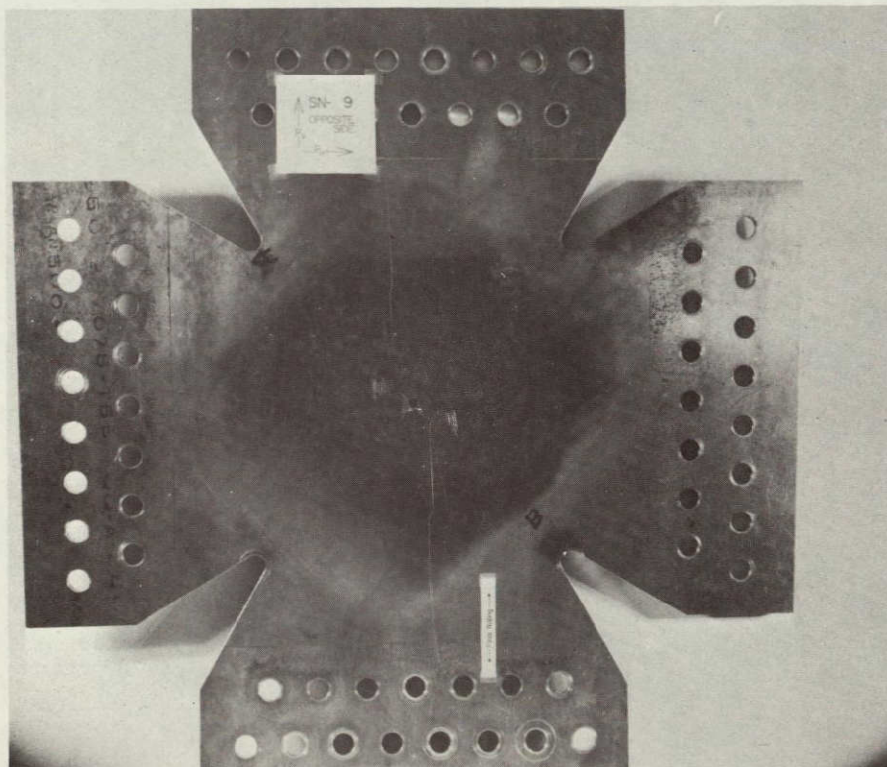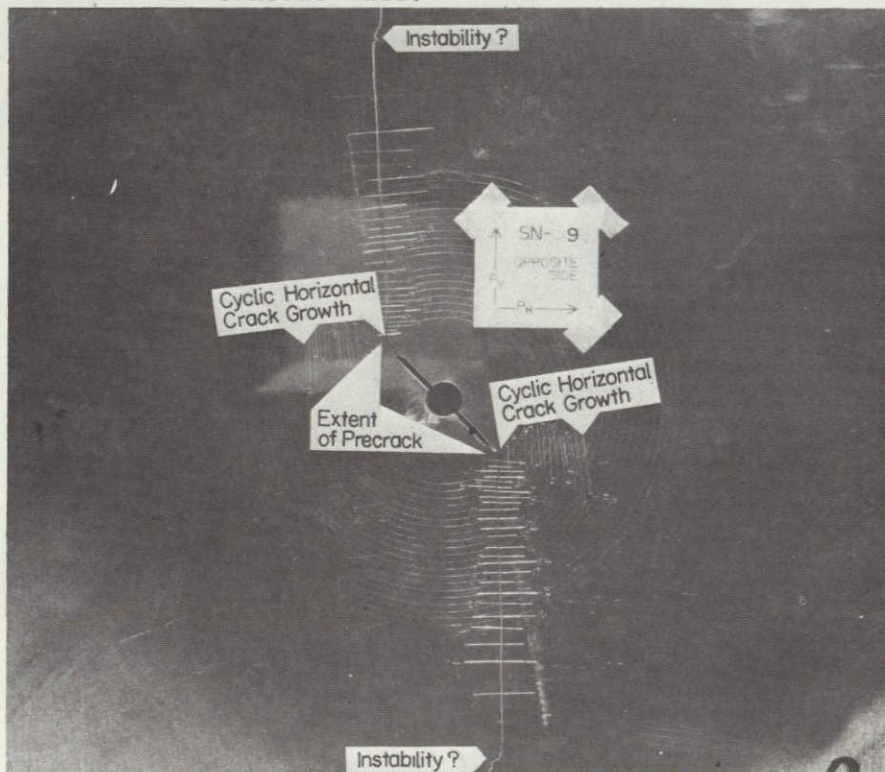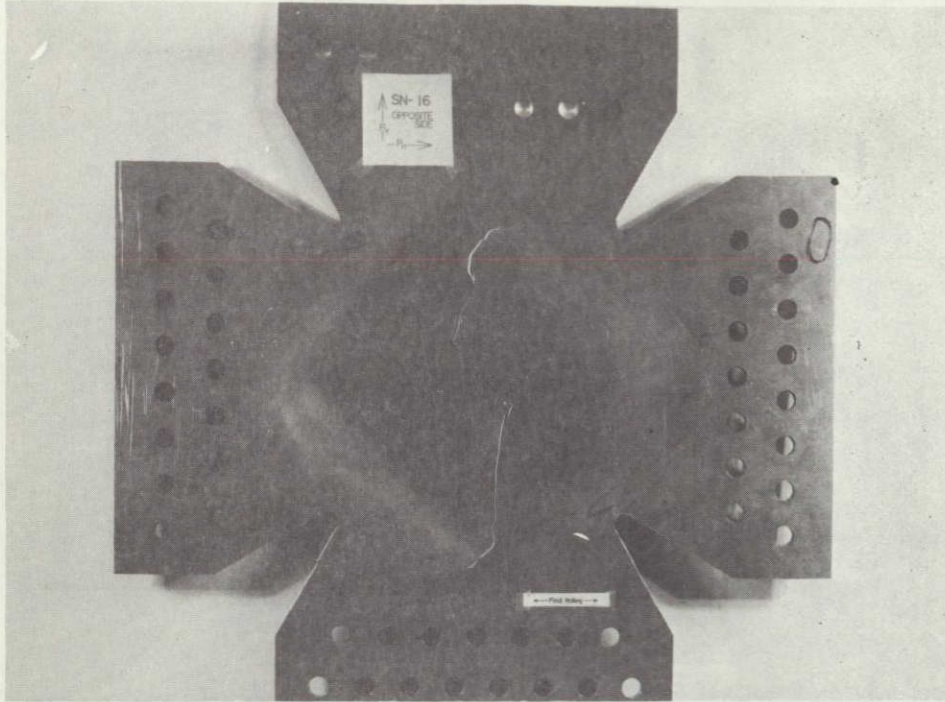
Figure 45. - Overall View of SN-16 after Testing.
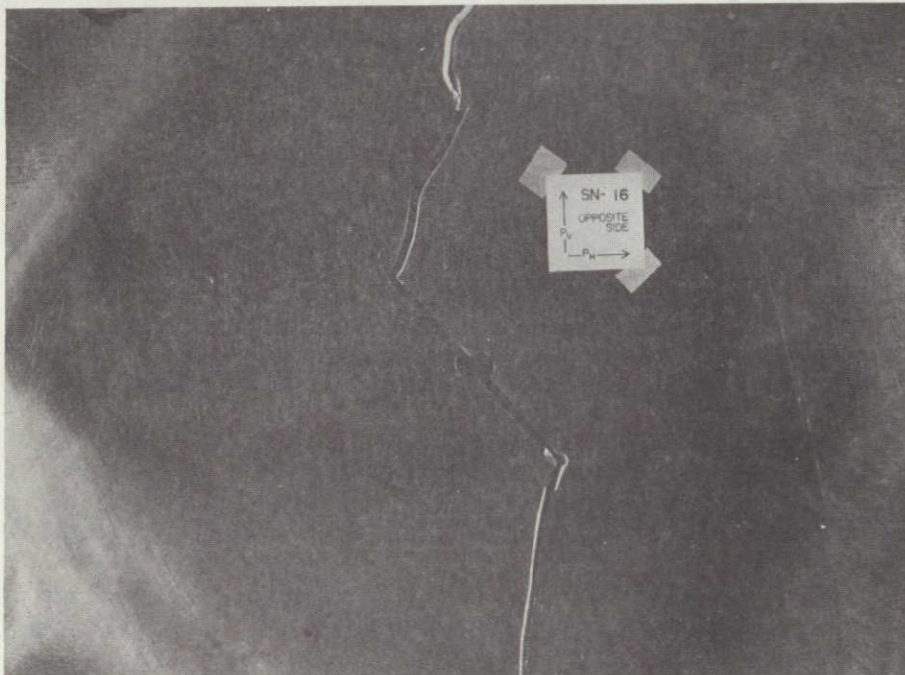
Figure 46. - Central Portion of SN-16 after Testing.

216
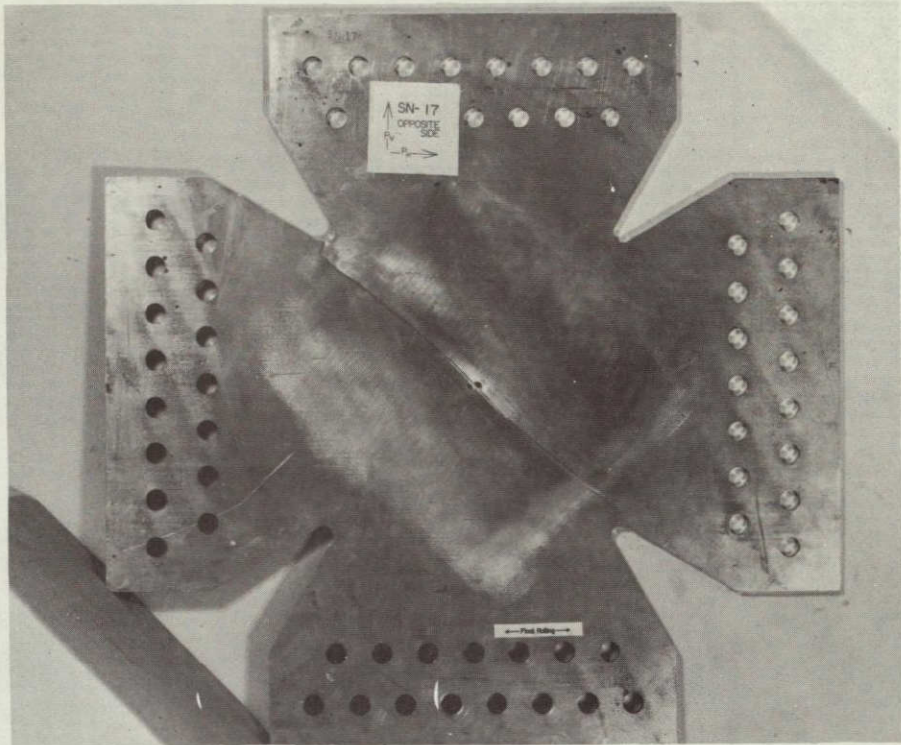
Figure 47. - SN-17 after Testing.
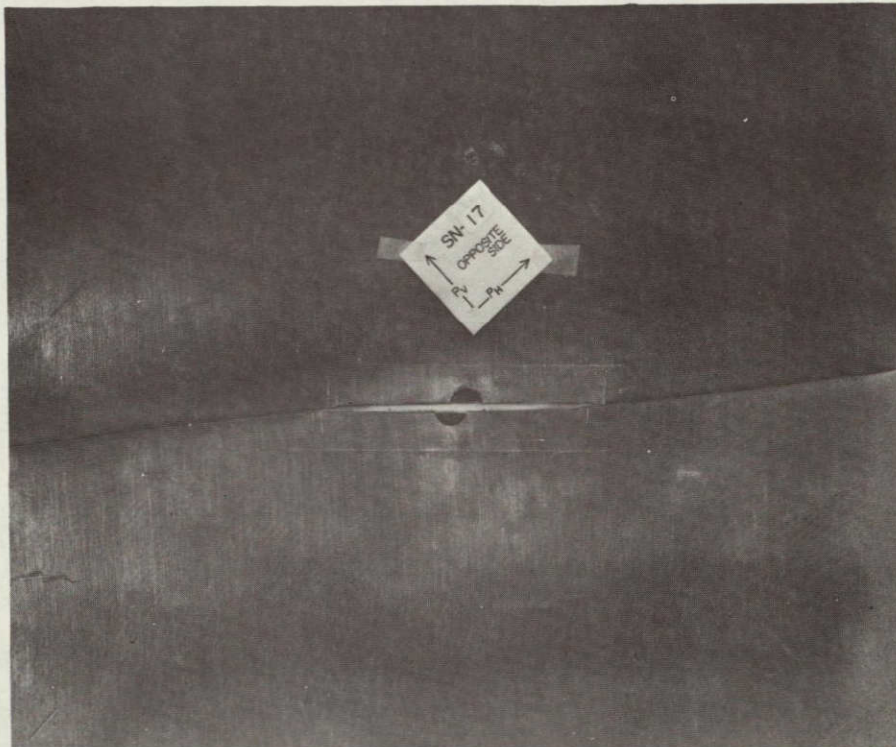
Figure 48. - Central Portion of SN-17 after Testing.

217
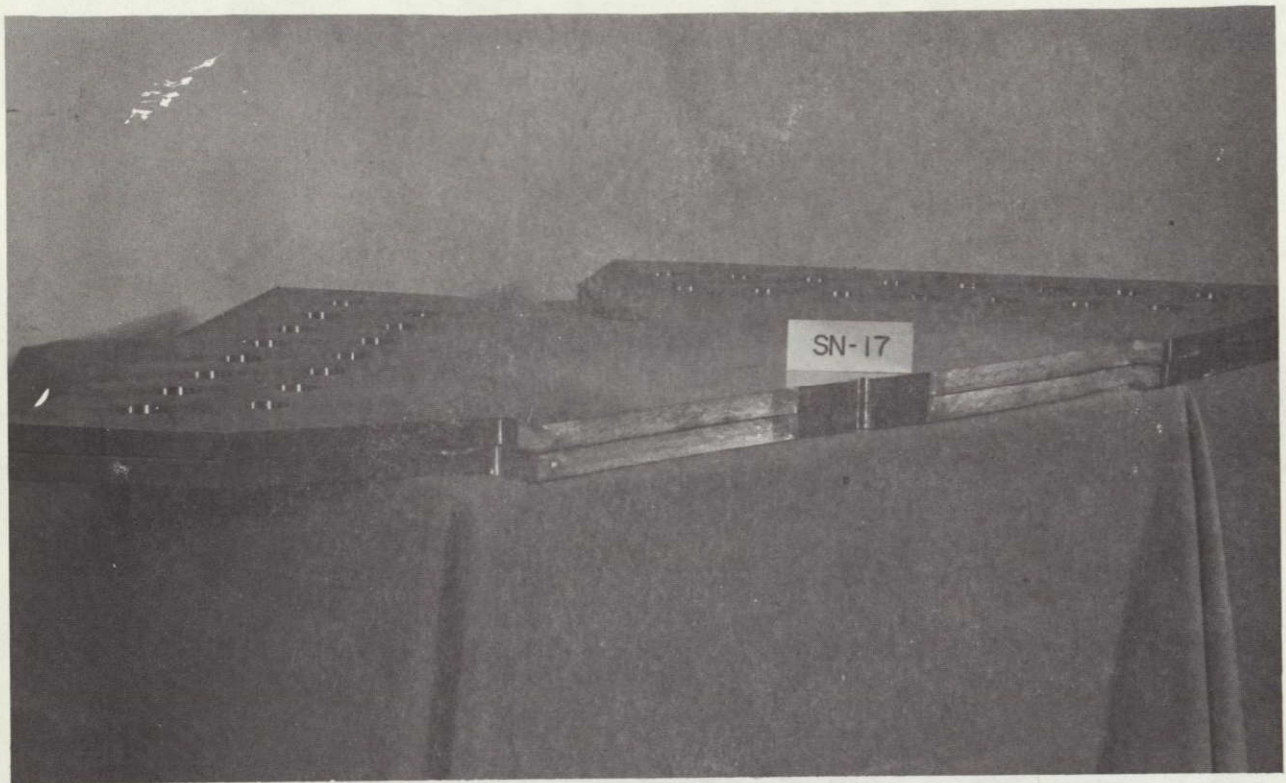
49. – Fracture Surface of SN–17.
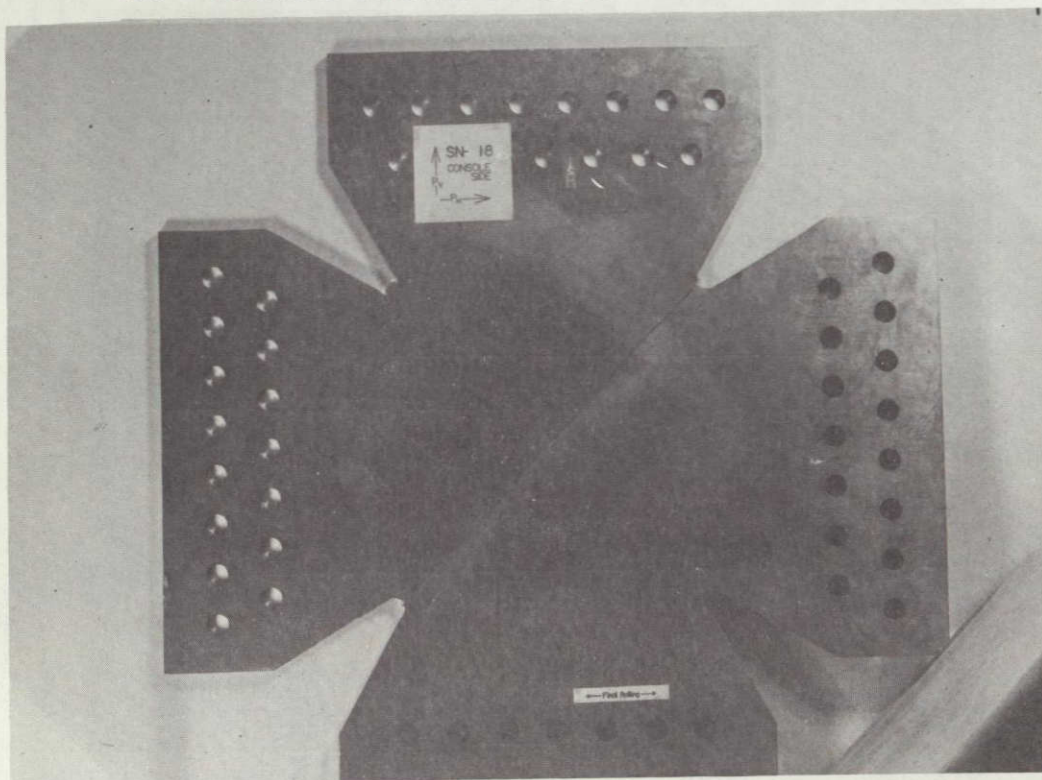
Figure 50. – SN–18 after Test.
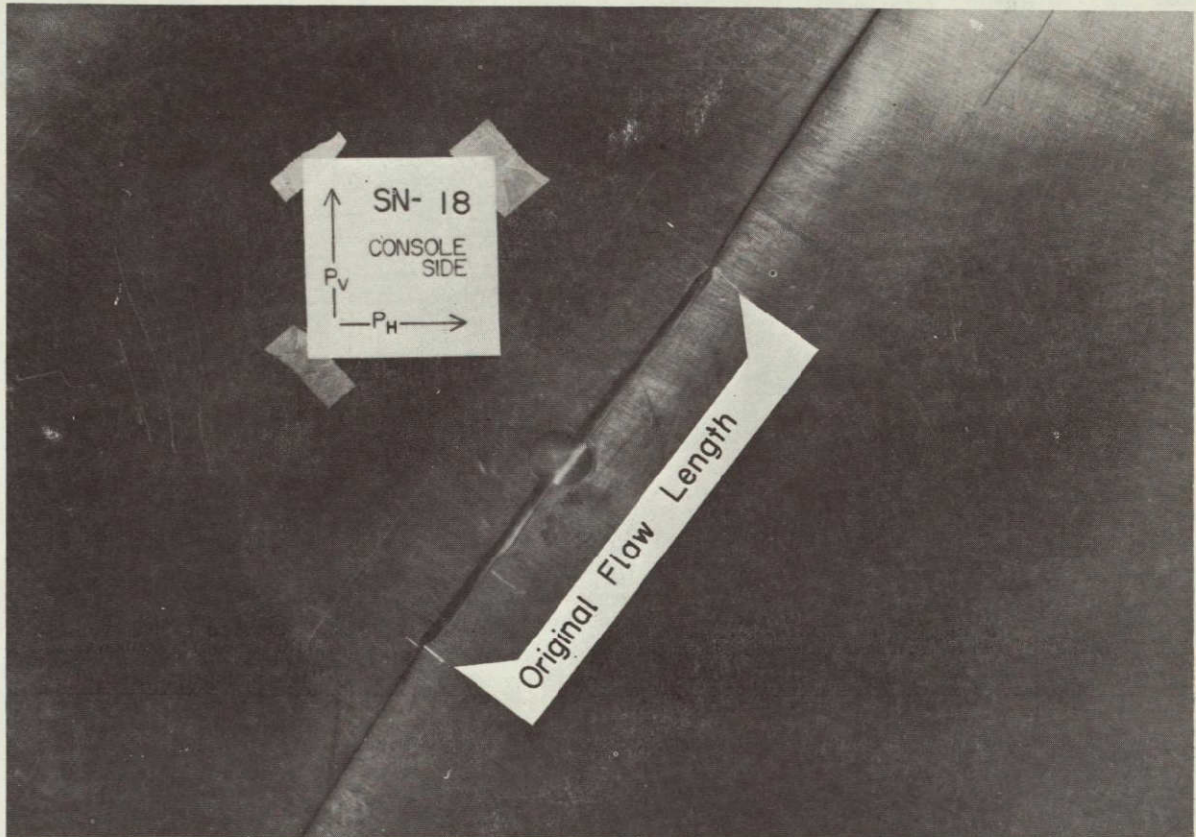
Figure 51. – SN–18 after Test, Central Region.
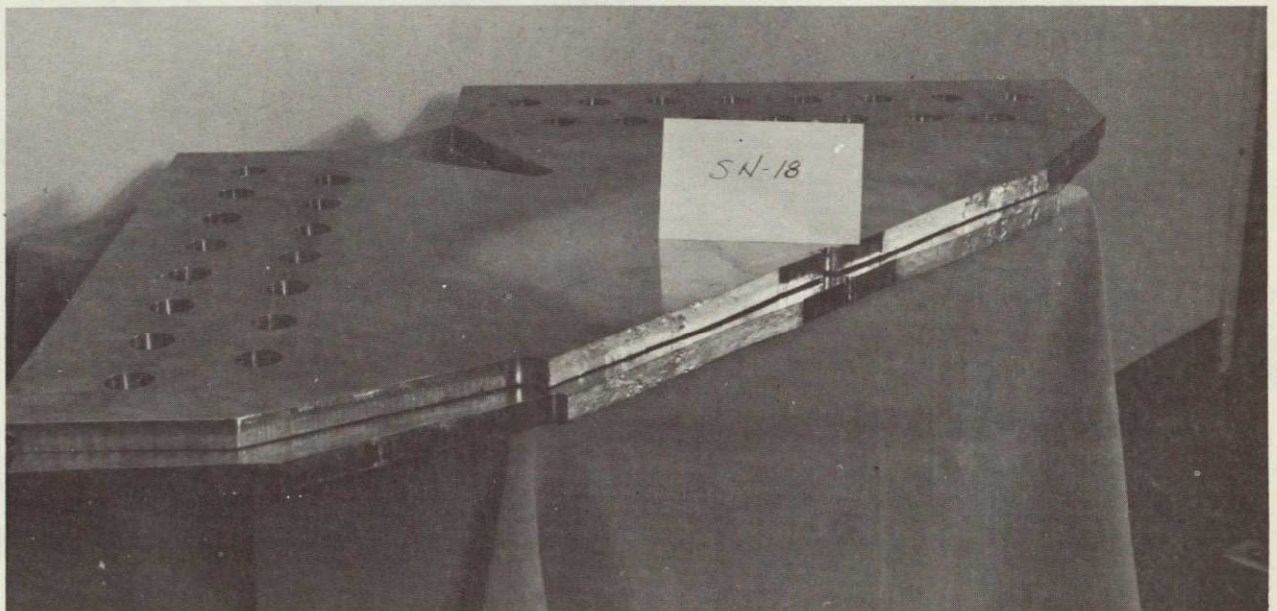
Figure 52. – Fracture Surface of SN–18.
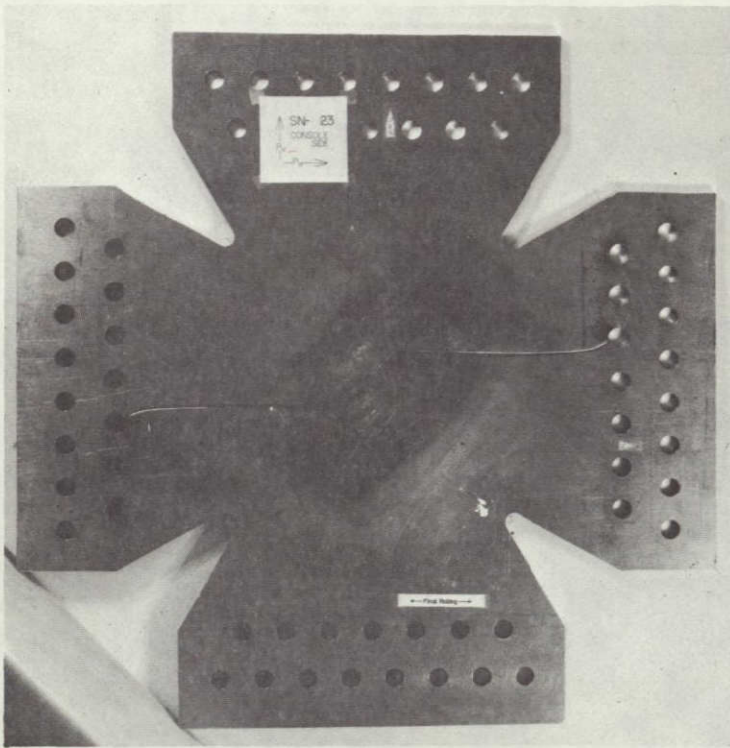
Figure 53. - SN-23 after Test.
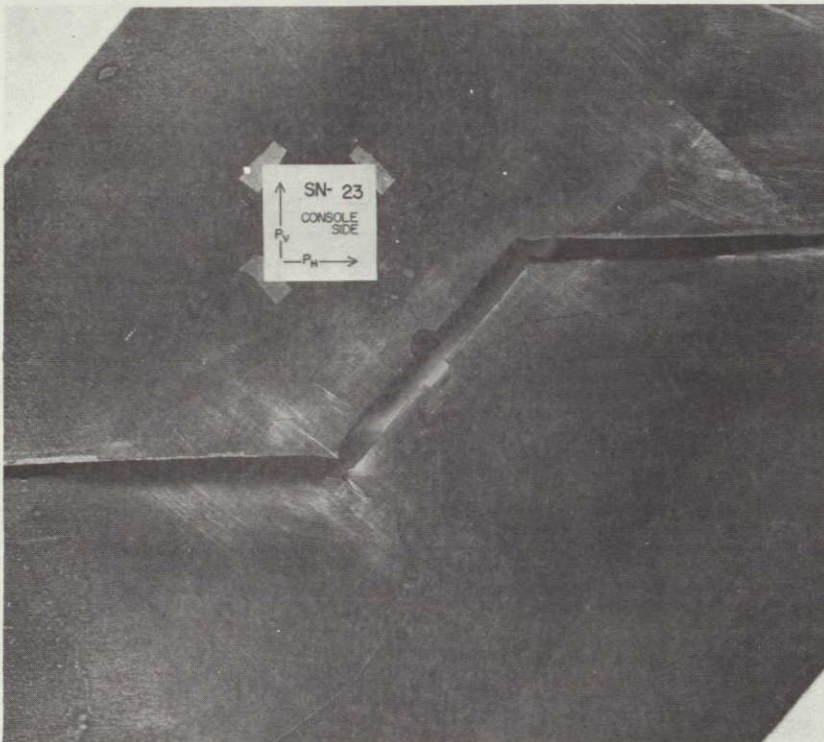
Figure 54. - SN-23 after Test, Central Region.
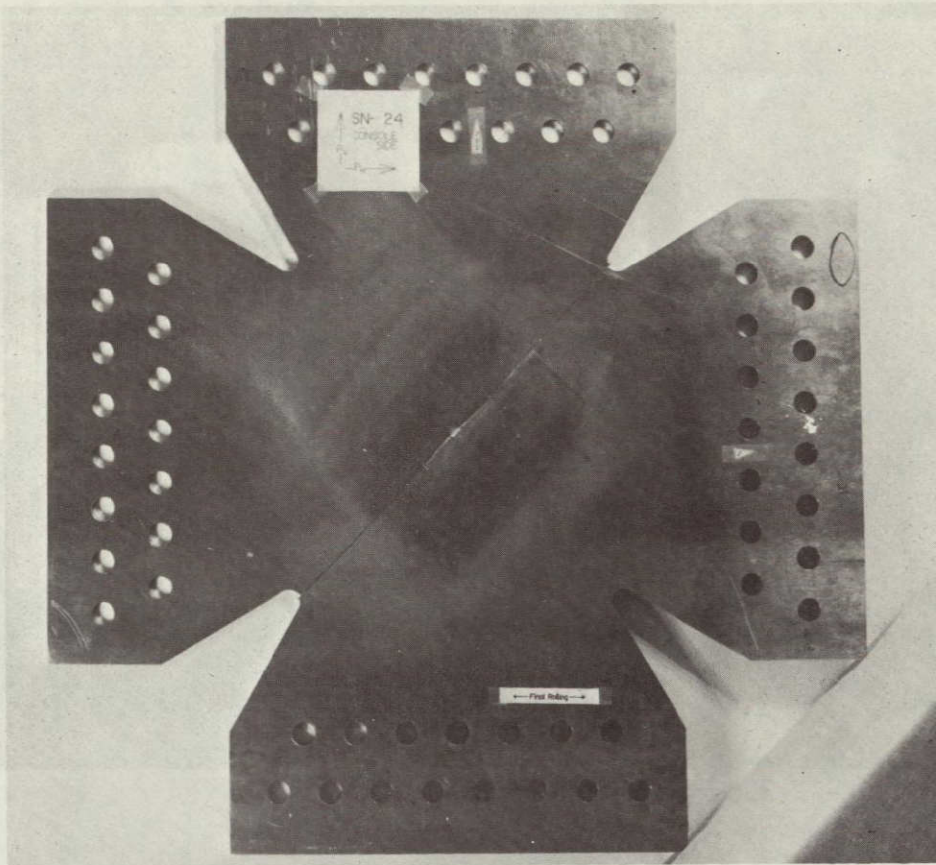
Figure 55. - SN-24 after Test.
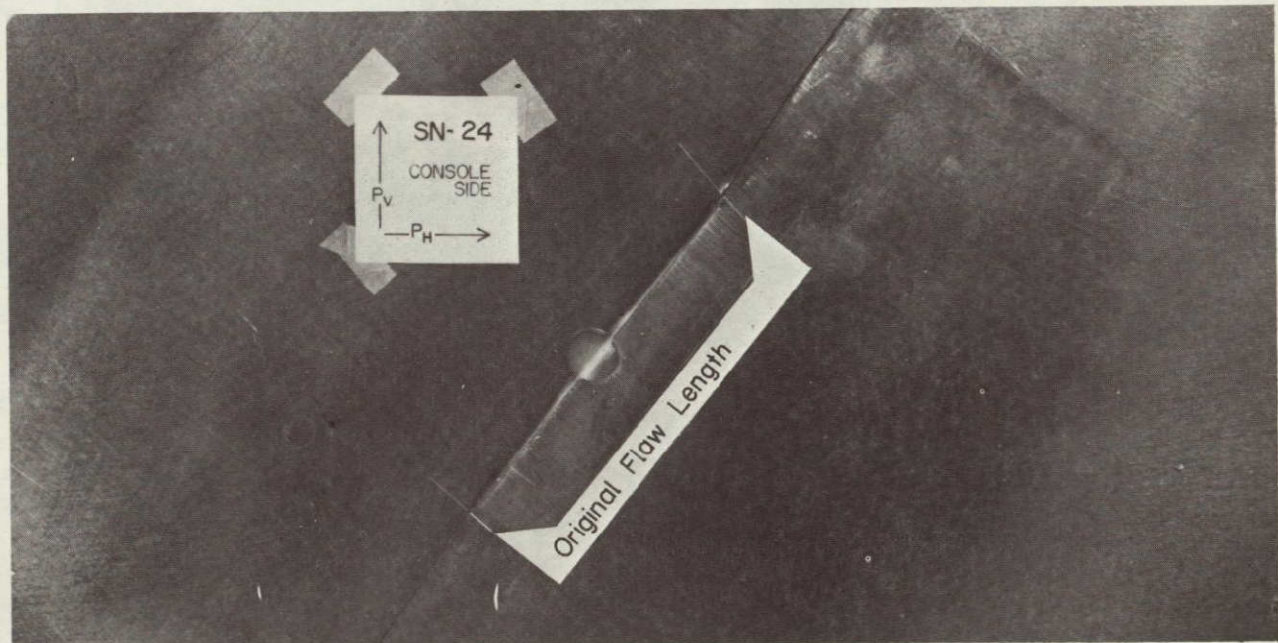
Figure 56. - SN-24 after Test, Central Region.

221
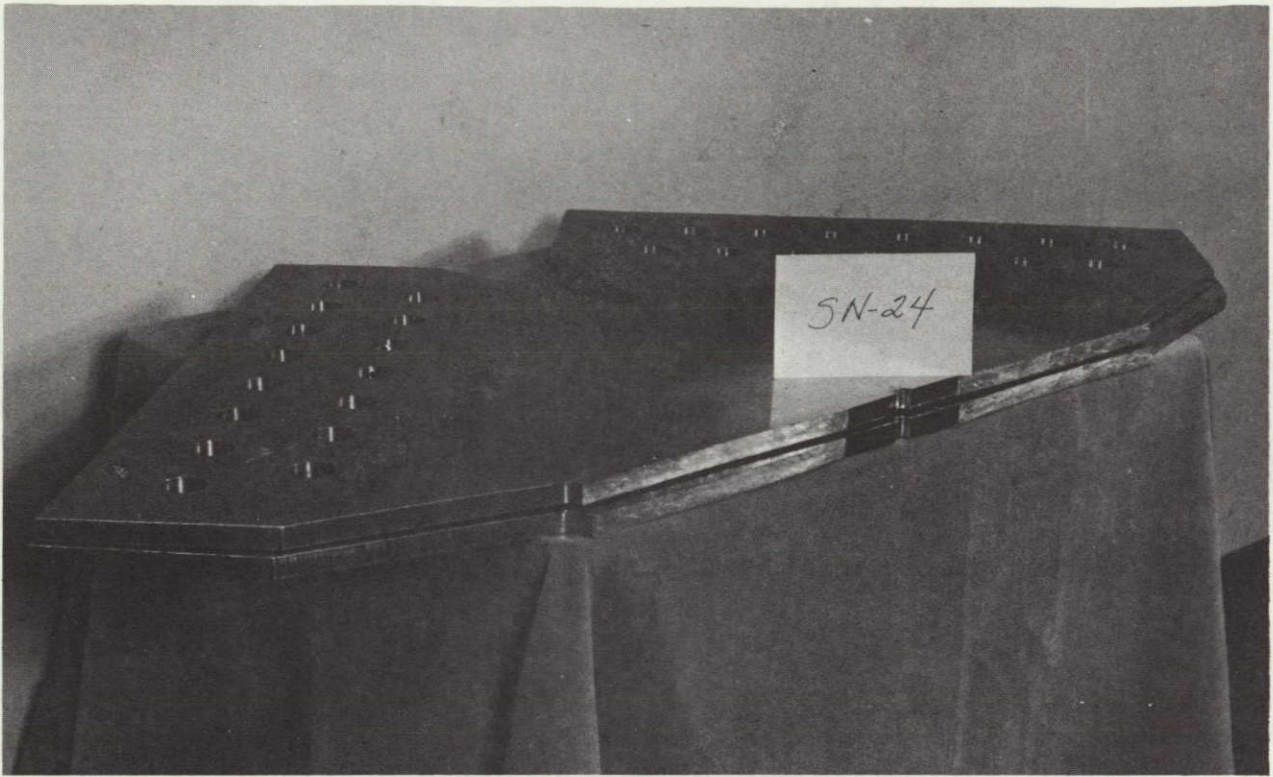
Figure 57. - Fracture Surface of SN-24.
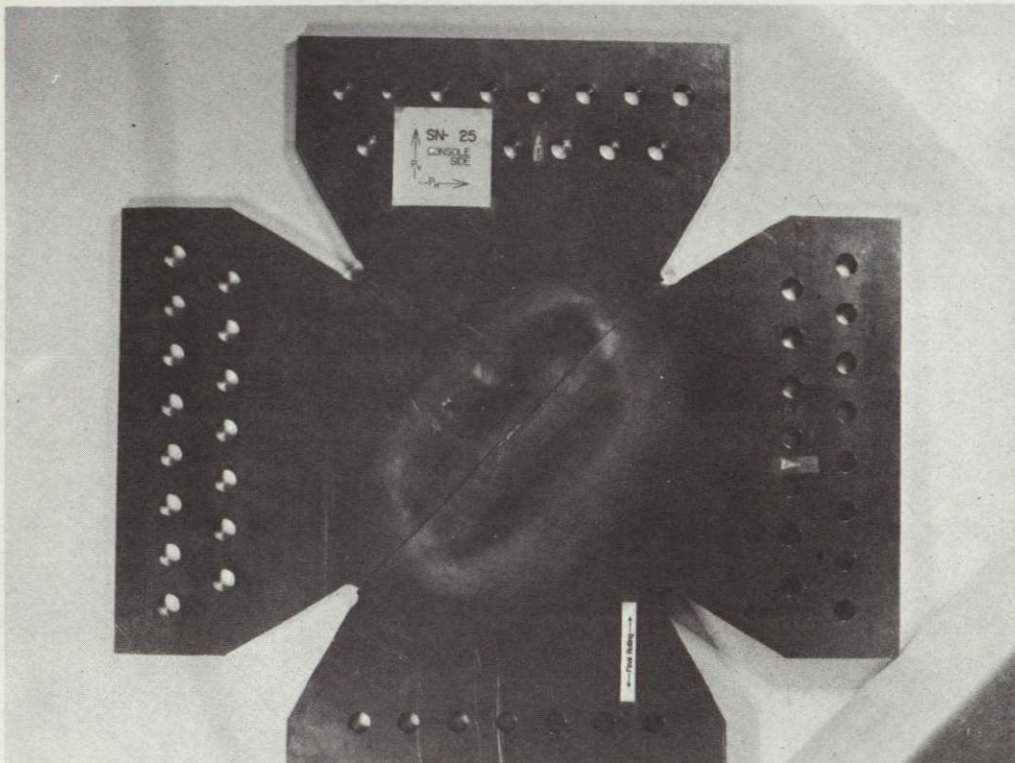
Figure 58. - SN-25 after Test.
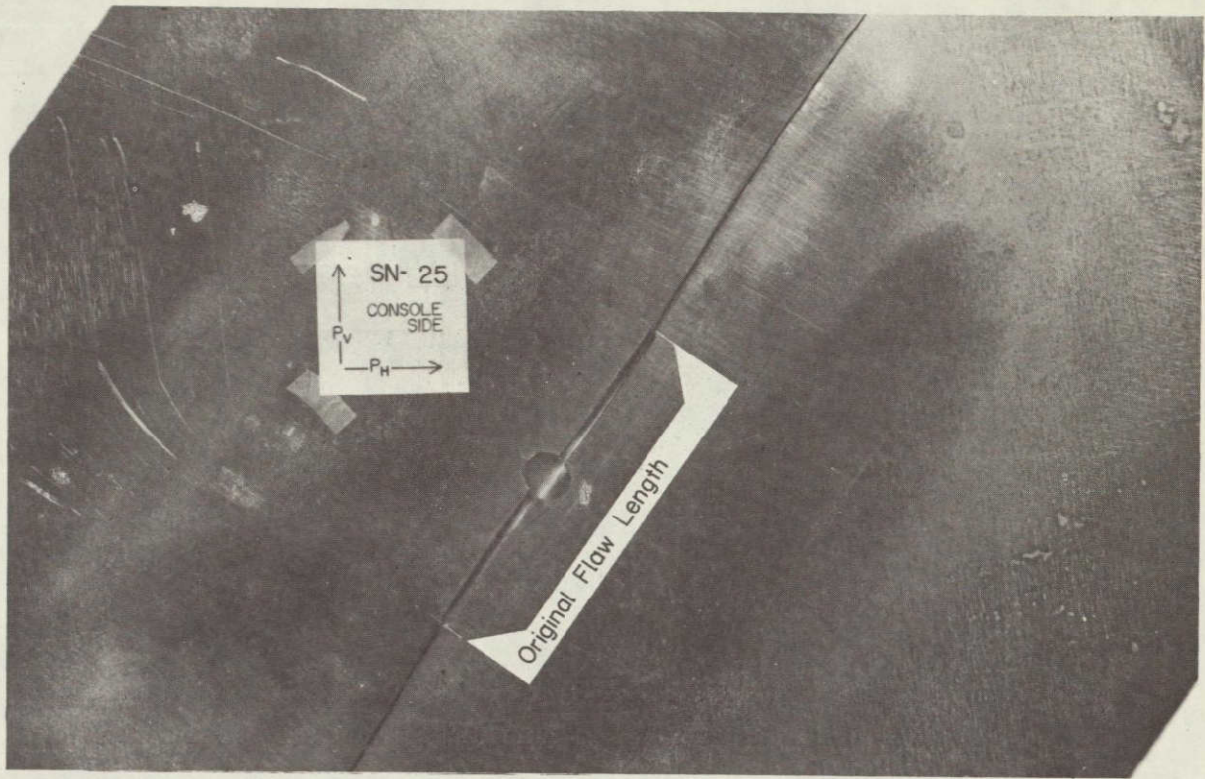
Figure 59. - SN-25 after Test, Central Region.
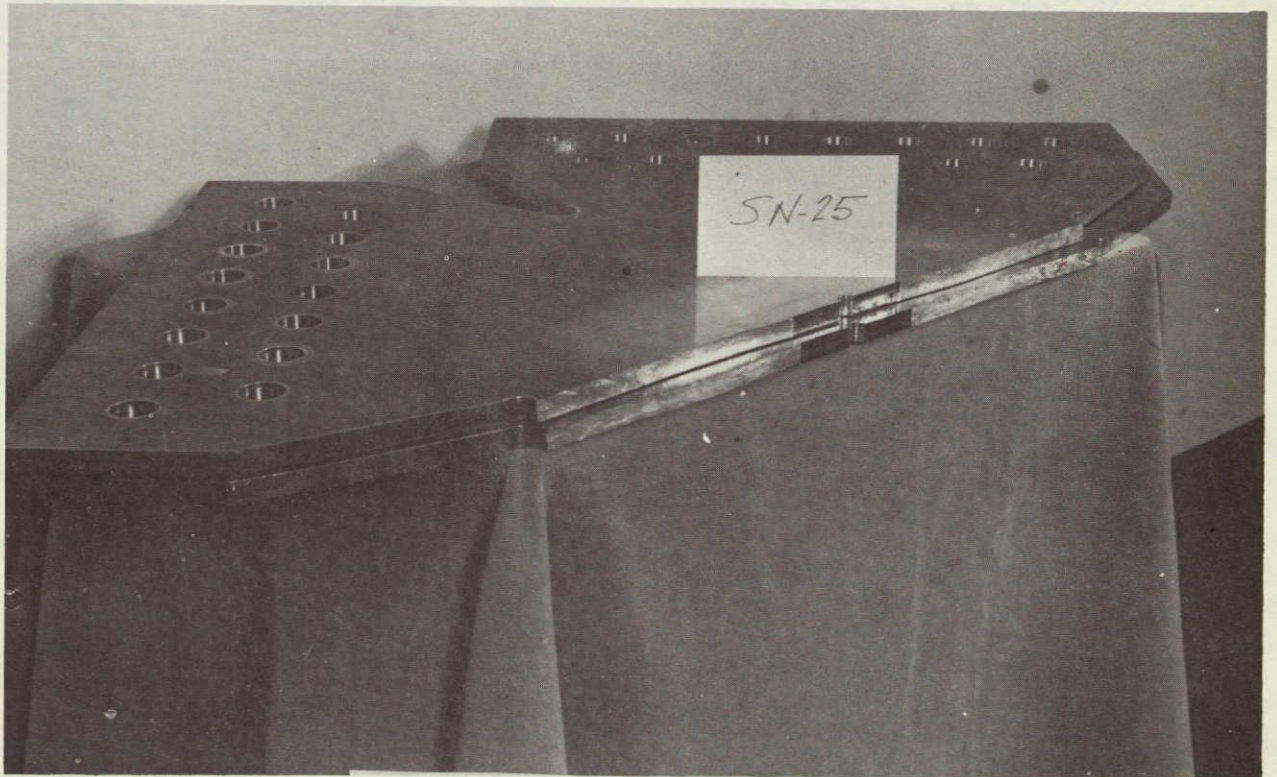
Figure 60. - Fracture Surface of SN-25.
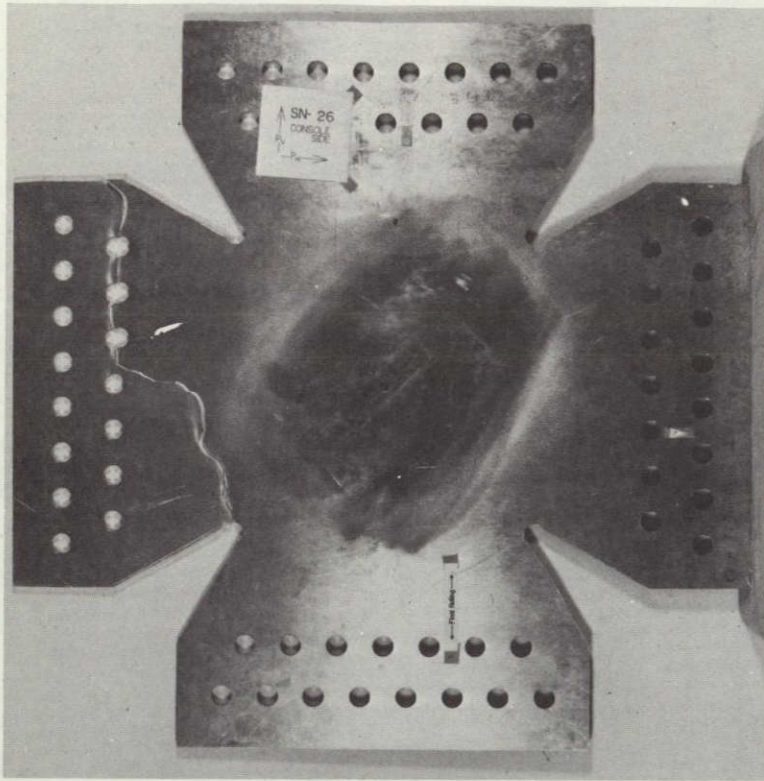
Figure 61. - SN-26 after Test.
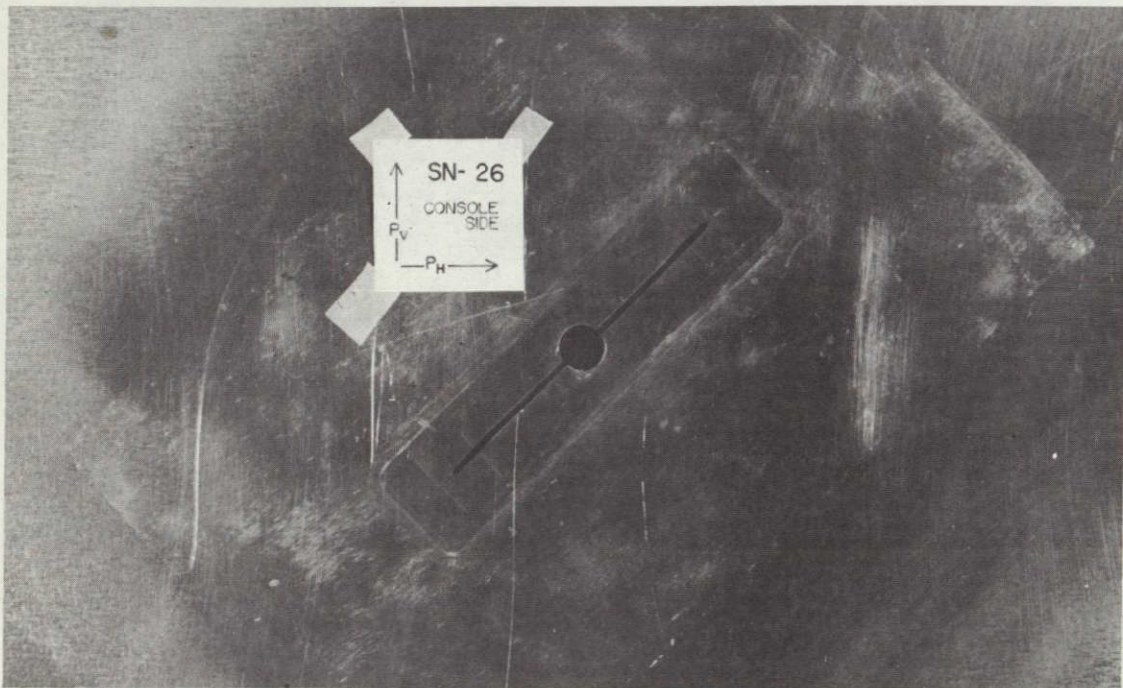
Figure 62. - SN-26 after Test, Central Region.

224
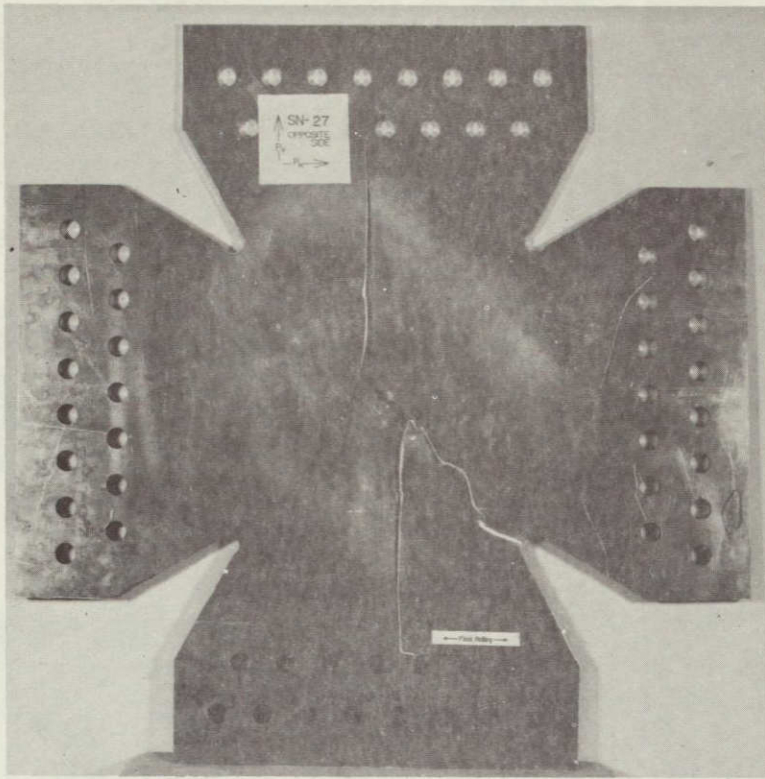
Figure 63. - SN-27 after Testing.
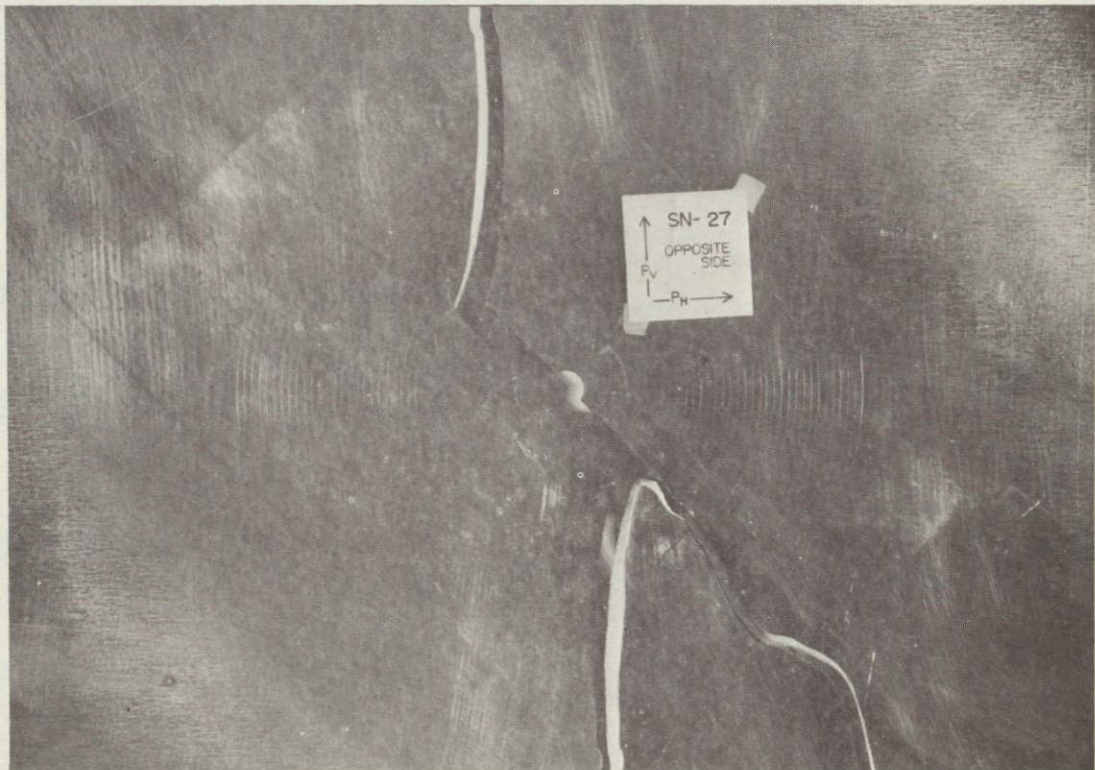
Figure 64. - Central Portion of SN-27 after Testing.

225

APPENDIX F SYMBOLS

A   Area of specimen appropriate to applied stress in the expressions for stress intensity.

a   One-half actual crack length.

a_{cr} Critical value of a.

a_i One-half initial crack length, after precracking.

a_{ii} Coefficients in Sih theory.

$\tilde{a}_{ii}$ $a_{ii} [2E/(1+\nu)(1-2\nu)]$

a_i^H One-half the arc length of curved flaws after cyclic, but before static, testing. Used for Holston analysis.

a_i^I The projection of a_i^H perpendicular to final fracture direction. Used for Iida analysis. Also, one half the projection of branched cracks after cyclic but before static testing.

Δa_{HB} Increment of branched crack growth at the bottom in the horizontal direction.

Δa_{HT} Increment of branched crack growth at the top in the horizontal direction.

Δa_{VB} Increment of branched crack growth at the bottom in the vertical direction.

Δa_{VT} Increment of branched crack growth at the top in the vertical direction.

b   One-half plate width--Iida analysis.

b_λ Six times the equivalent linearized crack slant length for the Iida analysis. Used to establish relation between crack length and equivalent plate width of Maltese cross specimens.

C   Compression. Also generalized coefficient in stress intensity expression.

C_f Generalized coefficient in crack growth equation.

COD	Crack opening displacement.
CSD	Crack shear displacement.
E	Young's modulus.
G	Crack extension force.
G_{cr}	Critical value of G.
K_i	Stress intensity in the ith mode.
k_i	$K_i / \sqrt{\pi}$.
K_I	Mode I stress intensity.
K_{II}	Mode II stress intensity.
K_{Ic}	Critical value of K_I.
K_{IIc}	Critical value of K_{II}.
K_{Iu}	Mode I stress intensity at fracture.
K_{IIu}	Mode II stress intensity at fracture.
$\tilde{K}_I$	Mode I stress intensity coefficient in Holston analysis.
$\tilde{K}_{II}$	Mode II stress intensity coefficient in Holston analysis.
L	Measure of plastic zone size.
M_{SI}	Mode I stress intensity coefficient in Iida analysis.
M_{SII}	Mode II stress intensity coefficient in Iida analysis.
N	Number of cycles of loading.
ΔN	Increment of cycles per load block.
n	Experimental value of K_{II} / K_I at any time. Also curve fitting exponent in crack growth equation.
P	Load.
P_a	Load perpendicular to predominant crack direction or branch, Iida analysis.

P_A Load in A axis direction.

P_B Load in B axis direction.

P_H Horizontal load.

P_V Vertical load.

R   Radius of arc crack. Also crack extension resistance.

S   Intensity of strain energy density, Sih theory.

T   Tension. Also period of cyclic load.

t   Thickness. Also time lag of horizontal load axis.

U   Strain energy density, Sih theory.

$\tilde{u}$ Crack shearing displacement normalized to infinite plate value.

$\tilde{v}$ Crack opening displacement normalized to infinite plate value.

α One-half interior angle of sector defined by arc crack.

θ Arctan $\left(K_{Iu} / K_{IIu} \right)$.

θ_c Angle in polar coordinates defining the predicted fracture direction.

λ a/b= normalized projected crack length.

ν Poisson's ratio.

$\tilde{\nu}$ ν for plane strain; $\nu/(1+\nu)$ for plane stress.

σ Normal stress.

σ_a Sress parallel to load direction.

σ_b Stress perpendicular to load direction.

σ_c Stress at center of unflawed plate under equal biaxial loads.

σ_{cr} Critical value of σ.

σ_H Horizontal stress.

σ_i Assumed stress levels for construction of R curve, $i = 1, 2, \ldots$

σ_N Normal stress.

σ_V Vertical stress.

σ_{ys} Yield strength.

$\sigma_{\theta\theta}$ Tangential stress in polar coordinate system.

τ Shear stress.

ϕ_E Arctan K_I / K_{II}.

ϕ_S Arctan $3K_{II} / K_I$.

REFERENCES

1. Shah, R. C.: *Effects of Proof Loads and Combined-Mode Loadings on Fracture and Flaw Growth Characteristics of Aerospace Alloys.* NASA CR-134611, Boeing Aerospace Co., Seattle, Washington, March 1974.

2. Ranganath, S. and Gupta, Y.P.: *Fracture of 7075-T651 Aluminium under Combined-Mode Loading.* ATC Report No. B94400/4TR-10, Advanced Technology Center, Dallas, Texas, February 1974.

3. Ranganath, S. and Goolsby, R. D.: *Effect of Specimen Thickness on the Fracture Behavior of 7075-T6, -T651 Aluminum under Combined-Mode Loading.* ATC Report No. B-94400/4TR-29, Advanced Technology Center, Dallas, Texas, September 1974.

4. Liu, A. F.: *Crack Growth and Failure of Aluminum Plate under In-Plane Shear.* AIAA Paper No. 73-253, 11th Aerospace Sciences Meeting, Washington, D.C., January 1973.

5. Cotterell, B.: "Brittle Fracture in Compression." *International Journal of Fracture*, Vol. 8, No. 2, June 1972, pp. 195-203.

6. Hussian, M. A., Pu, S. L., and Underwood, J.: *Strain Energy Release Rate for a Crack Under Combined Mode I and Mode II.* STP 564 ASTM. Philadelphia, Pennsylvania, 1975.

7. Erdogan, F. and Sih, G. C.: "On the Crack Extension in Plates under Plane Loading and Transverse Shear." *Journal of Basic Engineering*, Trans. ASME, Series D, Vol. 85, 1963, pp. 519-527.

8. Sih, G. C.: *A Special Theory of Crack Propagation. Methods of Analysis and Solutions of Crack Problems*, edited by G. C. Sih, Noordhoof International Publishing, Leyden, Netherlands, 1972.

9. Iida, S. and Kobayashi, A. S.: "Crack Propagation Rate in 7075-T6 Plates under Cyclic Tensile and Transverse Shear Loadings." *Journal of Basic Engineering*, Trans. ASME, Series D, Vol. 91, 1969, pp. 764-769.

10. Roberts, R. and Kibler, J. J.: "Mode II Fatigue Crack Propagation." *Journal of Basic Engineering*, Trans. ASME, Series D., Vol. 93, 1971, pp. 671-680.

11.. Yokobori, T., Kamei, A. and Yokobori, At. T.: "Fatigue Crack Propagation under Mode II Loading." *International Journal of Fracture*, Vol. 12, No. 1, February 1976, pp. 158-160.

12. Holston, A.: "A Mixed-Mode Crack Tip Finite Element." *International Journal of Fracture*, Vol. 12, No. 6, December, 1976, pp. 887-899.

13. Abbatiello, A. A. and Derby, R. W.: *Notch Sharpening in a Large Tensile Specimen by Local Fatigue*. ORNL-TM-3925, Oak Ridge National Laboratory, November 1972.

14. Tada, H., Paris, P. and Irwin, G.: *The Stress Analysis of Cracks Handbook*, Del Research Corporation, Hellertown, Pennsylvania, 1973.

15. Campbell, J. E.; Berry, W. E.; and Feddersen, C. E.: *Damage-Tolerant Design Handbook*. HB-01, Battelle Columbus Laboratories, Columbus, Ohio, December 1972.

16. *Astronautics Structures Manual*. NASA Marshall Flight Space Center, November 1972, Section E-2, p. 31.

17. Collipriest, J. E., Ehret, R. M. and Thatcher, C.: *Fracture Mechanics Equations for Cyclic Crack Growth*. NASA Technology Utilization Report, MFS-24447, Rockwell International, April 19, 1973.

18. Wilson, W. K., Clark, W. G. and Wessel, T. E.: *Fracture Mechanics Technology for Combined Loading and Low-to-Intermediate Strength Metals*. Westinghouse Corporation, Pittsburgh, Pennsylvania, November 18, 1968.

19. Pook, L. P.: "The Effect of Crack Angle on Fracture Toughness." *Journal of Engineering Fracture Mechanics*, Vol. 3, No. 3., 1971, pp. 205-218.

DISTRIBUTION LIST

	No. of Copies

NASA-Lewis Research Center
21000 Brookpark Road
Cleveland, OH 44135

Attn:	Contracting Officer, MS 500-313	1
	Technical Report Control Office, MS 5-5	1
	Technical Utilization Office, MS 3-16	1
	AFSC Liaison Office, MS 501-3	1
	Library, MS 60-3	1
	R. H. Johns, MS 49-3	1
	G. T. Smith, MS 49-3	35
	M&S Contract File, MS 49-1	1
	J. C. Frethe, MS 49-1	1

National Aeronautics & Space Administration
Washington, DC 20546

Attn:	KT/Technology Utilization Office	1
	Library	1
	RWS/D. A. Gilstad	1

NASA Scientific and Technical Information Facility
Attn: Accessioning Department
P.O. Box 8757
Balt/Wash International Airport, MD 21240   10

NASA-Ames Research Center
Moffett Field, CA 94035

Attn:	Library	1
	D. Williams	1

NASA-Flight Research Center
P.O. Box 273
Edwards, CA 93523
Attn: Library   1

NASA-Goddard Space Flight Center
Greenbelt, MD 20771
Attn: Library   1

NASA-John F. Kennedy Space Center
Kennedy Space Center, FL 32931
Attn: Library   1

No. of
Copies

NASA-Langley Research Center
Hampton, VA 23365
Attn: Library   1
      R. W. Leonard   1
      H. Hardrath   1
      W. Elber   1

NASA-Manned Spacecraft Center
Houston, TX 77001
Attn: Library   1
      R. E. Johnson   1
      S. V. Glorioso   1
      R. Forman   1

NASA-Marshall Space Flight Center
Marshall Space Flight Center, AL 35812
Attn: Library   1
      S&E-ASTN/AA/C. Lifer   1
      S&E-ASTN/ASR/C. Crockett   1
      S&E-ASTN-AS/H. Coldwater   1

Air Force Office of Scientific Research
Washington, DC 20333
Attn: Library   1

Air Force Rocket Propulsion Laboratory (RPM)
Edwards, CA 93523
Attn: Library   1

Air Force Systems Command
Aeronautical Systems Division
Wright-Patterson AFB, OH 45433
Attn: Library   1
      C. F. Tiffany, Code ENF   1

Air Force Systems Command
Andrews Air Force Base
Washington, DC 20332
Attn: Library   1

Wright-Patterson Air Force Base
Wright Patterson Air Force Base, OH 45433
Attn: AFML Library   1
      D. M. Forney   1

No. of
Copies

Wright-Patterson Air Force Base
Wright-Patterson Air Force Base, OH 45433
Attn: AFFDL
      H. A. Wood   1

Department of the Army
U.S. Army Material Command
Washington, DC 20315
Attn: AMCRD-RC   1

Commanding Officer
U.S. Army Research Office (Durham)
Box CM, Duke Station
Durham, NC 27706
Attn: Library   1

Bureau of Naval Weapons
Department of the Navy
Washington, DC 20360
Attn: RRRE-6   1

Brown University
Providence, RI 02912
Attn: Technical Library   1
      J. R. Rice (Dr.)   1

California Institute of Technology
Pasadena, CA 91125
Attn: Technical Library   1
      V. F. Zackay   1

Case Western Reserve University
10090 Euclid Ave.
Cleveland, OH 44115
Attn: Technical Library   1

Carnegie Institute of Technology
Department of Civil Engineering
Pittsburgh, PA 15213
Attn: Library   1

No. of
Copies

Colorado State University
Department of Mechanical Engineering
Ft. Collins, CO 80521
Attn: F. Smith (Dr.)   1

Cornell University
Departmentof Materials Science and Engineering
Ithaca, NY 14830
Attn: Library   1

Pennsylvania State University
State College, PA 16802
Attn: Library   1

University of Denver
Denver Research Institute
P.O. Box 10126
Denver, CO 80210
Attn: Security Office   1

Aerospace Corp.
2400 E. El Segundo Blvd.
Los Angeles, CA 90045
Attn: Library-Documents   1

Bell Aerosystems, Inc.
Box 1
Buffalo, NY 14240
Attn: J. Davis   1

Brunswich Corp.
Defense Products Division
P.O. Box 4594
43000 Industrial Ave.
Lincoln, NE 68504
Attn: Library   1

Chrysler Corp.
Space Division
P.O. Box 29200
New Orleans, LA 70129
Attn: P. Munafo   1
       Library   1

No. of
Copies

Del Research Corp.
427 Main St.
Hellertown, PA 18055
Attn: P. Paris (Dr.)   1

Del West Associates, Inc.
6324 Variel Ave.
Suite C
Woodland Hill, CA 91364
Attn: Mr. Creager (Dr.)   1

General American Transportation Corp.
General American Research Division
7449 N. Natchez Ave.
Niles, IL 60648
Attn: R. N. Johnson (Dr.)   1

Commander
U.S. Naval Ordnance Laboratory
White Oak
Silver Springs, MD 20910
Attn: Library   1

Director, Code 6180
U.S. Naval Research Laboratory
Washington, DC 20390
Attn: Library   1
      H. W. Carhart   1
      J. M. Krafft   1

Atomic Energy Commission
Division of Reactor Development and Technology
Washington, DC 20767   1

National Science Foundation
Engineering Division
1800 G Street, NW
Washington, DC 20540
Attn: Library   1

Denver Federal Center
U.S. Bureau of Reclamation - Translation Group
P.O. Box 25007
Denver, CO 80225
Attn: P. M. Lorenz

No. of
Copies

atelle Memorial Institute
05 King Avenue
olumbus, OH 43201
ttn: Library   1
        E. Hulbert (Dr.)   1
        G. Hahn (Dr.)   1
        C. Bell (Dr.)   1

IT Research Institute
echnology Center
hicago, IL 60616
ttn: Library   1

tanford Research Institute
333 Ravenswood Ave.
enlo Park, CA 94025
ttn: Library   1

cDonnell Douglas Aircraft Corp.
.O. Box 516
ambert Field, MO 63166
ttn: Library   1

cDonnell Douglas Astronautics
estern Division
301 Bolsa Ave.
untington Beach, CA 92647
ttn: Library   1
        H. Babel   1
        R. Rawe   1

orth American Rockwell Space Division
2214 Lakewood Blvd.
owney, CA 90241
ttn: J. E. Collipriest   1

orthrop Space Laboratories
301 West Broadway
awthorne, CA 90250
tn: Library   1
        A. F. Liu (Dept. 3853, Zone 82)   1

No. of
Copies

North American Rockwell, Inc.
Rocketdyne Division
6633 Canoga Ave.
Canoga Park, CA 91304
Attn: Library, Dept. 596-306   1
      G. Vorman   1

General Dynamics
P.O. Box 748
Ft. Worth, TX 76101
Attn: Library   1
      C. D. Little   1

General Dynamics/Convair Aerospace
P.O. Box 1128
San Diego, CA 92112
Attn: Library   1
      J. Jensen   1
      W. Witzel   1
      J. Haskins   1

Grumman Aircraft Engineering Corp.
Bethpage, Long Island, NY 11714
Attn: Library   1

Jet Propulsion Laboratory
4800 Oak Grove Dr.
Pasadena, CA 91103
Attn: Library   1
      J. Lewis   1

Ling-Temco-Vought Corp.
P.O. Box 5907
Dallas, TX 75222
Attn: Library   1
      R. Goolsby   1
      S. Ranganath   1

Lockheed Missiles and Space Co.
P.O. Box 504
Sunnyvale, CA 94087
Attn: Library   1
      R. E. Lewis   1

No. of
Copies

Republic Aviation Fairchild Hiller Corp. Farmingdale, NY 11735 Attn: Library	1
Thiokol Chemical Corp. Wasatch Division P.O. Box 524 Brigham City, UT 84302 Attn: Library Section	1
TRW Systems, Inc. One Space Park Redondo Beach, CA 90278 Attn: Technical Library, Document Acquisitions	1
United Aircraft Corp. Corporate Library 400 Main St. East Hartford, CT 06108 Attn: Library	1
United Aircraft Corp. Pratt and Whitney Division Florida Research and Development Center P.O. Box 2691 West Palm Beach, FL 33402 Attn: Library	1
Westinghouse Research Laboratories Beulah Rd., Churchill Borough Pittsburgh, PA 15235 Attn: Library	1
W. K. Wilson	1
G. T. Wessel	1
Massachusetts Institute of Technology Cambridge, MA 02139 Attn: Library	1
Purdue University W. Lafayette, IN 47906 Attn: Library	1
C. T. Sun	1